Distribution Agreement

In presenting this thesis or dissertation as a partial fulfillment of the requirements for an advanced degree from Emory University, I hereby grant to Emory University and its agents the non-exclusive license to archive, make accessible, and display my thesis or dissertation in whole or in part in all forms of media, now or hereafter known, including display on the world wide web. I understand that I may select some access restrictions as part of the online submission of this thesis or dissertation. I retain all ownership rights to the copyright of the thesis or dissertation. I also retain the right to use in future works (such as articles or books) all or part of this thesis or dissertation.

Signature:

_____ _____

Shengyuan Wang Date

α-helical peptide Self-assembly Structure Design and Characterization

By

Shengyuan Wang

Doctor of Philosophy

Chemistry

_____

Vincent Conticello, Ph.D.

Advisor

_____

David Lynn, Ph.D.

Committee Member

_____

Khalid Salaita, Ph.D.

Committee Member

Accepted:

_____

Lisa A. Tedesco, Ph.D.

Dean of the James T. Laney School of Graduate Studies

_____

Date

α-helical peptide Self-assembly Structure Design and Characterization

By

Shengyuan Wang

B.S., Georgia Institute of Technology, 2015

Advisor: Vincent Conticello, Ph.D.

An abstract of

A dissertation submitted to the Faculty of the

James T. Laney School of Graduate Studies of Emory University

in partial fulfillment of the requirements for the degree of

Doctor of Philosophy

in Chemistry

2021

Abstract

α-helical peptide Self-assembly Structure Design and Characterization

By Shengyuan Wang

Functionalized nanomaterials are extensively researched in the past decades due to their high functionalization density, and unique physical and mechanical properties compared to their macro-scale material counterparts. Among them, protein and peptide-based nanomaterials are especially sought after, as they encode life-related functions that are often not accessible by current technologies. However, precise control and rational design of protein and peptide-based nanomaterials are difficult to achieve. This thesis presents the design and characterization of three α-helical peptide systems with the recently discovered, novel cross-α tertiary structure that self-assemble into nanofibrils, nanosheets from fibril lamination, and nanotubes from nanosheet wrapping; and the design and characterization of one α-helical coiled-coil peptide system with designed coiled-coil interfaces promoting 2D lateral association of coiled-coil bundles that self-assemble into nanosheets. The results will enhance our understandings of protein self-assembly principles and hopefully contribute to protein and peptide-based nanomaterial designs in the future.

α-helical peptide Self-assembly Structure Design and Characterization

By

Shengyuan Wang

B.S., Georgia Institute of Technology, 2015

Advisor: Vincent Conticello, Ph.D.

A dissertation submitted to the Faculty of the

James T. Laney School of Graduate Studies of Emory University

in partial fulfillment of the requirements for the degree of

Doctor of Philosophy

in Chemistry

2021

Acknowledgements

First I must express my deepest gratitude towards my advisor Dr. Vincent Conticello, as well as my committee members Dr. David Lynn and Dr. Khalid Salaita for your guidance and support during my time at Emory. Also to the wonderful Conticello lab members: Dr. Spencer Hughes, Dr. Charles Modlin, and current lab members Duong Nyugen, Jessalyn Rogers, Ordy Gnewou, Ayda Gonzales and George Chen, staff at The Robert P. Apkarian Integrated Electron Microscopy Core at Emory: Dr. Ricardo Guerrero-Ferreira, Hong Yi and Art McCanna, collaborators: Dr. Ed Egelman at University of Virginia and his lab members Christella Gorrdon, Youngsun Kim

Table of Contents

Table of Figures

Chapter 1: Introduction to 1D and 2D Self-assembled Peptide Nanomaterials

1.1 Introduction

Nanomaterials have proven themselves useful over the past decades serving as high-performance semiconductors, materials with unique mechanical[1], thermal[2] and electrical[3] properties, applications in biology and medicine[4], and many more. While inorganic nanoparticles[5] and small-molecule frameworks[6-7] are often explored as functional nanomaterials due to their stability and ease of preparation and modification, bio-nanomaterials based on nucleic acids and amino acids remain as a hot research topic as they encode information obtained through billions of years of evolution, acting as stepping stones or points of direction when developing novel functions. To illustrate, as of Nov. 30th, 2020 there are 171,588 biological macromolecular structures deposited in the Protein Database Bank (https://www.rcsb.org/)[8] including 137,402 naturally occurring protein structures, and 34,186 synthetic or *de novo* structures. In comparison, while MOFDB at Northwestern University has a comparable size at 163396 entries of metal-organic-framework structures (https://mof.tech.northwestern.edu/), and CoRE-COF offers 450 entries of covalent-organic-framework structures (https://github.com/core-cof/CoRE-COF-Database/tree/master/CoRE-COFs_DT449-v4.0-qeq)[9], most of them are synthetic structures and do not encode natural functions. Not only many of these functions encoded in proteins support life, some of the enzyme-catalyzed reactions hold reactivity, selectivity and yield unobtainable through modern synthetic chemistry approaches, thus understanding these protein functions gathers a great interest to this date. Exploring and understanding the principles of bio-macromolecule self-assembly will help understand how these molecules fold into a particular shape to perform functions, and subsequently help with repurposing and redesigning their functions.

Nucleotide and its polymer form, DNA naturally encode genetic information up to billions of nucleotide base-pairs[10], that would translate to gigabytes of data in a micro-scale, or an outstandingly high data density. DNAs has also been shown to self-assemble into well-controlled, pre-defined shapes, patterns and structures[11]. On the other hand, amino acid and its polymer form, peptide and protein offer much more complexity, where protein structures are classified into 4 degrees of structural levels, and there are 20 naturally occurring amino acids compared to 4 naturally occurring nucleotides. However, protein self-assembly is much harder to control compared to DNA self-assembly. While a huge amount of effort characterizing, predicting and designing protein structures has been made over the past 20 years towards protein structure and function design[12-13], the precise control of protein self-assembly pathway and protein function is still difficult as to this date, illustrated by the lack of success in protein design (no activities[14-15]; no experimental confirmation[16]; or with a marginal success rate[17]) and the severe lack of support from computational chemistry communities developed such related softwares (for example, prospr, a re-implementation of Deepmind's top protein structure prediction performing algorithm competed in Critical Assessment of Structure Prediction (CASP) 2018, received no updates since 13 months ago and is currently broken for novice users, perhaps due to a discouraging peer-review process[18]), despite several successful computational enzyme design examples using an iterative method were presented back in 2010-2012[19-21]. On top of the difficulty of accurately predicting protein structures, it also requires a huge amount of time and effort characterizing protein structures via crystallization [22] and/or cryo-electron microscopy[23] to confirm the designed protein structures. Nonetheless, progress still has been made over the past decades on characterizing and designing peptide self-assemblies through rational or computational design, albeit many at a much simpler level towards forming straightforward geometric shapes. The following sections will give a brief overview of the current developments of α-helix based peptide self-assembly structures and designs, as well as a brief comparison of peptide self-assemblies between α-helix and other protein secondary structures.

1.2 α-helix peptide self-assembly

α-helix peptides are capable of forming a variety of self-assemblies including fibrils, tapes, nanosheets and crystals. A native α-helix has a 3.6 residues / turn geometry, or 18 residues / 5 turns in whole numbers, effectively dividing a helix to an 18-face cylinder[24]. As a result, it's difficult to manually predict and design native α-helix interfaces, reflected by α-helices often tilt and stack at an angle[25-26] in self-assembly structures (Figure 1.1), thus α-helix peptide self-assemblies are often predicted by computational methods[27-28] using softwares such as Rosetta.

A B

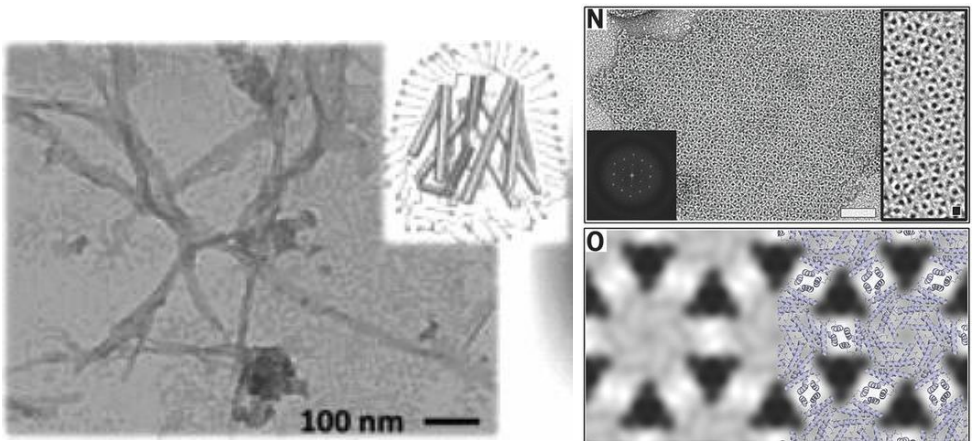

Figure 1.1. A) amyloid-like α-helical fibril LacY, figure adapted from ref [26]. B) computationally designed peptide P6_H with a P6 space group symmetry, figure adapted from ref [27].

Despite the difficulties predicting α-helix self-assembly, manually designed α-helix peptide self-assemblies achieved success nonetheless. Hughes et al. redesigned naturally existing leucine-rich protein repeat motifs (PDB ID: 3LTJ and 1LRV) to form α-barrel nanotubes, where highly conserved residues in the repeat sequences are preserved, solvent-exposing residues are re-designed to polar residues, and turn motifs in the repeat sequences are removed to allow axial stacking interactions, i.e. nanotube elongation[29]. The designed HEAT_R1 and LRV_M3del1

systems form robust fibril assemblies, and HEAT_R1 has been demonstrated to be functionalized with proof-of-concept mCherry red fluorescent protein without hindering its fibril formation, enabling nanomaterial functionalization applications.

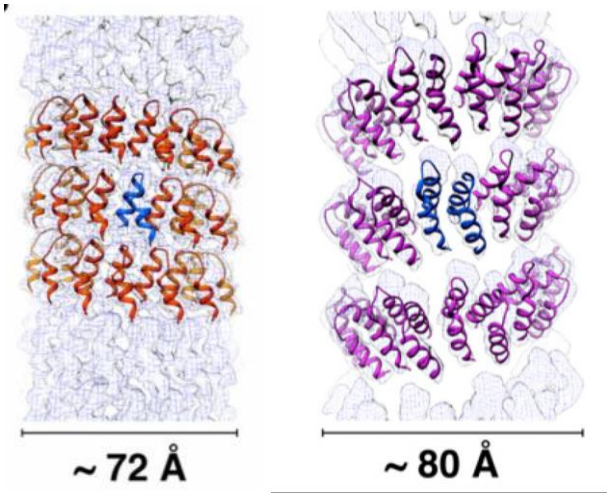

Figure 1.2. atomic model of HEAT_R1 (left, PDB ID:6MK1) and LRV_M3del1 (right, PDB ID: 6HQE). Figure adapted from ref [30].

As for more "*de novo* from scratch" designs, Magnotti et al. designed 3 symmetric interfaces in an α-helix system 3FD[31] (Figure 1.3), where 6 residues account for each interface, 2 large hydrophobic residues such as Leu and Ile are at position 3 and 4 to act as the main driving force of self-assembly; 2 small hydrophobic residues Ala are at position 2 and 5 to supplement the hydrophobic interfaces; and lastly 2 complimentarily charged residues E and K are at position 1 and 6 to form salt-bridges in the interface. This system expects each 3FD monomer to interact with 3 other monomers, achieving a 3-fold symmetry and 2D propagation. Two peptides, 3FD-IL and 3FD-LL robustly self-assemble into 2D nanosheets with tolerability towards salt concentration up to 1M NaCl, however this system is susceptible to hydrophobic residue mutations and functionalizations at its C and N termini. In addition, a designed 4 symmetric interfaces derivative

of this system, could be termed 4FD, doesn't self-assemble, further illustrating the difficulty predicting α-helical self-assemblies.

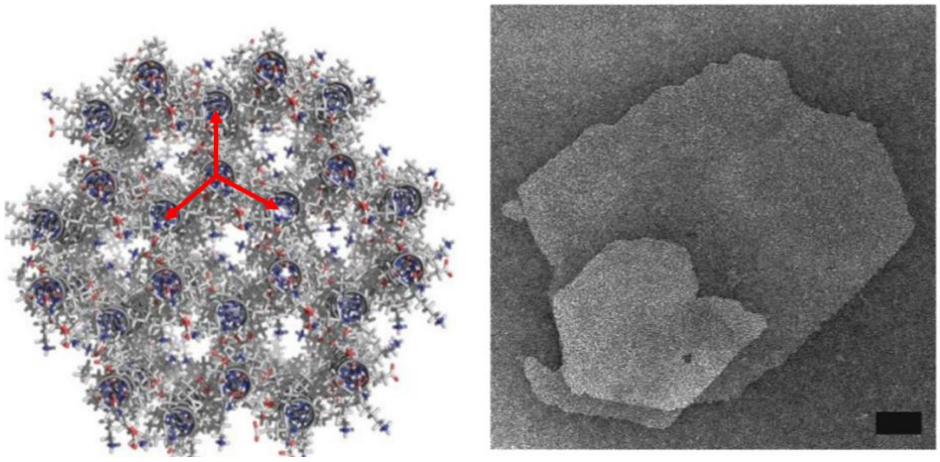

Figure 1.3. Proposed structure model (left) and TEM micrograph (right, scale bar = 200 nm) of 3FD-IL, figure adapted from ref [32].

One other α-helix based tertiary structure is the recently discovered cross-α structure by Tayeb-Fligelman et al.[33], where phenol soluble modulin α3 (PSMα3) secreted by *Staphylococcus aureus* is shown to stack and mate into a fibril structure (Figure 1.4A), similar to cross-β amyloid fibril structures where β-strand stacking and mating are the signature structural features of cross-β fibrils. PSMα3's cross-α structure has been argued to be detrimental to PSMα3's cytotoxicity, but this hypothesis is still under debate[34-35]. It appears cross-α structures may be somewhat common in nature, especially in amphiphilic antimicrobial peptides[36], and may possess antimicrobial/cytotoxicity importance. Cross-α design principles have been explored recently as well; inspired from a natural membrane protein αAm_{mem}, a coiled-coil optimized system has been shown to mate as a coiled-coil dimer, and the dimers stack to afford fibril elongation similar to PSMα3[37] (Figure 1.4B), enabling design space for cross-α structures.

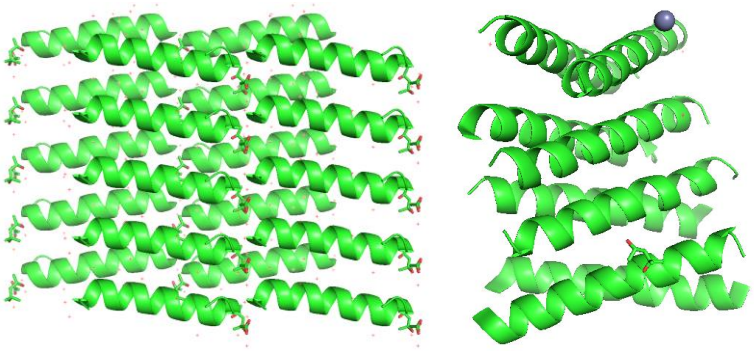

Figure 1.4. (left)PDB ID: 5I55. (right)PDB ID: 6C4X. models rendered in PyMol.

One well-characterized α-helix rational design system is coiled-coil. Coiled-coils are α-helices wind around each other into a supercoil, instead of packing like straight straws like in PSMα3's cross-α structure presented above. The slight twist in coiled-coil helices changed their geometries to 3.5 residues / turn, or 7 residues / 2 turns, effectively divide each coiled-coil helix into 7 distinct interfaces to allow a coiled-coil sequence to be plotted on a heptad helical wheel. Two of the interfaces, typically labelled *a* and *d*, are often hydrophobic to drive self-assembly as these two interfaces interact to form a hydrophobic core. Residues at these interfaces form knobs-into-holes interactions, where each residue from one interface (knob) are effectively sandwiched between two residues from the other interface (hole) (Figure 1.5).

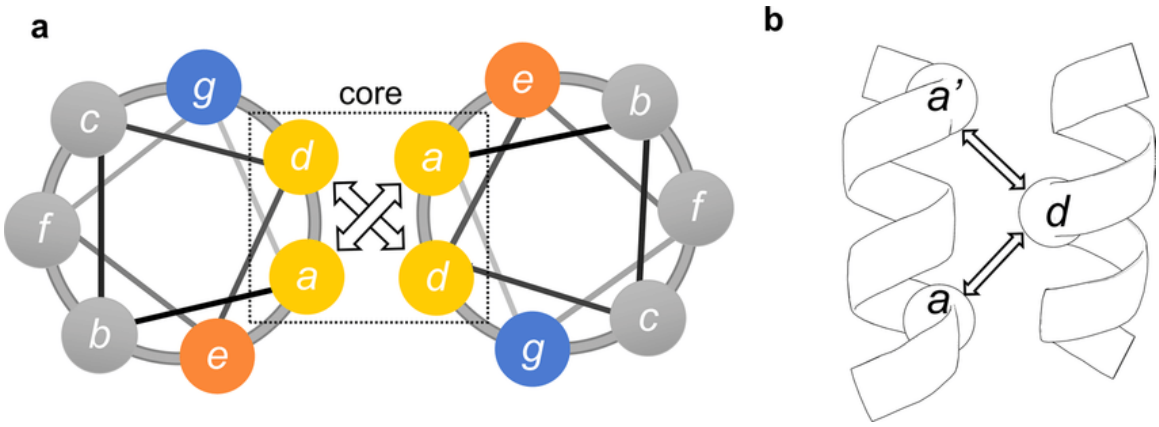

Figure 1.5. a) heptad representation of a generic coiled-coil. b) sideview of a generic coiled-coil showing the a-d knobs-into-holes interactions. Figure adapted from ref [38].

Coiled-coils can be designed to self-assemble into various dimensions. Walshaw and Woolfson classified coiled-coils into 4 types[39] (Figure 1.6): the traditional dimer is termed type-N, where a coiled-coil dimer is expected via *a, d* face interactions to form a hydrophobic core; type-1 describes a coiled-coil bundle where 3 faces (*a, d, e* or *a, d, g*) participate in inter-helix interactions; type-2 describes a bundle where 4 faces (*a, d, e, g*) participate in inter-helix interactions; and finally type-3 describes a bundle where a non-consecutive pair of 2 faces participate in inter-helix interactions, such as *a, d* faces and *b, f* faces shown below.

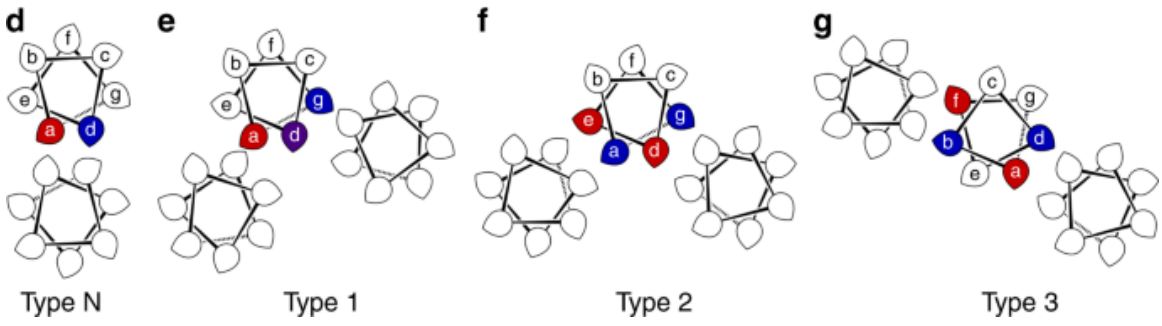

Figure 1.6. 4 types of coiled-coil bundles, inter-helix interactions are labeled with colors. Figure adapted from ref [40].

Naturally, the identity of amino acids at these inter-helix interacting positions can have profound impacts on the resulting structure (Figure 1.7), such as β-branched amino acids can direct the orientation and the number of helices in the coiled coil bundle[40-41]; special motifs such as an Arg motif can change how helices interact[42]. In general, type N, 1 and 2 form coiled-coil bundles and small α-barrels, where type 3 leads to gigantic α-barrels, or stacking α-helices resulting in tapes, resembling of the cross-α structure mentioned above. Coiled-coil bundles can extend through sticky-end designs[43-44] or bundle stackings[40, 45-46] to form 1D assemblies, as well as propagate in a P321 space group symmetry to form crystals via computational design[47]. Although coiled-coils have been well characterized ~20 years ago, recent discoveries of type 2 αAm[37] and type 3 Form[42] cross-α structures showed coiled-coils could be much more versatile in protein design, which will be explored in some of the later chapters presented in this thesis.

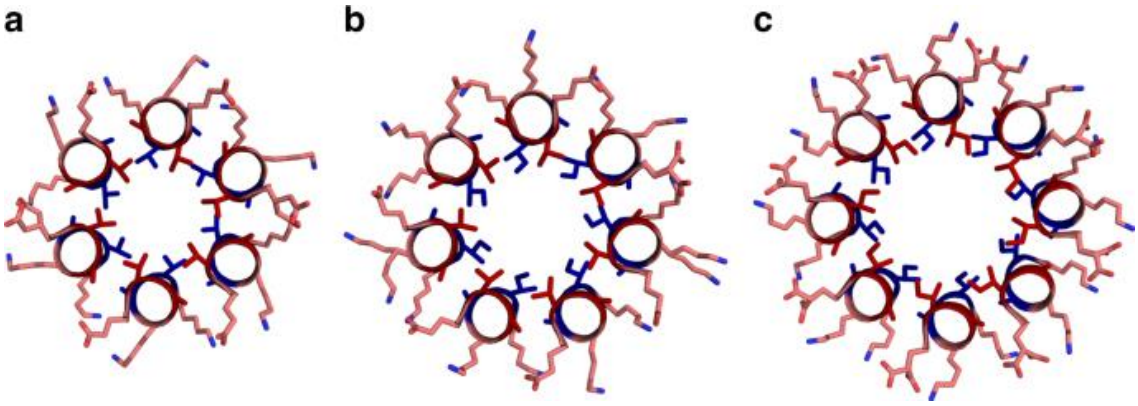

Figure 1.7. effect of amino acid identities at a, d positions of a type 2 coiled-coil system, CC-Type2, on the number of helices in a coiled-coil bundle. a) all Val at a, d faces, hexamer; b) Ile at a, Val at d faces, heptamer; c) all Ile at a, d faces, octamer. Figure adapted from ref [40].

1.3 1D peptide self-assembly based on other structural motifs.

Dipeptide is perhaps the simplest 1D peptide self-assembly system. As simple as two amino acids, diphenylalanine (FF) is shown to self-assemble into well-behaving nanotubes [48, 49]. FF is first seen as a motif from Alzheimer's β-amyloid structure, but this motif alone is able to self-assemble into nanotubes driven by aromatic π-π stacking and hydrophobic interactions in a hexagonal pattern[50] (Figure 1.8).

A B

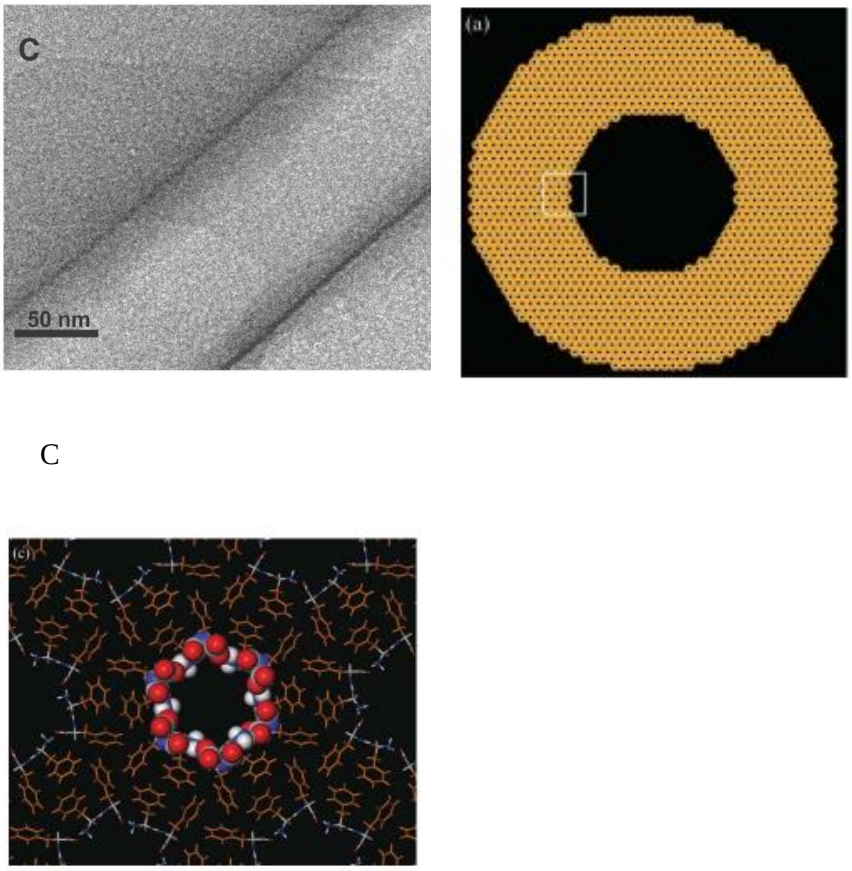

C

Figure 1.8. A) TEM of FF nanotube, figure adapted from ref [49]. B), C) proposed structure of FF nanotubes, figure adapted from ref [50].

Due its disassembly nature when diluted in solution, FF has been explored as a drug delivery vehicle aimed to achieve a slow drug release[51-52] (Figure 1.9A). FF fibril formation can also be

directed on a seeded surface by electric field[53] or aniline vapor[54], where the former could be utilized into energy storage (Figure 1.9B). While most FF self-assemblies require dissolving in cytotoxic 1,1,1,3,3,3-hexafluoro-2-propanol (HFIP), FF is also shown to assemble under physiologically relevant conditions after HFIP is dialyzed[55], enabling FF assemblies to be used for bio-related applications. FF is also investigated to be conjugated with other nanoparticles such as nucleic acid[56], metal nanoparticles[57] and drug molecules[58] (Figure 1.9C), although functionalized FFs no longer assemble into fibrils but nanoparticles instead. As expected, FF functionalization occurs at its C and N termini to be conjugated with other molecules or moieties.

A

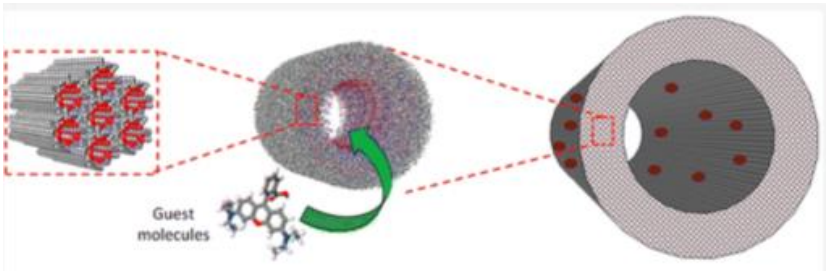

B

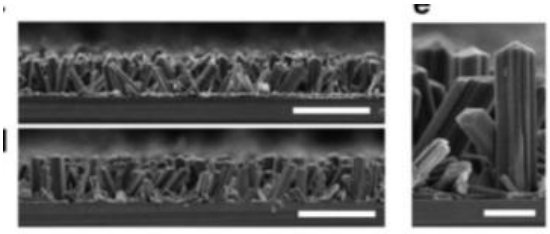

C

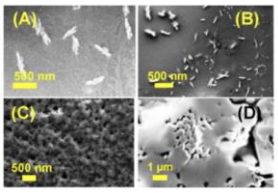

Figure 3. SEM images of NP (A) **7c** (H-Phe-Phe-*tz*-G^{NHiBu}-*aeg*-OEt), (B) **7d** (H-Phe-Phe-*tz*-T-*aeg*-OEt), (C) **8c** (Boc-Phe-Phe-*tz*-G-*aeg*-OH), and (D) **8d** (Boc-Phe-Phe-*tz*-T-*aeg*-OH).

Figure 1.9. A) Functionalized FF nanotube to introduce Rhodamine B inside the nanotube, figure adapted from ref [51].B) Controlled FF nanocrystal growth for power generation applications, figure adapted from ref [53]. C) SEM images of conjugated FF with DNA molecules, figure adapted from ref [56].

Cross-β amyloid and amyloid-like fibrils are perhaps the most famous β-strand based 1D structures. Amyloid fibrils are first found in patients with neurological diseases such as amyloidβ in Alzheimer's, which then led to the hypothesis that amyloid formation is the cause of neural cell degeneration, and inhibiting/reversing amyloid fibril formation would be a cure to such neurological diseases, thus gathered research interests[59]. Cross-β structure is defined as β-strands or β-hairpins, β-strands linked by a turn sequence, stack against the fibril direction while mating to form a bi-layered structure, resulting in a signature X-ray fibril diffraction pattern that shows both the β-strand stacking distance (~4.7 Å) and the β-strand mating distance (~10 Å)[60] (Figure 1.10). β-strand mating is usually through a dry interface, where β-strand stacking is usually facilitated by hydrogen-bonding via amino and carboxyl groups of amino acid residues, phenyl moieties from phenylanaline, tryptophan or tyrosine, and sometimes hygrogen-bonding via amide moieties from glutamine and asparagine[61].

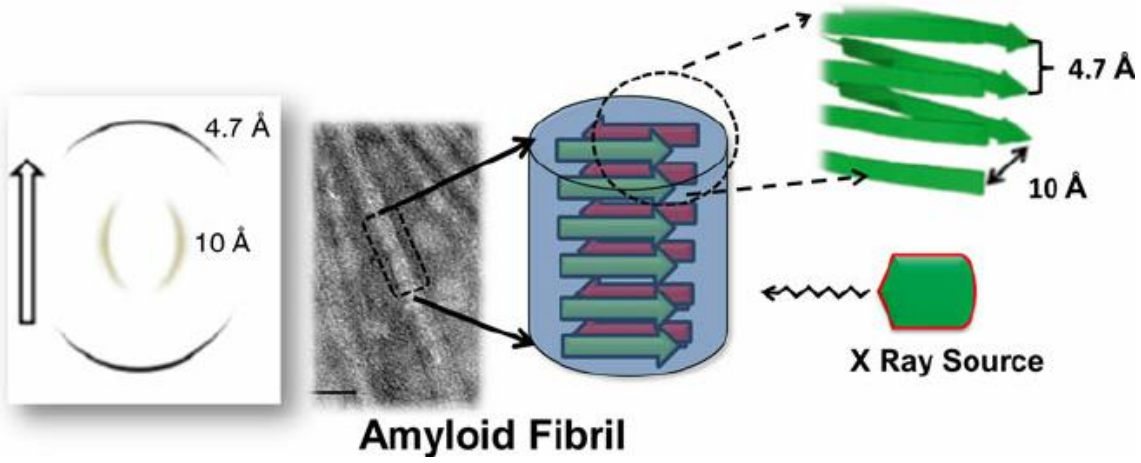

Figure 1.10. X-ray diffraction pattern of a monoclonal immunoglobulin light chain, figure adapted from ref [60].

Not only as potential medical targets, amyloids and cross-β structures are also explored as nanomaterials due to their superb stability and robustness[62-64]. However, while amyloids are shown to self-oligomerize/laminate into high-ordered nanotubes[65] and nanosheets[66-67], it's not hard to

notice their poor morphology selectivity and polymorphic nature[68-69], rendering them difficult to be further designed as functional nanomaterials. In addition, amyloids are often assembled under the presence of acetonitrile and have a long self-assembly time in aqueous conditions, further limiting their bio-application scope. Many proposed functional amyloid applications focus on the detection and inhibition of existing amyloid fibrils with functionalized amyloid peptide counterparts[70-72].

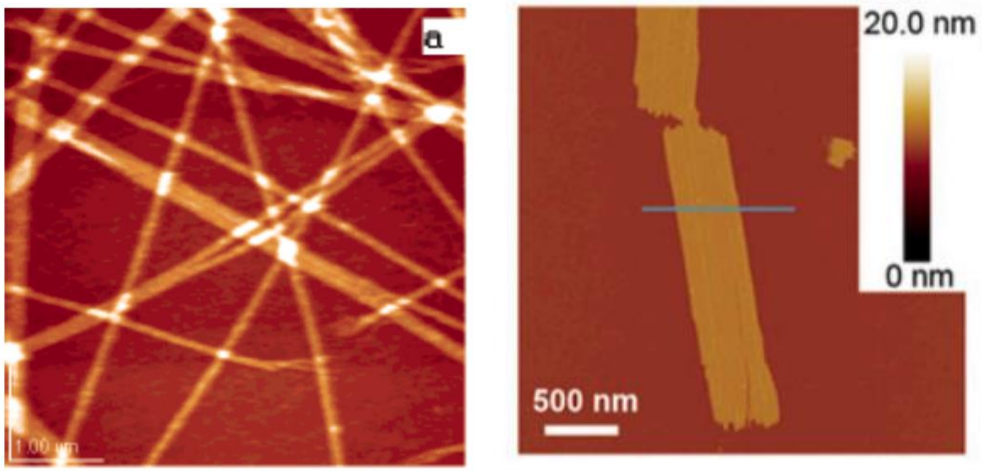

Figure 1.11 A) Aβ(16−22) laminated nanotube self-assembly, adapted from ref [65]. B) KLVFFAK nanosheet self-assembly, adapted from ref [67].

Amphiphilic peptides (PA) are also capable of self-assembling into 1D nanotube structures, much similar to the Aβ(16−22) laminated nanotube self-assembly presented above. Amphiphilic peptides are often polar amino acid residues tagged with a hydrophobic tail[73], or a chain of non-polar amino acid residues[74], where the hydrophobic portion will laminate into a micelle-like ring but stacks to afford fibril elongation (Figure 1.12). PA self-assembly can be controlled by modifying the length of the hydrophobic tail, controlled by disulfide bond formation/dissociation of Cys residues, and of course the identity of hydrophilic amino acid residues affecting the resulting fibril's length and stiffness[73]. PAs have been explored as antimicrobial peptides[75], self-healing

materials, semiconductors and others, but in the perspective of functionalized materials, PAs are limited by the fact there's only one site for functionalization at the hydrophilic terminus.

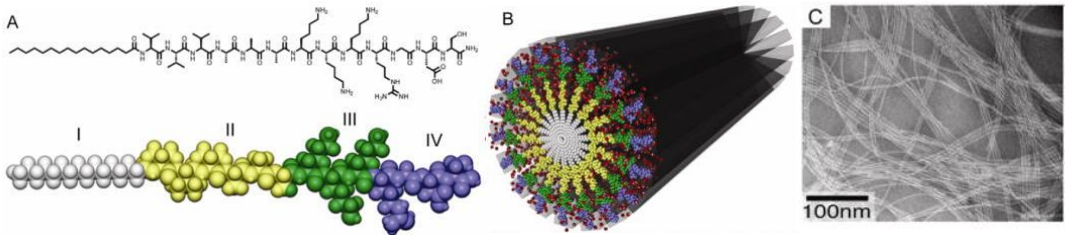

Figure 1.12. A) sequence of IKVAV-PA; B) proposed structure of IKVAV-PA; C) TEM micrograph of IKVAV-PA. figure adapted from ref [76].

Collagen and collagen-mimetic peptides (CMP) are yet another family of peptides capable of adopting 1D self-assemblies. These peptides typically adopt a tripeptide pattern (X-Y-Gly) where 3 amino acids represent a block, each CMP will have blocks that are positively charged, negatively charged or hydrophobic to have stacked or staggered alignments in triple helical bundles to form fibrils (Figure 1.13). Sun et al. reported CMP2 and CMP3, which are tolerable to incorporating the synthetic triple helical peptide integrin and lanthanide ion binding motif GFOGER, can still self-assemble into fibrils and be used as a Lanthanide ion-mediated assembly motif that bind and detect integrin motifs from HeLa cells. Functionalizing CMPs often involves CMP and collagen hybrids that retain the hybrids' self-assembly behaviors[77].

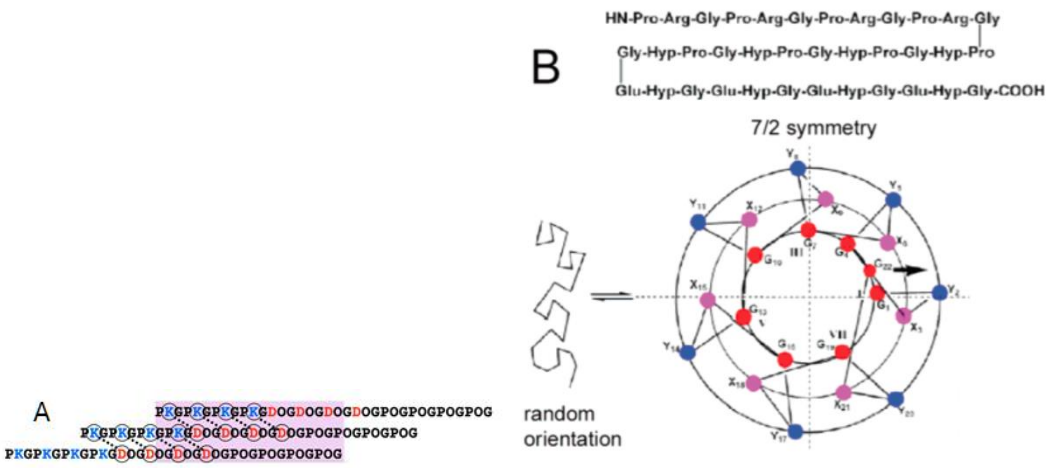

Figure 1.13. A) staggered sequence alignment of F1, figure adopted from ref[78]. B) Proposed triple-helical wheel diagram of CPII, figure adopted from ref[79].

1.4 2D peptide self-assembly based on other structural motifs

2D peptide self-assemblies promise applications in healing soft-materials, catalytic platforms, bio-related nanodevices, and platforms to assemble into 3D structures, but the difficulty controlling twice the number of interfaces to direct 2D propagation compared to 1D is not an easy obstacle to overcome, it has been suggested all of the interfaces must have equivalent interface binding energies to avoid self-associating into 1D assemblies instead[67].

Cross-β amyloids have the tendency to laterally associate into 2D tapes, but often with twisting angles to wrap into helical tapes and nanotubes[66]. Non-twisting cross-β fibril lamination has been reported by Lamm et al.[66], where the authors propose the alternative D-Pro and L-Pro in the central turn region of the peptide's strand-turn-strand β-hairpin monomer structure breaks the fibril's tendency to twist, thus resulting in a non-twisting morphology (Figure 1.14A). While promising, this is difficult to reproduce in other systems without a hairpin monomer motif. Dai et al. reported a cross-β amyloid system able to associate into nanosheets, where the amyloid fibril's two solvent-facing interfaces can interact with all others (Figure 1.14B)[67] in roughly equivalent binding energies. However, this may also be difficult to implement in other systems, as the authors did not present another cross-β amyloid 2D self-assembly system based on this design principle.

A

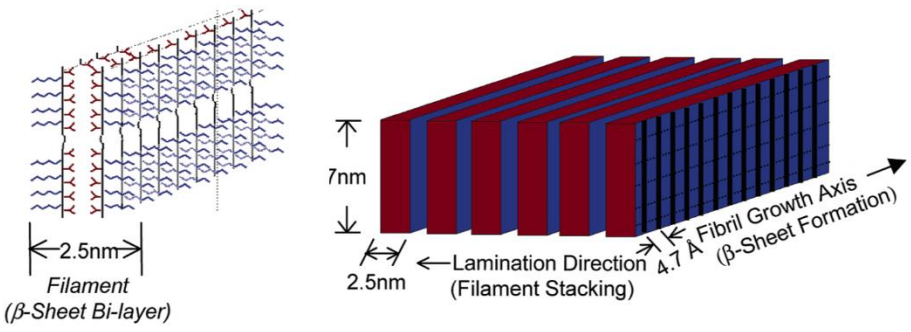

B

Figure 1.14. A) Proposed structure of $(VK)_4$-V^DPPT-$(KV)_4$, figure adapted from ref [66]. B) Interface illustrations of KLVFFAK, figure adapted from ref [67].

Lin et al. reported a peptide amphiphile, F6C11, assembled into single-layer 2D assembly[80] (Figure 1.15). The authors reported both the hydrophobic tail's and the hydrophilic residues' strength contribute to this 2D self-assembly, shortening the hydrophobic tail, incorporating less Phe or mutating Phe to Val all inhibited 2D self-assembly. While promising, unfortunately converting a peptide sequence into a peptide amphiphile may not guarantee 2D self-asssembly.

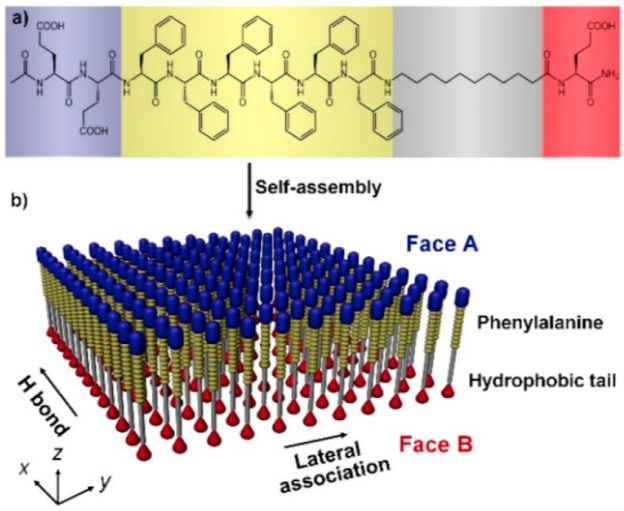

Figure 1.15. Proposed structure of F6C11. Figure adapted from ref [80].

Lastly, several structurally defined with potential precise structure control 2D CMP self-assembly cases have been reported. Tao et al. designed a CMP system, NSII with matching number

of polar and non-polar tripeptide blocks to promote 2D propagation through the polar blocks' complimentary electrostatic interactions[81] (Figure 1.16). Furthermore, Tao et al. showed extending the length of one polar blocks can make the resulting CMP, named CP+ and CP-, 2D assembly positively or negatively charged; co-assembling CP+ and CP- can result in lego/sandwiched stacked-layer sheets[82]. Later, Merg et al. showed CMPs with varied lengths of non-polar tripeptide blocks, the $4S(X)_{4n4}$ series, can co-assemble as well, effectively creating mixed CMP 2D nanosheets with various heights at different regions of the resulting nanosheet[83]. These results are very promising to achieve 2D and 3D bio-nanomaterials with precise structure control.

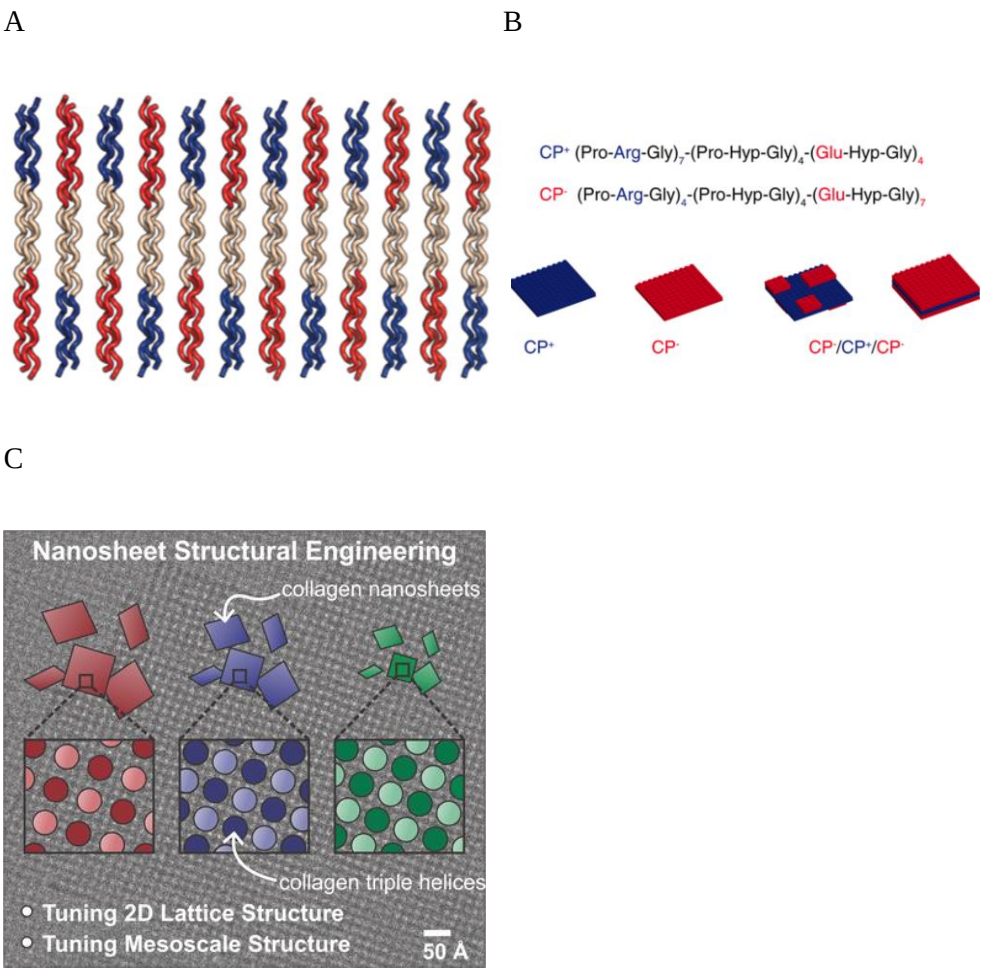

Figure 1.16. A) Proposed structure of NSI and NSII, figure adapted from ref [81]. A) Sequence and proposed structure of CP+ and CP-, figure adapted from ref [82]. A) Illustration of the $4S(X)_{4n4}$ peptides, figure adapted from ref [83].

1.5 Conclusion

This chapter gives an overview of the current development of 1D and 2D peptide-assemblies. While metal-organic frameworks, metal-based nanoparticles, graphene-based carbon nanotubes and nanosheets and others have gathered much research interests, bio-inspired materials using peptides and DNA as building blocks have the unique advantage of a bottom-up approach where the interactions of each monomer building block can be controlled, and being bio-related allows these materials to harvest the bio-related functions encoded by nature.

α-helix is a common protein secondary motif and is capable of self-assembling to a variety of structures. Compared to dipeptide, β-strand and CMP, α-helix are stable, structurally diverse, and well-characterized to have a range of computational tools like Rosetta to help with the protein design/prediction process. With the protein structure characterization tool cryo-EM gaining another wave of popularity by being awarded the Nobel Prize in Chemistry in 2017, as well as the recent advances in artificial intelligence alphaFold2 on protein folding prediction, the future is bright to achieve easily prepared (α-helical based) peptide nanomaterials with precise structure control, and direct years of academic research efforts into real-world applications.

References

1. Wu, Q.; Miao, W.-s.; Zhang, Y.-d.; Gao, H.-j.; Hui, D., Mechanical properties of nanomaterials: A review. *Nanotechnol Rev* **2020,** *9* (1), 259-273.
2. Qiu, L.; Zhu, N.; Feng, Y.; Michaelides, E. E.; Żyła, G.; Jing, D.; Zhang, X.; Norris, P. M.; Markides, C. N.; Mahian, O., A review of recent advances in thermophysical properties at the nanoscale: From solid state to colloids. *Physics Reports* **2020,** *843*, 1-81.
3. Minea, A. A., A Review on Electrical Conductivity of Nanoparticle-Enhanced Fluids. *Nanomaterials-Basel* **2019,** *9* (11).
4. Salata, O. V., Applications of nanoparticles in biology and medicine. *J Nanobiotechnology* **2004,** *2* (1), 3.
5. Khan, I.; Saeed, K.; Khan, I., Nanoparticles: Properties, applications and toxicities. *Arabian Journal of Chemistry* **2019,** *12* (7), 908-931.
6. Baumann, A. E.; Burns, D. A.; Liu, B.; Thoi, V. S., Metal-organic framework functionalization and design strategies for advanced electrochemical energy storage devices. *Communications Chemistry* **2019,** *2* (1), 86.
7. Geng, K.; He, T.; Liu, R.; Dalapati, S.; Tan, K. T.; Li, Z.; Tao, S.; Gong, Y.; Jiang, Q.; Jiang, D., Covalent Organic Frameworks: Design, Synthesis, and Functions. *Chemical Reviews* **2020,** *120* (16), 8814-8933.
8. Berman, H. M.; Westbrook, J.; Feng, Z.; Gilliland, G.; Bhat, T. N.; Weissig, H.; Shindyalov, I. N.; Bourne, P. E., The Protein Data Bank. *Nucleic Acids Research* **2000,** *28* (1), 235-242.
9. Tong, M.; Lan, Y.; Yang, Q.; Zhong, C., Exploring the structure-property relationships of covalent organic frameworks for noble gas separations. *Chemical Engineering Science* **2017,** *168*, 456-464.
10. Hood, L.; Rowen, L., The Human Genome Project: big science transforms biology and medicine. *Genome Med* **2013,** *5* (9), 79-79.
11. Ong, L. L.; Hanikel, N.; Yaghi, O. K.; Grun, C.; Strauss, M. T.; Bron, P.; Lai-Kee-Him, J.; Schueder, F.; Wang, B.; Wang, P.; Kishi, J. Y.; Myhrvold, C.; Zhu, A.; Jungmann, R.; Bellot, G.; Ke, Y.; Yin, P., Programmable self-assembly of three-dimensional nanostructures from 10,000 unique components. *Nature* **2017,** *552* (7683), 72-77.
12. Beberg, A. L.; Ensign, D. L.; Jayachandran, G.; Khaliq, S.; Pande, V. S. In *Folding@home: Lessons from eight years of volunteer distributed computing*, 2009 IEEE International Symposium on Parallel & Distributed Processing, 23-29 May 2009; 2009; pp 1-8.
13. Leman, J. K.; Weitzner, B. D.; Lewis, S. M.; Adolf-Bryfogle, J.; Alam, N.; Alford, R. F.; Aprahamian, M.; Baker, D.; Barlow, K. A.; Barth, P.; Basanta, B.; Bender, B. J.; Blacklock, K.; Bonet, J.; Boyken, S. E.; Bradley, P.; Bystroff, C.; Conway, P.; Cooper, S.; Correia, B. E.; Coventry, B.; Das, R.; De Jong, R. M.; DiMaio, F.; Dsilva, L.; Dunbrack, R.; Ford, A. S.; Frenz, B.; Fu, D. Y.; Geniesse, C.; Goldschmidt, L.; Gowthaman, R.; Gray, J. J.; Gront, D.; Guffy, S.; Horowitz, S.; Huang, P.-S.; Huber, T.; Jacobs, T. M.; Jeliazkov, J. R.; Johnson, D. K.; Kappel, K.; Karanicolas, J.; Khakzad, H.; Khar, K. R.; Khare, S. D.; Khatib, F.; Khramushin, A.; King, I. C.; Kleffner, R.; Koepnick, B.; Kortemme, T.; Kuenze, G.; Kuhlman, B.; Kuroda, D.; Labonte, J. W.; Lai, J. K.; Lapidoth, G.; Leaver-Fay, A.; Lindert, S.; Linsky, T.; London, N.; Lubin, J. H.; Lyskov, S.; Maguire, J.; Malmström, L.; Marcos, E.; Marcu, O.; Marze, N. A.; Meiler, J.; Moretti, R.; Mulligan, V. K.; Nerli, S.; Norn, C.; Ó'Conchúir, S.; Ollikainen, N.; Ovchinnikov, S.; Pacella, M. S.; Pan, X.; Park, H.; Pavlovicz, R. E.; Pethe, M.; Pierce, B. G.; Pilla, K. B.; Raveh, B.; Renfrew, P. D.; Burman, S. S. R.; Rubenstein, A.; Sauer, M. F.; Scheck, A.; Schief, W.; Schueler-Furman, O.; Sedan, Y.; Sevy, A. M.; Sgourakis, N. G.; Shi, L.; Siegel, J. B.; Silva, D.-A.; Smith, S.; Song, Y.; Stein, A.; Szegedy, M.; Teets, F. D.; Thyme, S. B.; Wang, R. Y.-R.;

Watkins, A.; Zimmerman, L.; Bonneau, R., Macromolecular modeling and design in Rosetta: recent methods and frameworks. *Nature Methods* **2020,** *17* (7), 665-680.
14. Araujo, B. S. P. Computational Enzyme Design. Ph.D. Thesis, California Institute of Technology, 2014.
15. Johansson, K. E. Computational Protein Design. Ph. D. Thesis, University of Copenhagen, 2012.
16. Li, Z. Computational protein design: assessment and applications. Ph.D. Thesis, Indiana University, 2015.
17. Jindal, G.; Slanska, K.; Kolev, V.; Damborsky, J.; Prokop, Z.; Warshel, A., Exploring the challenges of computational enzyme design by rebuilding the active site of a dehalogenase. *Proceedings of the National Academy of Sciences* **2019,** *116* (2), 389.
18. Billings, W. M.; Hedelius, B.; Millecam, T.; Wingate, D.; Corte, D. D., ProSPr: Democratized Implementation of Alphafold Protein Distance Prediction Network. *bioRxiv* **2019**, 830273.
19. Siegel, J. B.; Zanghellini, A.; Lovick, H. M.; Kiss, G.; Lambert, A. R.; St Clair, J. L.; Gallaher, J. L.; Hilvert, D.; Gelb, M. H.; Stoddard, B. L.; Houk, K. N.; Michael, F. E.; Baker, D., Computational design of an enzyme catalyst for a stereoselective bimolecular Diels-Alder reaction. *Science (New York, N.Y.)* **2010,** *329* (5989), 309-313.
20. Privett, H. K.; Kiss, G.; Lee, T. M.; Blomberg, R.; Chica, R. A.; Thomas, L. M.; Hilvert, D.; Houk, K. N.; Mayo, S. L., Iterative approach to computational enzyme design. *Proceedings of the National Academy of Sciences of the United States of America* **2012,** *109* (10), 3790-3795.
21. Linder, M., Computational Enzyme Design: Advances, hurdles and possible ways forward. *Comput Struct Biotechnol J* **2012,** *2*, e201209009-e201209009.
22. McPherson, A.; Gavira, J. A., Introduction to protein crystallization. *Acta Crystallogr F Struct Biol Commun* **2014,** *70* (Pt 1), 2-20.
23. Murata, K.; Wolf, M., Cryo-electron microscopy for structural analysis of dynamic biological macromolecules. *Biochimica et Biophysica Acta (BBA) - General Subjects* **2018,** *1862* (2), 324-334.
24. Qin, Z.; Fabre, A.; Buehler, M. J., Structure and mechanism of maximum stability of isolated alpha-helical protein domains at a critical length scale. *The European Physical Journal E* **2013,** *36* (5), 53.
25. Sun, X.; Lai, L., Protein Fibrils Formed by Rationally Designed α-Helical Peptides. *Langmuir* **2020,** *36* (22), 6126-6131.
26. Stroobants, K.; Kumita, J. R.; Harris, N. J.; Chirgadze, D. Y.; Dobson, C. M.; Booth, P. J.; Vendruscolo, M., Amyloid-like Fibrils from an α-Helical Transmembrane Protein. *Biochemistry-Us* **2017,** *56* (25), 3225-3233.
27. Gonen, S.; DiMaio, F.; Gonen, T.; Baker, D., Design of ordered two-dimensional arrays mediated by noncovalent protein-protein interfaces. *Science* **2015,** *348* (6241), 1365.
28. Brodin, J. D.; Ambroggio, X. I.; Tang, C.; Parent, K. N.; Baker, T. S.; Tezcan, F. A., Metal-directed, chemically tunable assembly of one-, two- and three-dimensional crystalline protein arrays. *Nature Chemistry* **2012,** *4* (5), 375-382.
29. Hughes, S. A.; Wang, F.; Wang, S.; Kreutzberger, M. A. B.; Osinski, T.; Orlova, A.; Wall, J. S.; Zuo, X.; Egelman, E. H.; Conticello, V. P., Ambidextrous helical nanotubes from self-assembly of designed helical hairpin motifs. *Proceedings of the National Academy of Sciences* **2019,** *116* (29), 14456.
30. Hughes, S. A.; Wang, F.; Wang, S.; Kreutzberger, M. A. B.; Osinski, T.; Orlova, A.; Wall, J. S.; Zuo, X.; Egelman, E. H.; Conticello, V. P., Ambidextrous helical nanotubes from self-assembly of designed helical hairpin motifs. *Proc Natl Acad Sci U S A* **2019,** *116* (29), 14456-14464.
31. Magnotti, E. L.; Hughes, S. A.; Dillard, R. S.; Wang, S.; Hough, L.; Karumbamkandathil, A.; Lian, T.; Wall, J. S.; Zuo, X.; Wright, E. R.; Conticello, V. P., Self-Assembly of an α-Helical

Peptide into a Crystalline Two-Dimensional Nanoporous Framework. *J Am Chem Soc* **2016,** *138* (50), 16274-16282.
32. Jiang, T.; Magnotti, E. L.; Conticello, V. P., Geometrical frustration as a potential design principle for peptide-based assemblies. *Interface Focus* **2017,** *7* (6), 20160141-20160141.
33. Tayeb-Fligelman, E.; Tabachnikov, O.; Moshe, A.; Goldshmidt-Tran, O.; Sawaya, M. R.; Coquelle, N.; Colletier, J. P.; Landau, M., The cytotoxic Staphylococcus aureus PSMalpha3 reveals a cross-alpha amyloid-like fibril. *Science* **2017,** *355* (6327), 831-833.
34. Zheng, Y.; Joo, H. S.; Nair, V.; Le, K. Y.; Otto, M., Do amyloid structures formed by Staphylococcus aureus phenol-soluble modulins have a biological function? *Int J Med Microbiol* **2018,** *308* (6), 675-682.
35. Tayeb-Fligelman, E.; Salinas, N.; Tabachnikov, O.; Landau, M., Staphylococcus aureus PSMalpha3 Cross-alpha Fibril Polymorphism and Determinants of Cytotoxicity. *Structure* **2020,** *28* (3), 301-313 e6.
36. Salinas, N.; Tayeb-Fligelman, E.; Sammito, M.; Bloch, D.; Jelinek, R.; Noy, D.; Uson, I.; Landau, M., The Amphibian Antimicrobial Peptide Uperin 3.5 is a Cross-α/Cross-β Chameleon Functional Amyloid. *bioRxiv* **2020**, 2020.05.31.126045.
37. Zhang, S.-Q.; Huang, H.; Yang, J.; Kratochvil, H. T.; Lolicato, M.; Liu, Y.; Shu, X.; Liu, L.; DeGrado, W. F., Designed peptides that assemble into cross-α amyloid-like structures. *Nature Chemical Biology* **2018,** *14* (9), 870-875.
38. Barczewski, A. H.; Ragusa, M. J.; Mierke, D. F.; Pellegrini, M., The IKK-binding domain of NEMO is an irregular coiled coil with a dynamic binding interface. *Scientific Reports* **2019,** *9* (1), 2950.
39. Walshaw, J.; Woolfson, D. N., Extended knobs-into-holes packing in classical and complex coiled-coil assemblies. *J Struct Biol* **2003,** *144* (3), 349-361.
40. Rhys, G. G.; Wood, C. W.; Lang, E. J. M.; Mulholland, A. J.; Brady, R. L.; Thomson, A. R.; Woolfson, D. N., Maintaining and breaking symmetry in homomeric coiled-coil assemblies. *Nature Communications* **2018,** *9* (1), 4132.
41. Harbury, P. B.; Zhang, T.; Kim, P. S.; Alber, T., A switch between two-, three-, and four-stranded coiled coils in GCN4 leucine zipper mutants. *Science* **1993,** *262* (5138), 1401.
42. Egelman, E. H.; Xu, C.; DiMaio, F.; Magnotti, E.; Modlin, C.; Yu, X.; Wright, E.; Baker, D.; Conticello, V. P., Structural plasticity of helical nanotubes based on coiled-coil assemblies. *Structure* **2015,** *23* (2), 280-9.
43. Diao, J., Crystal structure of a super leucine zipper, an extended two-stranded super long coiled coil. *Protein science : a publication of the Protein Society* **2010,** *19* (2), 319-326.
44. Papapostolou, D.; Smith, A. M.; Atkins, E. D. T.; Oliver, S. J.; Ryadnov, M. G.; Serpell, L. C.; Woolfson, D. N., Engineering nanoscale order into a designed protein fiber. *Proceedings of the National Academy of Sciences* **2007,** *104* (26), 10853.
45. Burgess, N. C.; Sharp, T. H.; Thomas, F.; Wood, C. W.; Thomson, A. R.; Zaccai, N. R.; Brady, R. L.; Serpell, L. C.; Woolfson, D. N., Modular Design of Self-Assembling Peptide-Based Nanotubes. *J Am Chem Soc* **2015,** *137* (33), 10554-10562.
46. Xu, C.; Liu, R.; Mehta, A. K.; Guerrero-Ferreira, R. C.; Wright, E. R.; Dunin-Horkawicz, S.; Morris, K.; Serpell, L. C.; Zuo, X.; Wall, J. S.; Conticello, V. P., Rational Design of Helical Nanotubes from Self-Assembly of Coiled-Coil Lock Washers. *J Am Chem Soc* **2013,** *135* (41), 15565-15578.
47. Lanci, C. J.; MacDermaid, C. M.; Kang, S.-g.; Acharya, R.; North, B.; Yang, X.; Qiu, X. J.; DeGrado, W. F.; Saven, J. G., Computational design of a protein crystal. *Proceedings of the National Academy of Sciences* **2012,** *109* (19), 7304.
48. Görbitz, C. H., Nanotube Formation by Hydrophobic Dipeptides. *Chemistry – A European Journal* **2001,** *7* (23), 5153-5159.
49. Reches, M.; Gazit, E., Casting Metal Nanowires Within Discrete Self-Assembled Peptide Nanotubes. *Science* **2003,** *300* (5619), 625.

50. Görbitz, C. H., The structure of nanotubes formed by diphenylalanine, the core recognition motif of Alzheimer's β-amyloid polypeptide. *Chemical Communications* **2006,** (22), 2332-2334.
51. Silva, R. F.; Araújo, D. R.; Silva, E. R.; Ando, R. A.; Alves, W. A., L-diphenylalanine microtubes as a potential drug-delivery system: characterization, release kinetics, and cytotoxicity. *Langmuir : the ACS journal of surfaces and colloids* **2013,** *29* (32), 10205-12.
52. Mao, L.; Wang, H.; Tan, M.; Ou, L.; Kong, D.; Yang, Z., Conjugation of two complementary anti-cancer drugs confers molecular hydrogels as a co-delivery system. *Chem Commun (Camb)* **2012,** *48* (3), 395-397.
53. Nguyen, V.; Zhu, R.; Jenkins, K.; Yang, R., Self-assembly of diphenylalanine peptide with controlled polarization for power generation. *Nature Communications* **2016,** *7* (1), 13566.
54. Ryu, J.; Park, C. B., High-Temperature Self-Assembly of Peptides into Vertically Well-Aligned Nanowires by Aniline Vapor. *Advanced Materials* **2008,** *20* (19), 3754-3758.
55. Yan, X.; He, Q.; Wang, K.; Duan, L.; Cui, Y.; Li, J., Transition of Cationic Dipeptide Nanotubes into Vesicles and Oligonucleotide Delivery. *Angewandte Chemie International Edition* **2007,** *46* (14), 2431-2434.
56. Datta, D.; Tiwari, O.; Gupta, M. K., Self-Assembly of Diphenylalanine–Peptide Nucleic Acid Conjugates. *ACS Omega* **2019,** *4* (6), 10715-10728.
57. Khanra, S.; Abdullah-Al Mamun, M.; Ferreira, F. F.; Ghosh, K.; Guha, S., Functionalized Self-Assembled Peptide Nanotubes with Cobalt Ferrite Nanoparticles for Applications in Organic Electronics. *ACS Applied Nano Materials* **2018,** *1* (3), 1175-1187.
58. Zhang, H.; Fei, J.; Yan, X.; Wang, A.; Li, J., Enzyme-Responsive Release of Doxorubicin from Monodisperse Dipeptide-Based Nanocarriers for Highly Efficient Cancer Treatment In Vitro. *Advanced Functional Materials* **2015,** *25* (8), 1193-1204.
59. Eisenberg, D.; Jucker, M., The amyloid state of proteins in human diseases. *Cell* **2012,** *148* (6), 1188-1203.
60. Del Pozo-Yauner, L.; Becerril, B.; Ochoa-Leyva, A.; Rodr ́guez-Ambriz, S. L.; Carri ́on, J. I. P.; Zavala-Padilla, G.; S ́anchez-L ́opez, R.; Velasco, D. A. F. In *The Structural Determinants of the Immunoglobulin Light Chain Amyloid Aggregation*, Physical Biology of Proteins and Peptides, Cham, 2015//; Olivares-Quiroz, L.; Guzm ́an-L ́opez, O.; Jard ́on-Valadez, H. E., Eds. Springer International Publishing: Cham, 2015; pp 1-28.
61. Nelson, R.; Sawaya, M. R.; Balbirnie, M.; Madsen, A. Ø.; Riekel, C.; Grothe, R.; Eisenberg, D., Structure of the cross-beta spine of amyloid-like fibrils. *Nature* **2005,** *435* (7043), 773-778.
62. Li, Y.; Li, K.; Wang, X.; An, B.; Cui, M.; Pu, J.; Wei, S.; Xue, S.; Ye, H.; Zhao, Y.; Liu, M.; Wang, Z.; Zhong, C., Patterned Amyloid Materials Integrating Robustness and Genetically Programmable Functionality. *Nano Lett* **2019,** *19* (12), 8399-8408.
63. Li, C.; Qin, R.; Liu, R.; Miao, S.; Yang, P., Functional amyloid materials at surfaces/interfaces. *Biomaterials Science* **2018,** *6* (3), 462-472.
64. Knowles, T. P. J.; Mezzenga, R., Amyloid Fibrils as Building Blocks for Natural and Artificial Functional Materials. *Advanced Materials* **2016,** *28* (31), 6546-6561.
65. Lu, K.; Jacob, J.; Thiyagarajan, P.; Conticello, V. P.; Lynn, D. G., Exploiting Amyloid Fibril Lamination for Nanotube Self-Assembly. *Journal of the American Chemical Society* **2003,** *125* (21), 6391-6393.
66. Lamm, M. S.; Rajagopal, K.; Schneider, J. P.; Pochan, D. J., Laminated Morphology of Nontwisting β-Sheet Fibrils Constructed via Peptide Self-Assembly. *Journal of the American Chemical Society* **2005,** *127* (47), 16692-16700.
67. Dai, B.; Li, D.; Xi, W.; Luo, F.; Zhang, X.; Zou, M.; Cao, M.; Hu, J.; Wang, W.; Wei, G.; Zhang, Y.; Liu, C., Tunable assembly of amyloid-forming peptides into nanosheets as a retrovirus carrier. *Proceedings of the National Academy of Sciences* **2015,** *112* (10), 2996.

68. Fitzpatrick, A. W. P.; Debelouchina, G. T.; Bayro, M. J.; Clare, D. K.; Caporini, M. A.; Bajaj, V. S.; Jaroniec, C. P.; Wang, L.; Ladizhansky, V.; Müller, S. A.; MacPhee, C. E.; Waudby, C. A.; Mott, H. R.; De Simone, A.; Knowles, T. P. J.; Saibil, H. R.; Vendruscolo, M.; Orlova, E. V.; Griffin, R. G.; Dobson, C. M., Atomic structure and hierarchical assembly of a cross-β amyloid fibril. *Proceedings of the National Academy of Sciences* **2013,** *110* (14), 5468.
69. Ciudad, S.; Puig, E.; Botzanowski, T.; Meigooni, M.; Arango, A. S.; Do, J.; Mayzel, M.; Bayoumi, M.; Chaignepain, S.; Maglia, G.; Cianferani, S.; Orekhov, V.; Tajkhorshid, E.; Bardiaux, B.; Carulla, N., Aβ(1-42) tetramer and octamer structures reveal edge conductivity pores as a mechanism for membrane damage. *Nature Communications* **2020,** *11* (1), 3014.
70. Hao, S.; Li, X.; Han, A.; Yang, Y.; Fang, G.; Liu, J.; Wang, S., CLVFFA-Functionalized Gold Nanoclusters Inhibit Aβ40 Fibrillation, Fibrils' Prolongation, and Mature Fibrils' Disaggregation. *ACS chemical neuroscience* **2019,** *10* (11), 4633-4642.
71. Xiong, N.; Dong, X. Y.; Zheng, J.; Liu, F. F.; Sun, Y., Design of LVFFARK and LVFFARK-functionalized nanoparticles for inhibiting amyloid β-protein fibrillation and cytotoxicity. *ACS applied materials & interfaces* **2015,** *7* (10), 5650-62.
72. Sillerud, L. O.; Solberg, N. O.; Chamberlain, R.; Orlando, R. A.; Heidrich, J. E.; Brown, D. C.; Brady, C. I.; Vander Jagt, T. A.; Garwood, M.; Vander Jagt, D. L., SPION-enhanced magnetic resonance imaging of Alzheimer's disease plaques in AβPP/PS-1 transgenic mouse brain. *Journal of Alzheimer's disease : JAD* **2013,** *34* (2), 349-65.
73. Hartgerink, J. D.; Beniash, E.; Stupp, S. I., Self-assembly and mineralization of peptide-amphiphile nanofibers. *Science* **2001,** *294* (5547), 1684-8.
74. Meng, Q.; Kou, Y.; Ma, X.; Liang, Y.; Guo, L.; Ni, C.; Liu, K., Tunable Self-Assembled Peptide Amphiphile Nanostructures. *Langmuir* **2012,** *28* (11), 5017-5022.
75. Chang, R.; Subramanian, K.; Wang, M.; Webster, T. J., Enhanced Antibacterial Properties of Self-Assembling Peptide Amphiphiles Functionalized with Heparin-Binding Cardin-Motifs. *ACS Appl Mater Interfaces* **2017,** *9* (27), 22350-22360.
76. Matson, J. B.; Zha, R. H.; Stupp, S. I., Peptide Self-Assembly for Crafting Functional Biological Materials. *Curr Opin Solid State Mater Sci* **2011,** *15* (6), 225-235.
77. Yu, S. M.; Li, Y.; Kim, D., Collagen Mimetic Peptides: Progress Towards Functional Applications. *Soft Matter* **2011,** *7* (18), 7927-7938.
78. Sarkar, B.; O'Leary, L. E. R.; Hartgerink, J. D., Self-Assembly of Fiber-Forming Collagen Mimetic Peptides Controlled by Triple-Helical Nucleation. *J Am Chem Soc* **2014,** *136* (41), 14417-14424.
79. Rele, S.; Song, Y.; Apkarian, R. P.; Qu, Z.; Conticello, V. P.; Chaikof, E. L., D-Periodic Collagen-Mimetic Microfibers. *J Am Chem Soc* **2007,** *129* (47), 14780-14787.
80. Lin, Y.; Thomas, M. R.; Gelmi, A.; Leonardo, V.; Pashuck, E. T.; Maynard, S. A.; Wang, Y.; Stevens, M. M., Self-Assembled 2D Free-Standing Janus Nanosheets with Single-Layer Thickness. *J Am Chem Soc* **2017,** *139* (39), 13592-13595.
81. Jiang, T.; Xu, C.; Liu, Y.; Liu, Z.; Wall, J. S.; Zuo, X.; Lian, T.; Salaita, K.; Ni, C.; Pochan, D.; Conticello, V. P., Structurally Defined Nanoscale Sheets from Self-Assembly of Collagen-Mimetic Peptides. *Journal of the American Chemical Society* **2014,** *136* (11), 4300-4308.
82. Jiang, T.; Vail, O. A.; Jiang, Z.; Zuo, X.; Conticello, V. P., Rational Design of Multilayer Collagen Nanosheets with Compositional and Structural Control. *J Am Chem Soc* **2015,** *137* (24), 7793-7802.
83. Merg, A. D.; Touponse, G.; van Genderen, E.; Zuo, X.; Bazrafshan, A.; Blum, T.; Hughes, S.; Salaita, K.; Abrahams, J. P.; Conticello, V. P., 2D Crystal Engineering of Nanosheets Assembled from Helical Peptide Building Blocks. *Angew Chem Int Ed Engl* **2019,** *58* (38), 13507-13512.

Chapter 2: PSMα3 Selectively Self-assembles into cross-α Nanotubes

2.1 Introduction

Phenol-soluble modulins (PSMs) are a family of amphipathic, a-helical peptides secreted by *the Staphylococcus* family of bacteria. PSMs gained research interest as they are believed to have roles in the pathogenesis pathway of *S. aureus* infections[1], where S. aureus infections pose as a significant public health risk, total at an estimated 10-30 cases per 100,000 person-years in the developed world[2]. There are 7 PSM peptides secreted by *S. aureus*: four 22 residues long PSMα1 – PSMα4 peptides, two 44 residues long PSMβ1 and PSMβ2 peptides, and a 25 residues long PSMγ (or delta-toxin) peptide (Figure 2.1)[3]. These peptides are grouped by the operons they are encoded on. PSMα1 and PSMα2 have a large 85.7% sequence similarity. Charge-wise, PSMαs are positively charged, PSMβs are negatively charged, and PSMγ is neutral.

Figure 2.1. PSM sequences. All peptides shown are formylated (f) at the N-terminal. Figure adapted from ref. 3.

PSMαs and PSMγ were identified as critical virulence factors of community-associated methicillin-resistant S. aureus (CA-MRSA) infections[1, 4], as CA-MRSA mutants with PSMα and PSMγ production inhibited have a less mortality rate in mouse models compared to the wild type, and inhibiting PSMβ production did not have a significant impact on the mortality rate. Synthetic PSMα and PSMγ peptides showed high cytolytic activities (< 1 μM/dm^3 EC_{50} towards DPPC53 vesicles) toward human neutrophils, where PSMα3 is the most cytolytic, and PSMα4 and PSMβ

peptides showed low cytolytic activities (> 1 μM/dm^3 EC_{50} towards DPPC53 vesicles). It is also shown some less deadly *S. aureus* strains[5], and the overall less deadly strain *Staphylococcus epidermidis*[6] compared to *S. aureus* have a less PSMα and PSMγ expression rate, supporting the hypothesis of PSMαs and PSMγ being critical virulence factors.

PSM peptides are also shown to self-assemble into extracellular fibrils (Figure 2.2A)[7], where *S. aureus* mutants with all PSM productions inhibited are unable to produce the observed extracellular fibrils (Figure 2.2B). However, Zheng et al. showed conflicting evidence that extracellular fibrils are present in a PSM deficient *S. aureus* LAC (USA300) strain mutant (Figure 2.2C)[8]. PSMs are also shown to contribute to *S. aureus* biofilm stabilization[7, 9]. A mixture of synthesized, all 7 PSMs form fibrils (Figure 2.2D)[7] that binds to thioflavin T (ThT) and Congo red (CR), where ThT and CR are known to bind with amyloid fibrils[10], suggesting these fibrils may be structurally similar to amyloid fibrils. Exposing grown *S. aureus* biofilms to synthetic, solublized PSMα1 peptide caused biofilm disassembly; however, exposing grown biofilms to PSMα1 fibrils did not cause biofilm disassembly[7], suggesting the self-assembly of PSM peptides, or at least PSMα1 may inhibit some of the peptide's functions.

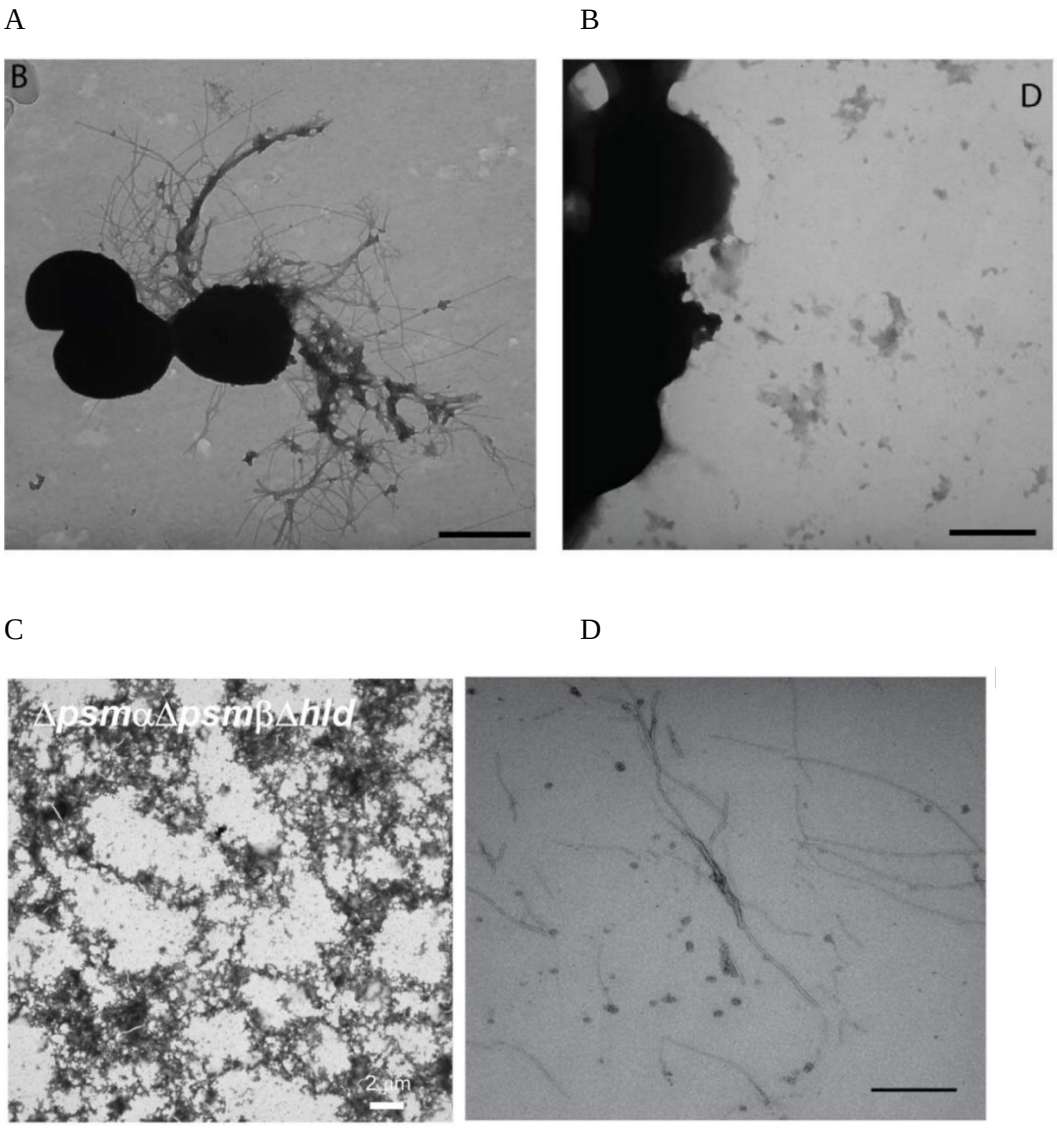

Figure 2.2. TEM micrographs of A) cells from S. aureus SH1000 biofilms grown in PNG media. B) An Agr knocked-off mutant (Agr regulates PSM expression) of the S. aureus SH1000 strain does not produce extracellular fibers. C) An Agr mutant of the S. aureus LAC (USA300) strain that does produce extracellular fibers. D) 48 hours after mixing 100 mg/mL each of the seven PSM peptides (a1–4, b1–2, and d-toxin), fibril structures are readily observed by TEM. Images adapted from ref 8, 9.

Recently, the in-solution structures of PSMα1 and α3 peptides, and the amyloid-like fibril structures of PSM α1, α3 and α4 were characterized. Both PSMα1 and PSMα3 form α-helices in

solution with 50% d-trifluoroethanol (d-TFE)[11]. PSMα1 and PSMα4 first assemble into α-helices, but then transition to β-sheet and ultimately form cross-β fibrils in aqueous solutions within several days (Figure 2.3A, B)[12]. In addition, PSMα3 forms a novel "cross-α" type amyloid fibril assembly (Figure 2.3C)[13], where the amphipathic PSMα3 α-helices are positioned perpendicular to the fibril axis, mate through their hydrophobic faces and stacks in the fibril axis direction to afford fibril growth, resembling those of cross-β structures. The PSMα3 cross-α fibrils also bind to Thioflavin T (ThT) similar to cross-β amyloid fibrils[13].

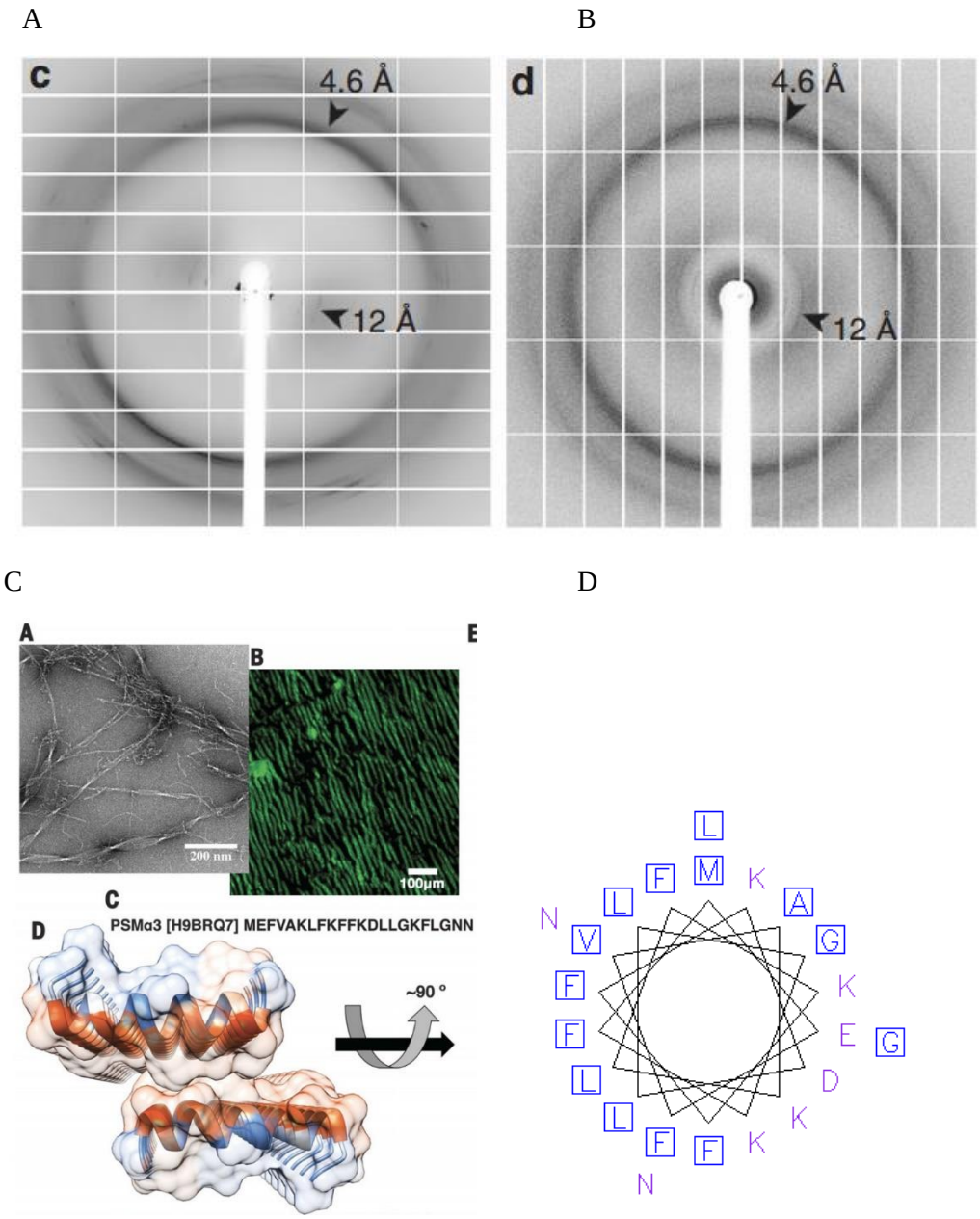

Figure 2.3. A) and B): X-ray fibril diffraction of A) PSMα1 and B) PSMα4 shows major diffraction orthogonal arches at 4.6 Å and 12 Å spacings. C) TEM and model of PSMα3, hydrophilic residues are colored blue, and hydrophobic residues are colored orange. D) Helical wheel representation of PSMα3, hydrophobic residues are boxed, showing clear amphipathic features. Images adapted from ref. 12, 13.

Tayeb-Fligelman et Al. performed alanine screens of PSMα3 and showed fibril formation and positive charges both contribute to PSMα3's cytotoxicity[14, 15]. Das et al. used all-atom classical

molecular dynamics simulation and found single PSMα3 helices are energetically unfavored to penetrate a two-model bilayer system[16], thus PSMα3 fibrillization might be essential to its cytolytic activities in penetrating cell membranes. Yao et al. used a stereochemical coassembly approach and showed a racemic mixture of L- and D- PSMα3 displayed extensive fibril formation, but no cytotoxicity towards HEK293FT cells[17]; both the pure L- and D- enantiomer of PSMα3 alone showed little to no fibril formation but maintains cytotoxicity, suggesting PSMα3's cytotoxicity might be attributed to the soluble form of PSMα3, instead of the insoluble amyloid-like fibril form. Zheng et al. also performed PSMα3 alanine screenings and have found many PSMα3 mutants maintained cytotoxicity without ThT binding[17], raising the question whether ThT bindings should be used to confirm the correlation between PSMα3 fibril formation and cytotoxicity. It's debatable and interesting whether this novel cross-α structure have any biological functions.

Cross-β amyloid structures are known to be polymorphic and have biological relevances[18]; PSMα3 already displays a good degree of polymorphism often in the supplemental information of published results. It is possible these polymorphic morphologies are controllable and lead to biological functions. This chapter's goal is to 1. screen and characterize any polymorphisms exhibited by PSMα3; 2. optimize conditions of each morphology identified for selectivity and further characterization; 3. isolate and determine the structure-cytotoxicity relationship of each morphology identified. This chapter will present the characterization of PSMα3's self-assembled nanotube structure, where PSMα3 selectively self-assembles into nanotubes via the lateral association of the previously identified cross-α PSMα3 fibrils.

2.2 Results and discussion

2.2.1 Self-assembly of PSMα3

PSMα3 was synthesized via solid-phase peptide synthesis with N-terminal acetylation and C-terminal amidation to reduce termini charges. Peptide was purified by preparative HPLC, characterized by MALDI and its purity was confirmed by MALDI and analytical HPLC. Because peptide self-assembly is affected by peptide concentration, as well as many external stimuli such as pH, temperature, salt concentration[19-22], PSMα3 was first screened in 10 mM buffers from pH 5.0 to pH 8.0 at an increment of pH 1.0, room temperature and annealed at 90 ℃, and 302 μM – 2 mM peptide concentrations to assess its self-assembly behavior. Fibrils can be seldomly found at above 755 μM PSMα3 peptide concentration (Figure 2.4D). At 302 – 755 μM PSMα3 peptide concentrations, PSMα3 assembled into a variety of morphologies that are pH and temperature dependent. In 10 mM pH 5.0 – pH 8.0 buffers at room temperature, as well as in 10 mM pH 5.0 and pH 6.0 buffers when annealed at 90 ℃, PSMα3 assembled into twisted fibrils after 24 h of incubation (Figure 2.4A). Nanotubes are also rarely seen at lower peptide concentration conditions at this pH range at ~5% of the total assembly. Both the twisted fibrils[23] and the nanotubes[17] were observed in previous studies, although at 800 μM and above peptide concentrations and were not selective. In 10 mM pH 7.0 and pH 8.0 buffers annealed at 90 ℃, PSMα3 assembled into nanotubes with two distinct populations with different diameters, 100 nm and 160 nm after 24 h of incubation (Figure 2.6B). While PSMα3 at pH 7.0 showed a mix of nanotubes and fibrils (Figure 2.4B), PSMα3 at pH 8.0 selectively assembled into nanotubes with varied diameters (Figure 2.4C). Precipitations were observed in both annealed samples after 24 h of incubation. In pH 2.0 HPLC water titrated with TFA both at room temperature and annealed at 90 ℃, PSMα3 assembled into nanotubes with an averaged 61 nm diameter (Figure 2.6A) after 24 h of incubation (Figure 2.5). The tubes were stable up to 1 month, and tube elongation up to tens of microns was observed.

A B

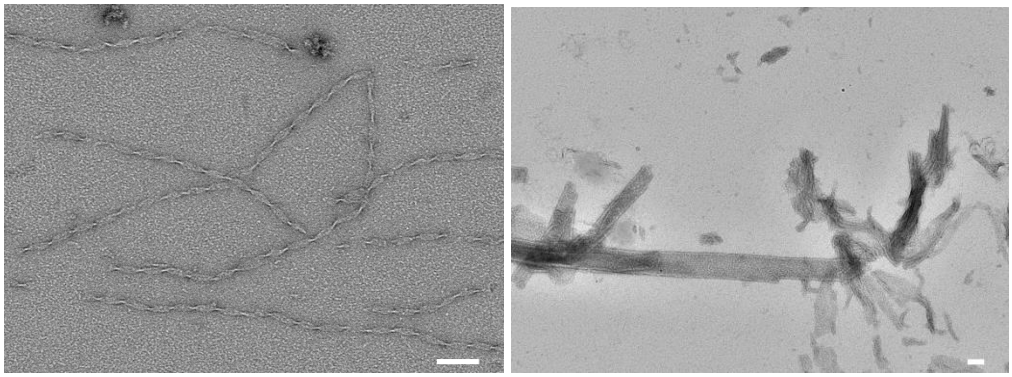

C D

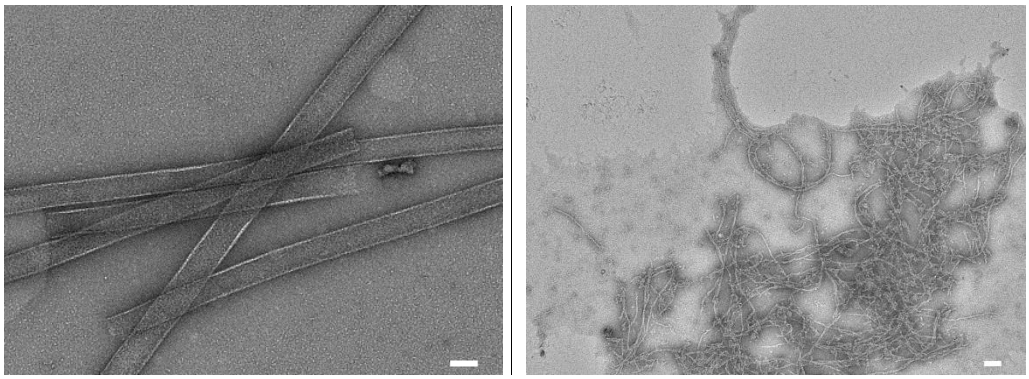

Figure 2.4. Representative TEM images of A) 453 μM PSMα3, after 7 days of assembly time, in 10 mM pH 7.0 MOPS; B) 453 μM PSMα3, after 7 days of assembly time, annealed at 90 ℃, in 10 mM pH 7.0 MOPS; C) 453 μM PSMα3, after 7 days of assembly time, annealed at 90 ℃, in 10 mM pH 8.0 TAPS; D) 1.1 mM PSMα3, after 1 day of assembly time, annealed at 90 ℃, in 10 mM pH 8.0 TAPS; All scale bars represent 100 nm.

A B

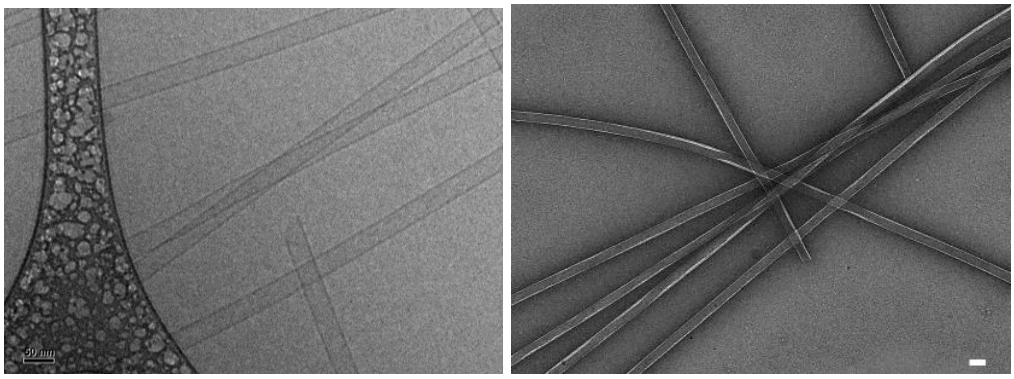

Figure 2.5. A) Cryo-EM image of 755 μM PSMα3, after 14 days of assembly time, in pH 2.0 water titrated with TFA, scale bar = 50 nm; B) TEM image of 755 μM PSMα3, after 14 days of assembly time, annealed at 90 ℃, in pH 2 water titrated with TFA, scale bar = 100 nm.

A B

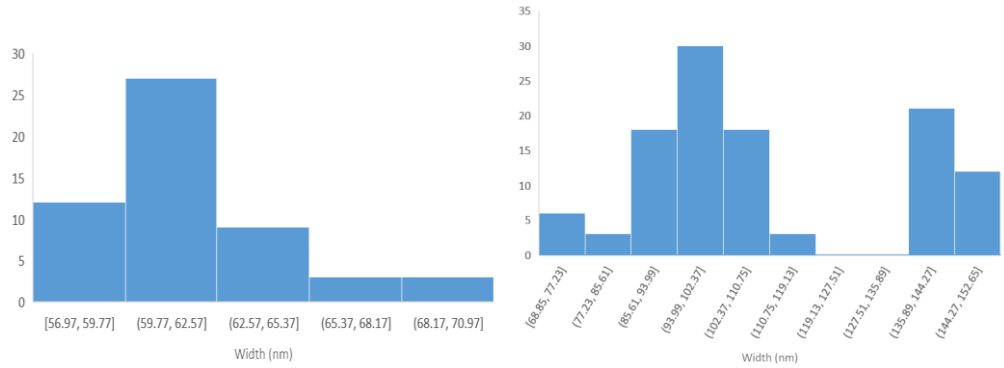

Figure 2.6. Histograms of nanotube widths measured via TEM in A) PSMα3 at pH 2.0; B) PSMα3 at pH 7.0 and pH 8.0, annealed at 90 ℃.

Circular dichroism (CD) spectroscopy was employed to both characterize the secondary structural properties of PSMα3 in the buffer conditions screened, as well as to identify any differences in CD spectra between the different morphologies. In order to compare CD signals from

samples with different concentrations, measured ellipticity was converted to molar ellipticity by dividing with a scale factor of [sample concentration in M] ×[number of amino acids in the sequence] × [CD cuvette cell path length in cm]. All PSMα3 concentrations were determined via measuring the sample's UV absorbance at 205 nm[24]. At pH 7.0 and 8.0 annealed at 90 ℃, the MRE signals are especially noisy due to the lower peptide concentration of these samples as precipitations were observed. PSMα3 in all conditions showed α-helical signatures with positive signals around 195 nm, and minima at around 209 nm and 224 nm (Figure 2.7), suggesting all of the observed morphologies are formed by α-helices. All conditions show similar $\theta_{224\,nm}/\ \theta_{209\,nm}$ ratios, indicating there is no significant differences in the various morphologies' secondary structures. Using the α-helical and β-strand content prediction software K2D3[25], in all conditions the α-helical contents are consistent around 20%, and the β-strand contents are consistent around 30%. There are no apparent differences in the secondary structure content between the nanotubes with different diameters and the fibrils.

A B

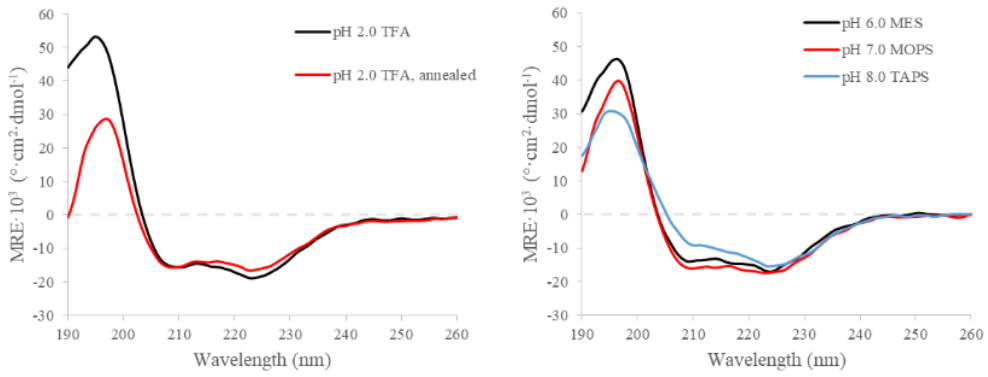

C

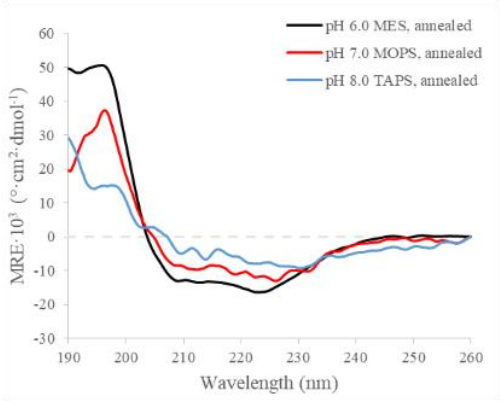

Figure 2.7. Circular dichroism spectra of A) 377 μM PSMα3 in pH 2 water titrated with TFA, pH 2 water titrated with TFA annealed at 90 ℃; B) 453 μM PSMα3 in 10 mM pH 6.0 MES, 10 mM pH 7.0 MOPS, 10 mM pH 8.0 TAPS; C) 453 μM PSMα3 in 10 mM pH 6.0 MES, 10 mM pH 7.0 MOPS, 10 mM pH 8.0 TAPS, all annealed at 90 ℃.

These preliminary results revealed PSMα3 can selectively assemble into a variety of ordered morphologies by controlling the assembly condition's pH and temperature: 90 nm and 150 nm wide nanotubes can be induced with a neutral and basic pH and thermal annealing; 60 nm wide nanotubes can be induced with an extremely acidic pH, while thermal annealing does not change the assembly type to 90 nm nanotubes; twisting fibrils can be induced with a slightly acidic to slightly basic pH and no thermal annealing. Further structure characterizations were performed to determine whether and how these structures arise from the previously reported PSMα3 cross-α structure.

2.2.2 Characterization of PSMα3 nanotubes at pH 2

2.2.2.1 Kinetics and critical pH survey of PSMα3 nanotubes at pH 2

PSMα3 was screened at different incubation times via TEM to probe the assembly kinetics of the observed 60 nm width "narrow" nanotubes in pH 2 water titrated with TFA. PSMα3 was first dissolved in TFE and TFE was evaporated in a fume hood to eliminate any pre-formed structures in the peptide powder state[26]. In 10 minutes after the 302 μM PSMα3 sample in water was titrated to pH 2.0 with dilute TFA, the sample already showed an α-helical CD signature (Figure 2.8D) and nanotube assembly (Figure 2.8A); some helical ribbons and nanotube-helical ribbon hybrids also exist as possible precursors to the nanotube assembly (Figure 2.8B). The helical ribbons have a varied tape width between 60 to 90 nm and a varied pitch between 140 to 160 nm, but all have a rather consistent turn angle of 150 °. After 24 h of incubation, helical ribbons and imperfect nanotubes were no longer commonly observed, and most assemblies matured to nanotubes (Figure 2.8C). This data agrees with the previously reported fast ThT binding time of PSMα3 maturing in merely hours[27]. While some PSMα3 tube assembly process can be seen at early assembly time points as the nanotubes are developed from helical ribbons, PSMα3 kinetics is too fast to have any conclusions drawn at this point.

A B

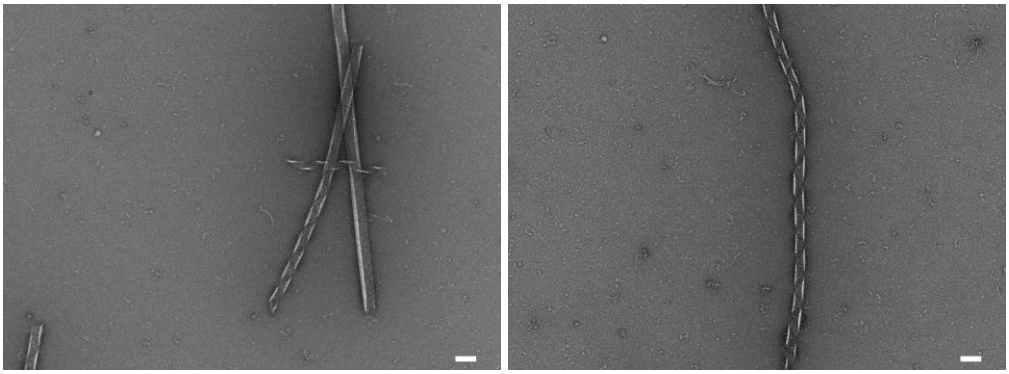

C D

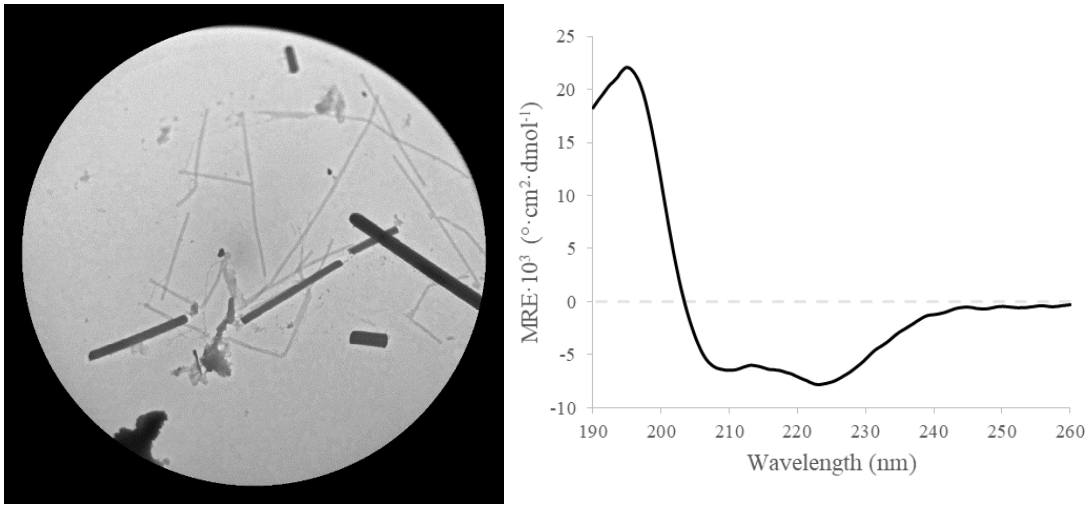

*Figure 2.8. A)-C): Representative TEM images of 302 μM **PSMα3** in pH 2 water titrated with TFA, TEM sample prepared immediately after titration. A) and B) scale bars = 100 nm. C) A zoomed out view showing the relative populations of each morphologies, where nanotube is the major species. D) Circular dichroism spectrum of 302 μM PSMα3 in pH 2 water titrated with TFA, CD taken immediately after titration.*

To determine the critical pH required of the PSMα3 narrow nanotube assemblies, further screenings of 377 μM PSMα3 assembled in pH 1.60, 1.81, 2.26, 2.50 and 3.10 water were performed. At pH 1.60, only fibrils and peptide aggregates were observed (Figure 2.9A). At pH 1.81, nanotubes were observed along with a lot of peptide aggregates (Figure 2.9B), although the

population of tubes in this condition is significantly less than in pH 2.00. Sometimes a striation pattern can be observed on the nanotubes. FFT analysis on the patterns did not yield any distinct spacing, but manual measurements yielded a ~8 nm spacing, roughly corresponding to double the single fibril width observed earlier. At pH 2.26, predominately narrow nanotubes were observed (Figure 2.9C). At pH 2.50 and pH 3.10, tubes were no longer observed, twisted fibrils were instead the major population of assemblies (Figure 2.9D).

A B

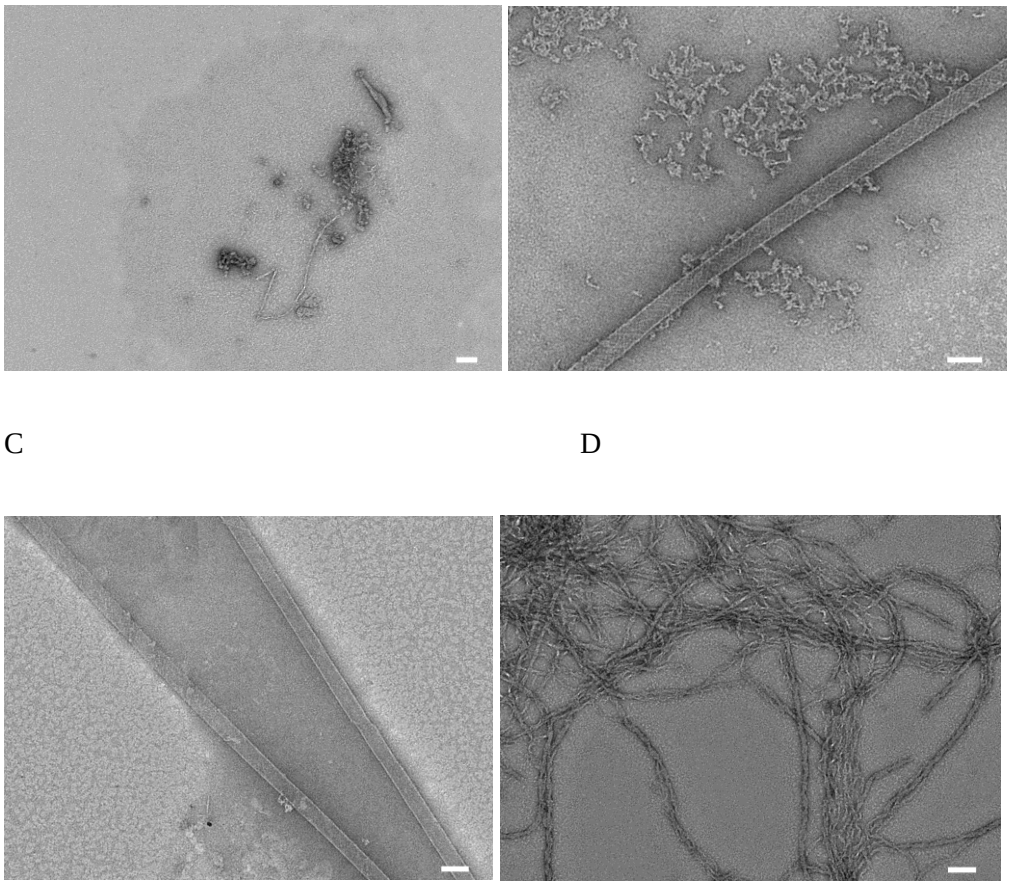

C D

Figure 2.9. Representative TEM images of 377 μM PSMα3, after 1 day of assembly time, A) in 0.1% TFA in pH 1.60 water; B) in 0.1% TFA in pH 1.81 water; C) in 0.1% TFA in pH 2.26 water; D) in 0.1% TFA in pH 2.50 water; E) in 0.1% TFA in pH 3.10 water. All scale bars represent 100 nm.

All conditions display α-helical CD signatures with minima around 207 nm and 222 nm (Figure 2.10); K2D3 calculations suggest pH 1.60 and pH 1.81 conditions have the most α-helical content at ~70% and the least β strand content at < 3%, and others have similar α-helical contents at ~20% and β strand contents at ~30%. In combination with the TEM data, PSMα3's cross-α structure likely did not form at pH 1.60, and only started to form at pH 1.81 or higher. The fibrils and nanotubes observed at > pH 2.5 and pH 2.0 – 2.26 could be the same species but with different arrangements, originating from the PSMα3 cross-α fibrils. To confirm this claim, these morphologies are further analyzed via high-resolution structure characterization techniques such as cryo-EM and SAXS.

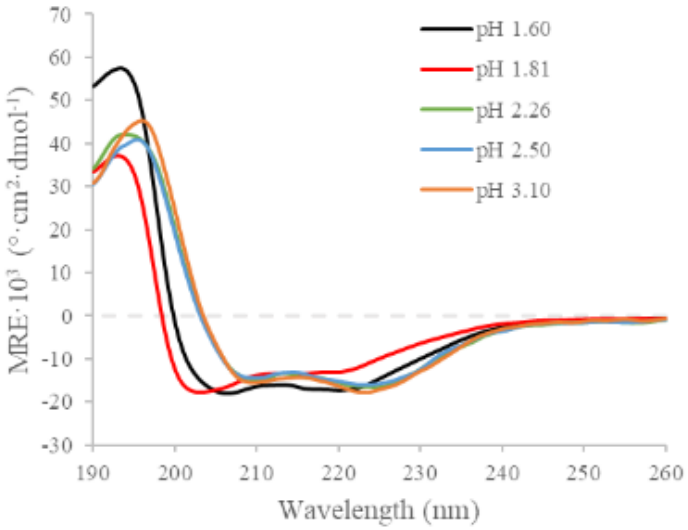

Figure 2.10. Circular dichroism spectra of 377 μM PSMα3 in pH 1.60, pH 1.81, pH 2.26, pH 2.50, pH 3.10, water titrated with TFA.

2.2.2.2 Cryo-EM determined PSMβ2 nanotube structure

PSMα3 nanotubes assembled in pH 2 water were analyzed with cryo-EM. cryo-EM reconstruction of these nanotubes revealed they are actually polymorphic with slightly different diameters: 346 Å with a C7 symmetry, 4.13 Å rise and a 26.8° twist (Figure 2.11A), and 376 Å with a C1 symmetry, 0.63 Å rise and a -138.3° twist (Figure 2.11B). While both models need to be further refined due to the difficulty distinguishing the two populations in cryo-EM data, it is clear both nanotube models are composed of cross-α fibrils.

A B

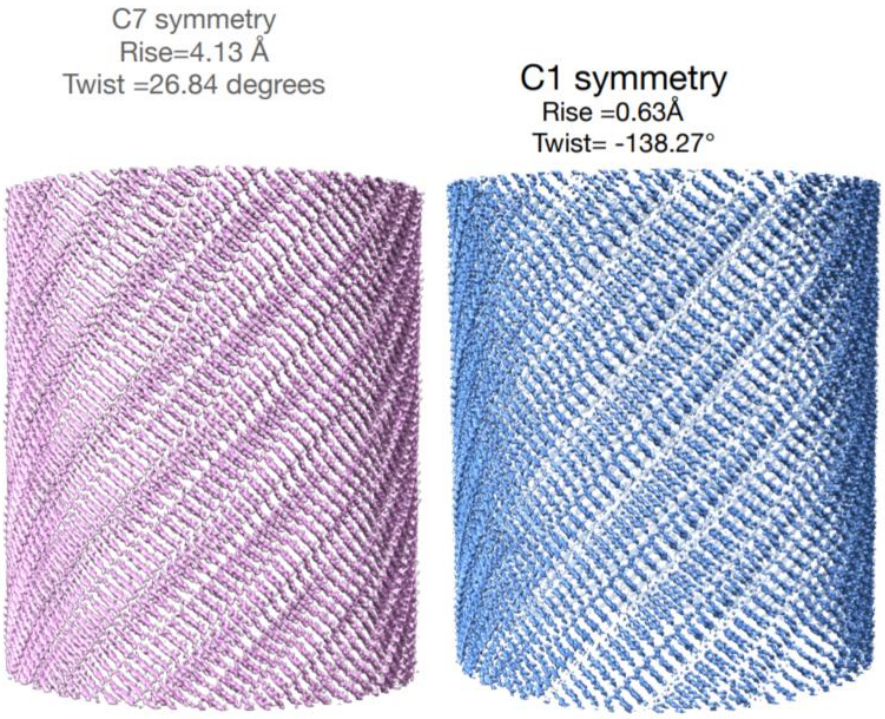

Figure 2.11: preliminary cryo-EM reconstruction of PSMα3 nanotubes.

Atomic force microscopy was employed to characterize the wall thickness of the narrow PSMα3 nanotubes. Assuming the nanotubes are fully flattened on AFM mica disks, the measured height should reflect twice of PSMα3 nanotube wall thickness. The measured nanotube height

follows a normal distribution at an average of 5.06 nm, or 2.53 nm for a single wall (Figure 2.12), roughly corresponds to double of the PSMα3's cross-α fibril mating spacing of 11.3 Å, suggesting PSMα3 nanotubes are double-layered.

A B

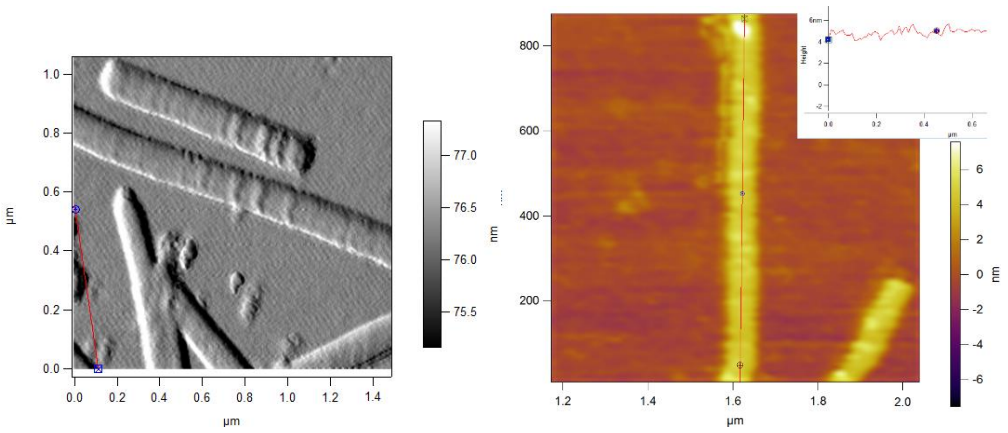

Figure 2.12: Representative AFM image of 302 µM PSMα3 in pH 2 water titrated with TFA, A) in amplitude mode; B) in height mode, with height profile at top right.

Small-angle X-ray scattering (SAXS) was employed to characterize the in-solution structure of the narrow PSMα3 nanotubes. In contrary to the two nanotube models characterized via cryo-EM, SAXS signals showed signs of mono-dispersed hallow cylinder assembly in-solution (Figure 2.13). The scattering intensity I(Q) was measured as a function of the momentum transfer, q from .005 $Å^{-1}$ to 7.8 $Å^{-1}$. The oscillation in I(Q) suggests the sample contains monodispersed hallow cylindrical particles (Figure 2.13); although multiple populations of nanotubes with varied diameters exist under cryo-EM, it's possible the diameter follows a passion distribution and averages nicely under SAXS. The 1D scattering intensity for a hallow cylinder can be described by the following function[28-29]:

$$I(q) = \frac{N}{V}(\rho_p - \rho_0)^2 V_p^2 \mathrm{P(q)}$$

$$P(q) = (\text{scale}) V_{\text{shell}} \Delta\rho^2 \int_0^1 \Psi^2 \left[q_z, R_{\text{outer}}(1-x^2)^{1/2}, R_{\text{core}}(1-x^2)^{1/2} \right] \left[\frac{\sin(qHx)}{qHx} \right]^2 dx$$

$$\Psi[q,y,z] = \frac{1}{1-\gamma^2} \left[\Lambda(qy) - \gamma^2 \Lambda(qz) \right]$$

$$\Lambda(a) = 2J_1(a)/a$$

$$\gamma = R_{\text{core}}/R_{\text{outer}}$$

$$V_{\text{shell}} = \pi \left(R_{\text{outer}}^2 - R_{\text{core}}^2 \right) L$$

$$J_1(x) = (\sin(x) - x \cdot \cos(x))/x^2$$

Where P(q) is hallow cylinder's form function; R_{outer} is the outer radius of the cylinder, R_{inner} is the inner radius of the cylinder, or R_{outer} – the tube's wall thickness (T); scale is a factor constant; L is the cylinder length; H is half of L; J_1 is the 1st order Bessel function. This function was used to fit the SAXS data, where T was set to 20 and 30 Å because the flattened tube wall thickness measured via AFM is ~25 Å; L was set to be an arbitrarily large number 10,000 Å to increase the intensity of the fitted form factor's oscillation for an easier fit. This yielded a R_{inner} of 164 ± 8 Å with T as 30 Å, or a R_{inner} of 176 ± 9 Å with T set as 20 Å; in both cases, the outer cylinder radius is about 200 Å. The values differs from the nanotube width measured via TEM, however if the nanotube is assumed to be fully flattened on the TEM grid, the expected *m*easured width would be half of the circumference, $R_{outer} * \pi = 200 * \pi = 628$ Å, which matches the measured width of ~60 nm via TEM.

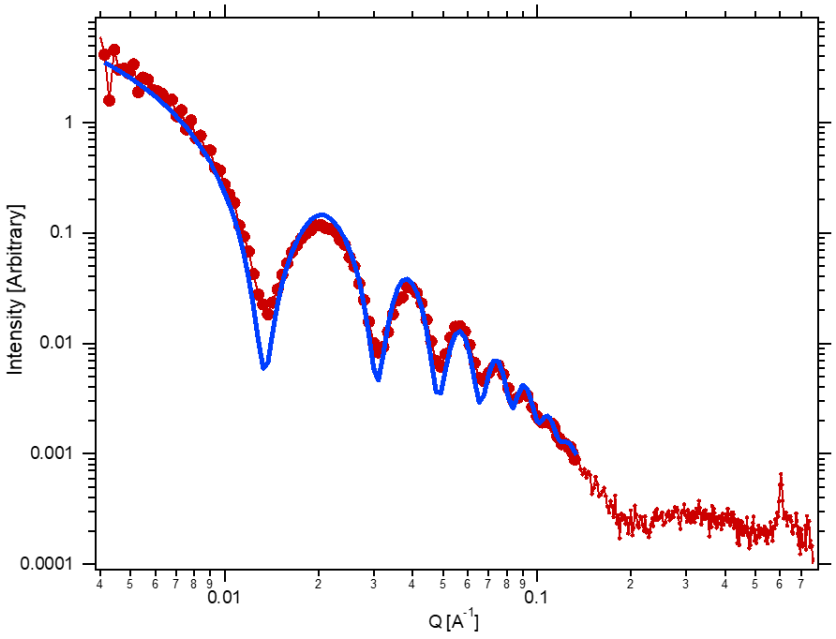

Figure 2.13. SAXS spectrum of 302 μM PSMα3 in pH 2 water titrated with TFA, red line is experimental data; blue line is fitting with T set as 30 Å and R_{inner} fitted as 164 Å.

Scanning transmission electron microscopy (STEM) was employed to characterize the amount of PSMα3 monomers in a given nanotube length. Dark field STEM confirmed the presence of 60 nm wide nanotubes in the 377 μM pH 2 PSMα3 sample (Figure 2.14). Using tobacco mosaic birus as the standard, the average mass per length (M/L) measurements of the nanotubes showed two tube populations: one at avg. 20 kDa/Å (Figure 2.14A), and the other at 30 – 40 kDa/Å (Figure 2.14B). Sometimes a wrapping pattern can be observed on the 30 kDa/Å tubes, and the tubes appear to be whiter than the 20 kDa/Å tubes and have another layer within the tube, suggesting some sort of polymorphism, or PSMα3 was likely unstable under STEM conditions and was partially disassembled in the process, where the tubes became unwrapped and stacked as outer-inner layers to result in higher M/L measurements. Using PSMα3 cross-α fibril's 10.5 Å helix stack rise distance, the 22.052 kDa/Å M/L measurement translates to 87 monomers per turn; with PSMα3 cross-α

fibril's 4 monomer per asymmetric unit parameter, this roughly equals to 11 asymmetric units per turn. This number will be confirmed once both PSMα3 nanotube cryo-EM models are further refined.

A B

Figure 2.14. Dark field STEM images of 302 µM PSMα3 in pH 2, A) nanotubes with ~20 kDa/Å M/L; B) nanotubes with ~30 kDa/Å M/L.

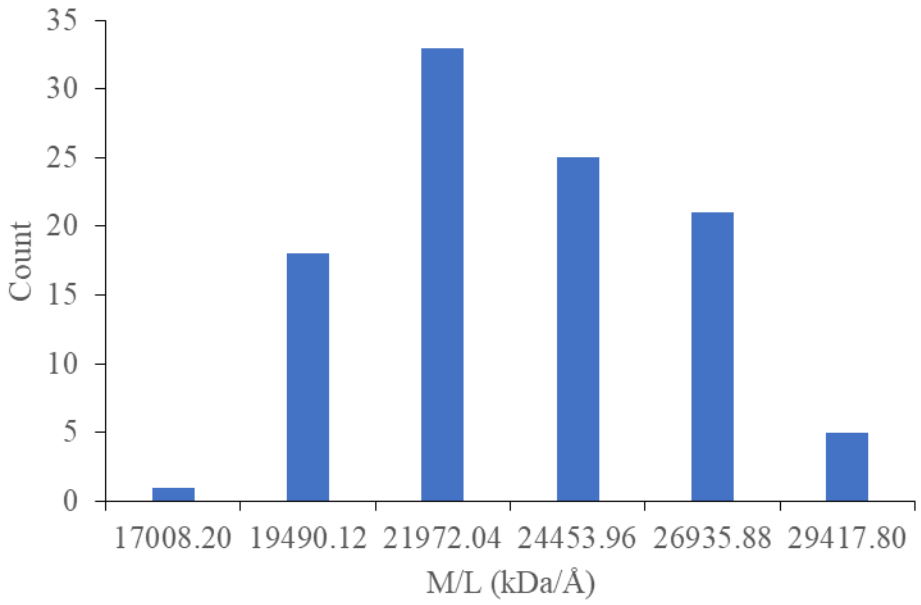

Figure 2.15. Histogram of PSMα3 nanotube M/L measurements. Average = 22.052 kDa/Å.

In conclusion, PSMα3 are shown to very robustly self-assemble into apparently monodisperse nanotubes at a narrow pH range of pH 1.81 – 2.26; 2 models of PSMα3 nanotubes arise from PSMα3 cross-α fibrils were shown by cryo-EM, but due to their slight variance in diameter (34.6 nm vs 37.6 nm), the models still needs to be refined. SAXS signals of these PSMα3 nanotubes fitted a mono-disperse hallow cylinder system with the calculated cylinder diameter matching to the width measured via TEM. AFM suggests PSMα3 nanotubes are double-layered, and STEM suggests there are 11 PSMα3 cross-α units per turn of PSMα3 nanotubes.

2.2.3 Characterization of PSMα3 nanotubes at pH 8

Because the PSMα3 90 and 150 nm width "wide" nanotube assemblies observed at pH 8 annealed at 90 ℃ for 30 minutes were only rarely observed at pH 7 annealed 90 ℃, PSMα3 was then further screened at 377 μM peptide concentration, in pH 7.5 MOPS, pH 8.5 TAPS, pH 9 CHES, pH 10 and pH 11 CAPS, and pH 12 and pH 13 KCl buffers, all annealed at 90 ℃ for 30 minutes to investigate the critical pH required to induce the formation of these wider nanotubes, and whether pH could selectively induce a uniform nanotube width of either 90 nm or 150 nm to allow the use of other characterization methods such as SAXS. After 24 h of incubation, a significant number of fibrils was observed at pH 7.5 (Figure 2.16A). At pH 8.5, tubes, broken tubes and wrapping tapes were observed (Figure 2.16B). At pH 9, tubes were still present but tapes became the most common assembly type (Figure 2.16C); some large sheets show a striation pattern (Figure 2.16E), FFT on the patterns yields a 6.7 nm/cycle fibril spacing (Figure 2.16E). This 6.7 nm/cycle spacing roughly corresponds to the ~8 nm spacing measured from the pH 1.81 PSMα3 sample, although the latter could not be distinguished via FFT. The tape width in pH 9 and pH 10 seems to be distributed from 50 nm to 90 nm, but most seems to be 70 nm wide (Figure 2.17). This tape width distribution matches the measured helical tape width in the pH 2 PSMα3 sample at 10 minutes, suggesting the possibility these tapes share the same structure. At pH 10, the assemblies are similar to pH 9's (Figure 2.16D). At pH 11, only singular fibrils were observed (Figure 2.16F). At pH 12 and above, no assemblies were observed (Figure 2.16G).

A

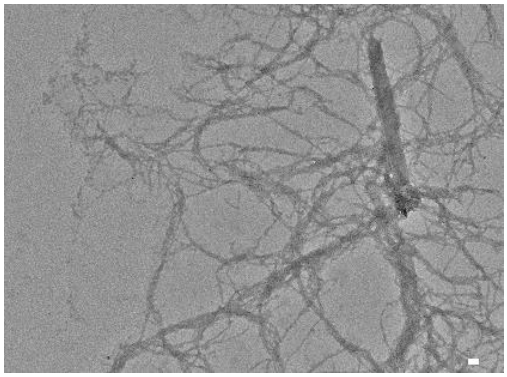

B

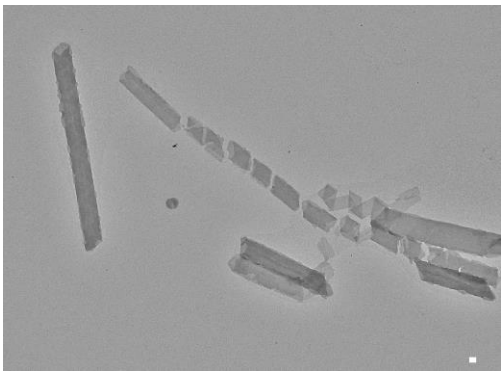

C

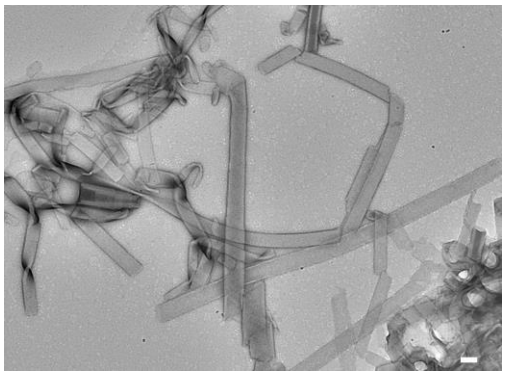

D

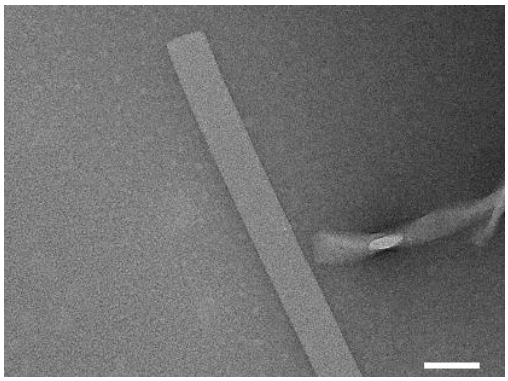

E

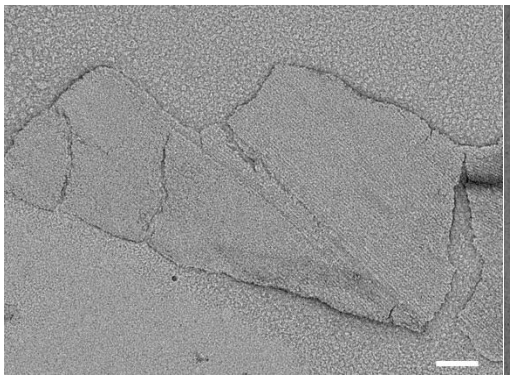

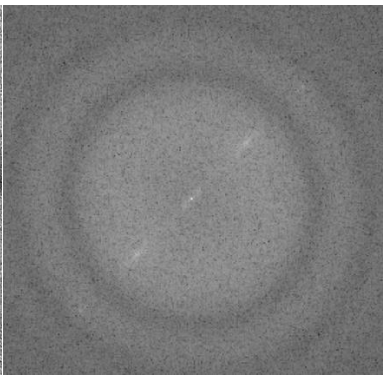

F G

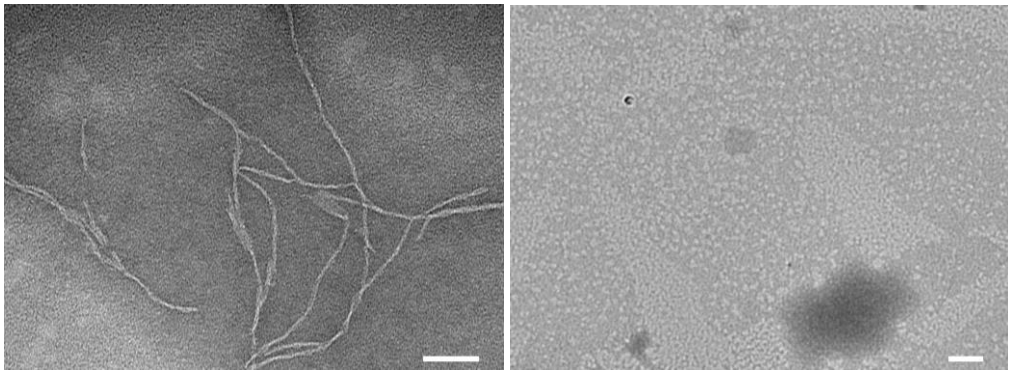

Figure 2.16: Representative TEM images of 377 μM PSMα3, after 7 days of assembly time, A) 10mM pH 7.5 MOPS; B) 10mM pH 8.5 TAPS; C) 10mM pH 9 CHES; D) 10mM pH 10 CAPS; E) 10mM pH 9 CHES with a FFT of the striations, spacing = 6.7 nm/cycle; F) 10mM pH 11 CAPS; G) 10mM pH 12 KCl. All scale bars = 100 nm.

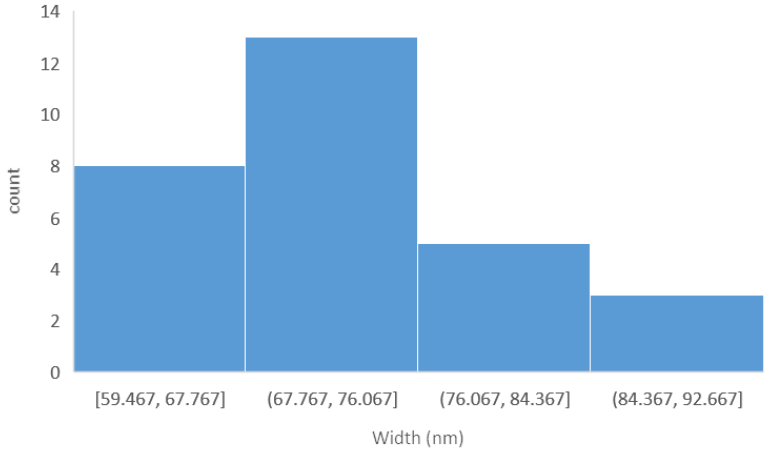

Figure 2.17. Histograms of tape widths measured via TEM in 377 μM PSMα3 pH 9 CHES and pH 10 CAPS, average = 71.2 nm.

Both pH 7 and pH 8 display α-helical CD signatures with minima at 209 nm and ~224 nm (Figure 2.18A). At above pH 9, CD signals are especially noisy potentially due to poor solubility to draw any conclusions (Figure 2.18B), but both show very weak α-helical CD signatures with local minima at 220-230 nm and 210-220 nm.

A B

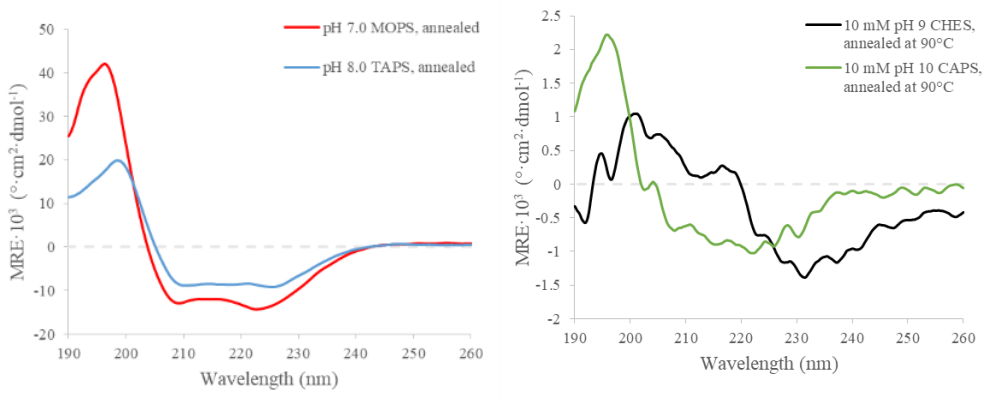

Figure 2.18. Circular dichroism spectra of A) 377 µM PSMα3 in pH 7.0 MOPS, pH 8.0 TAPS annealed at 90 ℃; B) 377 µM PSMα3 in pH 9.0 CHES, pH 10.0 CAPS annealed at 90 ℃.

To determine the critical temperature inducing the wide PSMα3 nanotube assembly, CD melting experiment was performed on a 377 µM PSMα3 in pH 8.0 TAPS prepared at room temperature sample, monitoring the MRE at the global max absorption 223 nm, with a melting profile increasing from 5 ℃ to 95 ℃ in 60 minutes (Figure 2.19A). A melting transition can be observed between 76.3 ℃ and 79.7 ℃ (Figure 2.19B).

A B

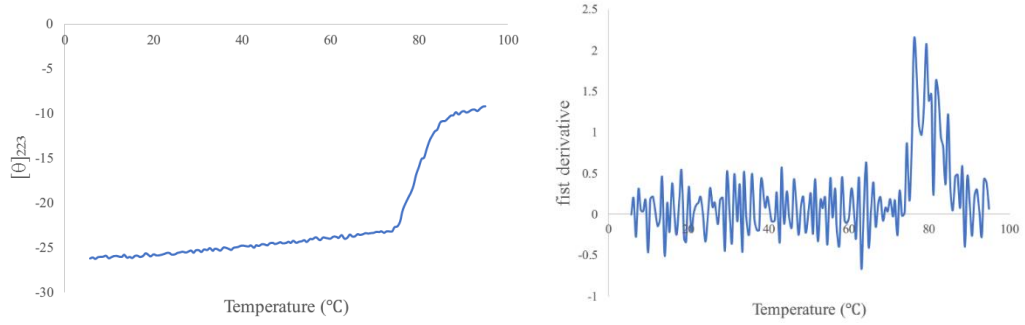

Figure 2.19. CD melting spectrum of 377 µM PSMα3 in pH 8.0 TAPS buffer from 5 ℃ to 95 ℃, monitoring the MRE at 223 nm; B) first derivative of A), indicating a melting transition between 76.3 ℃ and 79.7 ℃.

PSMα3 was then screened at 377 μM peptide concentration in 10 mM pH 8 TAPS buffer, annealed at 37 ℃, 50 ℃, 70 ℃ and 80 ℃ respectively for 30 minutes then slowly cooled to room temperature at 1 ℃ / 5 min, to confirm if the observed 76.3 ℃ melting transition is detrimental inducing wide nanotube assembly. After 24 h of incubation, all conditions except for annealed at 80 ℃ showed minor nanotube assemblies all with a large amount of fibrils present. Interestingly, all of these nanotubes have a measured width of 55 – 60 nm similar to the narrow PSMα3 nanotubes, suggesting temperature can induce nanotube formation perhaps similarly to acidic pH 2 condition. In annealed at 80 ℃, 90 nm wide nanotubes were the major assembly species, confirming 76.3 ℃ - 79.7 ℃ could be the critical temperature range inducing wide PSMα3 nanotube formation.

A B

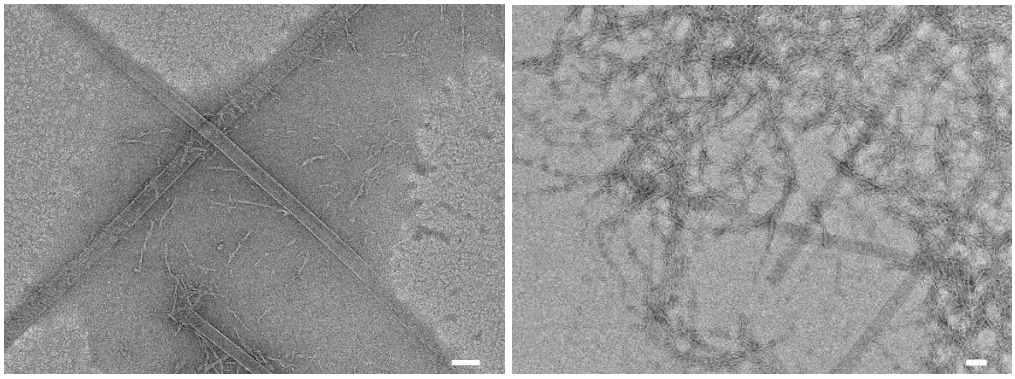

C D

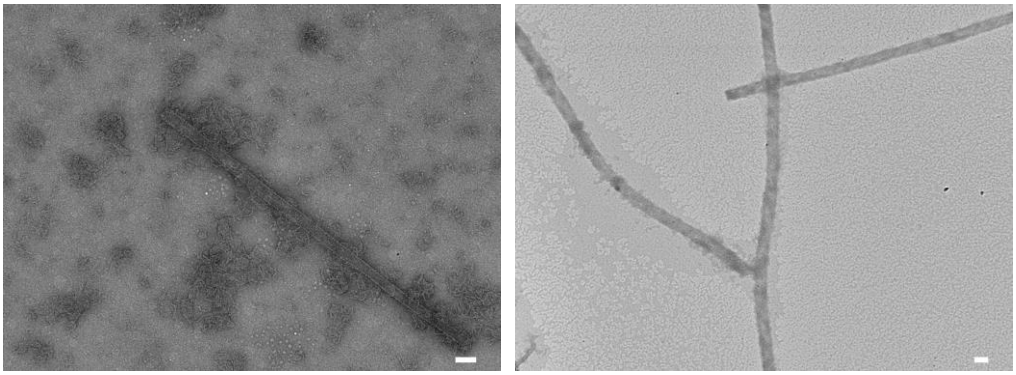

Figure 2.20. Representative TEM images of 377 μM PSMα3 in pH 8.0 TAPS, A) annealed at 37 ℃ for 30 min, then incubated at room temperature for 24 h; B) annealed at 50 ℃ for 30 min, then incubated at room temperature for 24 h; C) annealed at 70 ℃ for 30 min, then incubated at room temperature for 24 h; D) annealed at 80 ℃ for 30 min, then incubated at room temperature for 24 h. All scale bars = 100 nm.

Encouraged by the observation of narrow PSMa3 nanotubes at a more biologically relevant condition compared to pH 2, PSMα3 was further screened at 377 μM peptide concentration in pH 8.0 TAPS, with various incubation cycles between 37 ℃ and room temperature. After 72 h of incubation at 37 ℃, PSMα3 showed a majority nanotube formation with varied nanotube widths, but most nanotubes have a width of 60 nm (Figure 2.21A). When this sample was then incubated at room temperature for another 72 h, most nanotubes reverted to twisting fibrils (Figure 2.21B). Majority nanotubes were observed once again after this sample was incubated at 37 ℃ for another 72 h (Figure 2.21C), suggesting this nanotube assembly process directed by temperature is reversible and repeatable. When this sample was incubated at 37 ℃ for 1 week, further incubations at room temperature no longer induced nanotubes to revert to twisting fibrils at a large scale (Figure 2.21D). PSMα3 was found to assemble into predominantly nanotubes when incubated at 37 ℃, allowing further characterizations via cryo-EM, SAXS and STEM.

A B

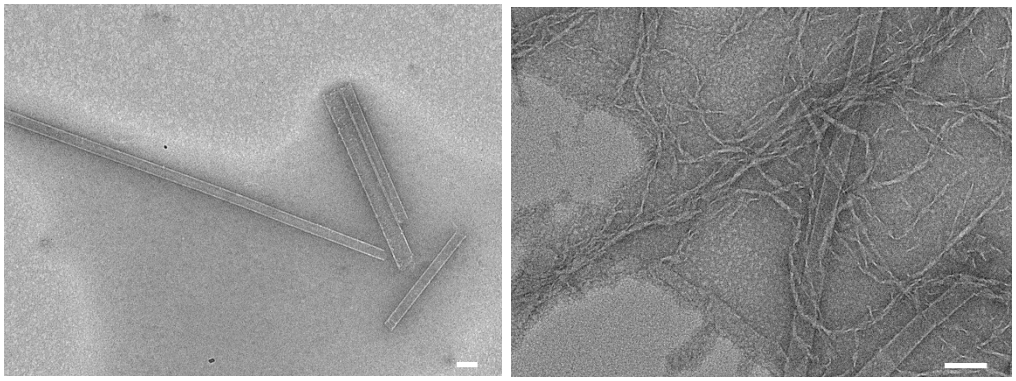

C D

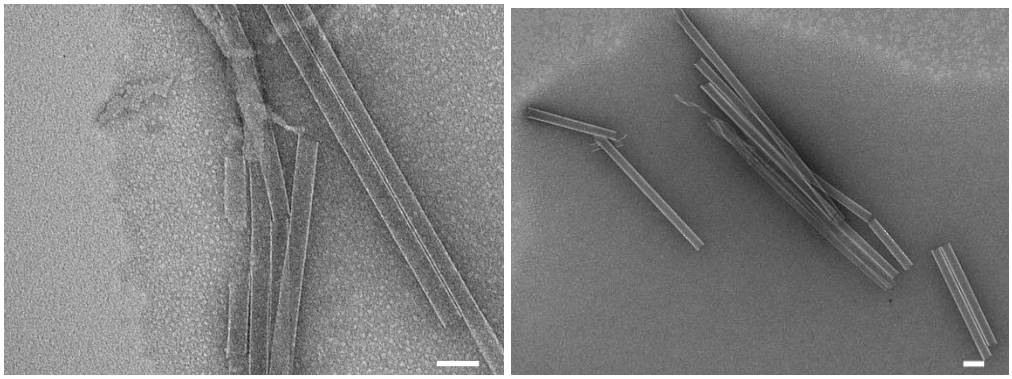

Figure 2.21. Representative TEM images of a 377 μM PSMα3 in pH 8.0 TAPS sample, A) first incubated at 37 ℃ after 1 day; B) after A), then incubated at room temperature for 72 h; C) after B), then incubated at 37 ℃ for 72 h; D) after C) is further incubated at 37 ℃ for 1 week, then incubated at room temperature for 72 h. All scale bars = 100 nm.

PSMα3 was then screened at 10 mM pH 5.0 acetate, pH 6.0 MES, pH 7.0 and 7.5 MOPS, pH 7.5 and 8.5 TAPS, pH 9.0 CHES and pH 10.0 CAPS, all incubated at 37 ℃ to determine whether PSMα3 can assemble into nanotubes at pH other than 8.0. After 72 h of incubation, only both conditions at pH 7.5 showed ~55 nm wide nanotube and fibril assemblies (Figure 2.22D and E), while others only showed twisting and non-twisting fibrils (Figure 2.22 A-C, F-H). PSMα3 nanotube morphology is shown to be very selective towards a narrow pH range of pH 7.5 - 8 when

incubated at 37 ℃, similar to the previously shown pH 1.81-2.26 range required for PSMα3 to assemble into nanotubes under room temperature.

A

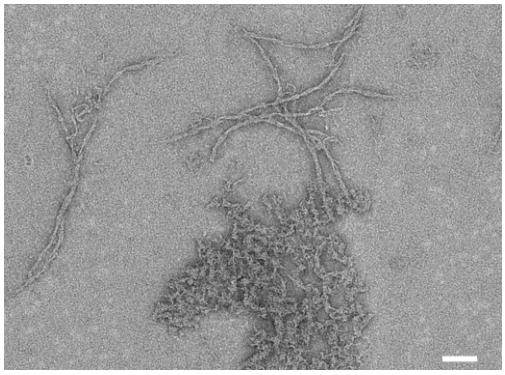

B

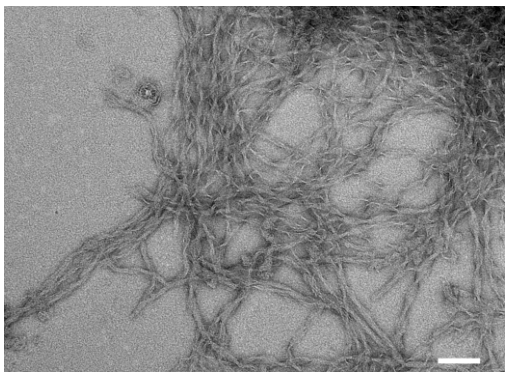

C

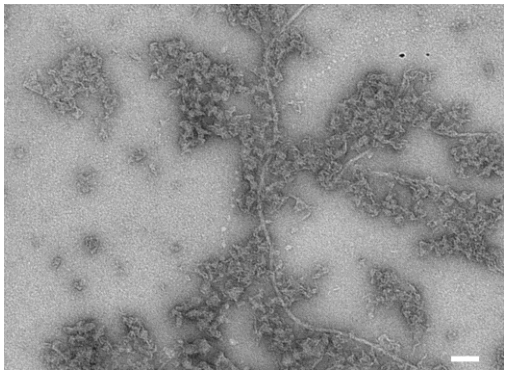

D

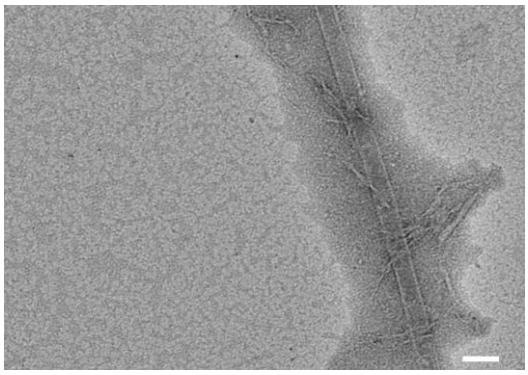

E

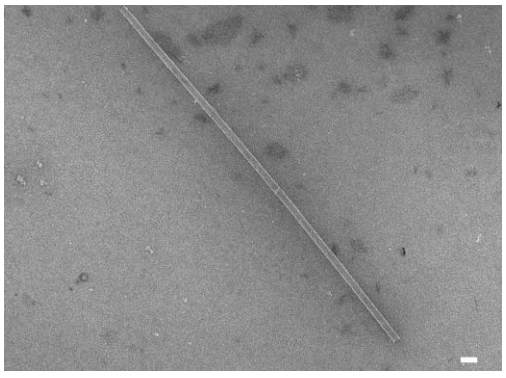

F

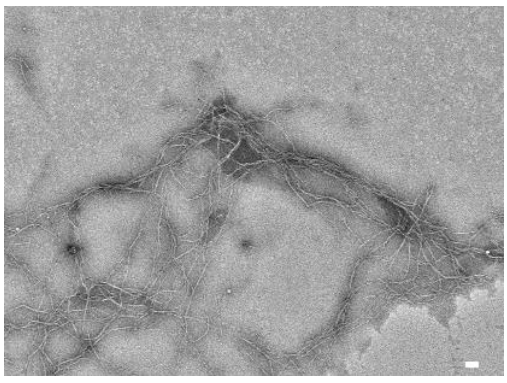

G

H

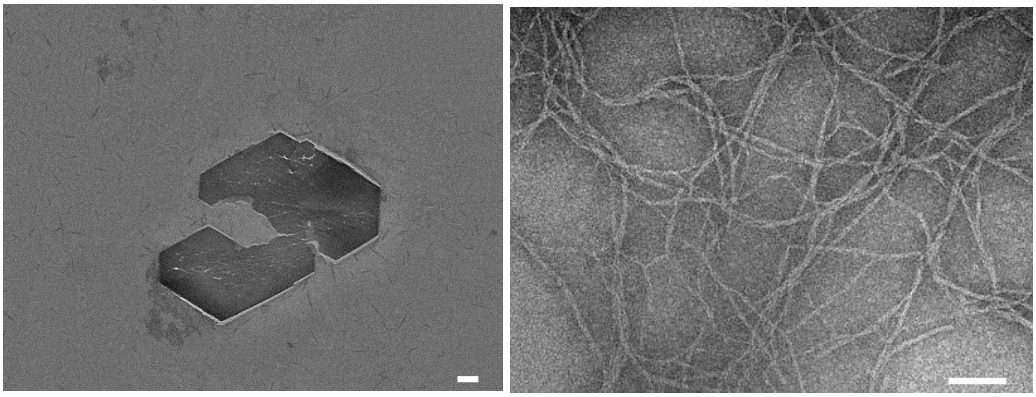

Figure 2.22 Representative TEM images of 377 μM PSMα3, incubated at 37 ℃ for 3 days, in A) 10 mM pH 5.0 acetate; B) 10 mM pH 6.0 MES; C) 10 mM pH 7.0 MOPS; D) 10 mM pH 7.5 MOPS; E) 10 mM pH 7.5 TAPS; F) 10 mM pH 8.5 TAPS; G) 10 mM pH 9.0 CHES; H) 10 mM pH 10.0 CAPS. All scale bars = 100 nm.

In summary, the results above showed 1. PSMα3 could selectively self-assemble into 90 nm and 150 nm wide nanotubes at pH 7.5 - 8.0 and when annealed at 80 ℃ or more, and a basic pH (> pH 9) inhibits nanotube wrapping to direct sheets with a uniform width instead; 3. PSMα3 can selectively self-assemble into nanotubes at pH 7.5 – pH 8.0 when incubated at 37 ℃, where its diameter is similar to PSMα3 nanotube at pH 2's; 3. PSMα3 narrow nanotubes at 37 ℃ is reversible to some degree. Because such reversibility is commonly observed in nature[30-31] or exploited in designs to achieve peptide/drug release and delivery, it is very possible PSMα3 holds some structure-related activity related to its reversible nature.

2.2.4 Screening of amphipathic peptides potentially posing cross-α structures

It has been suggested in the literature the cross-α structure might commonly exist, despite it only being recently discovered: αAm_{mem} is a membrane-spanning Zn transporter protein that has been used to design cross-α fibrils[32]; stacked α-helices perpendicular to the nanotube elongation direction could laterally associate through termini to form nanotubes[33]; an unconfirmed case of α-helical fibrils with the fibril width matching the peptide helical length, suggesting the helices are perpendicular to the fibril axis[34]; and recently, an antimicrobial peptide Uperin 3.5 is found to somewhat adopt a cross-α structure[35]. Both αAm_{mem} and PSMα3 show an amphipathic helix nature. Amphipathic α-helices are commonly used as design targets[36] or in nature such as antimicrobial peptides[37], where the polar interface of the helix is suggested to help disrupt cell membranes leading to cell death[38-39], and peptide self-assembly has been suggested as one of the mechanism of action by forming pores and channels on the membrane[40]. Antimicrobial peptides often self-assemble into fibrils and tapes alike, and it's been shown these structures are related to the antimicrobial activities[41-43]. With these, we propose that amphipathic and antimicrobial peptides can commonly self-assemble into cross-α structures, and such self-assemblies could be detrimental to the antimicrobial functions. To explore this hypothesis, the antimicrobial peptide warnericin RK was screened as a candidate. Warnericin RK is the first isolated antimicrobial peptide shows activities against the *Legionella* genus, but this peptide was ultimately chosen as the initial screening candidate due to its amphipathic nature and its sequence similarity to PSMα3 (Figure 2.23). From the helical wheel representations, warnericin-RK also has a phe-leu rich hydrophobic interface and lys rich hydrophilic interface; both have basic residues near the hydrophobic interface and acidic residues at the middle. These features might promote α-helix stacking and mating to form a cross-α structure similar to PSMα3's.

Warnericin-RK:MQFITDLIKKAVDFFKGLFGNK

PSMα3: MEFVAKLFKFFKDLLGKFLGNN

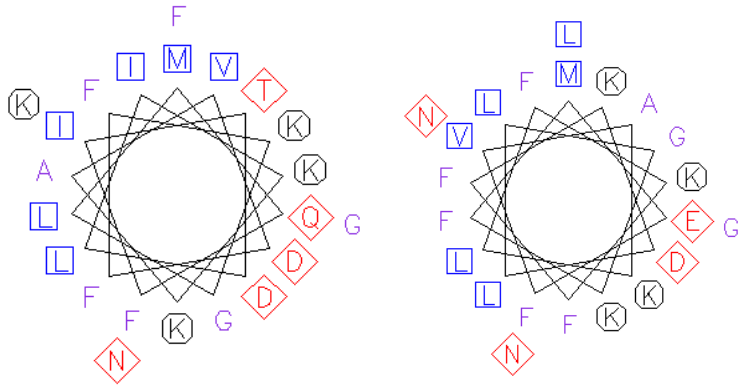

Figure 2.23. helical wheel representation of Warnericin RK (left) and PSMα3 (right), hydrophilic residues are labeled with red diamonds (acidic) and black octagons (basic)

Warnericin-RK was synthesized via solid-phase peptide synthesis with N-terminal acetylation and C-terminal amidation to reduce termini charges. Peptide was purified by preparative HPLC, characterized by MALDI and its purity was confirmed by MALDI and analytical HPLC. Warnericin-RK was screened in conditions where PSMα3 (wildtype) was shown to assemble into nanotubes. Warnericin-RK assembled into a mixture of nanotubes and tapes with varied width ranges from 100 nm – 300 nm in pH 5.0 – 8.0, both at room temperature or incubated at 37 ℃ (Figure 2.24). All assemblies display α-helical CD signatures (Figure 2.25). Because Warnericin-RK's polymorphic nature make it difficult to characterize a specific structure, further optimization is need to selectively direct Warnericin-RK's self-assembly for characterization with high-resolution methods such as cryo-EM. However, this preliminary result suggests amphipathic peptides may self-assemble into some high-order structures arising from fibrils, which may adopt the cross-α structure shown by PSMα3.

A B

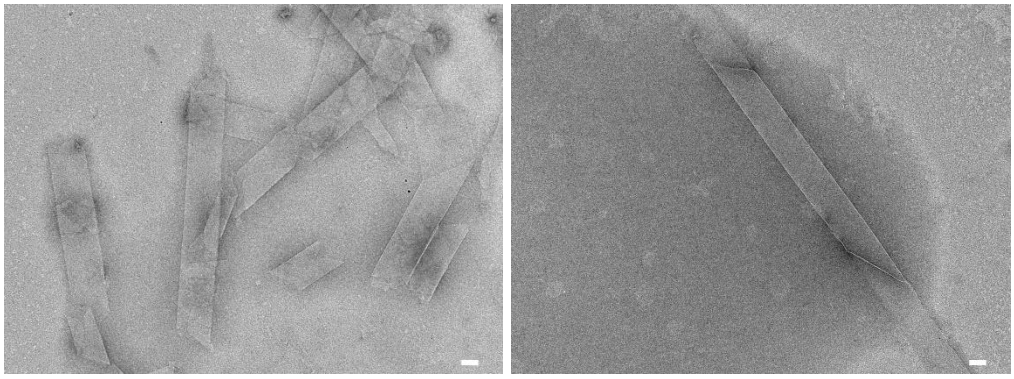

C

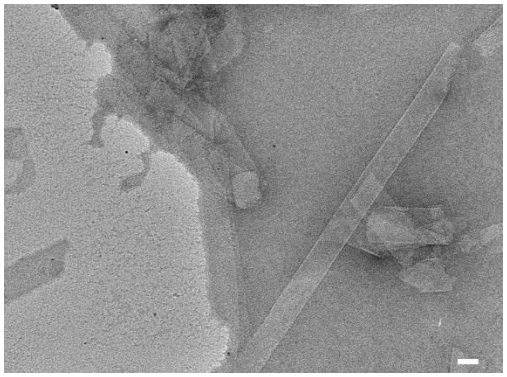

Figure 2.24. Representative TEM images of 518 µM warnericin-RK in A) pH 6.0 MES, B) pH 6.0 MES incubated at 37 ℃ and C) pH 8.0 TAPS buffer incubated at 37 ℃, with 2 days of assembly time. All scale bars = 100 nm.

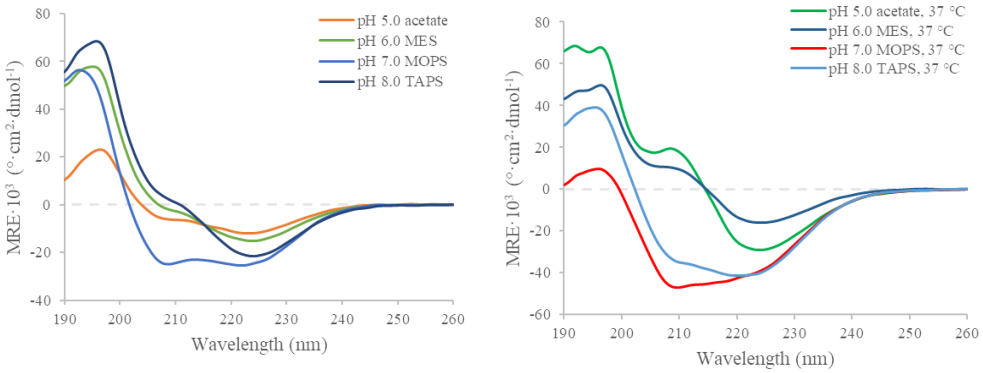

Figure 2.25. CD spectra of 518 µM warnericin-RK in pH 5.0 – 8.0 buffer, room temperature (left) and incubated at 37 ℃ (right).

2.3 Conclusion

Presented in this chapter, PSMα3 is shown to self-assemble into nanotubes under extreme acidic conditions at pH 2.0. PSMα3's assembly kinetics is very fast, although some nanotube precursor morphologies, such as helical ribbons with somewhat uniform tape width, can be occasionally observed at very early time points. These nanotubes were previously observed in the literature, although fibrils were the dominant species. Through optimizing assembly conditions, PSMα3 selectively assembled into nanotubes, allowing for further characterization by SAXS and cryo-EM. The atomic model of PSMα3 nanotubes characterized via cryo-EM reveals the nanotubes are a result of lateral associations of the previously observed cross-α PSMα3 fibrils, but two or more populations of nanotubes with distinct diameters present.

Further screenings of other PSMα3 nanotube conditions yielded interesting results: PSMα3 was able to form possibly the same structure under near neutral pH conditions as at pH 2.0, and this nanotube formation is reversible to some degree when cooled from 37 ℃ to 20 ℃. This opens the possibility PSMα3 nanotube structure has biological relevance since it could be selectively self-assembled under biologically relevant conditions. While it might be redundant to also characterize these tubes' structures via cryo-EM, especially since the nanotube assemblies at pH 2 are polymorphic and would be difficult to determine the structures this way, SAXS, AFM and STEM might suffice to confirm the PSMα3 nanotubes at pH 2.0 and pH 8.0 share similar structures. Once confirmed, determining whether PSM peptides self-assemble into this nanotube structures at these assembly conditions will help determine whether these nanotube structures actually have a biological role, and what are the roles.

PSMα3 was also found to selectively self-assemble into wide nanotubes but with two distinct width populations at 100 nm and 150 nm. While this polymorphism adds difficulty for further characterization of these nanotubes, it is still hypothesized these wider nanotubes are structurally similar to the previously characterized PSMα3 nanotubes and originate from the same

cross-α fibrils. This would be interesting to serve as a starting point for tuning nanotube structures. Such tuning effects on fibrils were achieved through changing an aromatic moiety in close-contact[44], computational design[45], assembly conditions[46] and more, and it's not uncommon to manipulate self-assembly structures via temperature. PSMα3 can be developed into temperature-sensitive nanomaterials with morphology, nanotube diameter and critical temperature controls. Preliminary mutagenesis and redesign results of PSMα3-H showed the PSMα3 nanotube assembly is tolerable to mutations, and thus a promising candidate for nanomaterial application re-designs.

Lastly, the preliminary data of warnericin-RK's nanotube self-assembly showed some weak evidences that the cross-α structure might be common in natural, amphipathic peptides. Amphipathic peptides are known self-assemble into fibrils and even higher order structures[42-43, 47-48], and it wouldn't be surprising if these nanotube structures have some modulation or facilitation effects towards fibril formation and displaying antimicrobial activities.

These experimental results achieved 2 of the 3 goals defined in this chapter's introduction: one of the polymorphic PSMα3 assemblies is optimized to be selectively assembled, allowed for further characterization that will be completed in the near future. Data shows promising leads toward the last goal, to determine whether these morphologies have a function, which may reveal the cytotoxicity mechanism of PSMα3 via a cross-α related pathway, or even add to the understanding antimicrobial activity originates from cross-α structures.

2.4 Methods

Materials and Reagents. All Fmoc protected amino acids were purchased from Aapptec; all other chemical reagents were purchased from Sigma-Aldrich, unless otherwise specified. Peptide synthesis resin was ordered from Applied Biosystems (Foster City, CA).

Peptide Synthesis. PSMα3 was prepared via a microwave assisted solid phase peptide synthesis, on a CEM Liberty Blue instrument as the *N*-acetyl, *C*-amide capped derivatives. Applied Biosystem's Fmoc-PAL-PEG-PS resin was used for synthesizing these peptides at a 0.1 mmol scale. Coupling reactions were conducted with 0.2 M N-fluorenylmethyloxycarbonyl (Fmoc)-protected amino acids in N,N-Dimethylformamide (DMF, activated with 0.5 M N,N'-Diisopropylcarbodiimide (DIC) in DMF and 0.5 M Ethyl cyanohydroxyiminoacetate (oxyma) in DMF. The coupled amino acid was deprotected using 20% piperidine in DMF. All amino acids were deprotected with 5 ml piperidine solution, 75 ℃ temperature and 155 W microwave power for 15 seconds as the first stage, and 75 ℃ temperature and 155 W microwave power for 15 seconds as the second stage; coupled with 2.5 ml DIC solution, 75 ℃ temperature and 170 W microwave power for 15 seconds as the first stage, and with 2.5 ml oxyma solution, 90 ℃ temperature and 30 W microwave power for 110 seconds as the second stage. C-terminal amide modification was done after all amino acids were coupled, with 2.5 ml 20% acidic anhydride in DMF, 75 ℃ temperature and 155 W microwave power for 15 seconds as the first stage, and 75 ℃ temperature and 155 W microwave power for 15 seconds as the second stage. Peptides were cleaved from the resin by incubation at room temperature for 3 hours in a 20 ml cocktail consisting of 92.5% trifluoroacetic acid (TFA), 2.5% distilled water, 2.5% triisopropylsilane, and 2.5% 2,2'- (ethylenedioxy)-diethanethiol. The cleaved peptide solution was filtered and precipitated with 60 ml of 4 ℃ diethyl ether. The peptide/diethyl ether mixture was then centrifuged at 4 ℃ at 4,000 rpm for 10 min. The supernatant was then discarded, and the precipitate allowed to desiccate overnight. Following

desiccation, the crude peptide gels were resolubilized in 3 mL of a 50:50 mixture of acetonitrile and water (0.1% TFA additive) and purified by reversed-phase high-pressure liquid chromatography (HPLC) using two Shimadzu LC-20AP pumps running at 60 ml/min, a Shimadzu SPD-20A UV detector monitoring at 220 nm, on a Kinetex 5 μm C18 column, 250 mm long * 30 mm wide with a water-acetonitrile (0.1% TFA-additive) gradient. For PSMα3, the gradient used was 50% acetonitrile at 0 min, then gradually increased to 85% acetonitrile at 35 min, and finally was held at 90% acetonitrile for 10 min; PSMα3 eluted at 12.3 min. Peptide mass was confirmed using MALDI-TOF mass spectrometry on an Applied Biosystems AB4700 Proteomics analyzer in reflectron positive ion mode, with α-Cyano-4-hydroxycinnamic acid as the matrix. Purified HPLC fractions were then lyophilized, sealed, and stored at -30 ℃.

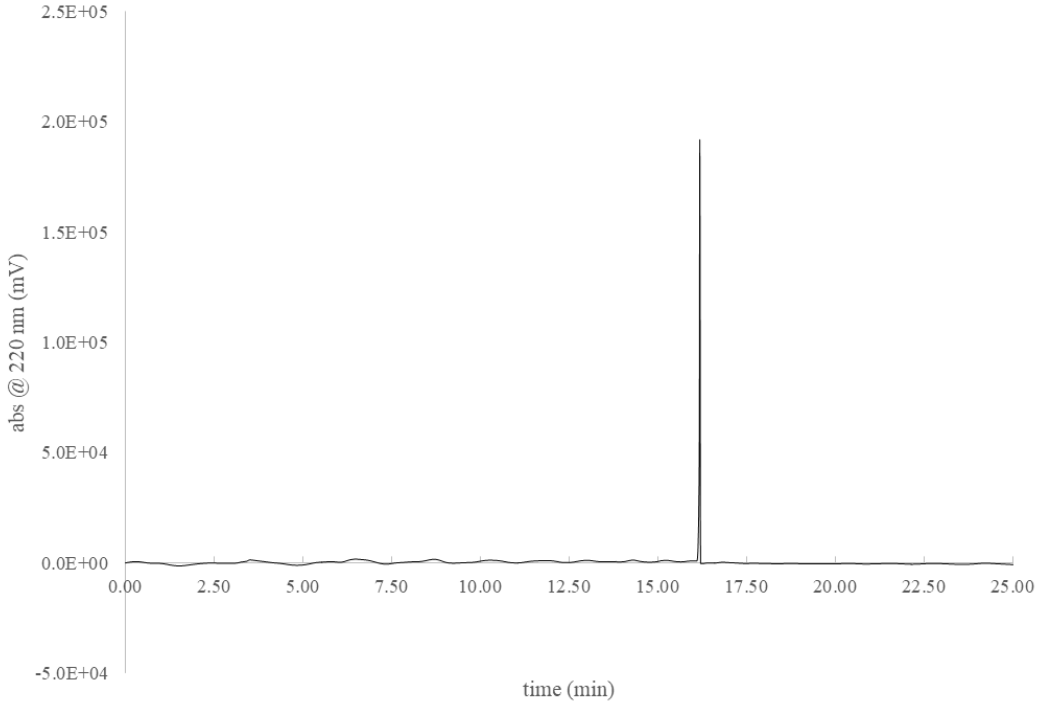

Figure 2.26. Analytical HPLC trace of PSMa3.

Peptide Assembly. Stock solutions of PSMa3 were prepared by solubilizing 0.5 to 1.5 mg of purified, lyophilized peptide in 1 mL of HPLC water; 10 mM acetate, pH 2.6, 2.9 and 5; 10 mM MES, pH 6.0 and 6.5; 10 mM MOPS, pH 7.0 and 7.5; 10 mM TAPS, pH 8.0 and 8.5; 10 mM CAPS, pH 9.0 and 9.5; or 10 mM CHES, pH 10.0 buffer, at a final peptide concentration of 189 μM to 556 189 μM. Immediately after mixture, the solutions were titrated to the respective buffer pH using 100 mM sodium hydroxide solution except for the PSMa3 sample with HPLC water, where dilute trifluoroacetic acid solution was used to titrate to pH 2. For samples other than in water, solutions were thermally annealed using the following thermal cycler protocol: (1) rapid heating to 90 ℃ for 30 minutes; and (2) cooling to 25 ℃ at a rate of 0.2 ℃ / minute.

Circular Dichroism Spectropolarimetry. CD measurements were performed on a Jasco J-1500 CD spectropolarimeter in 0.1 mm quartz cells (Hellma Analytics), at various peptide self-assembly conditions. Spectra were recorded from 260 to 190 nm at a scanning rate of 100 nm/min and a data pitch of 0.2 nm. CD melting experiments were performed in the temperature range of 5 ℃ to 95 ℃, at a heating rate of 60 ℃/hour; the intensity of the CD signal at 209 nm was monitored as a function of temperature.

Transmission Electron Microscopy. TEM specimens were prepared from aqueous solutions of PSMa3. To cover the entire sample grid, 4 μL of the samples were deposited onto 200 mesh carbon-coated copper grids from Electron Microscopy Services (Hatfield, PA). After 90 seconds of incubation period, the samples were wicked away until a thin film of sample remained, then the grids were stained with 1% uranyl acetate solution, filtered with 0.2 μm Whatman filter from G.E. Healthcare Services. After 60 seconds of stain incubation period, all liquids were wicked away, and the grids were dried in a tabletop desiccator under vacuum. TEM measurements were acquired on a Hitachi HT-7700 transmission electron microscope with a tungsten filament and AMT CCD camera, at an accelerating voltage of 80 kV.

Atomic Force Microscopy. AFM specimens were prepared from 1.2 mg/mL PSMa3 in pH 2 water with TFA. The PSMα3 solution was diluted to 0.3 mg/mL using 0.85% TFA in water right before deposition on a freshly cleaved mica substrate (TedPella). A total of 100 μL of sample was deposited on mica for 5 minutes before being wicked away. The AFM experiments were performed using a MFP-3D-BIO from Asylum Research. Silicon AFM tips (MikronMasch) with a force constant (5.4-16 N/m) were used to image the specimens in tapping mode, at a scan rate of 1 Hz.

Cryo-electron Microscopy and Image Processing. The sample was applied to glow-discharged lacey carbon grids and vitrified in a Vitrobot Mark IV (FEI, Inc.). Grids were imaged in a Titan Krios at 300 keV and recorded with a Falcon II direct electron detector at 1.05 Å per pixel. Images were collected using a defocus range of 0.5–3.0 μm, with a total exposure of 2 s (amounting to 70 electrons ·Å-2) dose-fractionated into seven chunks. All the images were first motion corrected by the MotionCorr v2 (1), and then the CTFFIND3 (2) program was used for determining the actual defocus of the images. Images with poor CTF estimation as well as defocus > 3 μm were discarded. A total of 386 images were selected and peptide filaments of varying lengths were boxed using the e2helixboxer program within EMAN2 (3). The CTF was corrected by multiplying the images from the first two chunks (containing a dose of ~ 20 electrons ·Å -2) with the theoretical CTF. Overlapping 256-px long boxes with a shift of 5 pixels (~ 1.5 times of the axial rise) were cut from the long filaments. The determination of the helical symmetry was by trial and error, searching for a symmetry which yielded recognizable secondary structure. Power spectra from the filaments suggested a variability in the helical parameters.

Scanning Transmission Electron Microscopy. STEM data were acquired at Brookhaven National Laboratory (BNL). The STEM instrument operates at 40 keV with a scanning probe of 0.3 nm diameter produced from a cold field-emission source. Each electron emerging from the specimen is detected by one of the scintillator photomultiplier detectors collecting 0−15 mRadian (bright field), 15−40 mRadian (small-angle dark field) and 40−200 mRadian (large-angle dark

field). The large-angle signal is proportional to the mass of atoms in the path of the beam. Specimen quality and mass calibration were assessed by detailed comparison of the image to the known structure of tobacco mosaic virus (TMV). For mass-per-length (M/L) measurements, TMV rafts at a theoretical M/L value of 13.1 kDa/Å were employed for calibration.

Specimens were deposited on thin carbon (circa 2 nm thick) supported on a thicker holey carbon film mounted on a titanium grid using the wet-film, hanging-drop method. TMV was added to the grid first as an internal control, followed by injection buffer, then specimen solution (in pH 2 water) for 1 min, then 10 washes of 20 mM ammonium acetate pH 7.0. Excess solution was wicked from the edge with filter paper between each injection. After the last wash, the grid was wicked to a thin layer (ca. 1 mm), fast frozen by plunging into liquid nitrogen slush and stored under liquid nitrogen. Grids were freeze-dried overnight in an ion pumped chamber with an efficient cold trap and transferred under vacuum to the STEM cold stage (−160 °C). Imaging typically uses a dose of 20 e–/Å2 (causing < 5% mass loss, corrected by comparison to TMV). Mass per length measurements of the PSMβ2 nanotubes were performed with the software PCMass32.

Small- and Wide-Angle X-Ray Scattering Measurements. Synchrotron SAXS/WAXS measurements were taken at the 12-ID-B beamline of the Advanced Photon Source at Argonne National Laboratory in Lemont, Illinois. PSMα3 nanotube sample was dialyzed into pH 2 water, with a 1% glycerol additive to stabilize against X-ray radiation damage. SAXS/WAXS measurements were then taken on the peptide solutions at 25 ℃ in a quartz capillary flow cell (1.5 mm). The solutions were raised and lowered in the flow cell to minimize radiation damage. Twenty 2D images were collected per sample, and then azimuthally averaged into 1D SAXS scattering curves after solid angle correction and normalization against the transmitted X-ray beam intensity, using the software package at beamline 12-ID-B. The 1D scattering curves were then averaged, and the averaged signal from the MES buffer was subtracted out.

1. Wang, R.; Braughton, K. R.; Kretschmer, D.; Bach, T. H.; Queck, S. Y.; Li, M.; Kennedy, A. D.; Dorward, D. W.; Klebanoff, S. J.; Peschel, A.; DeLeo, F. R.; Otto, M., Identification of novel cytolytic peptides as key virulence determinants for community-associated MRSA. *Nature medicine* **2007,** *13* (12), 1510-4.
2. Tong, S. Y. C.; Davis, J. S.; Eichenberger, E.; Holland, T. L.; Fowler, V. G., Staphylococcus aureus Infections: Epidemiology, Pathophysiology, Clinical Manifestations, and Management. *Clinical Microbiology Reviews* **2015,** *28* (3), 603-661.
3. Peschel, A.; Otto, M., Phenol-soluble modulins and staphylococcal infection. *Nat Rev Microbiol* **2013,** *11* (10), 667-73.
4. Cheung, G. Y.; Joo, H. S.; Chatterjee, S. S.; Otto, M., Phenol-soluble modulins--critical determinants of staphylococcal virulence. *FEMS microbiology reviews* **2014,** *38* (4), 698-719.
5. Bonesso, M. F.; Yeh, A. J.; Villaruz, A. E.; Joo, H. S.; McCausland, J.; Fortaleza, C. M.; Cavalcante, R. S.; Sobrinho, M. T.; Ronchi, C. F.; Cheung, G. Y.; Cunha, M. L.; Otto, M., Key Role of alpha-Toxin in Fatal Pneumonia Caused by Staphylococcus aureus Sequence Type 398. *Am J Respir Crit Care Med* **2016,** *193* (2), 217-20.
6. Cheung, G. Y.; Rigby, K.; Wang, R.; Queck, S. Y.; Braughton, K. R.; Whitney, A. R.; Teintze, M.; DeLeo, F. R.; Otto, M., Staphylococcus epidermidis strategies to avoid killing by human neutrophils. *PLoS Pathog* **2010,** *6* (10), e1001133.
7. Schwartz, K.; Syed, A. K.; Stephenson, R. E.; Rickard, A. H.; Boles, B. R., Functional amyloids composed of phenol soluble modulins stabilize Staphylococcus aureus biofilms. *PLoS Pathog* **2012,** *8* (6), e1002744.
8. Zheng, Y.; Joo, H. S.; Nair, V.; Le, K. Y.; Otto, M., Do amyloid structures formed by Staphylococcus aureus phenol-soluble modulins have a biological function? *International journal of medical microbiology : IJMM* **2018,** *308* (6), 675-682.
9. Le, K. Y.; Villaruz, A. E.; Zheng, Y.; He, L.; Fisher, E. L.; Nguyen, T. H.; Ho, T. V.; Yeh, A. J.; Joo, H. S.; Cheung, G. Y. C.; Otto, M., Role of Phenol-Soluble Modulins in Staphylococcus epidermidis Biofilm Formation and Infection of Indwelling Medical Devices. *Journal of molecular biology* **2019,** *431* (16), 3015-3027.
10. Xue, C.; Lin, T. Y.; Chang, D.; Guo, Z., Thioflavin T as an amyloid dye: fibril quantification, optimal concentration and effect on aggregation. *Roy Soc Open Sci* **2017,** *4* (1), 160696-160696.
11. Towle, K. M.; Lohans, C. T.; Miskolzie, M.; Acedo, J. Z.; van Belkum, M. J.; Vederas, J. C., Solution Structures of Phenol-Soluble Modulins alpha1, alpha3, and beta2, Virulence Factors from Staphylococcus aureus. *Biochemistry* **2016,** *55* (34), 4798-806.
12. Salinas, N.; Colletier, J. P.; Moshe, A.; Landau, M., Extreme amyloid polymorphism in Staphylococcus aureus virulent PSMalpha peptides. *Nat Commun* **2018,** *9* (1), 3512.
13. Tayeb-Fligelman, E.; Tabachnikov, O.; Moshe, A.; Goldshmidt-Tran, O.; Sawaya, M. R.; Coquelle, N.; Colletier, J. P.; Landau, M., The cytotoxic Staphylococcus aureus PSMalpha3 reveals a cross-alpha amyloid-like fibril. *Science* **2017,** *355* (6327), 831-833.
14. Cheung, G. Y.; Kretschmer, D.; Queck, S. Y.; Joo, H. S.; Wang, R.; Duong, A. C.; Nguyen, T. H.; Bach, T. H.; Porter, A. R.; DeLeo, F. R.; Peschel, A.; Otto, M., Insight into structure-function relationship in phenol-soluble modulins using an alanine screen of the phenol-soluble modulin (PSM) α3 peptide. *FASEB journal : official publication of the Federation of American Societies for Experimental Biology* **2014,** *28* (1), 153-61.
15. Tayeb-Fligelman, E.; Salinas, N.; Tabachnikov, O.; Landau, M., Staphylococcus aureus PSMalpha3 Cross-alpha Fibril Polymorphism and Determinants of Cytotoxicity. *Structure* **2020,** *28* (3), 301-313 e6.

16. Das, M.; Dash, S.; Bhargava, B. L., Computational studies of fibrillation induced selective cytotoxicity of cross-α amyloid – Phenol Soluble Modulin α3. *Chemical Physics* **2020,** *535*, 110777.
17. Yao, Z.; Cary, B. P.; Bingman, C. A.; Wang, C.; Kreitler, D. F.; Satyshur, K. A.; Forest, K. T.; Gellman, S. H., Use of a Stereochemical Strategy To Probe the Mechanism of Phenol-Soluble Modulin α3 Toxicity. *Journal of the American Chemical Society* **2019,** *141* (19), 7660-7664.
18. Gallardo, R.; Ranson, N. A.; Radford, S. E., Amyloid structures: much more than just a cross-β fold. *Current Opinion in Structural Biology* **2020,** *60*, 7-16.
19. Kumaraswamy, P.; Lakshmanan, R.; Sethuraman, S.; Krishnan, U. M., Self-assembly of peptides: influence of substrate, pH and medium on the formation of supramolecular assemblies. *Soft Matter* **2011,** *7* (6), 2744-2754.
20. Chen, J.; Zou, X., Self-assemble peptide biomaterials and their biomedical applications. *Bioactive Materials* **2019,** *4*, 120-131.
21. Lee, S.; Trinh, T. H. T.; Yoo, M.; Shin, J.; Lee, H.; Kim, J.; Hwang, E.; Lim, Y.-B.; Ryou, C., Self-Assembling Peptides and Their Application in the Treatment of Diseases. *Int J Mol Sci* **2019,** *20* (23), 5850.
22. Edwards-Gayle, C. J. C.; Hamley, I. W., Self-assembly of bioactive peptides, peptide conjugates, and peptide mimetic materials. *Organic & Biomolecular Chemistry* **2017,** *15* (28), 5867-5876.
23. Tayeb-Fligelman, E.; Salinas, N.; Tabachnikov, O.; Landau, M., Staphylococcus aureus PSMα3 Cross-α Fibril Polymorphism and Determinants of Cytotoxicity. *Structure* **2020,** *28* (3), 301-313.e6.
24. Anthis, N. J.; Clore, G. M., Sequence-specific determination of protein and peptide concentrations by absorbance at 205 nm. *Protein Sci* **2013,** *22* (6), 851-858.
25. Louis-Jeune, C.; Andrade-Navarro, M. A.; Perez-Iratxeta, C., Prediction of protein secondary structure from circular dichroism using theoretically derived spectra. *Proteins* **2012,** *80* (2), 374-381.
26. Pachahara, S. K.; Adicherla, H.; Nagaraj, R., Self-Assembly of Aβ40, Aβ42 and Aβ43 Peptides in Aqueous Mixtures of Fluorinated Alcohols. *Plos One* **2015,** *10* (8), e0136567.
27. Zheng, Y.; Joo, H. S.; Nair, V.; Le, K. Y.; Otto, M., Do amyloid structures formed by Staphylococcus aureus phenol-soluble modulins have a biological function? *Int J Med Microbiol* **2018,** *308* (6), 675-682.
28. Guinier, A.; Fournet, G. r., *Small-angle scattering of X-rays*. Wiley: New York,, 1955; p 268 p.
29. Lindner, P.; Zemb, T., *Neutrons, X-rays, and light : scattering methods applied to soft condensed matter*. 1st ed.; Elsevier: Amsterdam ; Boston, 2002; p x, 541 p.
30. Remedios, C. G. D.; Chhabra, D.; Kekic, M.; Dedova, I. V.; Tsubakihara, M.; Berry, D. A.; Nosworthy, N. J., Actin Binding Proteins: Regulation of Cytoskeletal Microfilaments. *Physiological Reviews* **2003,** *83* (2), 433-473.
31. Needleman, D.; Dogic, Z., Active matter at the interface between materials science and cell biology. *Nature Reviews Materials* **2017,** *2* (9), 17048.
32. Zhang, S.-Q.; Huang, H.; Yang, J.; Kratochvil, H. T.; Lolicato, M.; Liu, Y.; Shu, X.; Liu, L.; DeGrado, W. F., Designed peptides that assemble into cross-α amyloid-like structures. *Nature Chemical Biology* **2018,** *14* (9), 870-875.
33. Egelman, E. H.; Xu, C.; DiMaio, F.; Magnotti, E.; Modlin, C.; Yu, X.; Wright, E.; Baker, D.; Conticello, V. P., Structural plasticity of helical nanotubes based on coiled-coil assemblies. *Structure* **2015,** *23* (2), 280-9.
34. Klok, H.-A.; Vandermeulen, G. W. M.; Nuhn, H.; Rösler, A.; Hamley, I. W.; Castelletto, V.; Xu, H.; Sheiko, S. S., Peptide mediated formation of hierarchically organized solution and solid state polymer nanostructures. *Faraday Discussions* **2005,** *128* (0), 29-41.

35. Salinas, N.; Tayeb-Fligelman, E.; Sammito, M.; Bloch, D.; Jelinek, R.; Noy, D.; Uson, I.; Landau, M., The Amphibian Antimicrobial Peptide Uperin 3.5 is a Cross-α/Cross-β Chameleon Functional Amyloid. *bioRxiv* **2020**, 2020.05.31.126045.
36. Moser, R., Design, synthesis and structure of an amphipathic peptide with pH-inducible haemolytic activity. *Protein Engineering, Design and Selection* **1992,** *5* (4), 323-331.
37. Elliott, A. G.; Huang, J. X.; Neve, S.; Zuegg, J.; Edwards, I. A.; Cain, A. K.; Boinett, C. J.; Barquist, L.; Lundberg, C. V.; Steen, J.; Butler, M. S.; Mobli, M.; Porter, K. M.; Blaskovich, M. A. T.; Lociuro, S.; Strandh, M.; Cooper, M. A., An amphipathic peptide with antibiotic activity against multidrug-resistant Gram-negative bacteria. *Nat Commun* **2020,** *11* (1), 3184.
38. Tossi, A.; Sandri, L.; Giangaspero, A., Amphipathic, alpha-helical antimicrobial peptides. *Biopolymers* **2000,** *55* (1), 4-30.
39. Kumar, P.; Kizhakkedathu, J. N.; Straus, S. K., Antimicrobial Peptides: Diversity, Mechanism of Action and Strategies to Improve the Activity and Biocompatibility In Vivo. *Biomolecules* **2018,** *8* (1), 4.
40. Epand, R. M.; Walker, C.; Epand, R. F.; Magarvey, N. A., Molecular mechanisms of membrane targeting antibiotics. *Biochim Biophys Acta* **2016,** *1858* (5), 980-7.
41. Engelberg, Y.; Landau, M., The Human LL-37(17-29) antimicrobial peptide reveals a functional supramolecular structure. *Nature Communications* **2020,** *11* (1), 3894.
42. Lombardi, L.; Falanga, A.; Del Genio, V.; Galdiero, S., A New Hope: Self-Assembling Peptides with Antimicrobial Activity. *Pharmaceutics* **2019,** *11* (4), 166.
43. Malekkhaiat Häffner, S.; Malmsten, M., Influence of self-assembly on the performance of antimicrobial peptides. *Curr Opin Colloid In* **2018,** *38*, 56-79.
44. Tarabout, C.; Roux, S.; Gobeaux, F.; Fay, N.; Pouget, E.; Meriadec, C.; Ligeti, M.; Thomas, D.; Ijsselstijn, M.; Besselievre, F.; Buisson, D.-A.; Verbavatz, J.-M.; Petitjean, M.; Valéry, C.; Perrin, L.; Rousseau, B.; Artzner, F.; Paternostre, M.; Cintrat, J.-C., Control of peptide nanotube diameter by chemical modifications of an aromatic residue involved in a single close contact. *Proceedings of the National Academy of Sciences* **2011,** *108* (19), 7679.
45. Shen, H.; Fallas, J. A.; Lynch, E.; Sheffler, W.; Parry, B.; Jannetty, N.; Decarreau, J.; Wagenbach, M.; Vicente, J. J.; Chen, J.; Wang, L.; Dowling, Q.; Oberdorfer, G.; Stewart, L.; Wordeman, L.; De Yoreo, J.; Jacobs-Wagner, C.; Kollman, J.; Baker, D., De novo design of self-assembling helical protein filaments. *Science* **2018,** *362* (6415), 705-709.
46. Ozbas, B.; Kretsinger, J.; Rajagopal, K.; Schneider, J. P.; Pochan, D. J., Salt-Triggered Peptide Folding and Consequent Self-Assembly into Hydrogels with Tunable Modulus. *Macromolecules* **2004,** *37* (19), 7331-7337.
47. Edwards-Gayle, C. J. C.; Castelletto, V.; Hamley, I. W.; Barrett, G.; Greco, F.; Hermida-Merino, D.; Rambo, R. P.; Seitsonen, J.; Ruokolainen, J., Self-Assembly, Antimicrobial Activity, and Membrane Interactions of Arginine-Capped Peptide Bola-Amphiphiles. *ACS Applied Bio Materials* **2019,** *2* (5), 2208-2218.
48. Simonson, A. W.; Aronson, M. R.; Medina, S. H., Supramolecular Peptide Assemblies as Antimicrobial Scaffolds. *Molecules* **2020,** *25* (12), 2751.

Chapter 3: PSMβ2 Self-assembles into cross-α Nanotubes

3.1 Introduction

Following the success of characterizing PSMα3 cross-α amyloid like fibril associated nanotube, PSMβ peptides were investigated using a similar approach. There are 2 peptides in the PSMβ family: PSMβ1 and PSMβ2. Both peptides are 44 amino acids long, negatively charged, generally conserved between species[1], and share a similar amino acid sequence (Figure 3.1). In terms of biological functions, PSMβs have roles in structuring bacteria biofilms[2]; PSMβs show less cytolytic activities in comparison to other PSM peptides, and the production level of PSMβs are believed to be an indicator of the producing bacteria's degree of (low) virulence[2-3]. While PSMβs do not have the cytolytic activity to help the bacteria killing other competitive cells, the non-aggressive nature of these peptides may aid bacteria growth avoiding harming the host cell[4].

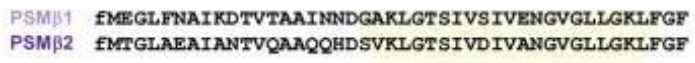

Figure 3.1. PSMβ sequences.

PSMβs are first shown to self-assemble into fibrils in a mixture of all 7 PSM peptides, and these fibrils bind to ThT and CR[5]; a subsequent study found while both PSMβ peptides show ThT bindings (Figure 3.2A), fibrils are extremely hard, albeit possible to detect via TEM (Figure 3.2B)[6].

A B

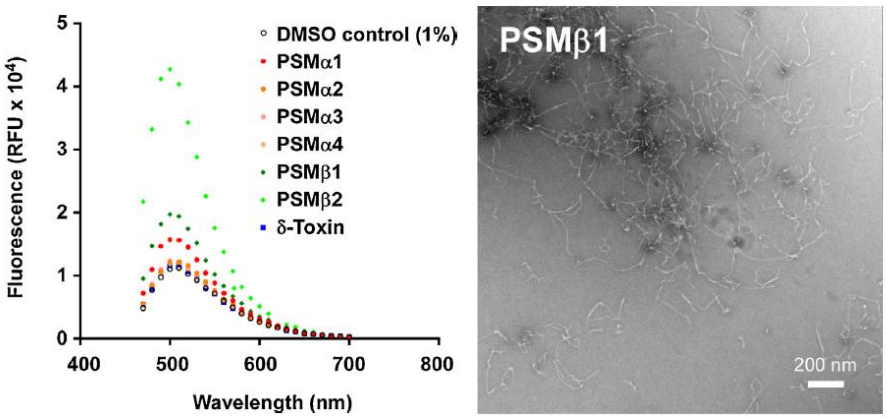

Figure 3.2. A) Synthetic PSMs were analyzed for the propensity to form amyloids using a ThT assay. PSMs were measured singly at 0.1 mg/ml upon incubation for 48 h. B) Transmission electron microscopy (TEM) of synthetic PSMβ1 at 0.1 mg/ml incubated for 48 h in water. Figures adapted from ref. 2.

The in-solution structure of PSMβ2 was characterized vas NMR[7]. In contrast to the shorter PSMα1 or PSMα3 being single α-helices in solution, PSMβ2 displays a helix-turn-helix-helix folding structure that exposes a mostly hydrophilic surface, hiding the hydrophobic core from the aqueous environment (Figure 3.3A); all of the individual helices all show amphipathic patterns (Figure 3.3B, C).

A

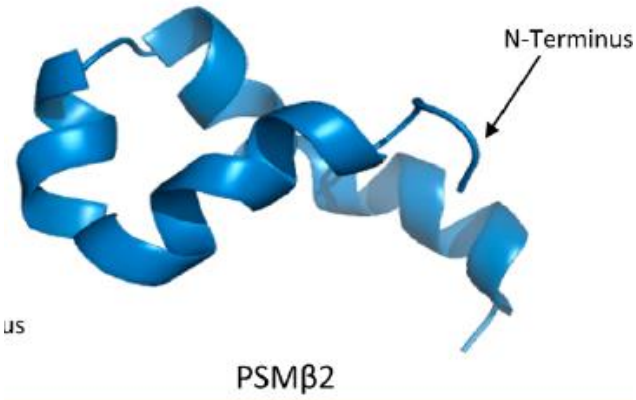

B C D

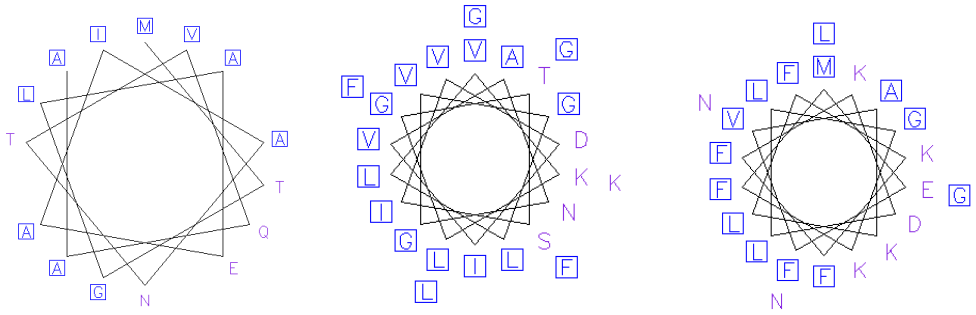

Figure 3.3. A) NMR solution structure of PSMβ2. B) helical wheels of PSMβ2, amino acids 1-15. C) helical wheels of PSMβ2, amino acids 20-44. D) helical wheels of PSMα3.

While PSMβs didn't gather as much research interest as PSMαs due to it being barely cytotoxic and thus not a virulence factor to *S. aureus*, both PSMβ peptides have evidence forming extracellular fibrils. PSMβ2 shows similar amphipathic helix features to PSMα3, which forms cross-α amyloid like fibrils and fibril-associated nanotubes, yielding the possibility PSMβs may form a similar fibril and even nanotube structure. This chapter's research goal is to screen, identify and characterize the self-assembly of PSMβs, and to compare these assemblies with PSMα3's to draw their structure-function relationships, in hope to determine the structural differences that may lead to these peptides' differences in cytotoxicity.

3.2 Results and discussion

3.2.1 Self-assembly of PSMβ1

N-terminal acetylated, C-terminal amidated PSMβ1 peptide was purchased from Synpeptide, Inc. PSMβ1 was first screened at PSMα3's self-assembly conditions: 427 μM peptide concentration, 10 mM pH 5.0 acetate, pH 6.0 MES, pH 7.0 MOPS and pH 8.0 TAPS buffers, to

assess its self-assembly ability under various pH conditions. PSMβ1 at this peptide concentration is not fully soluble, as all samples have solid deposits at the bottom after the insoluble peptide suspended in solution settled. PSMβ1's self-assembly is first screened with negatively-stained TEM. PSMβ1 assembled into twisting fibrils after 24 h of incubation (Figure 3.4). CD revealed all of the PSMβ1 samples display a β-sheet signature with a minimum at 222 nm after 24 h of incubation (Figure 3.5).

A B

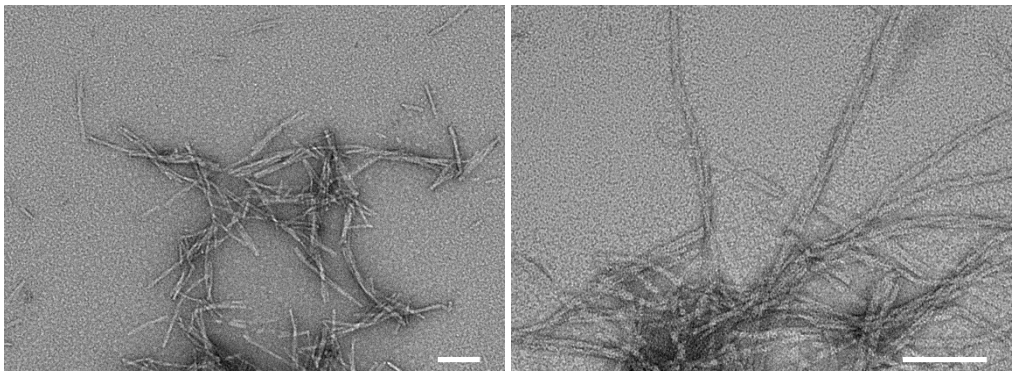

Figure 3.4. Representative TEM images of 427 μM PSMβ1, after 1 day of assembly time, in A) 10 mM pH 7 MOPS buffer; B) 10 mM pH 8 TAPS buffer. All scale bars = 500 nm.

A B

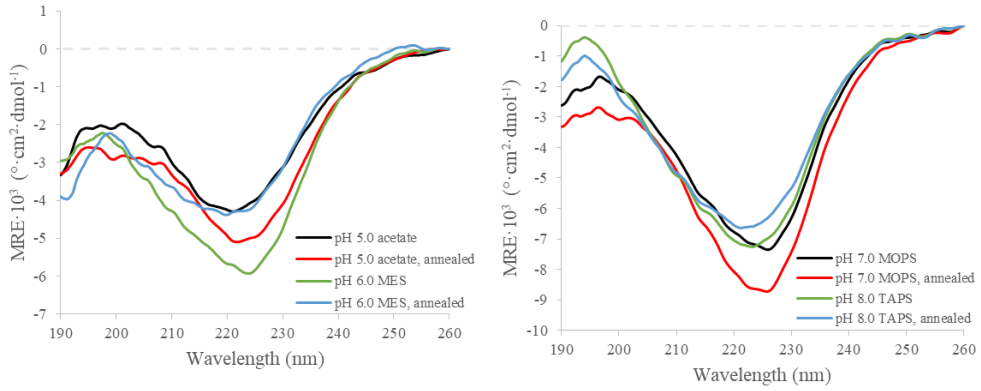

Figure 3.5. Circular dichroism spectra of 427 μM PSMβ1 in A) 10mM pH 5.0 acetate, room temp and annealed; pH 6 MES, room temp and annealed; B) pH 7.0 MOPS, room temp and annealed; and pH 8.0 TAPS buffer, room temp and annealed, all measured after 1 day of assembly.

PSMβ1 was further screened at 321 μM peptide concentration and the same above buffer conditions, with 50% v/v TFE added then allowed to evaporate, to solubilize PSMβ1 and induce α-helix formation. After TFE was evaporated and 24 h of incubation, all PSMβ1 samples still have a similar amount of precipitated peptide deposit at the bottom compared to the samples with no TFE added. CD revealed the TFE samples still adopt a β-sheet signature with a minimum at 222 nm (Figure 3.6). PSMβ1 was not characterized further as no α-helical assemblies were observed.

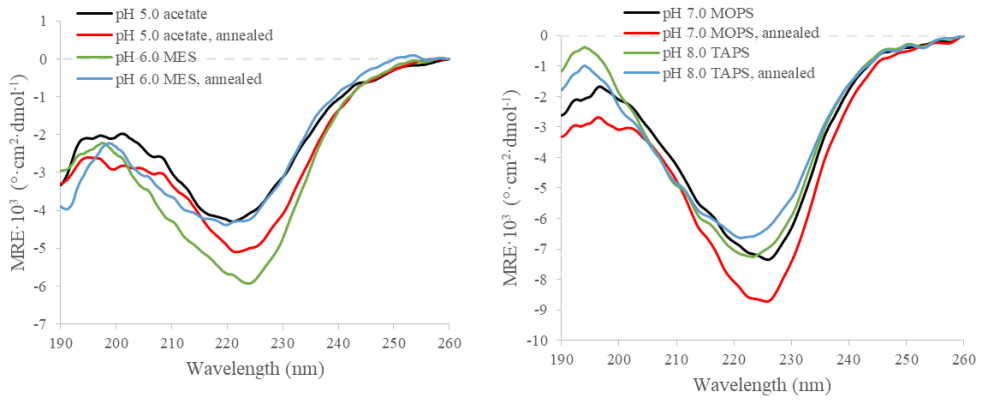

Figure 3.6. Circular dichroism spectra of 341 μM PSMβ1 in A) 10mM pH 5.0 acetate, room temp and annealed; pH 6 MES, room temp and annealed; B) pH 7.0 MOPS, room temp and annealed; and pH 8.0 TAPS buffer, room temp and

annealed, all with equal volumes of TFE added to the respective aqueous buffer then TFE was allowed to evaporate, spectra measured after 1 day of assembly.

3.2.2 Self-assembly of PSMβ2

N-acetylated, C-amidated PSMβ2 peptide was purchased from Synpeptide, Inc. PSMβ2 was first screened at PSMα3's self-assembly conditions: 556 μM peptide concentration, 10 mM pH 5.0 acetate, pH 6.0 MES, pH 7.0 MOPS and pH 8.0 TAPS buffers, to assess its self-assembly ability under various pH conditions. A higher peptide concentration was also screened, but PSMβ2 began to precipitate at > 556 μM peptide concentration. PSMβ1's self-assembly is first screened with negatively-stained TEM. PSMβ2 assembled into a variety of morphologies after 24 h of incubation, where the assemblies are directed by pH: at pH 5.0, twisting fibers with an average width of 5.51 nm (± 1.04 nm), tapes and ribbons were commonly found (Figure.3.7A); at pH 6.0, some order of periodicity and helicity in the twisting ribbon morphology can be observed (Figure.3.7B); at pH 7.0, nanotubes with a diameter of 42.00 nm (± 4.49 nm) were found, in addition to the twisting tapes and ribbons seen in lower pH conditions (Figure.3.7C, E); at pH 8.0, more nanotubes with an average diameter of 46.54 nm (± 4.04 nm) were found compared to the pH 7.0 condition's (Figure.3.7D). A longer incubation time up to one month did not have an apparent effect on the morphology types and their respective population, but tube elongation up to several microns was observed.

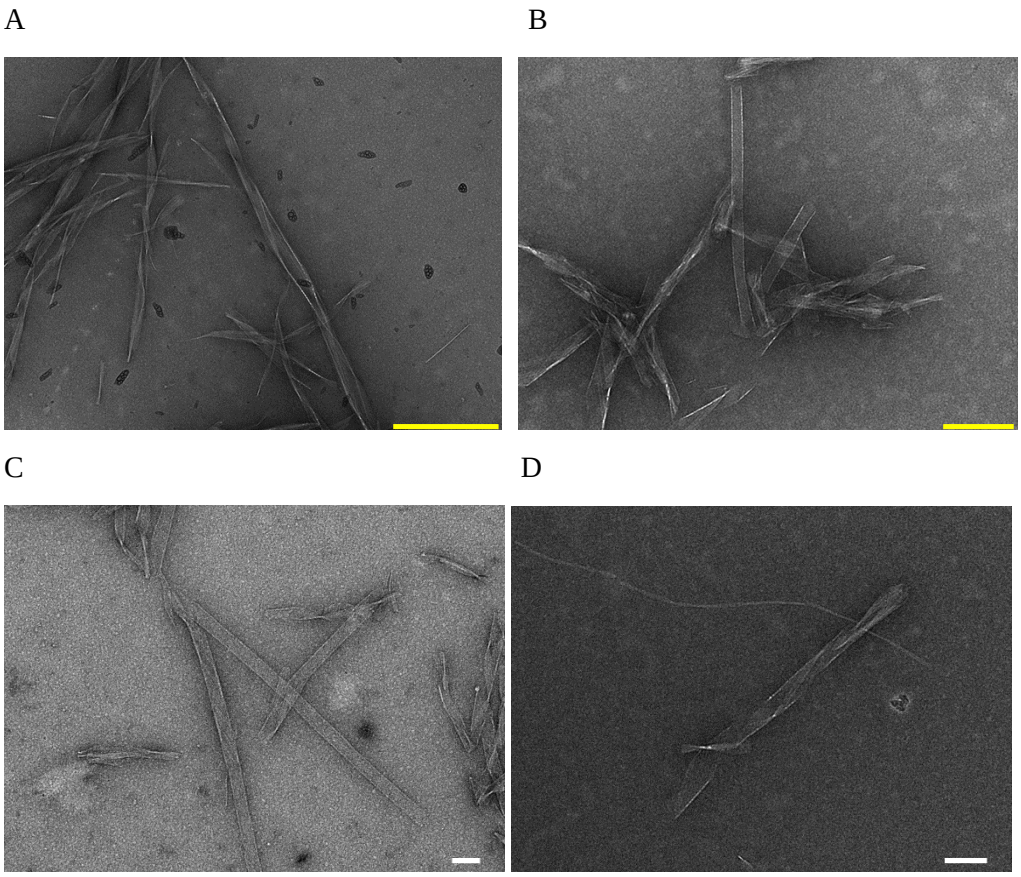

Figure.3.7. Representative TEM images of 556 μM PSMβ2, after 1 day of assembly time, in A) 10 mM pH 5 acetate buffer, scale bar = 500 nm; B) 10 mM pH 7 MOPS buffer, scale bar = 200 nm; C) 10 mM pH 8 TAPS buffer, scale bar = 100 nm; D) 10 mM pH 7 MOPS buffer, scale bar = 100 nm.

These morphologies could be interconnected that singular fibrils laterally associate into tapes, and tapes with a varied degree of twists grow into a certain size and wraps into nanotubes. This hypothesis is supported as distinct lateral association patterns can be distinguished from the tape morphology, such as 4 fibrils can be seen in the left twisting tape in Figure.3.7B; some twisting tapes looks like unraveled nanotubes, such as in Figure.3.7D; a pattern can sometimes be observed on nanotubes as well, such as in Figure.3.7C. Dividing the width of the twisting tapes by the visible number of the fibrils, as well as doing a fast Fourier transform on the fibril patterns yield an average fibril spacing of 7.4 nm, suggesting these morphologies may arise from the same kind of lateral association of the same fibrils.

Circular dichroism spectroscopy was employed to characterize the secondary structures of PSMβ2 in the buffer conditions screened, and identify any differences in secondary structuresg between the nanotube and the twisting fibril assemblies. In the all of the screened conditions, PSMβ2 showed an α-helical signature where the measured mean residue ellipticity (MRE) has a maximum at 195 nm and minima at 209 nm and 224 nm (Figure 3.8). These minima wavelengths are consistent with the published PSMβ2 CD data acquired in 50% d_3-trifluoroethanol at 40 ℃[7]. The lack of differences in CD maximum and minima in all screened PSMβ2 conditions despite different morphologies further suggests the observed different morphologies could arise from the same PSMβ2 α-helical monomer structure.

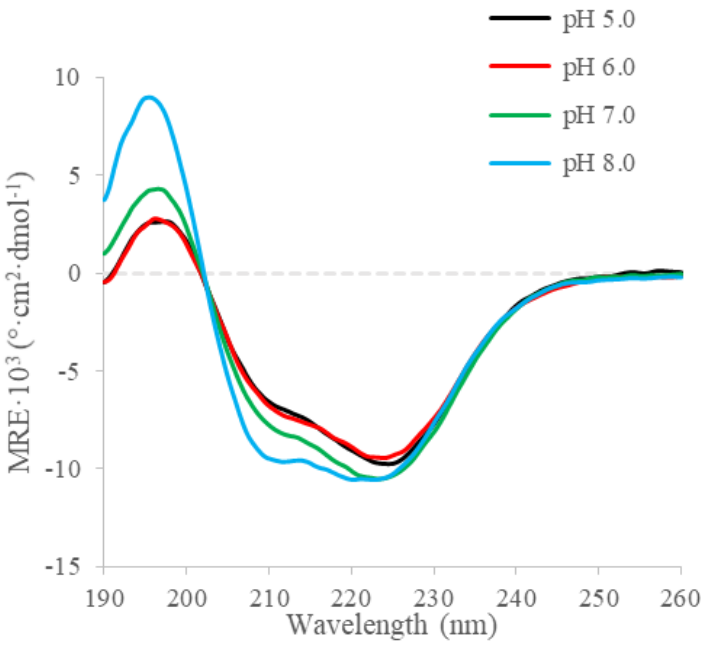

Figure 3.8. Circular dichroism spectra of 566 μM PSMβ2 in 10mM pH 5.0 acetate, pH 6.0 MES, pH 7.0 MOPS, and pH 8.0 TAPS buffer, measured after 1 day of assembly.

PSMβ2 was further screened at 556 μM peptide concentration and buffer conditions, with 50% v/v trifluoroethanol (TFE) added then evaporated, since PSMβ2's in-solution structure was solved in 50% v/v d-TFE in water. After 24 h and 1 week of incubation, only amorphous aggregates

were observed in all screened conditions (Figure 3.9). This is expected as the PSMβ2 monomer structure solved in 50% v/v TFE is in a 3-helix folded state exposing a mostly hydrophilic surface, thus would inhibit the hydrophobic interactions to drive monomer oligomerization and self-assembly.

A B

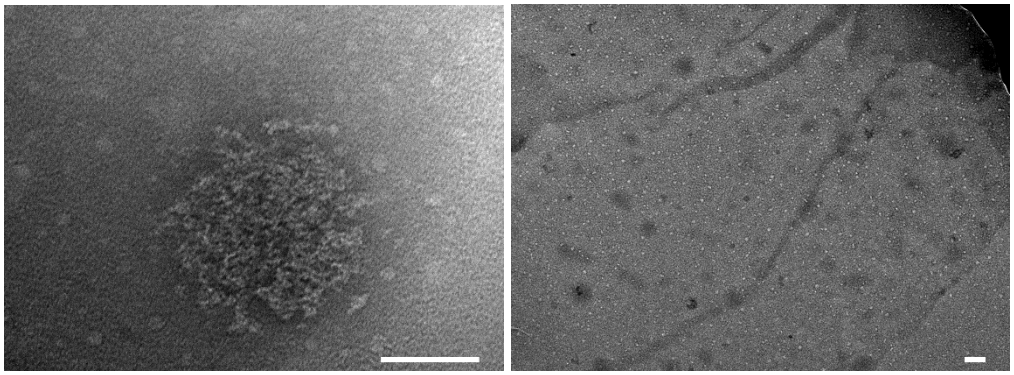

Figure 3.9. Representative TEM images of 556 μM PSMβ2, in A) 10 mM pH 7 MOPS buffer after 1 day of assembly time; B) 10 mM pH 8 TAPS buffer after 1 week of assembly time, scale bar = 100 nm.

In summary, PSMβ2 was shown to be able to self-assemble into nanotubes perhaps similar to PSMα3, but also shows a mixture of other morphologies that could be precursors leading to nanotubes. The next few chapters will focus on optimizing and characterizing the nanotube assembly with an hope to understand whether PSMβ2 also adopts a cross-α structure, the similarities of PSMβ2's and PSMα3's cross-α structures, and the reason PSMβ2 is less selective than PSMα3.

3.2.3 Structural Characterization of the PSMβ2 Nanotubes

3.2.3.1 Thermal stability of PSMβ2 morphologies

To determine the thermal stability of PSMβ2's multiple morphologies, CD melt experiment was performed on a 556 μM PSMβ2 in 10 mM pH 7.0 MOPS sample, monitoring the MRE at the global max absorption 209 nm, with a melting profile increasing from 5 ℃ to 95 ℃ in 60 minutes. While no distinct melting transition was observed (Figure 3.10A), the sharpest transition of MRE at 209 nm is at 76.4 ℃ (Figure 3.10B). The low MRE intensity at 95 ℃ in comparison to the MRE at room temperature (Figure 3.10D) could be due to a significant loss of solution while the sample was heated to 95 ℃. The sample still shows showed an α-helical signature with minima at 208 nm and 221 nm at 95 ℃, but the 221 nm minima is too noisy to draw any conclusions; the ratio of the molar ellipticity at 208 nm to 222 nm is however > 1, where this ratio was < 1 before the sample was heated (Figure 3.10C). This ratio difference indicates there is a change in the assembly type of PSMβ2 in pH 7 when heated up to 95 ℃; the 76.4 ℃ temperature at the sharpest transition of MRE is likely a critical melting temperature triggering this change.

A B

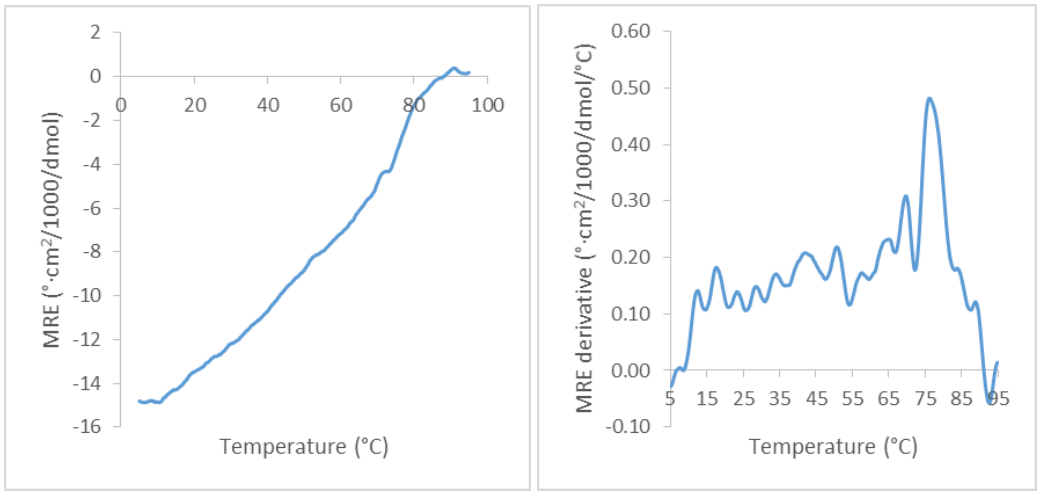

C D

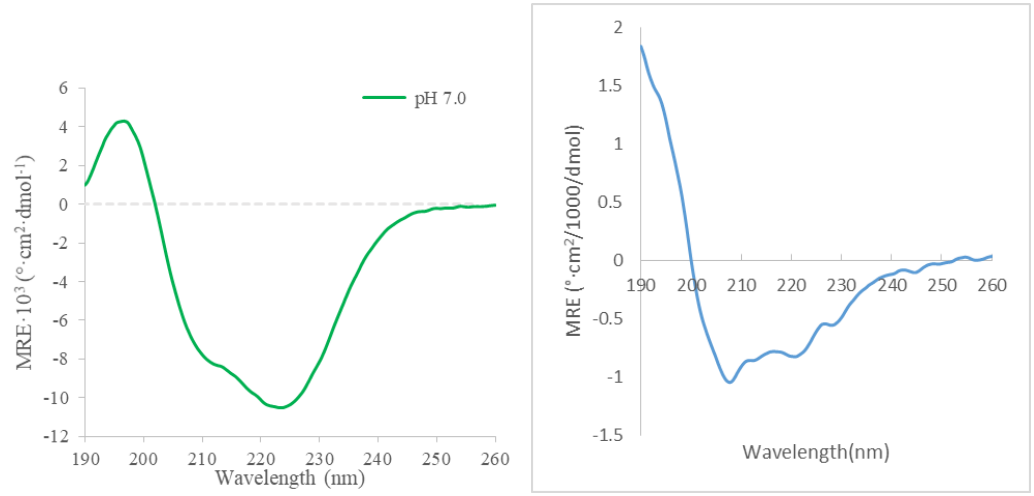

Figure 3.10: A) CD melting spectrum of 556 µM PSMβ2, in 10 mM pH 7 MOPS buffer; B) first derivative of A), indicates a possible melting transition at 76.4 ℃. C) CD spectrum of 556 µM PSMβ2 in 10mM pH 7 MOPS at room temperature. C) CD spectrum of 556 µM PSMβ2 in 10mM pH 7 MOPS, heated and held at 95 ℃.

To determine whether 76.4 ℃ triggers a melting transition of PSMβ2, PSMβ2 was assembled at 556 µM peptide concentration in 1X pH 7.4 PBS buffer, annealed at 37, 50, and 90 ℃ for 30 min respectively, then slowly cooled to room temperature by a 1 ℃ / 5 minutes temperature gradient. After 24 h of incubation, at 37 and 50 ℃, 40.94 nm (± 6.33 nm) and 38.08 nm (± 2.67

nm) wide nanotubes were still found (Figure 3.11A, B); at 90 ℃, only fibrils with an average width of 7.62 nm (± 1.05 nm) were found with no tube assemblies (Figure 3.11C). These fibrils do not associate to form a tape/ribbon like assembly, thus are likely a different type of fibrils than the thinner, laterally associating ones observed in the PSMβ2 samples at room temperature, suggesting that heating to 76.4 ℃ induced a morphology change in PSMβ2 samples.

A B

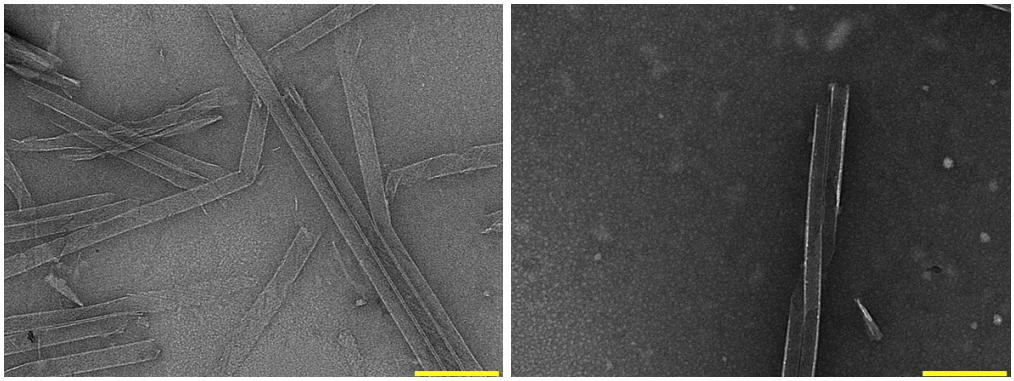

C

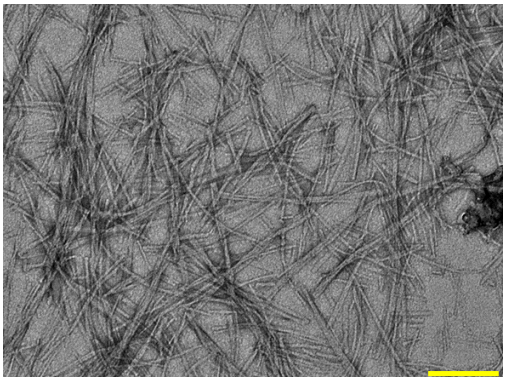

Figure 3.11: Representative TEM images of 556 μM PSMβ2 in 1X pH 7.4 PBS buffer, 1 day of assembly time, A) annealed at 37 ℃ for 30 minutes then cooled to room temperature; B) annealed at 50 ℃ for 30 minutes then cooled to room temperature; C) annealed at 90 ℃ for 30 minutes then cooled to room temperature. All scale bars = 200nm.

3.2.3.2 Salt stability of PSMβ2 morphologies

The stability of PSMβ2 nanotubes with a salt presence was analyzed by characterizing 556 μM PSMβ2 in 10 mM pH 10 CAPS with 50 mM, 500 mM and 1 M NaCl respectively. If the lateral association of fibrils are promoted through hydrophilic interactions of the residues' side chains, the degree of association could then be affected by the presence of salt. After 24 h of incubation, PSMβ2 in all conditions still assembled into nanotubes, although in lower populations (Figure 3.12B); these nanotubes are a bit fuzzier, and a larger 8.49 nm/cycle fibril spacing were observed in comparison to the previously observed 7.63 nm/cycle spacing (Figure 3.12A, C). This suggests salt presence does impact the lateral association of PSMβ2 fibrils, and subsequently impact the correct folding of the associated tapes into nanotubes.

A B

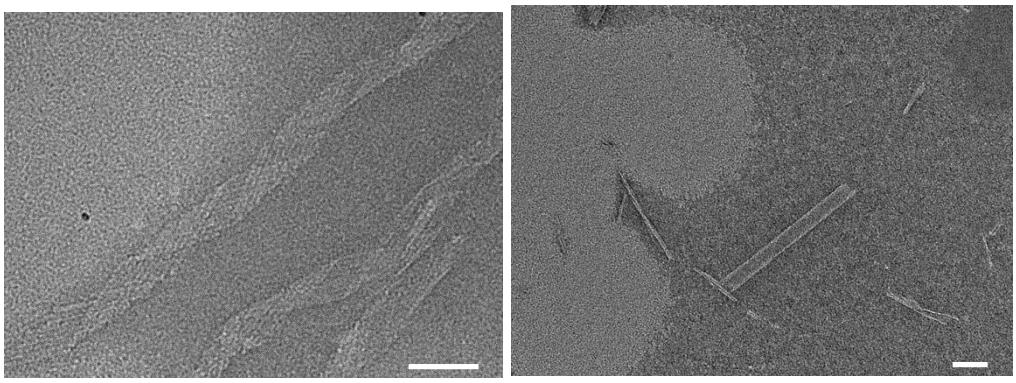

C

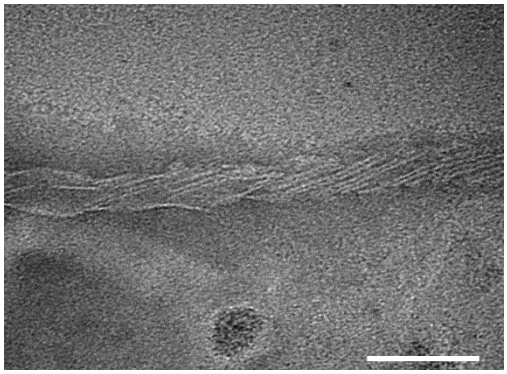

Figure 3.12. Representative TEM images of 556 μM PSMβ2 in 10 mM pH 10 CAPS buffer, after 1 day of assembly time, A) with 50 mM NaCl; B) with 500 mM NaCl; C) with 1 M NaCl. All scale bars = 100 nm.

3.2.3.3 Cryo-EM determined PSMβ2 nanotube structure

Fortunately PSMβ2 nanotubes have a decent population among other morphologies in conditions with pH 8 and above, and thus were further characterized by cryo-EM with a final resolution of 4.2 Å. Each PSMβ2 monomer displays a helix-turn-helix structure. A single PSMβ2 monomer is folded that one helix stacks with the other helix, exposing a hydrophobic surface to allow mating. Each PSMβ2 asymmetric unit displays a cross-α fibril structure, where 2 PSMβ2 monomers laterally associate through termini interactions to afford a fibril width of 67 Å, mate with another pair of monomers with a mating distance of ~10 Å, and stack accounting for elongation with stacking distances of 9-10 Å (Figure 3.13), which are similar to PSMα3's cross-α parameters. Each PSMβ2 fibril mates with another fibril through hydrophobic interactions between Met1 at the N-terminus, Phe42 and Gly43 at the C-terminus (Figure 3.14A). Instead of mating at a parallel orientation like PSMα3, PSMβ2 helices mate at 45° angle, perhaps due to the way His18 at the turn motif is organized to optimize the π-π interactions from the imidazole moiety of His (Figure 3.14B), as well as the lack of Phe-Leu mating interactions in PSMβ2 that were abundant in PSMα3 (Figure 3.14C).

A B

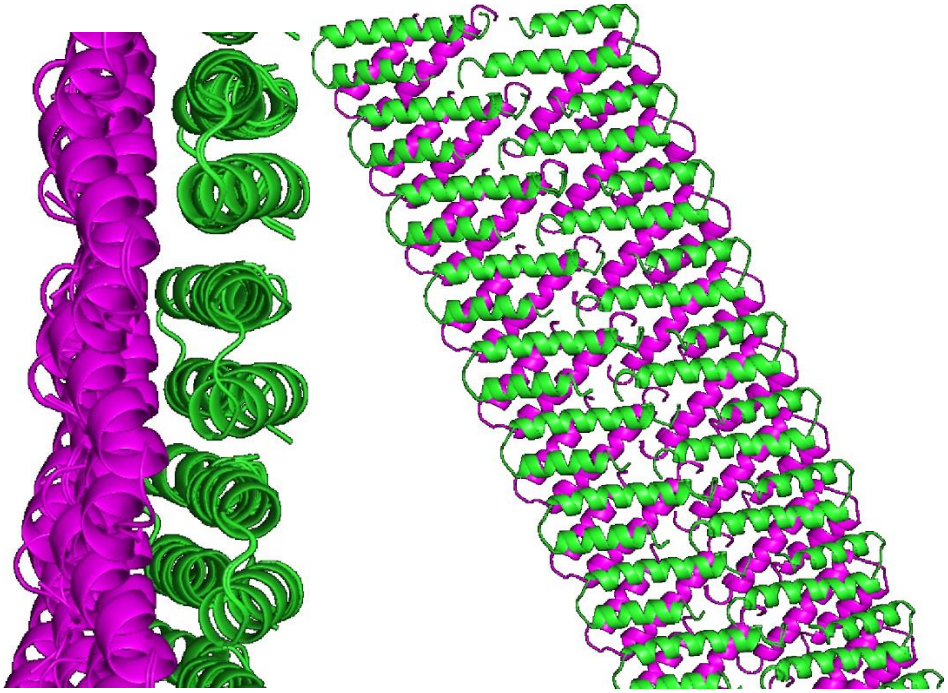

Figure 3.13. A) side view and B) front view of PSMβ2 cross-α fibril structure. Model rendered in PyMol.

A B

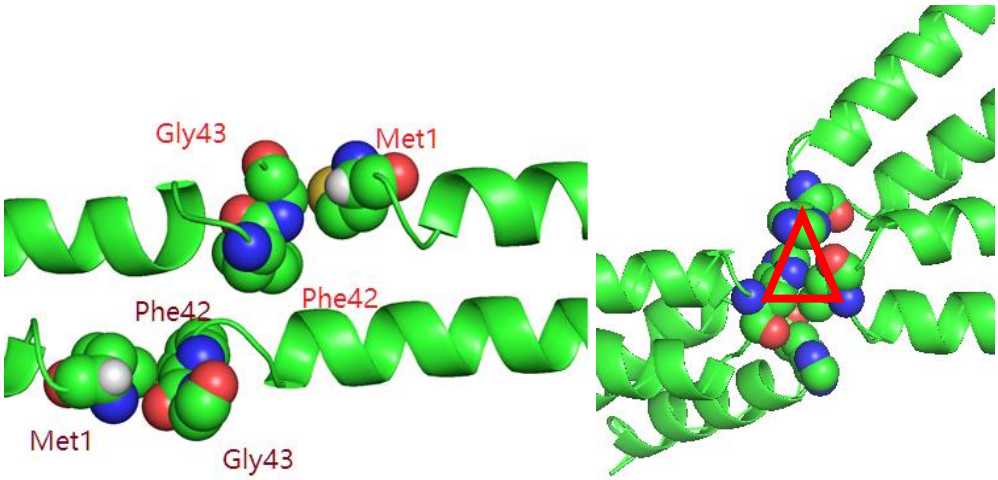

C

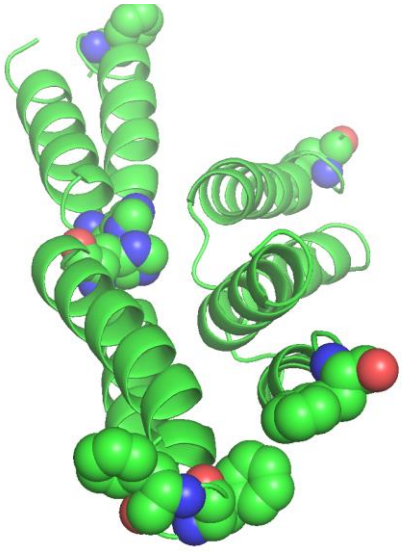

Figure 3.14. A) PSMβ2 monomer lateral association through termini Met1, Phe42 and Gly43 (shown in spheres, labelled); B) PSMβ2 fibril lateral association and mating through His18, shown in spheres, interactions highlighted by red lines; C) PSMβ2 monomer mating with F42 and F44 shown in spheres. Model rendered in PyMol.

PSMβ2 nanotube is left-handed, consists of 12 PSMβ2 cross-α fibrils laterally associating with each other, where each fibril has a 28.6 °twist to complete a full turn, resulting in a diameter of 297 Å with a double-layered wall thickness of 20 Å (Figure 3.15). Each turn affords a 16.4 A

rise. PSMβ2 fibrils laterally associate through the π-π interactions from the imidazole moiety of His18 (Figure 3.16). This lateral association affords a large 9 Å spacing and causes such spacing to be observable via TEM and STEM.

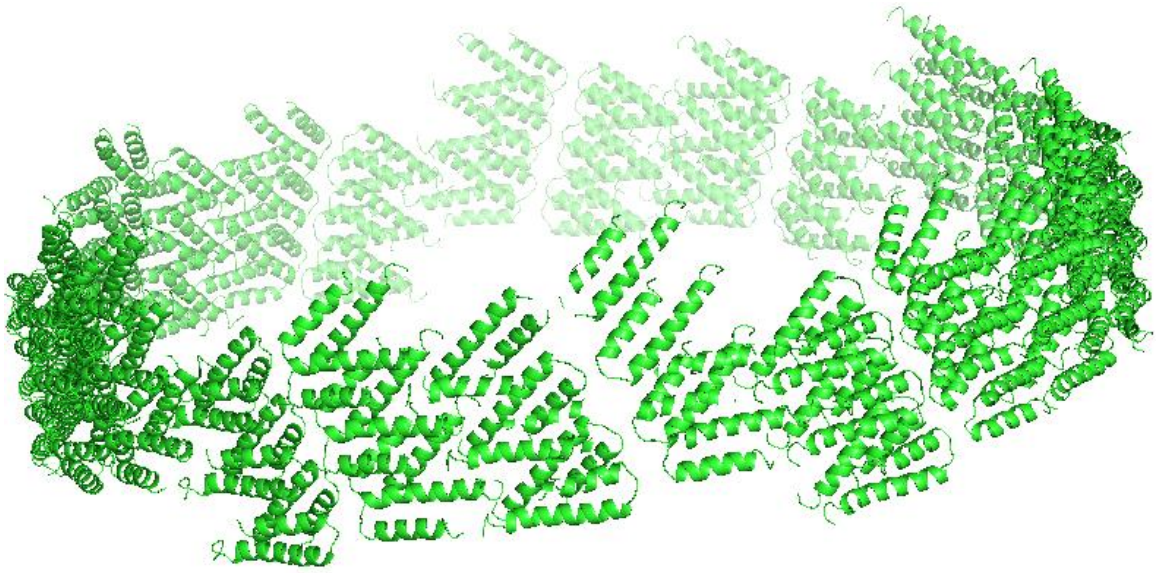

Figure 3.15. Front view of PSMβ2 cross-α nanotube structure. Model rendered in PyMol.

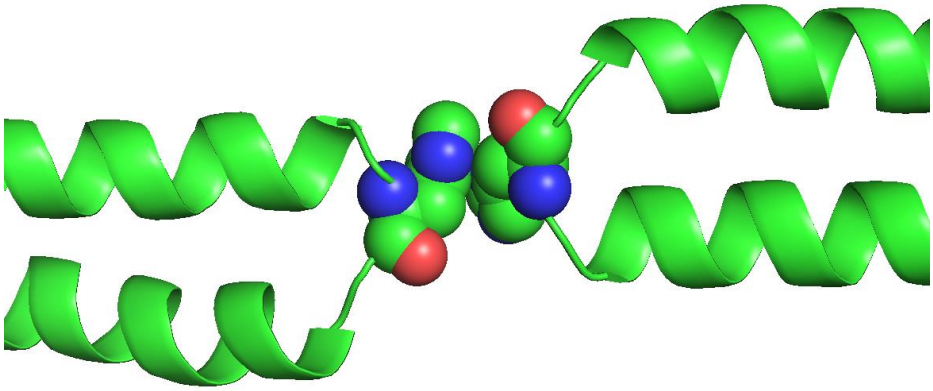

Figure 3.16. PSMβ2 fibril lateral association interactions through His18 (shown in spheres). Model rendered in PyMol.

3.2.3.4 TEM and STEM validated PSMβ2 nanotube's cryo-EM model

To validate the cryo-EM determined PSMβ2 nanotube structure, PSMβ2 nanotubes were further characterized via TEM and STEM and compared to the cryo-EM model. PSMβ2 nanotube's width measured from the negative-stain TEM images follows a normal distribution at an average of 45.14 nm (Figure 3.17). when assuming PSMβ2 nanotubes are fully flattened on TEM grids, the measured tube width via TEM would correspond to half of PSMβ2 nanotube's actual circumference, where the actual circumference is observed width / π, or 47.75nm / π = 30.4 nm; this calculated nanotube diameter corresponds well with the cyro-EM model's tube diameter of 29.7 nm.

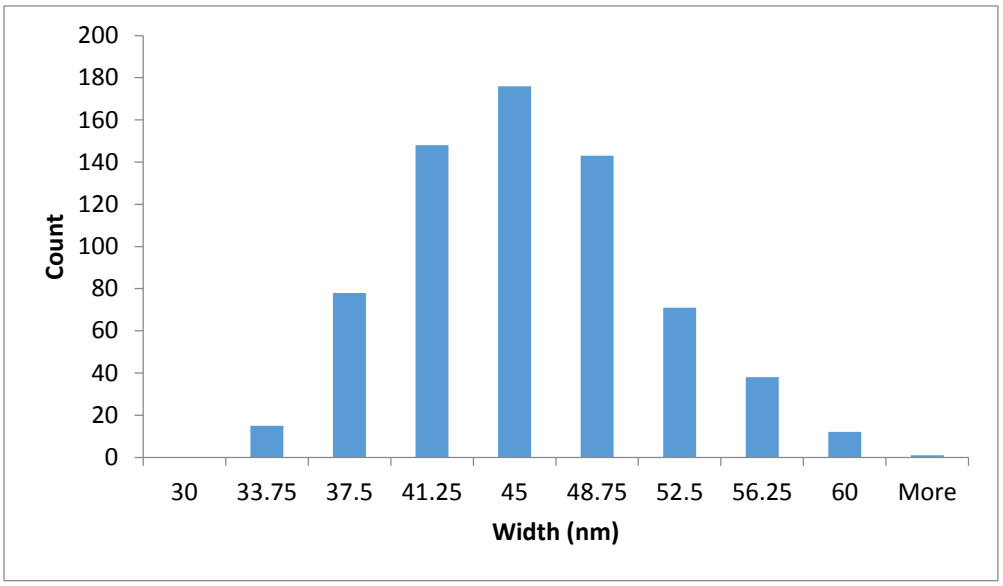

Figure 3.17: Histogram of width measurements of PSMB2 tubes, measurements taken from negative-stain TEM micrographs.

A cross fibril pattern can sometimes be observed on a tube (Figure 3.18A), and can be fast Fourier transformed to yield a 7.62 nm/cycle spacing (Figure 3.18B), which is consistent with the sum of 67 Å PSMβ2 cross-α fibril width and 9 Å PSMβ2 cross-α fibril spacing between each other. The angle of each cross line with respect to the tube wall is measured to be 21 ° (Figure 3.18A), which is consistent with the 22 °angle of PSMβ2 cross-α fibril with respect to the nanotube axis.

A B

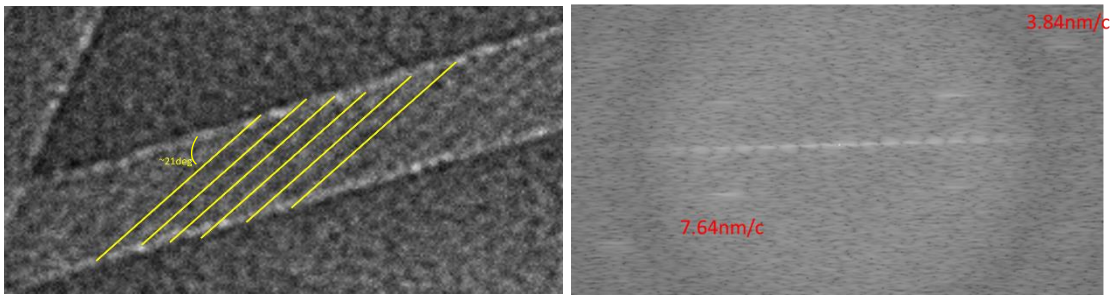

Figure 3.18: A) a TEM image of the PSMβ2 nanotube's cross patterns, helical angle is measured to be 21° with respect to the nanotube's direction. B) an FFT image of A), where the cross pattern spacing is measured to be 7.64 nm/cycle.

Using the flattened nanotube width of 47.75 nm and this 21 ° angle, a rectangular section of a full turn of the flattened PSMβ2 nanotube can be defined as a 47.75 nm * 130 nm rectangle (Figure 3.19). The length of the perpendicular line from the top left corner of this rectangle, to the diagonal line from the top right corner to the bottom left corner of this rectangle can then be calculated to be 46.6 nm; this roughly corresponds to 6 times the 7.62 nm/cycle spacing calculated from Figure 3.18B, suggesting 6 fibrils spanning a half turn of PSMβ2 tube wall, or 12 fibrils spanning a full turn of the PSMβ2 tube, which also consistent with the cryo-EM model's 12 fibrils accounting for a full turn. Overall, TEM analysis of PSMβ2 nanotubes agrees very well with PSMβ2 nanotube's cryo-EM model.

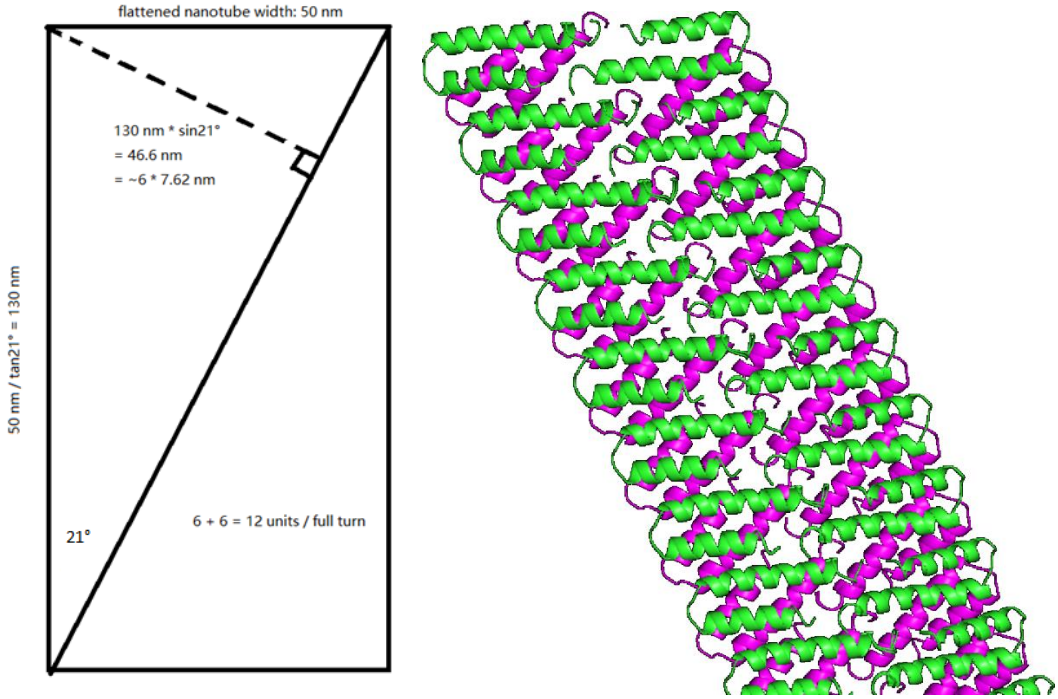

Figure 3.19: A) The calculated geometry model of the PSMβ2 nanotubes based on the cross-fibril patterns in Figure 3.18A. B) single PSMβ2 fibril from the PSMβ2 tube's cryo model.

PSMβ2 nanotube's mass per length (M/L) measured via STEM (Figuwre 3.20A) follows a normal distribution at an average of 11.1 kda/Å (Figuwre 3.20B), using tobacco mosaic virus as the standard, which corresponds well with PSMβ2 nanotube cryo-EM model's expected monomers per nanotube length: the model indicates 16.4 Å rise per 48 PSMβ2 monomer, together with PSMβ2's 4.49 kDa molecular weight, PSMβ2 nanotube would have an expected M/L value of 4.49 kDa * 48 / 16.4 Å = 13.1 kDa / Å. Cross patterns similar to the ones observed via TEM can also be observed from bright-field STEM images (Figuwre 3.20C). STEM analysis of PSMβ2 nanotubes also agrees very well with PSMβ2 nanotube's cryo-EM model.

A

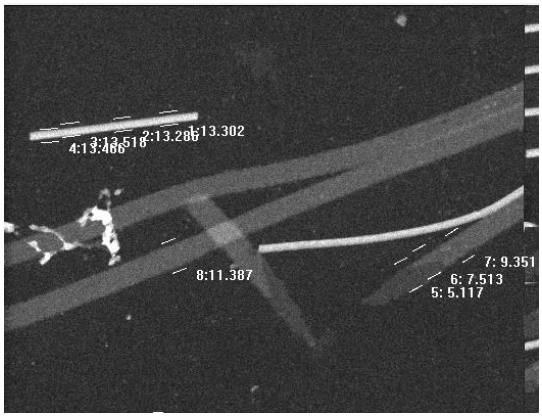

B

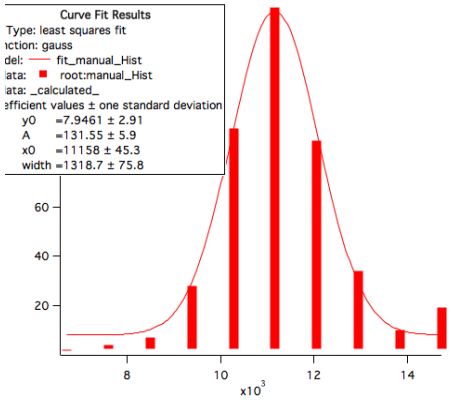

C

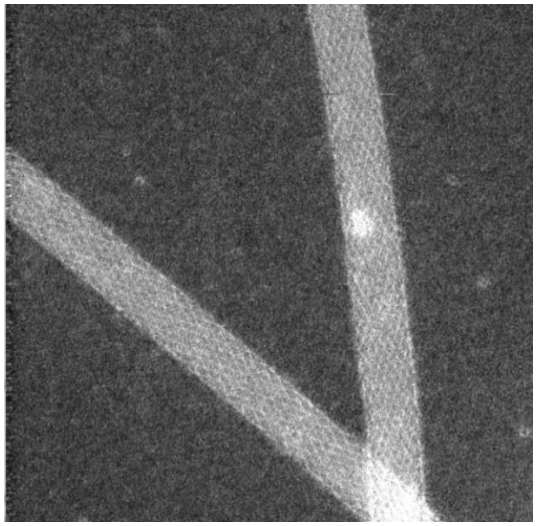

Figuwre 3.20: (A) A representative dark-field STEM image of 556 μM PSMβ2 in 10 mM pH 7 MOPS buffer, with M/L measurements on PSMβ2 (grey) and TMV (white) specimens; (B) histogram of M/L measurements of PSMβ2, averaged at 11.18 kDa/Å. (C) A dark-field STEM image of 556 μM PSMβ2 in 10 mM pH 7 MOPS buffer showing the visible cross patterns on the nanotube.

In summary, STEM and TEM measurements of PSMβ2 nanotubes match well with the expected parameters calculated from PSMβ2 nanotube's 4.2 Å resolution cryo-EM model, both validating the model and the trustworthiness of STEM and TEM measurements reflecting the

actual structure, enabling these techniques to be used to characterize other PSMβ2 morphologies presented in the next chapter.

3.2.4 Structural characterization of other PSMβ2 morphologies

3.2.4.1 pH dependency of PSMβ2 morphologies

Because a larger PSMβ2 tube population was observed in pH 8 compared to pH 7, suggesting a pH selective effect on the tube morphology, PSMβ2 was further screened at 556 μM peptide concentration, in 1X pH 7.4 PBS, 10 mM pH 9.0 CHES, and 10 mM pH 10.0 CAPS buffer conditions at room temperature to determine whether higher pH conditions would be selective towards PSMβ2 morphologies. In 1X pH 7.4 PBS, no apparent differences in morphology type or population were observed compared to in pH 7.0 (Figure 3.21A). In pH 9.0, tubes with an average diameter of 48.11 nm (± 4.00 nm) were found after 24 h of incubation (Figure 3.21B), along with a mixture of fibrils and twisting tapes; the tube population is similar to pH 8.0's. At pH 10.0, no apparent differences in the morphology types and population was observed compared to at pH 9.0, with the exception of very rare helical tapes (Figure 3.21C). For a very limited sample size of 3 observed helical tapes, each tape has a consistent pitch and width within itself, but has a different pitch and width than each other. These results suggest while the PSMβ2 tubes require pH > 7 to assemble, a more basic condition up to pH 10.0 only have a minor selection effect, if not none toward the tube morphology; higher pH conditions do not inhibit other morphologies; helical tapes were very rarely observed at the pH 10 condition, and they do seem to be unwrapped nanotubes.

A B

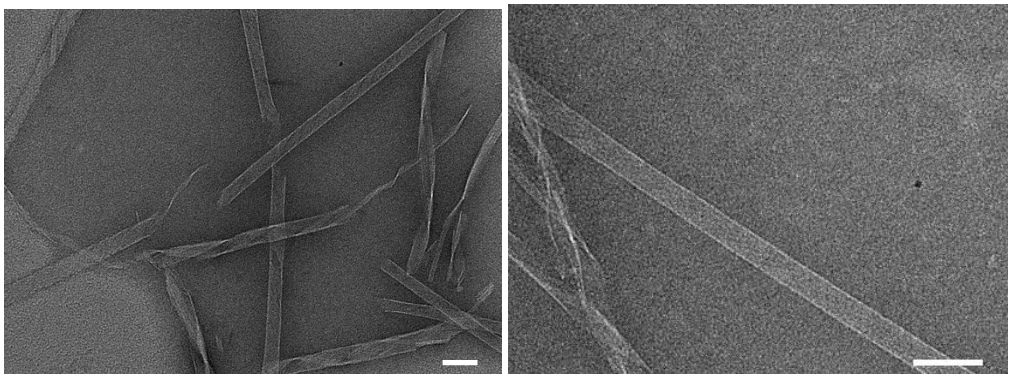

C

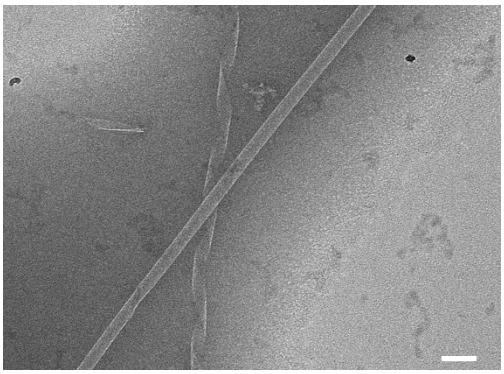

Figure 3.21 Representative TEM images of 556 μM PSMβ2, after 1 day of assembly time, in A) 1X PBS buffer; B) 10 mM pH 9 CHES buffer; C) 10 mM pH 10 CAPS buffer. Scale bar = 100 nm.

3.2.4.2 AFM and TEM characterization of PSMβ2 helical ribbons

Only less than 10 helical ribbons were analyzed via TEM and AFM due to their rare occurrences. Via TEM, the observed ribbons have the same 45 nm ribbon width, the same 160 ° twist angle with respect to the fibril axis, but different pitches (Figure 3.22A: 313 nm, B: 274 nm). The 45 nm ribbon width would correspond to roughly 6 PSMβ2 cross-α fibrils laterally associating, half of 12 PSMβ2 cross-α fibrils accounting for a full nanotube turn. Interestingly, in an instance where a nanotube is observed to be partially unwrapped (Figure 3.22C), the unwrapped portion also has a tape width of 45 nm and a twist angle of ~160 °, suggesting PSMβ2 nanotube and PSMβ2 helical ribbon are linked where one associates/dissociates into the other.

A B

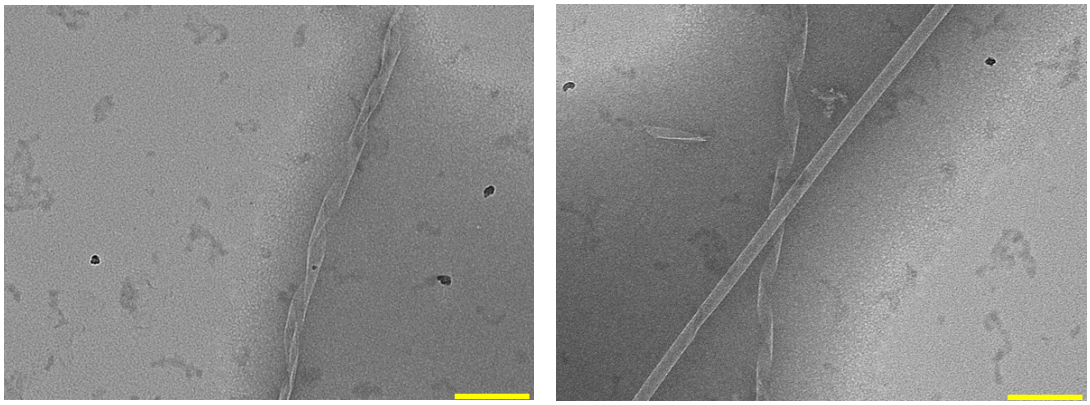

C

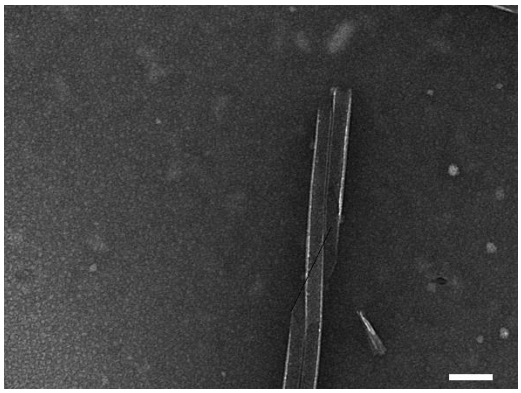

Figure 3.22. Representative TEM images of 556 µM PSMβ2, after 1 day of assembly time, in 10 mM pH 10 CAPS buffer. A) helical ribbon pitch = 313 nm, twist angle = 160 °, width = 45 nm. Scale bar = 200 nm. B) helical ribbon pitch = 274 nm, twist angle = 160 °, width = 45 nm. Scale bar = 200 nm. C) Partially unwrapped nanotube, the tape unwrapped from a nanotube has a width of ~46 nm. Scale bar = 100 nm.

Via AFM, PSMβ2 helical ribbons display a consistent width and pitch within one ribbon, but have different pitches among each other (

Figure 3.23). The ribbons show an averaged consistent height of 4.92 nm at the folded and overlapped areas and 2.21 nm at the non-overlapped areas, where 4.92 nm corresponds well with the 5.06 nm PSMβ2 nanotube height, further suggesting these two morphologies are linked.

A

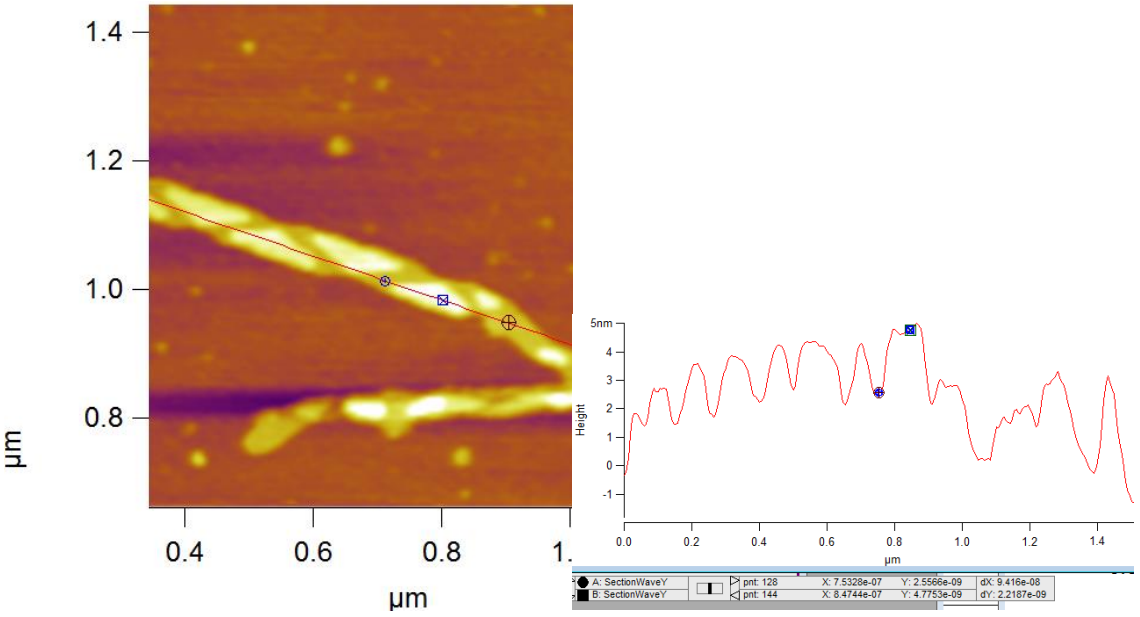

B

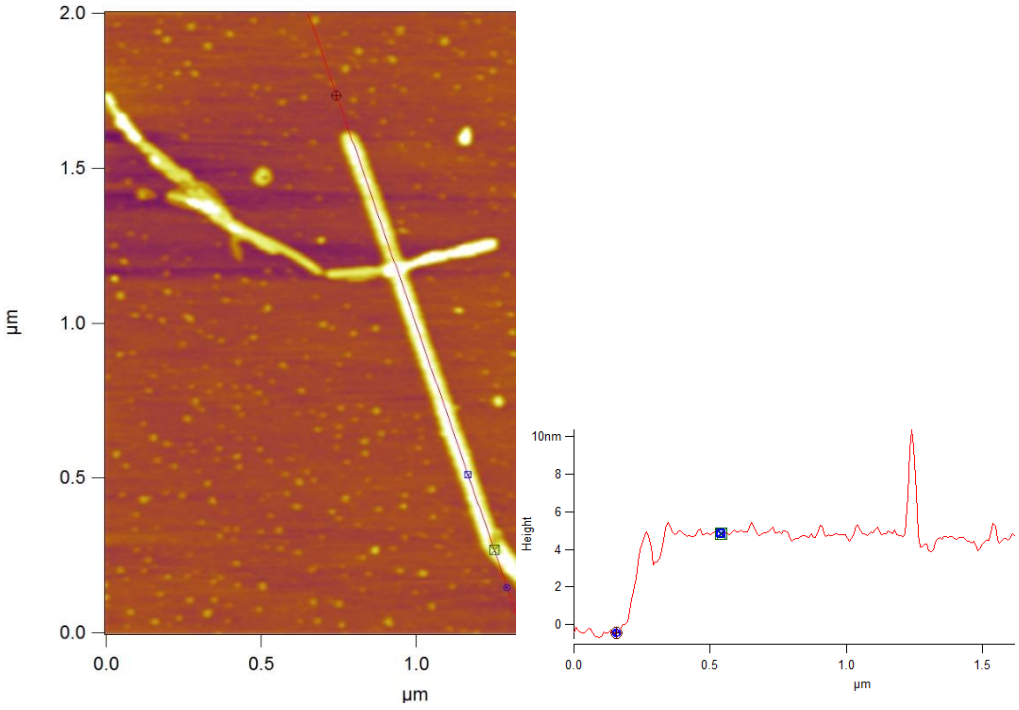

Figure 3.23. Representative AFM image of A) PSMβ2 helical ribbon, B) PSMβ2 nanotube in 556 µM peptide concentration, 10 mM pH 10 CAPS buffer, after 14 days of assembly time. Height difference shown (between blue box and blue circle) = A) 2.22 nm and B) 5.06 nm.

From this limited amount of AFM and TEM data, it seems either the helical ribbons are a result of unwrapped nanotubes with various pitches, or precursors of nanotubes that reached the ideal tape width but with a too high pitch; the latter would suggest a nanotube formation mechanism of helical ribbons closing down by reducing pitch, instead of growing in width to fully close to nanotubes. Since the helical ribbons were not observed in neutral pH conditions where nanotubes still present, it's more likely these ribbons are a result of nanotube unraveling, which would always result in helical ribbons with the same width. Unfortunately, it is difficult to further characterize these ribbons due to their rare occurrences.

3.2.4.3 TEM and STEM characterization of PSMβ2 fibrils

Many PSMβ2 morphologies observed via TEM have visible fibril patterns. Singular fibrils are rare and have an average width of 5.62±1.63 nm (Figure 3.24A). Fibril patterns can often be observed in PSMβ2 tape and nanotube assemblies, especially in samples incubated at 37 (Figure 3.24B). Measuring these fibril patterns yields an average fibril width of 7.50±0.58 nm, which corresponds well with the previously observed 7.64 nm FFT fibril pattern spacing on nanotubes.

A) B)

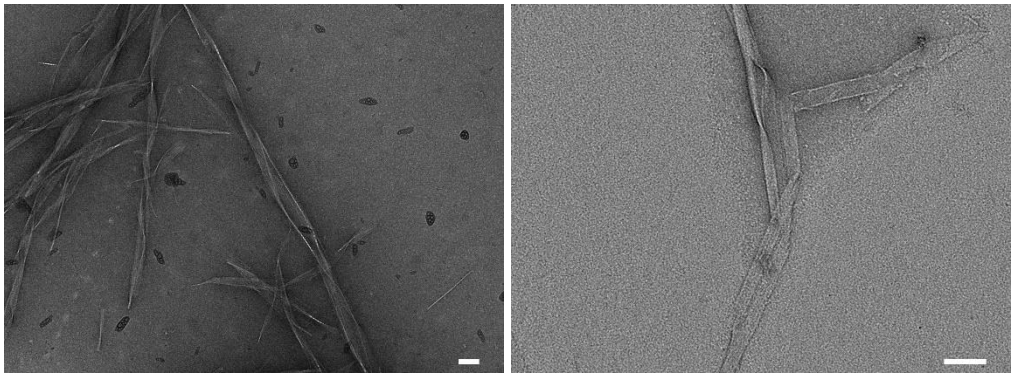

Figure 3.24. representative TEM images of A) 2.0 mg/mL PSMβ2 assembled in 10 mM pH 5 acetate at 1 day of incubation, B) 2.0 mg/mL PSMβ2 assembled in 10 mM pH 7 MOPS at 1 day of incubation at 37 ℃.

PSMβ2 fibrils with varied length can be observed via scanning transmission electron microscopy (Figure 3.25). While their M/L measurements are all different, they appear to be multiples of 1/12 of PSMβ2 nanotube's averaged M/L measurement. For example, Figure 3.25A shows fibrils with an averaged 1.32 kda/Å M/L measurement, corresponding to a single PSMβ2 cross-α fibril's M/L; Figure 3.25B shows fibrils with an averaged 2.93 kda/Å M/L measurement, corresponding to 3 PSMβ2 cross-α fibrils' M/L; and Figure 3.25C shows fibrils with an averaged 4.22 kda/Å M/L measurement, corresponding to 4 PSMβ2 cross-α fibrils' M/L.

A B

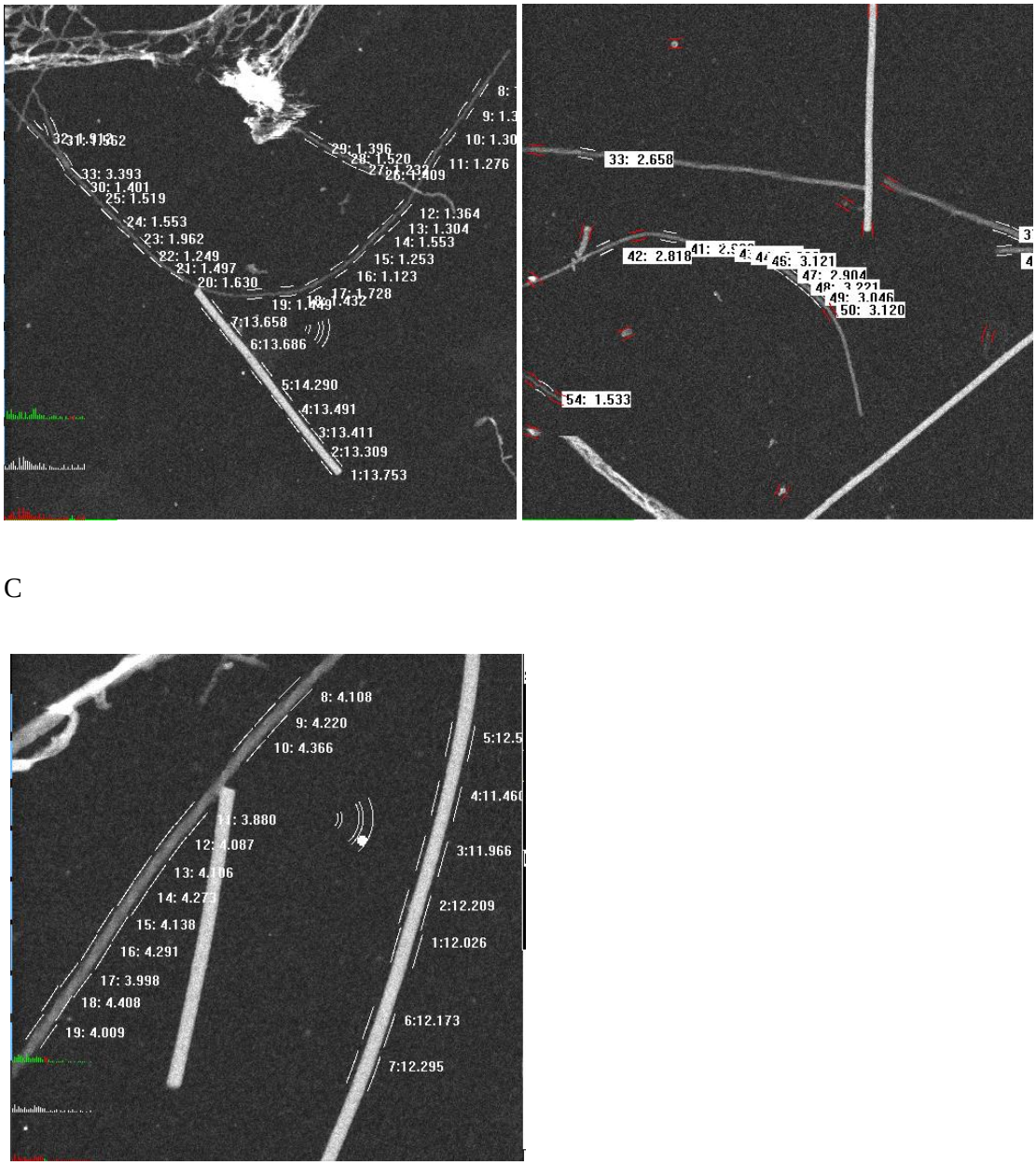

C

Figure 3.25. STEM images of PSMβ2 fibrils in 556 μM PSMβ2 in 10 mM pH 9 CHES buffer.

The extreme polymorphism of PSMβ2 fibrils made it difficult to be further characterized via cryo-EM or SAXS, but STEM and TEM data suggests these fibrils could be/arise from the same PSMβ2 cross-α fibrils associated into PSMβ2 nanotubes.

3.3 Conclusion

In summary, another peptide from the PSM family, PSMβ2 is also identified to assemble into a nanotube structure very similar to PSMα3's nanotube structure, despite the two peptides have differences in peptide sequence, monomer structure and cytotoxicity level. Fist, PSMβ2's helix-turn-helix monomer structure aligns through termini to form a dimer unit, this unit stacks in the fibril elongation direction and mates with another pair of dimers, although at 45 °angle, which exhibits cross-α structure signatures as shown in PSMα3's cross-α structure. PSMβ2 fibrils further laterally associate through PSMβ2 monomer's turn motif, resulting in polymorphic assemblies with limited selectivity towards temperature and pH. One of these morphologies, PSMβ2 nanotube structure was characterized via cryo-EM to afford a 4.5 Å resolution model.

PSMβ2's helix-turn-helix motif may be used as a redesign target to allow PSMβ2 morphologies to be controlled via designing the turn. For example, replacing His18 with amino acids containing other phenyl moieties, such as Phe and Trp, may strengthen or weaken the lateral association of the fibrils, resulting in a different selectivity towards tapes and nanotubes; removing the turn motif completely may force PSMβ2 to assemble similar to PSMα3; functionalizing Gln17 and Asp19 may enable stimulus control to nanotube self-assembly.

PSMβ2's cross-α structure paired with PSMβ2's low cytotoxicity raises the question whether cross-α structures contribute to cytotoxic or antimicrobial activities. Although multiple reports suggest cross-α is linked to antimicrobial activities[8-9], including the preliminary data of Warnaricin-RK shown in the previous chapter, the structure itself could not be the root-cause of such activities in PSMβ2's case. However, PSMβ2's polymorphic morphologies may hold other biological functions due to its weak assembly selectivity mainly dictated by pH, and this hypothesis can be tested especially if PSMβ2 assemblies can be observed in vivo.

3.4 Methods

Materials and Reagents. All chemical reagents were purchased from Sigma-Aldrich, unless otherwise specified. The PSMβ2 peptide was synthesized and purchased from Synpeptide Co Ltd (Shanghai, China). Its identity was determined by MALDI-TOF spectrometry, and its purity was determined by analytical HPLC to be 97.16%.

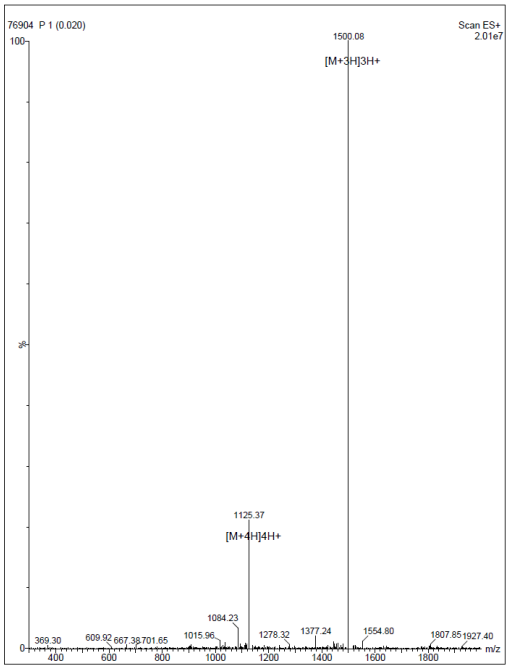

Figure 3.26. Electrospray ionization mass spectrum of PSMβ2.

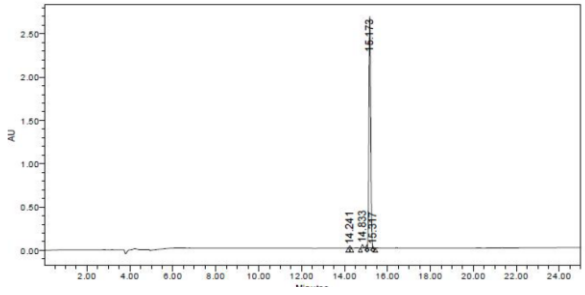

Figure 3.27. analytical HPLC spectrum of PSMβ2.

Peptide Assembly. Stock solutions of PSMβ2 were prepared by solubilizing 0.5 mg of purified, lyophilized peptide in 200 μL of 1X PBS, pH 7.45; 10 mM acetate, pH 5.0; 10 mM MES, pH 6.0; 10 mM MOPS, pH 7.0; 10 mM TAPS, pH 8.0; 10 mM CAPS, pH 9.0; or 10 mM CHES, pH 10.0 buffer, the final peptide concentration was 556 μM. Immediately after mixture, the solutions were titrated to the respective buffer pH using 100 mM sodium hydroxide solution. The samples were incubated at ~20 ℃ on the benchtop or 37.0 ℃ in an incubator. For some samples, solutions were thermally annealed using the following thermal cycler protocol: (1) rapid heating to 50/70/90 ℃ for 30 minutes; and (2) cooling to 25 ℃ at a rate of 0.2 ℃ / minute.

Circular Dichroism Spectropolarimetry. CD measurements were performed on a Jasco J-1500 CD spectropolarimeter in 0.1 mm quartz cells (Hellma Analytics), at 556 μM peptide concentration. Spectra were recorded from 260 to 190 nm, at a scanning rate of 100 nm/min and a data pitch of 0.2 nm, with 3 accumulations. CD melting experiments were performed with the same instrument and the same cuvette, in the temperature range of 5 ℃ to 95 ℃, at a heating rate of 60 ℃/hour and a data pitch of 0.2 ℃; the intensity of the CD signal at 209 nm was monitored as a function of temperature.

Transmission Electron Microscopy. TEM specimens were prepared from aqueous solutions of PSMβ2: 4 μL of the PSMβ2 samples were deposited onto 200 mesh carbon-coated copper grids from Electron Microscopy Services (Hatfield, PA). After 90 seconds of incubation period, the samples were wicked away until a thin film of sample remained, then the grids were stained with 4 μL of 1:1 mix of nano-W and nanoVan stains from Nanoprobes (Yaphank, NY). After 60 seconds of stain incubation period, all liquids were wicked away, and the grids were dried in a tabletop desiccator under vacuum. TEM measurements were acquired on a Hitachi HT-7700 transmission electron microscope with a tungsten filament and AMT CCD camera, at an accelerating voltage of 80 kV.

Cryo-electron Microscopy and Image Processing. The PSMβ2 peptide (4 μL of a 3 mg·mL-1 peptide concentration in 10 mM pH 9 CHES sample) was applied to glow-discharged lacey carbon grids and vitrified in a Vitrobot Mark IV (FEI, Inc.). Grids were imaged in a Titan Krios at 300 keV and recorded with a Falcon II direct electron detector at 1.05 Å per pixel. Images were collected using a defocus range of 0.5–3.0 μm, with a total exposure of 2 s (amounting to 70 electrons ·Å-2) dose-fractionated into seven chunks. All the images were first motion corrected by the MotionCorr v2 (1), and then the CTFFIND3 (2) program was used for determining the actual defocus of the images. Images with poor CTF estimation as well as defocus > 3 μm were discarded. A total of 386 images were selected and peptide filaments of varying lengths were boxed using the e2helixboxer program within EMAN2 (3). The CTF was corrected by multiplying the images from the first two chunks (containing a dose of ~ 20 electrons ·Å -2) with the theoretical CTF. Overlapping 256-px long boxes with a shift of 5 pixels (~ 1.5 times of the axial rise) were cut from the long filaments. The determination of the helical symmetry was by trial and error, searching for a symmetry which yielded recognizable secondary structure. Power spectra from the filaments suggested a variability in the helical parameters. A reference-based sorting procedure was used to bin the segments based on the axial rise and azimuthal rotation. Then 56,421 out of 356,100 segments were selected after this sorting and the IHRSR (4) method implemented in in Spider (5) was used to produce the final reconstructions at ~6 Å. The helical hand was determined by the fit of crystal structures into the cryo-EM map.

Scanning Transmission Electron Microscopy. STEM data were acquired at Brookhaven National Laboratory (BNL). The STEM instrument operates at 40 keV with a scanning probe of 0.3 nm diameter produced from a cold field-emission source. Each electron emerging from the specimen is detected by one of the scintillator photomultiplier detectors collecting 0−15 mRadian (bright field), 15−40 mRadian (small-angle dark field) and 40−200 mRadian (large-angle dark field). The large-angle signal is proportional to the mass of atoms in the path of the beam. Specimen

quality and mass calibration were assessed by detailed comparison of the image to the known structure of tobacco mosaic virus (TMV). For mass-per-length (M/L) measurements, TMV rafts at a theoretical M/L value of 13.1 kDa/Å were employed for calibration.

Specimens were deposited on thin carbon (circa 2 nm thick) supported on a thicker holey carbon film mounted on a titanium grid using the wet-film, hanging-drop method. TMV was added to the grid first as an internal control, followed by injection buffer, then specimen solution (in 10 mM MES buffer, pH 6.0) for 1 min, then 10 washes of 20 mM ammonium acetate pH 7.0. Excess solution was wicked from the edge with filter paper between each injection. After the last wash, the grid was wicked to a thin layer (ca. 1 mm), fast frozen by plunging into liquid nitrogen slush and stored under liquid nitrogen. Grids were freeze-dried overnight in an ion pumped chamber with an efficient cold trap and transferred under vacuum to the STEM cold stage (−160 °C). Imaging typically uses a dose of 20 e–/Å2 (causing < 5% mass loss, corrected by comparison to TMV). Mass per length measurements of the PSMβ2 nanotubes were performed with the software PCMass32.

References

1. Cheung, G. Y. C.; Joo, H.-S.; Chatterjee, S. S.; Otto, M., Phenol-soluble modulins – critical determinants of staphylococcal virulence. *FEMS Microbiology Reviews* **2014,** *38* (4), 698-719.
2. Wang, R.; Khan, B. A.; Cheung, G. Y.; Bach, T. H.; Jameson-Lee, M.; Kong, K. F.; Queck, S. Y.; Otto, M., Staphylococcus epidermidis surfactant peptides promote biofilm maturation and dissemination of biofilm-associated infection in mice. *J Clin Invest* **2011,** *121* (1), 238-48.
3. Otto, M., Staphylococcus epidermidis--the 'accidental' pathogen. *Nat Rev Microbiol* **2009,** *7* (8), 555-67.
4. Le, K. Y.; Villaruz, A. E.; Zheng, Y.; He, L.; Fisher, E. L.; Nguyen, T. H.; Ho, T. V.; Yeh, A. J.; Joo, H. S.; Cheung, G. Y. C.; Otto, M., Role of Phenol-Soluble Modulins in Staphylococcus epidermidis Biofilm Formation and Infection of Indwelling Medical Devices. *J Mol Biol* **2019,** *431* (16), 3015-3027.
5. Schwartz, K.; Syed, A. K.; Stephenson, R. E.; Rickard, A. H.; Boles, B. R., Functional Amyloids Composed of Phenol Soluble Modulins Stabilize Staphylococcus aureus Biofilms. *Plos Pathog* **2012,** *8* (6).
6. Zheng, Y.; Joo, H. S.; Nair, V.; Le, K. Y.; Otto, M., Do amyloid structures formed by Staphylococcus aureus phenol-soluble modulins have a biological function? *Int J Med Microbiol* **2018,** *308* (6), 675-682.
7. Towle, K. M.; Lohans, C. T.; Miskolzie, M.; Acedo, J. Z.; van Belkum, M. J.; Vederas, J. C., Solution Structures of Phenol-Soluble Modulins alpha 1, alpha 3, and beta 2, Virulence Factors from Staphylococcus aureus. *Biochemistry-Us* **2016,** *55* (34), 4798-4806.
8. Engelberg, Y.; Landau, M., The Human LL-37(17-29) antimicrobial peptide reveals a functional supramolecular structure. *Nature Communications* **2020,** *11* (1), 3894.
9. Tayeb-Fligelman, E.; Salinas, N.; Tabachnikov, O.; Landau, M., Staphylococcus aureus PSMalpha3 Cross-alpha Fibril Polymorphism and Determinants of Cytotoxicity. *Structure* **2020,** *28* (3), 301-313 e6.

Chapter 4: Designed Peptide Mimicking Cross-α Amyloid-like Fibrils

4.1 Introduction

Amyloids are peptides consisting of beta-strand secondary structure stacking on top of each strand, coined the cross-β structure. The strand stacking distance, often 4-5 Å, and the strand-strand mating distance, often 10-11 Å are signatures of cross-β amyloids, which can be observed on X-ray fibril diffraction patterns. Amyloid presence is found during the development of numerous diseases[1], such as Alzheimer's[2]; it's hypothesized the amyloid fibril structure is linked to, or the root cause of such diseases, and a tremendous research effort is put into characterizing amyloid structures, and determining the amyloid sequence-structure-cytotoxicity relationship[3]. In the meantime, amyloid fibrils are being explored as designable nanomaterials[4-5] due to 1. a vast variety of peptide sequences, long and short can self-assemble into amyloid fibrils, enabling a large theoretical design space; 2. amyloid fibrils utilize strong intermolecular hydrogen bonding for its main driving force of self-assembly[6], allowing them to achieve high moduli while maintaining reversibility, making it unique in comparison to extracellular fibrous materials with high moduli but little to no reversibility such as collagen, and intracellular fibrous materials with low moduli but are highly reversible such as actin. Some of the notable designed amyloid material applications include grafting short amyloid peptide sequences onto nanoparticles[7] and antibodies[8] to disrupt and inhibit amyloid formation, as food gelation agents[9], as functional templates to display grafted proteins on a fibrillar surface[10], as electron charge transfer and redox catalyzing wires[11], slow drug-release platforms[12] and others; however, due to difficulties in controlling the polymorphic nature of amyloids[13], concerns of the amyloid candidate acting as an amyloid nucleation inducing agent[14], often bio-incompatible peptide self-assembly conditions and other factors, amyloid-based

nanomaterials have yet to see commercialization. Nonetheless, cross-β amyloid-like structures are well worthy to be explored for their nanomaterial application potentials and biological activities.

Recently the discovery of PSMα3's cross-α fibril structure, mimicking cross-β amyloid structures but with α-helices instead of β-strands stacking in the direction of fibril growth, enabled another space of designability of amyloid-mimetic materials, and brought debates whether the cross-α structure contributes to biological functions[15-16]. Being a relatively new structure, cross-α's design rules are only briefly explored: one such example is αAm_{mem}[17], capable of adopting a heptad coiled-coil-like structure and self-assembling into cross-α amyloid-like fibrils through helix stacking. αAm_{mem}'s cross-α structure is approximated where helix mating is driven by coiled-coil *d-d* face, and helix stacking is driven by coiled-coil *e-e* and *g-g* face interactions (Figure 4.1c). Being a natural peptide, αAm_{mem} unsurprisingly does not completely follow the known stabilizing coiled-coil assembly principles, such as Ile at *b, c* faces where hydrophilic residues should be preferred at these solvent-facing positions. αAm_{mem}'s *d, e, g* faces are also not dominated by uniform residues like in most rationally designed coiled-coil systems, such as Ser11 at the *e* face is at the middle of the peptide facilitating close anti-parallel intra-helical *e-e* face interactions, while all other residues at the *e* face are Leu; Ala13 at the *g* face, and Ala17 at the *d* face both facilitate close anti-parallel intra-helical *g-g* face interactions, while all other *g, d* face residues are all Leu as well. To address these "imperfections," αAm_{mem} is engineered by applying known coiled-coil design principles and screened with mutations focusing at position 11 (Figure 4.1d), and the results suggested 1. αAm_{mem} can indeed be assumed as a coiled-coil system because αAm_S self-assembled, where all unoptimized residues in αAm_{mem} are optimized based on known coiled-coil design principles; 2. the amino acid's size at close intra-helical interaction positions is important, as mutating Ser11 to large residues such as Leu and Phe could not be characterized further due to poor solubility (αAm_F) or lead to a different structure (αAm_L); a derivative named αAm_{3L} mutating all position 11, 13 and 17 to Leu also only had limited solubility and couldn't be characterized further

to obtain an atomic structure. αAm_{mem} results suggest a generic coiled-coil based cross-α structure design might be possible.

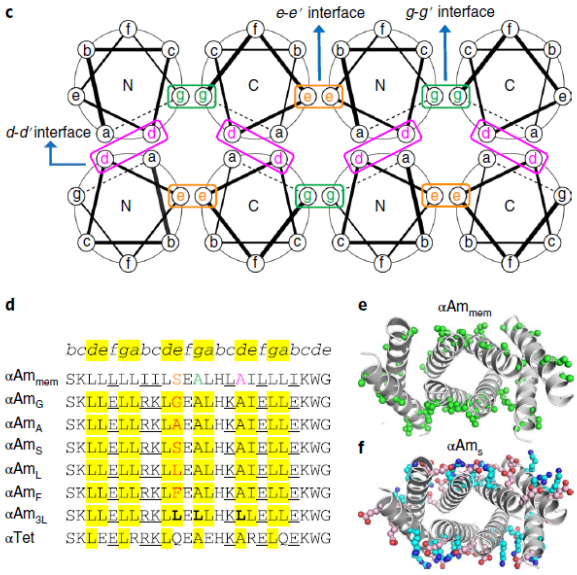

Figure 4.1. αAm_{mem}'s sequence and cross-α structure layout illustration.

This chapter will further explore the designability of coiled-coil based cross-α structures, focusing on the relationship between amino acid size and identities at *a*, *d*, *e*, *g* faces vs. the resultant peptide self-assembly structures. Like the studies conducted by Rhys et al. on exploring the designability of type 2 coiled-coil structures[18], this chapter will hopefully provide insights on the key design principles of cross-α structures.

4.2 Results and discussion

4.2.1 A designed cross cross-α fibril peptide ROX321

4.2.1.1 Design of ROX321

Coiled-coil based structure's designability has been well explored. A general coiled coil can be mapped into a heptad repeat labeled as ***abcdefg*** (Figure 4.2a). Residues at *a*, *d* faces can form knobs-into-holes interactions that create a hydrophobic core between the helices, resulting in a coiled-coil bundle (Figure 4.2b); the number of helices in a bundle can be directed by the identity of residues at these faces[19]. Residues at *e*, *g* faces are often designed to be complimentary polar residues, such as Glu and Lys, to form salt bridges in-between helices and help stabilize the resulting coiled-coil bundle[20]. Residues at *b*, *c*, *f* faces are often designed to promote helicity such as Ala[21], water-solubility using polar residues such as Gln, or serve as functionalization sites[22].

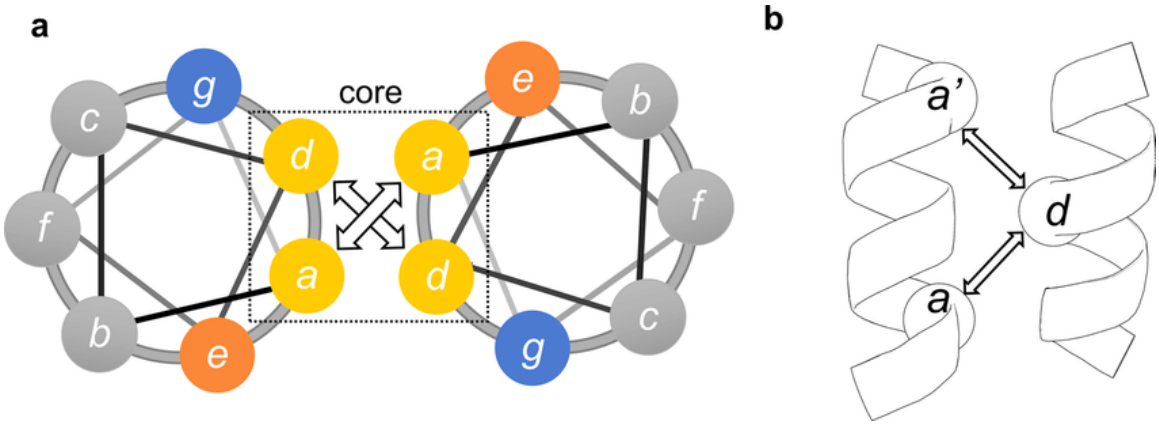

Figure 4.2. a) heptad representation of a generic coiled-coil. b) sideview of a generic coiled-coil showing the a-d knobs-into-holes interactions. Figure adapted from ref [23].

ROX321 was initially designed to explore type 2 coiled-coil assemblies. Rhys et al. defined coiled-coil dimers with knobs-into-holes *a*, *d* face interactions (2 consecutive interhelical interacting faces) as type N; coiled-coil bundles with knobs-into-holes *a*, *d*, *e* or *a*, *d*, *g* face

interactions (3 consecutive interhelical interacting faces) as type 1; coiled-coil bundles with knobs-into-holes *a, d, e, g* face interactions (4 consecutive interhelical interacting faces) as type 2; coiled-coil bundles with knobs-into-holes *a, d, e, g* face interactions (4 non- consecutive interhelical interacting faces) as type 3 (Figure 4.3)[18]. Type 2 deigns have been explored both through rational and computational design. Here, CC-HEX2 (PDB:4PN9) developed by the Woolfson group is shown as an example[24] (Figure 4.4B). CC-HEX2's design features include non β-branched Leu at the *a* face, β-branched Ile at the *d* face, and instead of complimentary polar residues at the *g, e* faces that direct a tetramer coiled-coil bundle[25], these faces are computationally optimized to be small residues Ala and Ser respectively. This peptide self-assembled into a hexameric coiled-coil bundle (Figure 4.4A); from its structure model determined by crystallography, one helix's *a-e* face (colored in red and green) can be seen mating with another helix's *d-g* face (colored in orange and blue). Type 2 designs have been systematically explored focusing on the effect of beta-branched amino acids such as Ile and Val, Leu and Phe on the coiled-coil bundle structure[18]. The results suggest the stereospecific beta-branching amino acids at the *a, d* faces preserve symmetry, and lead to coiled-coils with multiple monomers effectively resembling α-barrels with a huge cavity; the non-stereospecific, non-branching amino acid Leu, due to its symmetry ambiguity, leads to collapsed structures where the central cavity found in barrel structures is not present (Figure 4.5). The identities of amino acids at specific positions have profound effects, such as mutating all *d* face Val to Ile promoted an octameric coiled-coil bundle (PDB: 6G66) instead of a heptameric one (PDB: 6G67); mutating Leu17 to Glu promoted a heptameric barrel (PDB: 6G69) instead of a collapsed hexameric coiled-coil bundle (PDB: 6G68). Some of the effects can be attributed to amino acid sizes, for example replacing Val to a larger residue Ile promotes barrels with more monomers (6G65, Val at both *a, d,* hexamer; 6G66, Val at *d* and Ile at *a,* heptamer; 6G67, Ile at both *a, d,* octamer).

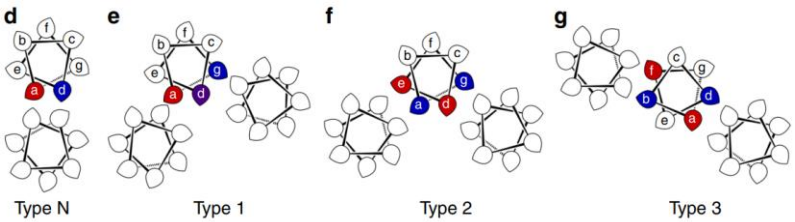

Figure 4.3. Classifications of high-order coiled-coil bundles. Figure adopted from ref.[18].

A B

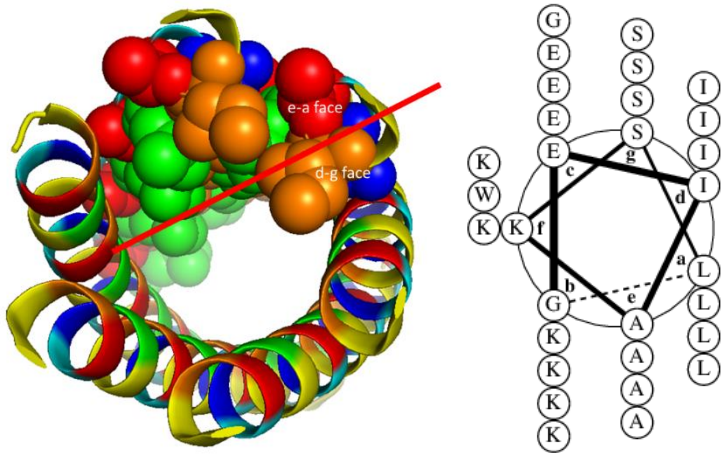

Figure 4.4. A) 3D model of CC-HEX2 (PDB: 4PN9). B) Heptad wheel representation of CC-HEX2.

A B

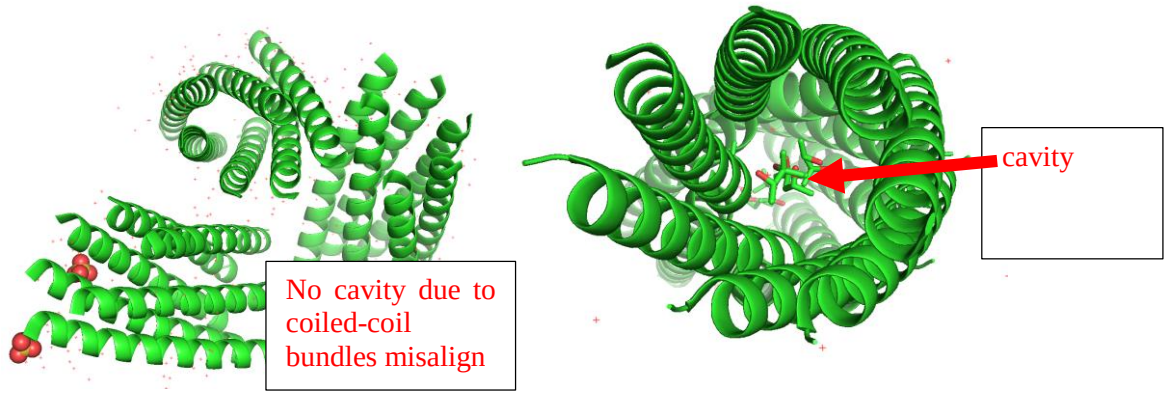

Figure 4.5: 3D models of A) a collapsed hexameric coiled-coil bundle (PDB: 6G68) and B) a heptameric coiled-coil bundle barrel (PDB: 6G69). The center cavity of barrels is labelled with a red arrow.

ROX321 is designed to be a coiled-coil type 2 structure, but placing Ala in the *a, d* faces and Leu in the *g, e* faces instead (Figure 4.6). ROX321 is capped by Glu and Lys to promote helix dipole[26]; a tyrosine in the *f* face is designed to determine the peptide's concentration accurately by UV[27]; all other amino acids in the *f* face is designed to be Gln to promote water solubility[25]; the *g* and *e* face are designed to be complimentary polar residues Glu and Lys as stabilization interfaces when they interact with each other. ROX321 is predicted have the following possible types of assembly: 1. The *a, d* face Ala will resemble a very tight hydrophobic core, resulting in a rather compact (and likely less oligomeric than CC-type2 series) coiled-coil bundle; 2. the *e, g* face Leu will direct inter-helical association along with the *a, d* face Ala, leaving the *a, d* face facing inwards forming a cavity; 3. the *e, g* face Leu will direct inter-helical association along with the *b,c* face complimentarily charged E and K, leaving the *a, d* face Ala facing outwards forming a polar cavity; 4. a fibril-like assembly where one helix's *e, a* face Leu and Ala form knobs-into-holes interactions with another helix's *d, g* face Leu and Ala (Figure 4.7). ROX321 is expected to assembly as the 2nd or 3rd type shown above to resemble an oligourea system[28], where a hydrophilic cavity is formed instead of a hydrophobic cavity, controlled by the choice of amino acid identities at certain positions.

```
          defgab cdefgab cdefga
ROX321: EALQLAK EALYLAE KALQLAK
```

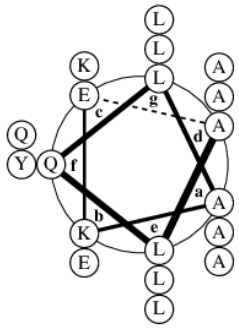

Figure 4.6. Heptad representation of ROX321.

A B

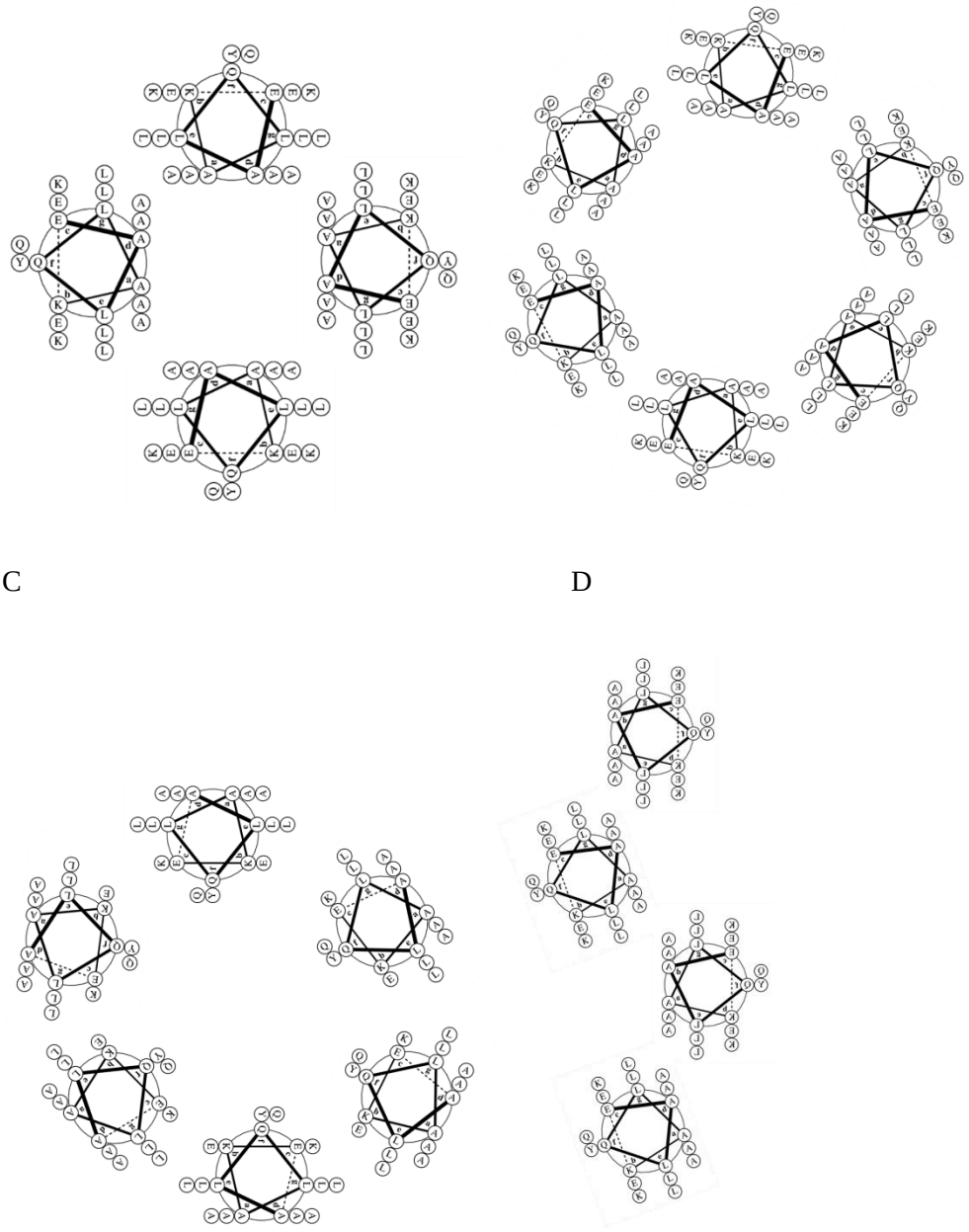

C D

Figure 4.7. Four possible type of assemblies proposed for ROX321. A) ROX321 forms a very tight hydrophobic core. B) ROX321 forms an a, d face Ala facing cavity. C) ROX321 forms a f face facing polar cavity. D) ROX321 forms a fibril-like structure.

4.2.1.2 Self-assembly of ROX321

ROX321 was synthesized via solid-phase peptide synthesis with N-terminal acetylation and C-terminal amidation to reduce termini charges. Peptide was purified by preparative HPLC, characterized by MALDI and its purity was confirmed by MALDI and analytical HPLC. Prior to screening, 20 mg ROX321 was dialyzed against 500 mL HPLC water for 4 times, dissolved in trifluoroethanol (TFE) and left under vacuum overnight, to eliminate pre-formed structures in powder with TFE addition and evaporation. ROX321 was first screened in 10 mM buffers from pH 4.0 to pH 8.0 at an increment of pH 1.0, room temperature and annealed at 90 ℃, at 849 mM peptide concentration to assess its self-assembly behavior. In all screened pH and temperature conditions, ROX321 assembled into 3.86 nm wide fibrils (Figure 4.9) within minutes after the samples were titrated to the respective pH (Figure 4.8). The fibrils were stable up to 1 month with no follow up after 1 month.

A B

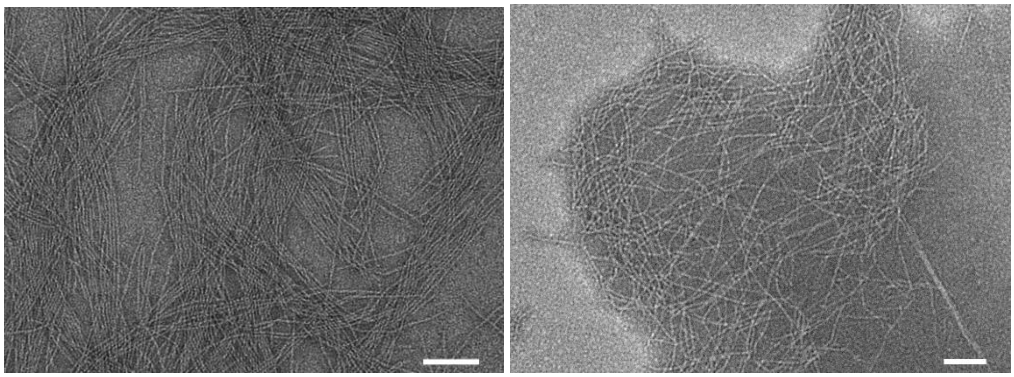

Figure 4.8. 2.0 mg/mL ROX321 in 10 mM pH 4 acetate buffer 10 min after preparation, A) room temperature and B) pH 7 MOPS buffer annealed at 90 ℃, 12 h after titration.

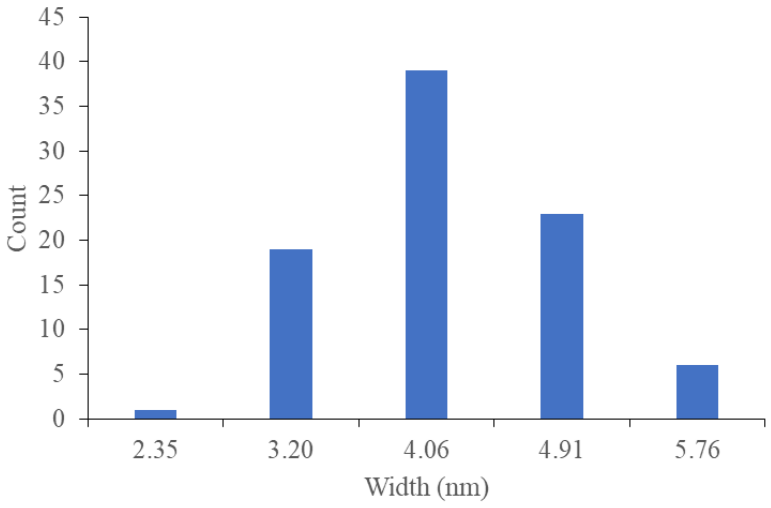

Figure 4.9. Histogram of ROX321 fibril width measured from TEM images, average = 3.86 nm.

All ROX321 fibril samples display α-helical CD signatures with minima at 208 nm and 223 nm (Figure 4.10A, B), and ROX321 assembled in 10 mM pH 4.0 acetate buffer shows an α-helical Fourier transformed infrared spectroscopy signature at 1653.6 cm^{-1} (Figure 4.10D). In particular, ROX321 in pH 4 buffer shows no CD change/development between at 5 minutes after preparation, 10 minutes after preparation and 30 minutes after preparation (Figure 4.10C); this result in combination with fibrils observed in samples 10 minutes after preparation in a wide range of pH suggest ROX321's fibril assembly is fast and robust. Additionally, the thermal stability of ROX321 assembled in 10 mM pH 4 acetate was assessed via monitoring the CD molar ellipticity at 223 nm from 5 to 95 ℃, and no significant melting transition was observed (Figure 4.11), suggesting ROX321's self-assemblies observed at room temperature and when annealed are likely identical.

A B

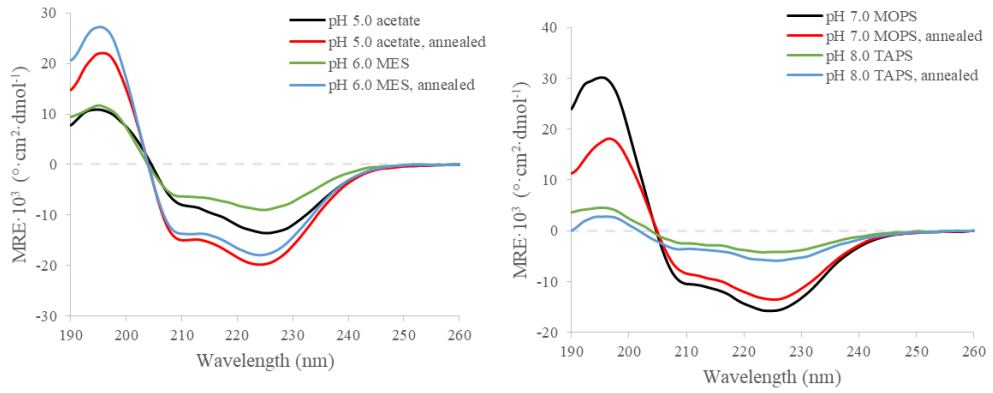

C D

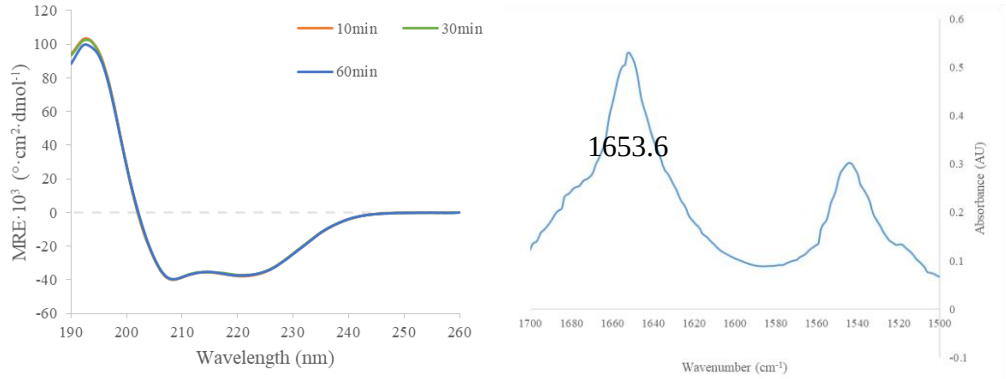

Figure 4.10 Circular dichroism spectra of 2.0 mg/mL ROX321 in A) 10 mM pH 5-6 buffer, at room temperature and anneaeled at 90 ℃; B) 10 mM pH 7-8 buffer, at room temperature and anneaeled at 90 ℃; C) 10 mM pH 4.0 acetate buffer, at 5/10/15 minutes after sample preparation. D) FT-IR spectrum of 2.0 mg/mL ROX321in 10 mM pH 4.0 acetate buffer.

A B

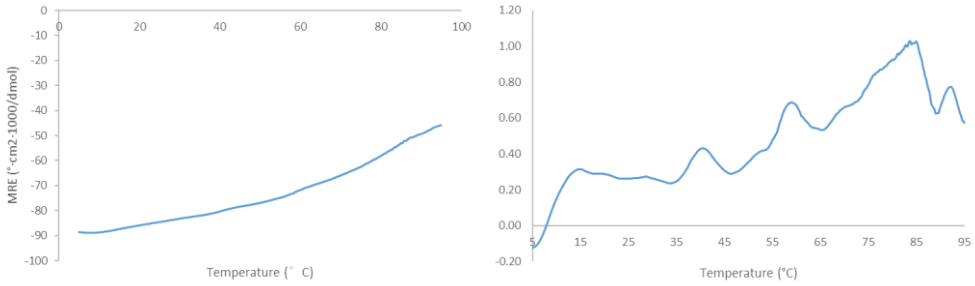

Figure 4.11 A) CD melting profile of ROX321 in 10 mM pH 4 acetate, monitoring at 223 nm, from 5 ℃ to 95 ℃; B) first derivative of A), no significant melting transition was observed.

From these preliminary data, ROX321 did assemble into α-helical fibril assemblies. The observed 3.8 nm fibril width is already larger than CC-HEX2's hexameric coiled-coil bundle's diameter of 2.39 nm, indicating ROX321 could have assembled into a larger α-barrel type of assembly. To confirm ROX321's design goal, ROX321 is further characterized with other microscopy methods such as cryo-EM.

4.2.1.3 Structure characterization of ROX321 via SAXS, STEM, cryo-EM and NMR

To further characterize ROX321's structure, the ROX321 fibril sample assembled in 2.0 mg/mL peptide concentration, 10 mM pH 4 acetate buffer, annealed at 90 ℃ was further analyzed by cryo-EM, NMR, STEM, SAXS. While the fibrils imaged with TEM shows a certain degree of flexibility, the cryo-prepared fibrils are stiff enough to yield a 4.0 Å resolution structure model using cryo-EM (Figure 4.12).

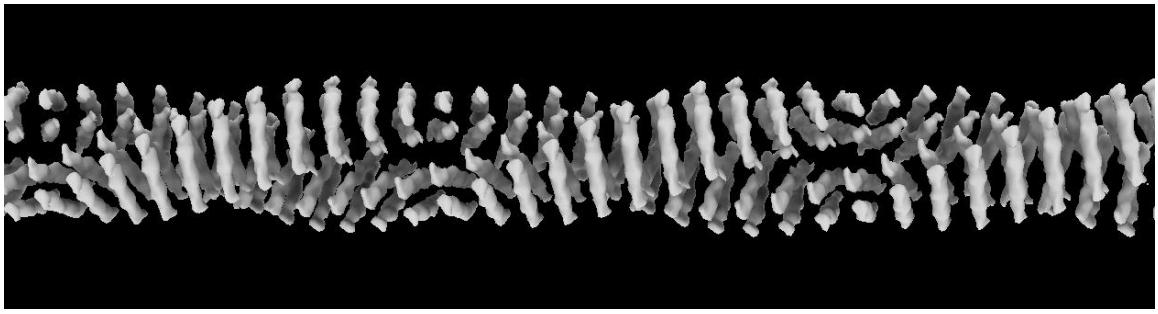

Figure 4.12. ROX321 fibril's cryo-EM model.

Instead of an α-barrel, ROX321 assembled into a cross-α structure very similar to αAm_{mem}; a similar assembly diagram (Figure 4.13) can be used to show ROX321 forms a coiled-coil dimer through its *a, d* face Ala knobs-into-holes interactions (Figure 4.14A), and achieved helix stacking through its *e, g* face Leu knobs-into-holes interactions (Figure 4.14B). ROX321's fibril structure poses a C1 point group symmetry, has 19 dimers per turn of a protofilament, a helical twist of -172° and a helical rise of 5.02 Å. Two protofilaments mate through hydrogen-bonding and polar interactions of the *f* face Gln and the complementarity charged *b, c* face Lys and Glu (Figure 4.15).

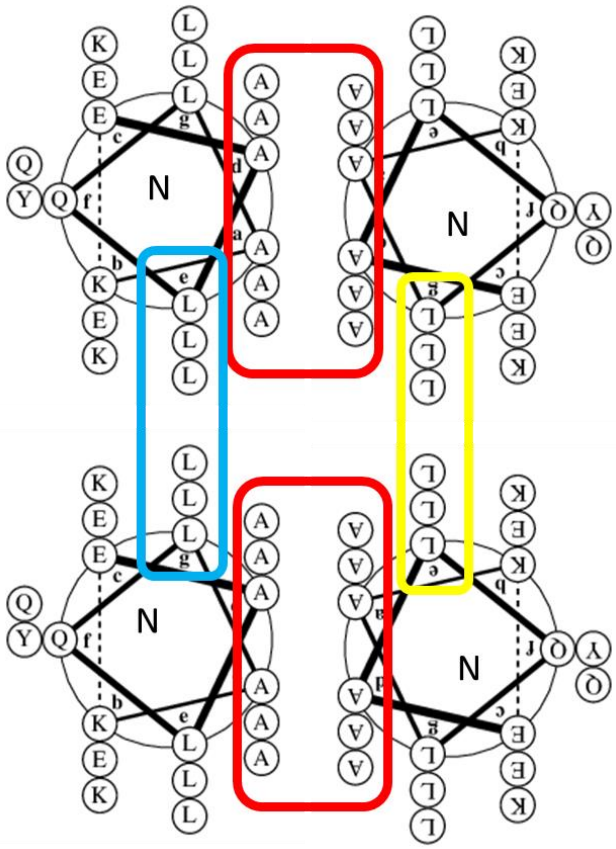

Figure 4.13. One of the possible (parallel) ROX321 protofilament's helix orientations in its cross-a like structure. a-d interfaces (resulting in a coiled-coil dimer) are boxed in red, and e-g interfaces (resulting in helix stacking) are boxed in cyan and yellow.

A B

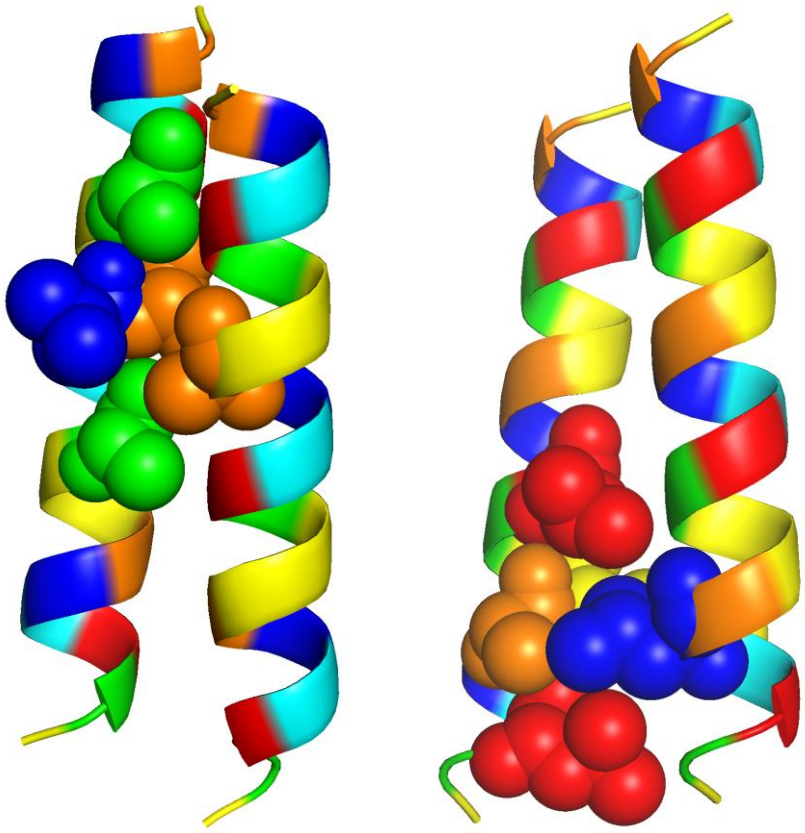

Figure 4.14. ROX321 models shown here assumes ROX321 helices align in a parallel fashion to form a dimer, orange = a face Ala, green = d face Ala, yellow = b face Lys, blue = g face Leu, red = e face Leu. A) ROX321 a-d face knobs-into-holes interaction, the right helix's orange Ala13 knob fits into a diamond-shape hole formed by the left helix's green Ala16 and Ala9, orange Ala13 and blue Leu12. B) ROX321 e-g face knobs-into-holes interaction, the right helix's blue Leu5 knob fits into a diamond-shape hole formed by the left helix's orange Ala6, yellow Lys7 and red Leu3 and Leu 10. Model rendered in PyMol.

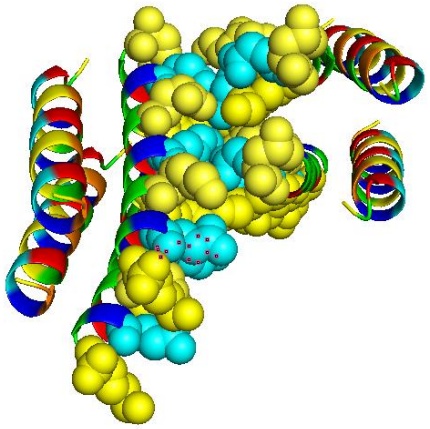

Figure 4.15. ROX321 protofilament mating through f (cyan), b and c (yellow) faces, f, b, c face residues shown in spheres. Model rendered in PyMol.

In comparison to αAm_{mem}, both systems' *e, g* faces are dominated by Leu; ROX321's *a, d* faces are Ala instead of αAm's Leu, as a result ROX321 formed a tighter coiled-coil dimer bundle (7.2 Å dimer helix-helix distance) than αAm_{mem} (9.1 Å dimer helix-helix distance), and had a smaller crossing angle (~10 °) than αAm_{mem} (~20 °). The effect of small residues at positions mediating close intra-helix interactions, such as *d* face Ala9, *e* face Leu10 and *g* face Leu12, was not considered in the design of ROX321, but doesn't seem to have an impact on ROX321's cross-α self-assembly. While both ROX's and αAm derivatives' solvent-facing *b, c, f* faces are designed to be polar, ROX321's polar interfaces promote fibril mating where αAm_{mem}'s does not.

Unfortunately the orientation of the helices in ROX321's *a, d* face interacting dimer bundle is ambiguous due to ROX321 cryo-EM model's 4 Å resolution limit; solid-state NMR (ssNMR) is used to determine the relative orientations of the monomers in collaboration with the Paravastu group at Georgia Institute of Technology, since ssNMR is commonly employed to determine helix orientations in helical bundles[29]. From the possible helix orientations, residues L3, K7, E14, and A20 are isotopically labelled, where for the parallel orientation, L3-L3, A20-A20, and E14-K7

from the two helices will show close NMR contacts; in the antiparallel orientation within the dimer, L3-A20 from the two helices will show NMR shifts (Figure 4.16).

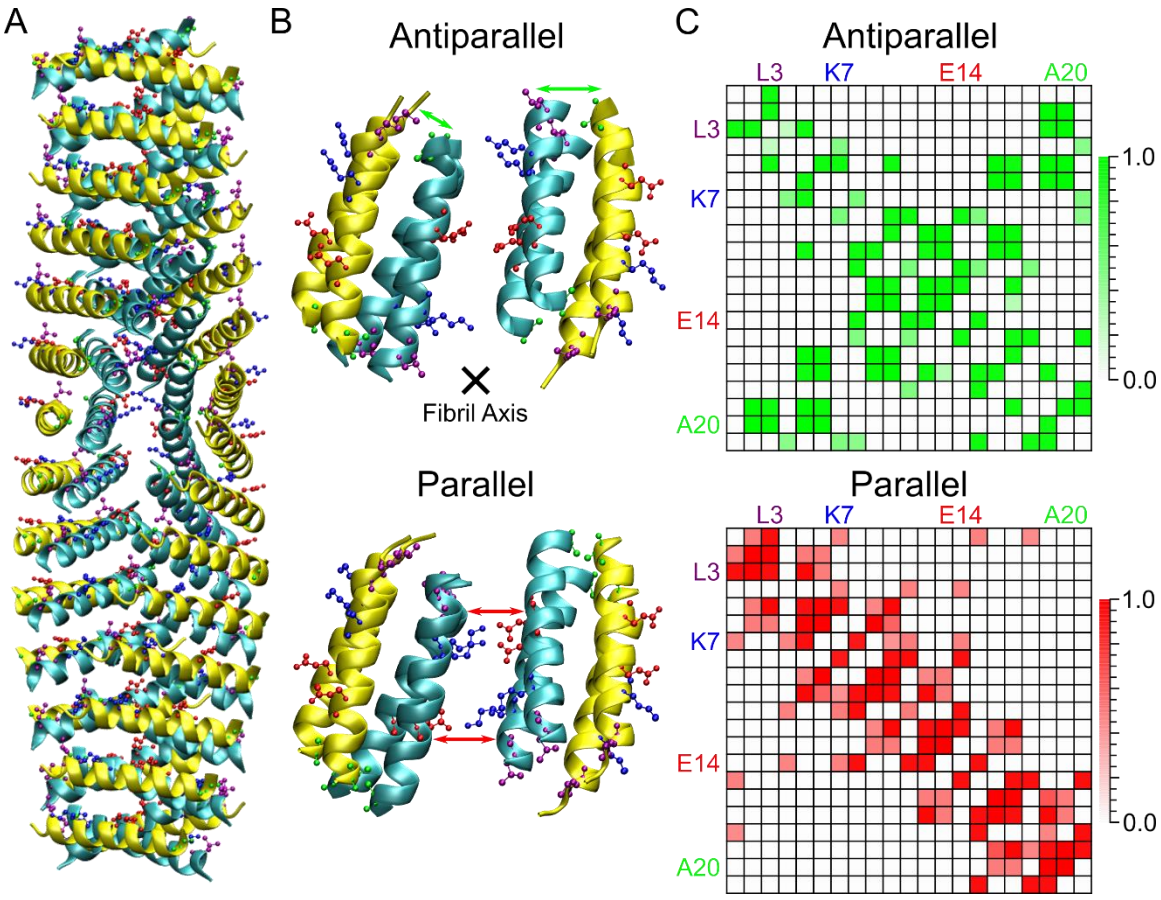

Figure 4.16. ssNMR labelling scheme of ROX321. Figure provided by Kong Wong, Paravastu group.

Isotopically labeled ROX321 was prepared via solid-phase peptide synthesis with N-terminal acetylation and C-terminal amidation, and assembles identical to ROX321 wildtype. ssNMR data showed both orientations exist in ROX321. Shown in Figure 4.17, expected L3-A10 close contacts are represented in purple-green diamonds; expected K7-E14 close contacts are represented in red-blue diamonds.

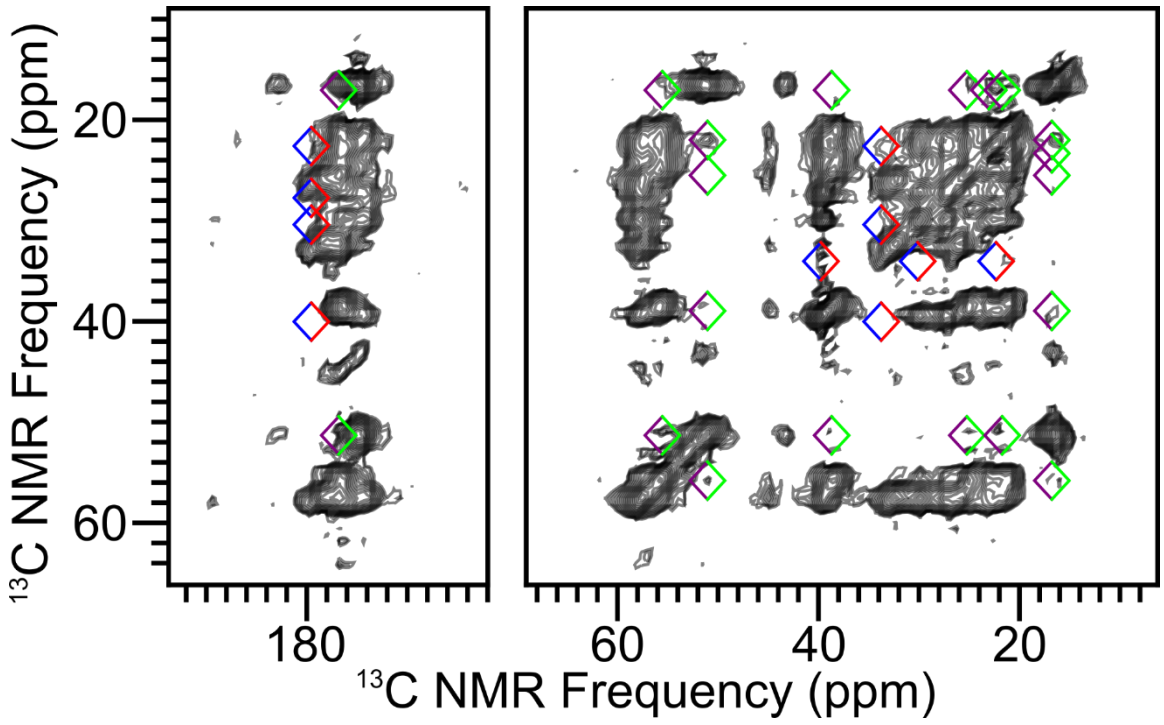

Figure 4.17 ssNMR spectrum of ROX321. Figure provided by Kong Wong, Paravastu group.

SAXS was used to identify ROX321 structural information to validate the cryo-EM model. From SAXS, the scattering intensity I(Q) was measured as a function of the momentum transfer, *q* from .005 $Å^{-1}$ to 9.4 $Å^{-1}$. In the small q region, a modified Guinier analysis for rodlike forms yielded a radius of cross-section gyration of 16.4 Å (Figure 4.18B), or a rod diameter of 46.5 Å, which roughly corresponds to ROX321's cryo-EM model fibril diameter of 36.0 Å and the 3.86 nm observed fiber diameter via TEM. One Braggs diffraction peak at q = 0.612$Å^{-1}$ is observed (Figure 4.18A); using the scattering vector equation $= \frac{4\pi\sin(\theta)}{\lambda}$, this peak translates to a distance of 10.26 Å, which corresponds to the stacking distance in ROX321's cryo-EM model (Figure 4.19).

A B

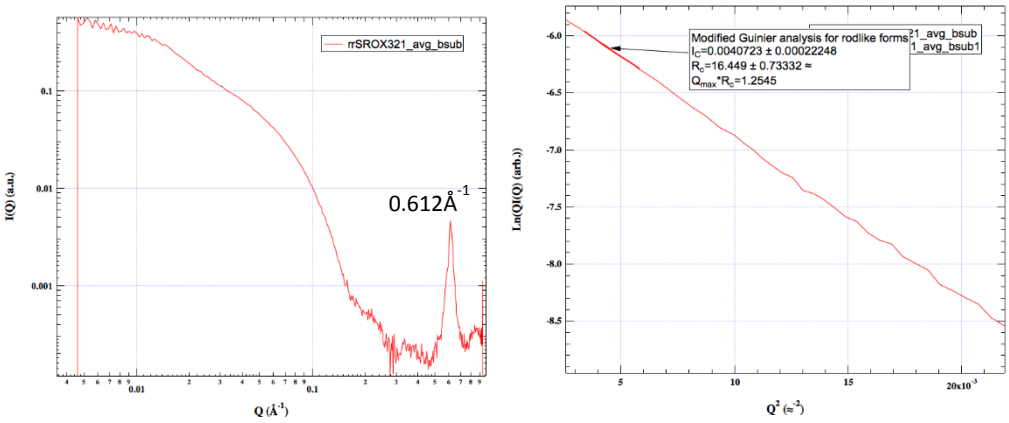

Figure 4.18. A) SAXS scattering profile of ROX321, a Braggs diffraction peak is observed at 0. 612Å^{-1}. B) Guinier analysis of ROX321's small q region SAXS scattering profile, treating the ROX321 fibrils as rodlike forms, approximated rod cross-section radius of gyration = 16.4 Å.

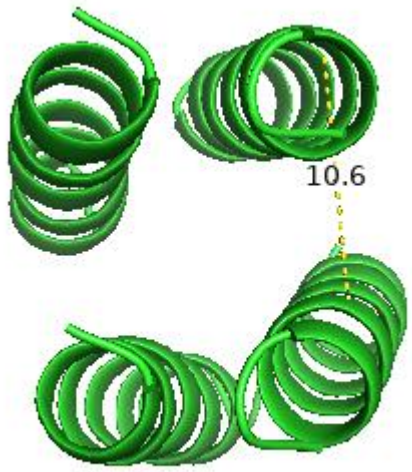

Figure 4.19. ROX321 coiled-coil dimer stacking distance = 10.6 Å, measured in PyMol.

STEM was used to identify ROX321 structural information to validate the cryo-EM model, where the number of ROX321 monomers in a particular ROX321 fibril length can be determined. Due to ROX321 fibrils being extremely thin, the measured mass per length of ROX321 fibrils have a rather large variance at 1097 da / Å ± 280 da / Å (Figure 4.20A, C), which translates to 3 – 5 monomers per nanometer. Another population of fibrils can sometimes be observed with 2-3X of the typical fibril's M/L, they appear to be whiter, stiffer and have a slightly larger width TEM

(Figure 4.20B). Due to their relatively thin fibril widths, these two species would be difficult to be distinguished previously via TEM. The 1097 da / Å experimental M/L value roughly corresponds with ROX321's cryo-EM model, where 4 monomers account for 10.7 Å helix elongation, resulting in a theoretical M/L value of 880 da / Å.

A B

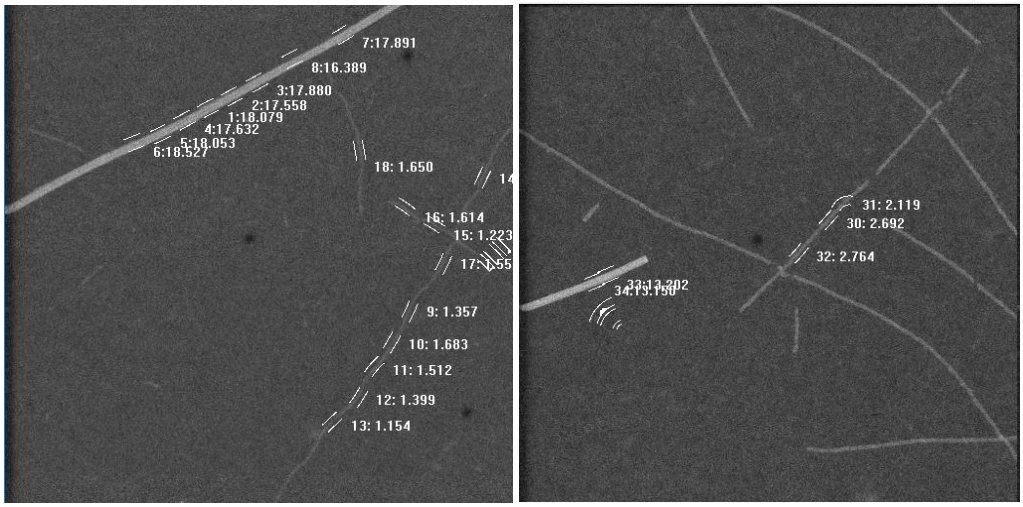

C

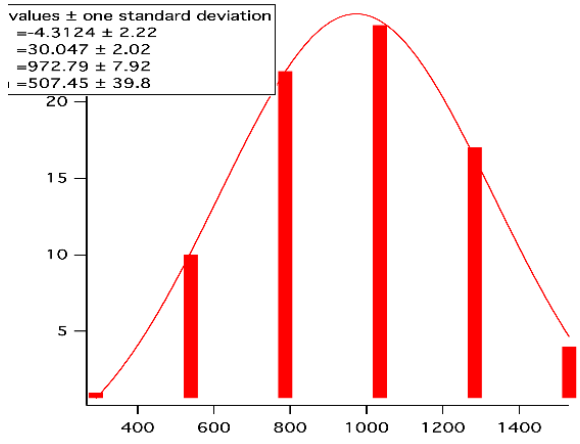

Figure 4.20. A, B) representative STEM images of A) typical ROX321 fibrils; B) thicker ROX321 fibrils with higher M/L values. C) Histogram of M/L measurements taken from typical ROX321 fibrils as in A), average = 1097 da / Å.

In summary, ROX321 is shown by cryo-EM to self-assemble into cross-α fibrils, and the cross-α stacking distance can be observed via SAXS. ROX321's cross-α structure resembles αAm system's cross-α structure, suggesting type 2 coiled-coil systems could adopt cross-α structures as well as traditional coiled-coil bundles. In the next few sections, ROX321 will be further explored on sequence length and amino acid identity at specific positions to determine ROX321's key design features that lead to a cross-α structure instead of a CC-HEX-like coiled-coil bundle.

4.2.2 Length variants of ROX321

4.2.2.1 Design of ROX314 and ROX328

Deriving from ROX321, the effect of peptide length on cross-α structures is investigated. Natural coiled-coil proteins often have conserved coiled-coil length[30-31], but coiled-coils ranging from 2 to 5 heptads are the most common[32]. For *de novo* coiled-coils, short peptides with only 1 heptad typically won't form stable two-stranded coiled-coils, and peptides with 4-5 heptads are optimized in terms of two-stranded coiled-coil formation[33]. Interestingly, all confirmed and suspected peptides with cross-α structures, PSMα3, αAm_{mem}, ROX321, two sub-helices in PSMβ2's helix-turn-helix motif, and Warnericin-RK are all around 3 heptads long. As a starting point, 2 heptads and 4 heptads versions of ROX321 are investigated to identify the heptad length's effect to its cross-α structure. The two peptides, named ROX314 and ROX328 respectively (Figure 4.21), have the same design principles as ROX321's: ROX314 deleted ROX321's first heptad, and ROX328 added a heptad EKALHLA maintaining the complimentary polar residues at the *c*, *b* faces, and incorporated a weakly basic His to balance out the barely acidic Gln4 and Gln18 at the *f* face. Both peptides are expected to form cross-α fibrils, but with ± ~1 nm difference in fibril widths in comparison to ROX321 as peptides are longer/shorter.

```
         cdefgab cdefgab cdefgab cdefgab
ROX314:          E ALYLAE KALQLA K
ROX321: E ALQLAK EALYLAE KALQLA K
ROX328: E ALQLAK EALYLAE KALQLAE KALHLA K
```

A B

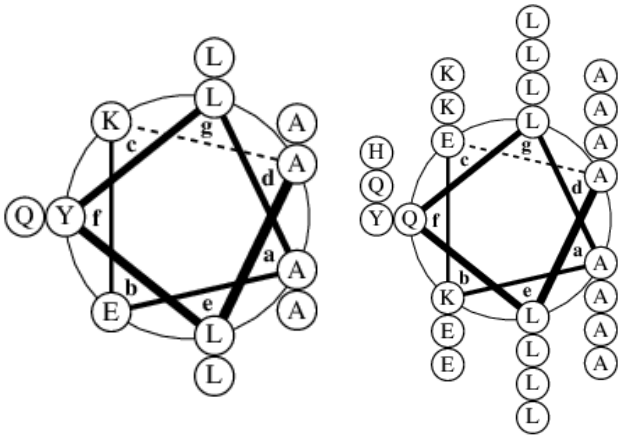

Figure 4.21. Heptad representations of A) ROX314 and B) ROX328.

4.2.2.2 Self-assembly of ROX314 and ROX328

ROX314 and ROX328 were synthesized via solid-phase peptide synthesis with N-terminal acetylation and C-terminal amidation to reduce termini charges. Peptides were purified by preparative HPLC, characterized by MALDI and its purity was confirmed by MALDI and analytical HPLC. Both peptides were screened in assembly conditions where ROX321 showed fibril assemblies. ROX314 showed polymorphic assemblies where fibrils with various widths were observed (Figure 4.22), and the observed fibril widths are all larger than ROX321 fibril's 4 nm width. ROX314 in all conditions shows α-helical CD signatures with minima at 205 nm and 223 nm (Figure 4.23A); the signal at 222 nm showed a lower negative ellipticity compared to ROX321, although a similar phenomenon was previously observed for coiled-coils with 2 heptads compared to 3[33]. ROX314 assembled in 10 mM pH 4.0 acetate buffer also shows an α-helical Fourier transformed infrared spectroscopy signature at 1654.2 cm^{-1} (Figure 4.23B). ROX314's polymorphic nature and the tendency of aggregation into twisting fibrils when frozen make it

difficult to further characterize ROX314's atomic structure model. The larger-than-expected ROX314 fibril width suggests either ROX314 does not adopt a cross-α structure, or the helices aggregate through complementary termini interactions to form thicker fibrils.

A B

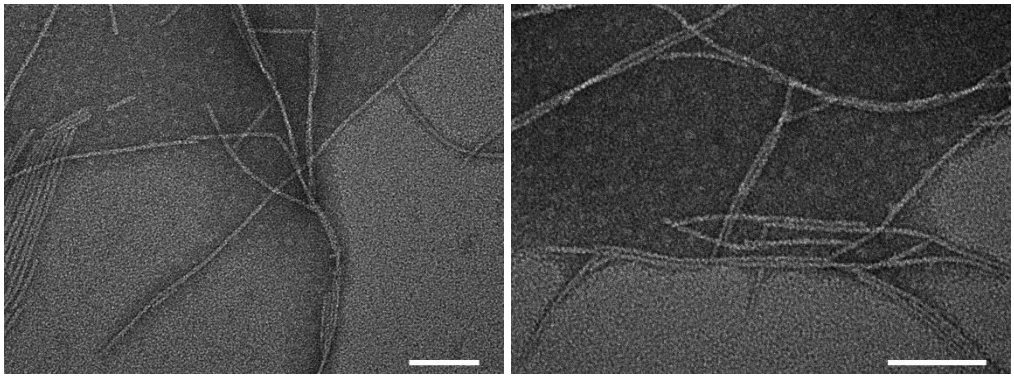

C

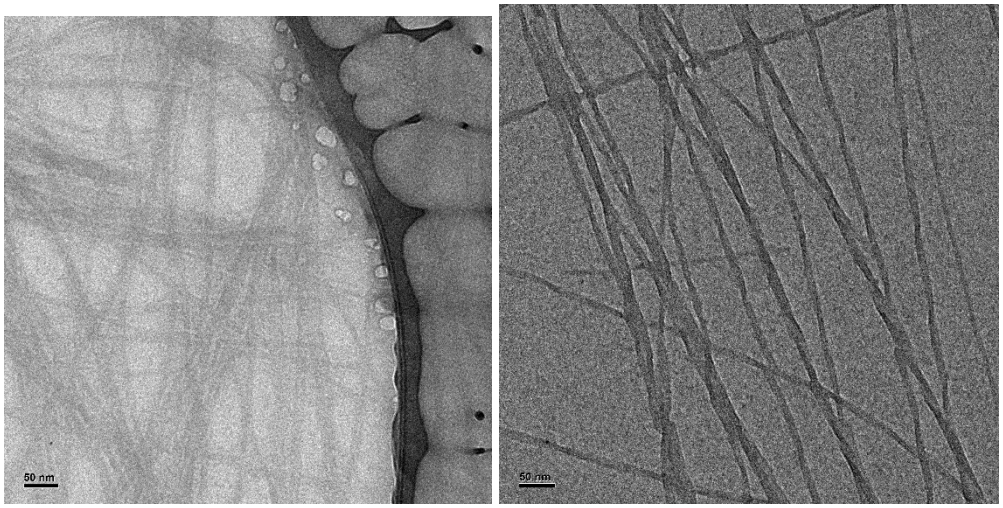

Figure 4.22. A) and B) TEM images of 2.9 mg/mL ROX314 in A) 10 mM pH 4 acetate, B) 10 mM pH 5 acetate, 1 day assembly time, scale bar = 100 nm. C,D) cryo-EM image of 2.9 mg/mL ROX314 in 10 mM pH 4 acetate, scale bar = 50 nm.

A B

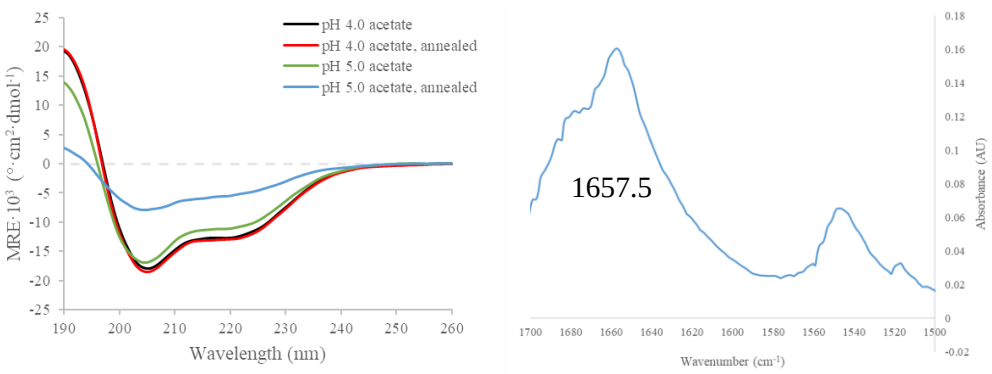

Figure 4.23. A) Circular dichroism spectra of 2.9 mg/mL ROX314 in A) 10 mM pH 4-5 buffer, at room temperature and anneaeled at 90 ℃; B) IR spectrum of 2.9 mg/mL ROX314 in 10 mM pH 4 acetate buffer; ROX314 shows an α-helical signature at 1654.2 nm^{-1}.

ROX328 assembled into 2 nm wide fibrils in all conditions screened (Figure 4.24); ROX328's fibril width is smaller than its helical length and thus, ROX328 can be expected to not adopt a cross-α structure; it is possible ROX328's coiled-coil bundles rather align in parallel to the fibril axis and form a type 2 coiled-coil structure instead. All ROX328 samples display α-helical CD signatures with minima at 208 nm and 223 nm (Figure 4.23A).

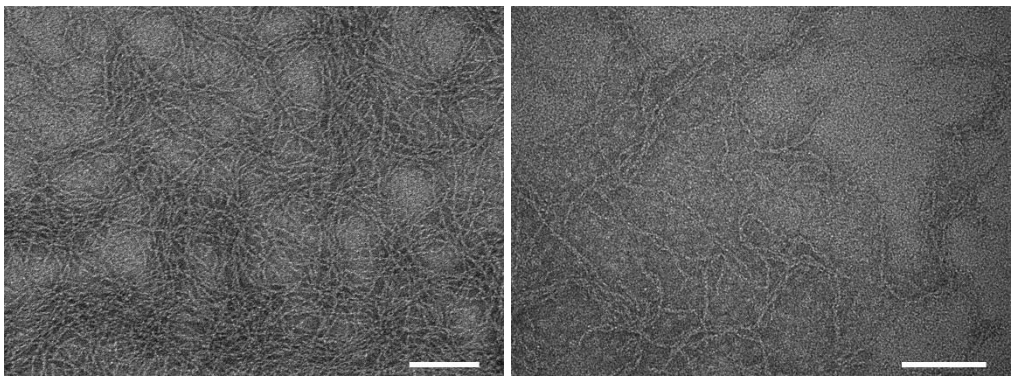

Figure 4.24. TEM images of 3.4 mg/mL ROX328 in A) 10 mM pH 5 acetate, B) 10 mM pH 6 MES annealed at 90 ℃, 1 day assembly time, scale bar = 100 nm.

A B

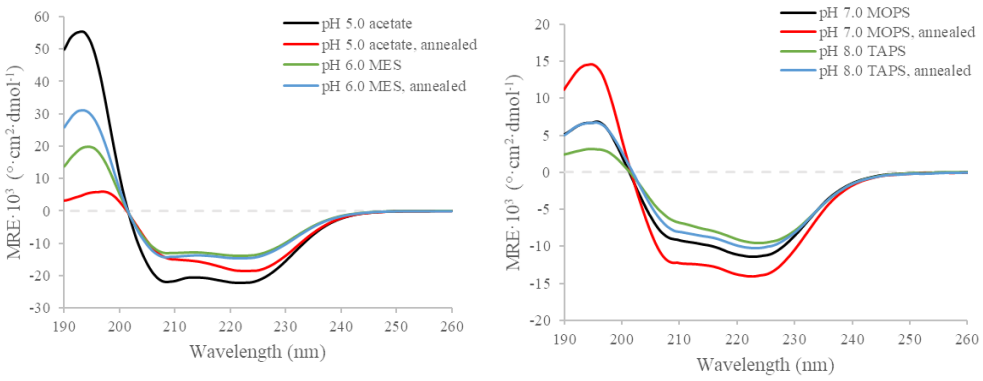

Figure 4.25. Circular dichroism spectra of 3.4 mg/mL ROX328 in A) 10 mM pH 5-6 buffer, B) 10 mM pH 7-8 buffer, all at room temperature and anneaeled at 90 ℃.

In conclusion, ROX321's cross-α structure is very sensitive to the number of heptads designed; 3 heptads seem to be the optimal length for ROX321's cross-α structure self-assembly, where longer and shorter sequences did not assemble into cross-α structures. This result follows the trend where cross-α forming peptide PSMα3, two helices of PSMβ2's helix-turn-helix structure, αAm_{mem} and its derivatives and possibly Warnericin-RK are all around 3 heptads long, it is possible peptide length is crucial for cross-α self-assembly. While ROX328 could not be characterized further to confirm this hypothesis, it is possible that the importance of small residues at close contact points between helices in αAm_{mem} systems is relevant in ROX328's case, where the peptide is longer and residues near the termini at the *a*, *d* faces could be too far to establish hydrophobic interactions in comparison to ROX321.

4.2.3 Stacking interface mutants of ROX321

4.2.3.1 Design of ROX321eIle and ROX321gIle

In ROX321's parallel orientation and anti-parallel orientation, *e-g* face interactions account for the stacking interface, instead of *e-e* and *g-g* interactions seen in αAm_{mem}. In ROX321's model, both residues are Leu and would not be expected to show a preference. In this section, the robustness of Leu at *e, g* positions is tested by mutations to beta-branching amino acids. Beta-branching amino acids are known to direct the number of monomers in a coiled-coil bundle, affect coiled-coil stabilities at the *a, d* faces of coiled-coil peptides[34], affect the interhelical interactions and self-assembly of a helical 2D crystalline network[35], and defining symmetry in comparison to gamma-branched amino acids such as Leu in coiled-coil systems that leads to α-barrels[18]. ROX321-eIle, gIle, and egIle are designed where all Leu on the *e*, *g*, or *e* and *g* faces are mutated to Ile respectively (Figure 4.27). ROX321-eIle and ROX321-gIle are expected to behave similarly due to ROX321's helix-stacking *e-g* interface interactions, thus should not differentiate Leu2Ile mutations at the *e* or *g* face; ROX321-egIle may behave differently than ROX321.

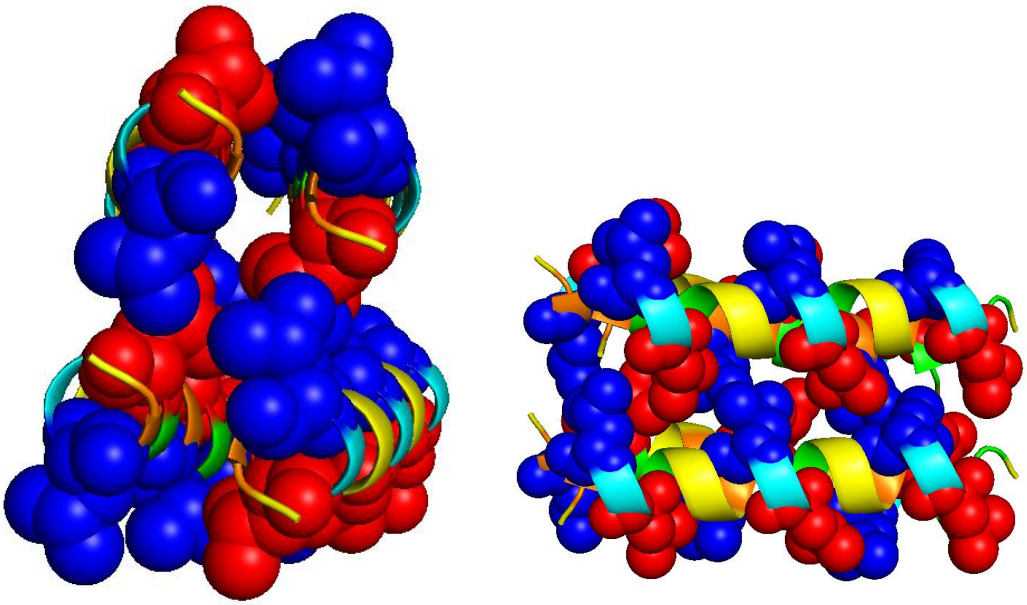

Figure 4.26. A) front and B) side view of ROX321 in all-parallel orientation, e face is colored in red, g face is colored in blue, both are shown in spheres. Model rendered in PyMol.

```
                    cdefgab cdefgab cdefgab
ROX321(all LEU):    EALQLAK EALYLAE KALQLAK
ROX321,eIle    :    EAIQLAK EAIYLAE KAIQLAK
ROX321,gIle    :    EAIQIAK EAIYIAE KAIQIAK
ROX321,egIle   :    EAIQIAK EAIYIAE KAIQIAK
```

A B C

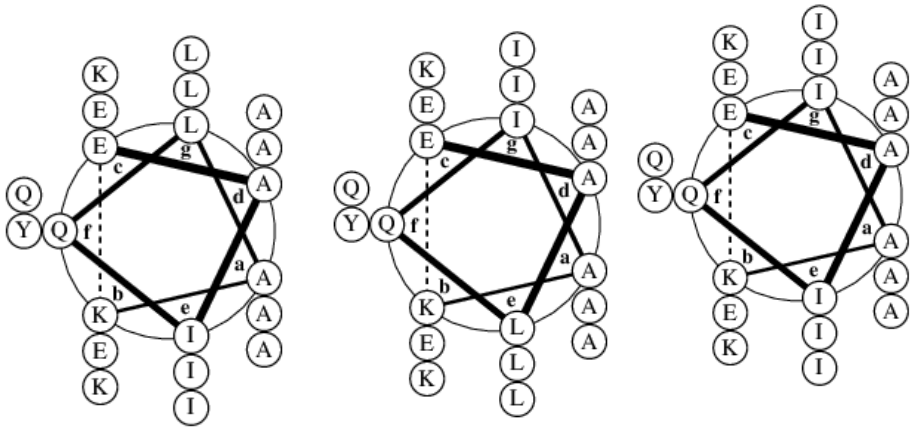

Figure 4.27. Heptad representation of A) ROX321eIle, B) ROX321gIle and C) ROX321egIle.

4.2.3.2 Self-assembly of ROX321eIle, ROX321gIle

Currently, only ROX321eIle and ROX321gIle have been screened. ROX321eIle and ROX321gIle were synthesized via solid-phase peptide synthesis with N-terminal acetylation and C-terminal amidation to reduce termini charges. Peptides were purified by preparative HPLC, characterized by MALDI and its purity was confirmed by MALDI and analytical HPLC. Both peptides were screened in assembly conditions where ROX321 showed fibril assemblies. ROX321eIle assembled into on average 3.93 nm wide fibrils (Figure 4.28, Figure 4.29), its fibril morphology and width are both similar to ROX321's, and likely adopt the same cross-α structure as ROX321. All ROX321eIle fibril samples display α-helical CD signatures with minima at 208 nm and 222 nm (Figure 4.30).

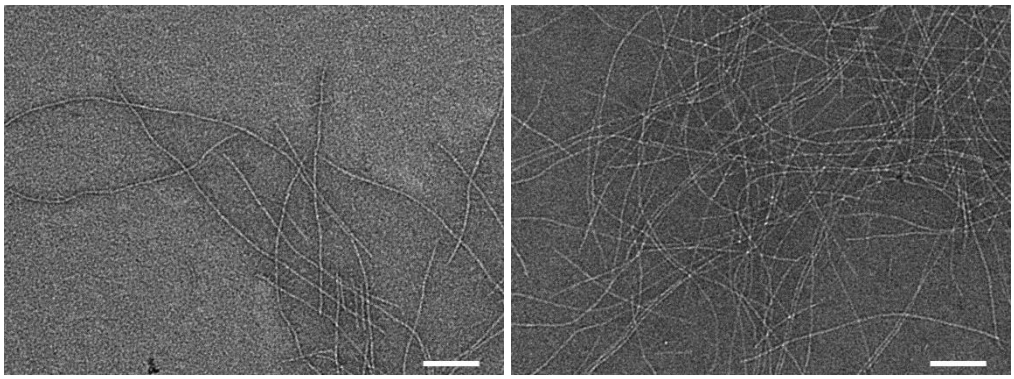

Figure 4.28. TEM images of 2.2 mg/mL ROX321eIle in 10 mM pH 6 MES buffer, 1 day assembly time. Scale bar = 100 nm.

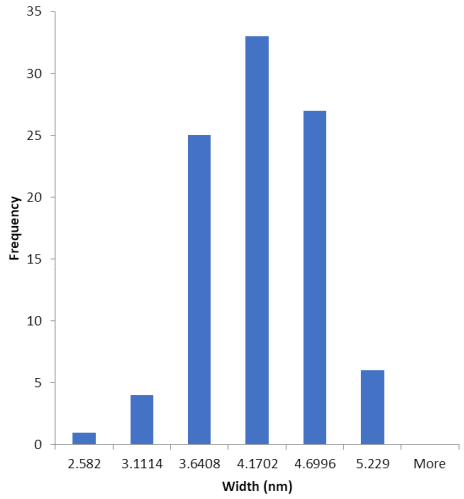

Figure 4.29. Histogram of ROX321eIle fibril width measured from TEM images, average = 3.93 nm.

A B

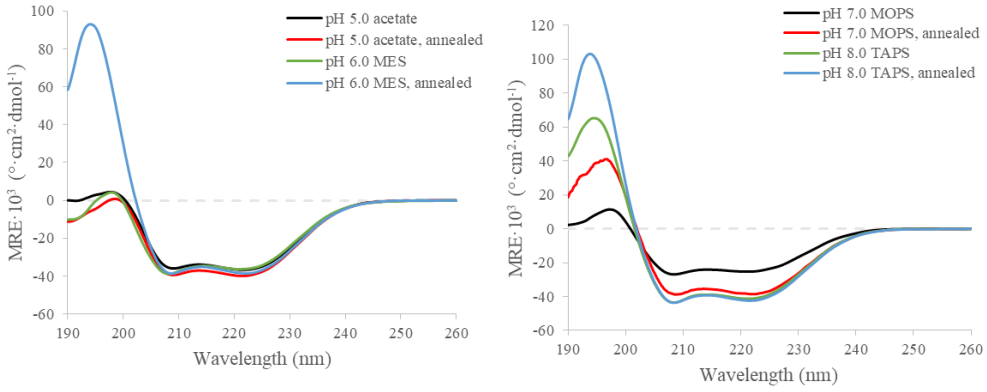

Figure 4.30. Circular dichroism spectra of 2.2 mg/mL ROX321eIle in A) 10 mM pH 5-6 buffer, B) 10 mM pH 7-8 buffer, all at room temperature and anneaeled at 90 ℃.

ROX321gIle assembled into thin ROX321-like fibrils in 10 mM pH 5 acetate when annealed at 90 ℃, and flexible ROX328-like fibrils in other conditions (Figure 4.31). The ROX321-like fibrils have an averaged width of 3.21 nm ± 0.46 nm (Figure 4.32), comparable to ROX321's

3.86 nm. All ROX321gIle fibril samples also display α-helical CD signatures with minima at 208 nm and 222 nm (Figure 4.33).

A B

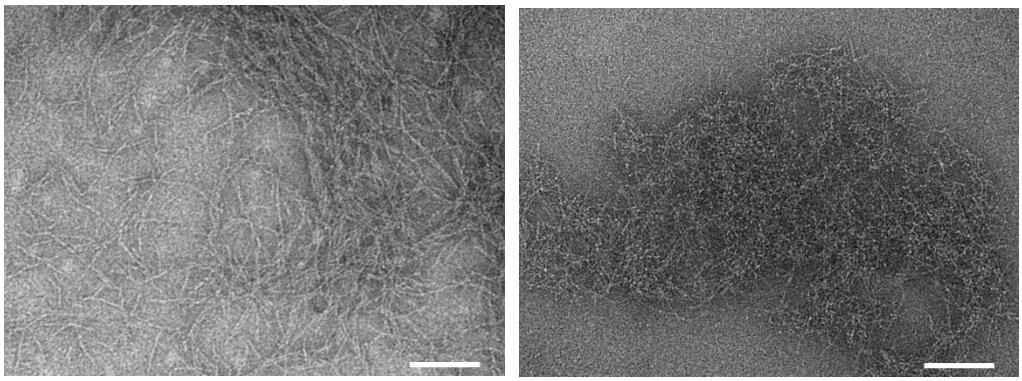

Figure 4.31. TEM images of 2.5 mg/mL ROX321gIle in A) 10 mM pH 5 acetate buffer, annealed at 90 ℃; B) 10 mM pH 7.2 MOPS buffer, 1 day assembly time. Scale bar = 100 nm.

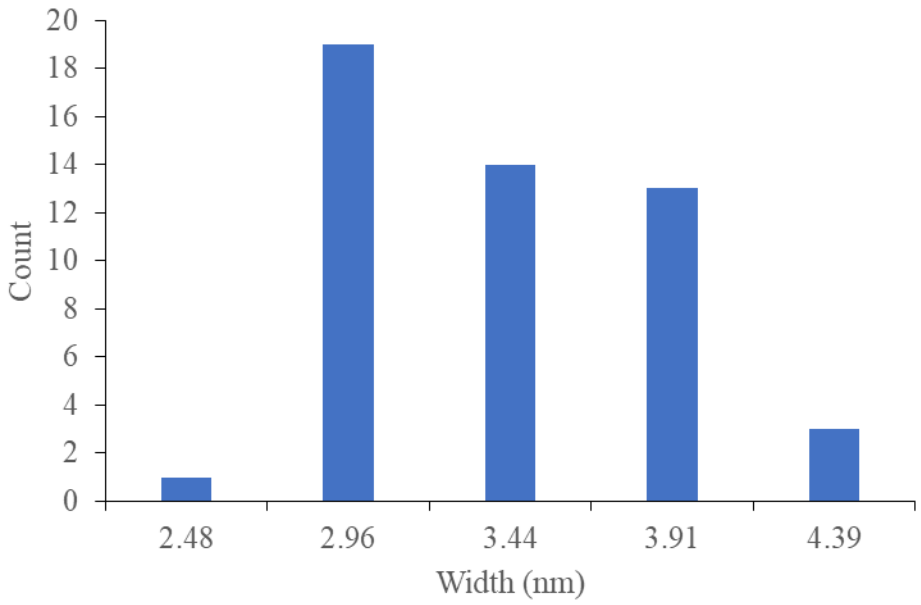

Figure 4.32. Histogram of ROX321gIle fibril width measured from TEM images, average = 3.21 nm.

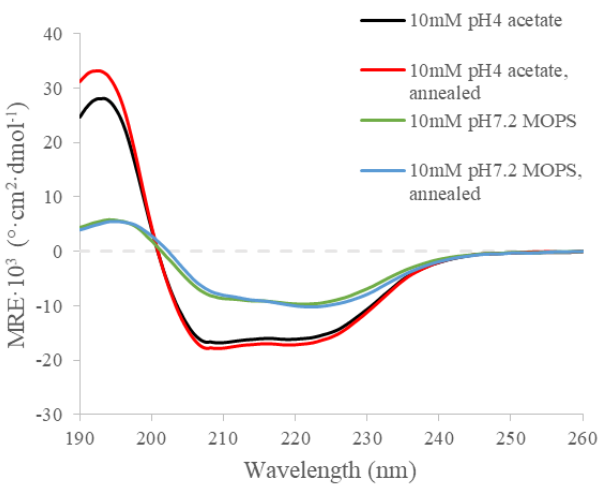

Figure 4.33 Circular dichroism spectra of 2.5 mg/mL ROX321gIle in 10 mM pH 4 and pH 7.2 buffer, all at room temperature and anneaeled at 90 ℃.

These preliminary results showed unpredicted results where a Leu2Ile mutation is differentiated on ROX321's *e, g* face. SAXS experiments will be conducted with these samples to investigate whether these samples pose ROX321's signature cross-α stacking distance diffraction peak. Such interface differentiation causing drastic self-assembly differences was reported for a cross-β system due to computationally simulated favored interface interactions[36], thus computational modeling of these interface differences using scoring functions such as ISAMBARD[37] or BUDE empirical free-energy forcefield[38] may help explain this phenomenon.

4.3 Conclusion

In summary, a generic *de novo* designed amphipathic coiled-coil peptide ROX321 is shown to self-assemble into a cross-α amyloid-like fibril structure. ROX321's cross-α structure is characterized via cryo-EM, the helix-helix stacking distance is observed in SAXS, and ROX321's mating dimer has both parallel and anti-parallel orientations revealed via ssNMR.

ROX321's design strategy was, although unexpected, successful at forming a very tight coiled-coil dimer with Ala at ROX321's *a* and *d* faces, providing a rather novel coiled-coil example because Ala is typically avoided in these positions in coiled-coil design due to its destabilizing nature[39]. ROX321's design can be classified to a type 2 coiled coil, but instead of an α-barrel type of assembly where 2 intra-helical interfaces are identified by the *e, a* faces and the *d, g* faces, 3 sets of intra-helical interfaces are present where the hydrophobic *a, d* faces still form a type-N coiled-coil dimer bundle, and the hydrophobic *e, g* faces afford helix stacking to achieve fibril elongation. A similarly unexpected discovery is also found in a type 3 coiled-coil structure exploration study[40], where an α-barrel was also expected but a degree of helix stacking was also observed instead, suggesting cross-α structures may be not limited to the type 2 coiled-coil structures and more common than the limited amount of examples explored so far. This potentially will enable new design strategies and methods to control fibril assemblies.

Lastly, some preliminary data exploring the designability of ROX321, including varying ROX321's peptide length and mutating Leucines on ROX321's *e* and *g* faces have suggested this system is very susceptible to sequence changes, but ROX321's cross-α structure may be retained in some redesigns, such as in ROX321eIle, giving hope ROX321's cross-α system has designability and can be functionalized. SAXS experiments are already being conducted for ROX321 mutants to determine whether their cross-α structure is retained. Encouraged by the data showing ROX321's

cross-α structure can be designed to some extent, a more thorough and systematic screening of other residues at ROX321's *a, d, e, g* positions will fully characterize the key factors leading to its cross-α structure self-assembly.

4.4 Methods

Materials and Reagents. All chemical reagents were purchased from Sigma-Aldrich, unless otherwise specified. All Fmoc protected amino acids were purchased from Aapptec; all other chemical reagents were purchased from Sigma-Aldrich, unless otherwise specified. Peptide synthesis resin was ordered from Applied Biosystems (Foster City, CA).

Peptide Synthesis. The ROX321, ROX314, ROX328, ROX321eILE, ROX321gILE, ROX321-NMR (A3, L20, K7, E14 isotope labelled) peptides were prepared via a microwave assisted solid phase peptide synthesis, on a CEM Liberty Blue instrument as the *N*-acetyl, *C*-amide capped derivatives. Applied Biosystem's Fmoc-PAL-PEG-PS resin was used for synthesizing these peptides at a 0.1 mmol scale. Coupling reactions were conducted with 0.2 M N-fluorenylmethyloxycarbonyl (Fmoc)-protected amino acids in N,N-Dimethylformamide (DMF, activated with 0.5 M N,N'-Diisopropylcarbodiimide (DIC) in DMF and 0.5 M Ethyl cyanohydroxyiminoacetate (oxyma) in DMF. The coupled amino acid was deprotected using 20% piperidine in DMF. All amino acids were deprotected with 5 ml piperidine solution, 75 ℃ temperature and 155 W microwave power for 15 seconds as the first stage, and 75 ℃ temperature and 155 W microwave power for 15 seconds as the second stage; coupled with 2.5 ml DIC solution, 75 ℃ temperature and 170 W microwave power for 15 seconds as the first stage, and with 2.5 ml oxyma solution, 90 ℃ temperature and 30 W microwave power for 110 seconds as the second stage. C-terminal amide modification was done after all amino acids were coupled, with 2.5 ml 20% acidic anhydride in DMF, 75 ℃ temperature and 155 W microwave power for 15 seconds as the first stage, and 75 ℃ temperature and 155 W microwave power for 15 seconds as the second stage. Peptides were cleaved from the resin by incubation at room temperature for 3 hours in a 20 ml cocktail consisting of 92.5% trifluoroacetic acid (TFA), 2.5% distilled water, 2.5% triisopropylsilane, and 2.5% 2,2'- (ethylenedioxy)-diethanethiol. The cleaved peptide solution was

filtered and precipitated with 60 ml of 4 ℃ diethyl ether. The peptide/diethyl ether mixture was then centrifuged at 4 ℃ at 4,000 rpm for 10 min. The supernatant was then discarded, and the precipitate allowed to desiccate overnight. Following desiccation, the crude peptide gels were resolubilized in 3 mL of a 50:50 mixture of acetonitrile and water (0.1% TFA additive) and purified by reversed-phase high-pressure liquid chromatography (HPLC) using two Shimadzu LC-20AP pumps running at 60 ml/min, a Shimadzu SPD-20A UV detector monitoring at 220 nm, on a Kinetex 5 μm C18 column, 250 mm long * 30 mm wide with a water-acetonitrile (0.1% TFA-additive) gradient. For ROX321, ROX321-NMR, ROX321eIle and ROX321gIle, the gradient used was 30% acetonitrile at 0 min, then gradually increased to 85% acetonitrile at 55 min, and finally was held at 90% acetonitrile for 10 min; all peptides eluted at ~20 min. For ROX314, the gradient used was 25% acetonitrile at 0 min, then gradually increased to 80% acetonitrile at 55 min, and finally was held at 90% acetonitrile for 10 min; ROX314 eluted at ~15 min. For ROX328, the gradient used was 15% acetonitrile at 0 min, then gradually increased to 70% acetonitrile at 55 min, and finally was held at 90% acetonitrile for 10 min; ROX314 eluted at ~40 min.Peptide masses were confirmed using MALDI-TOF mass spectrometry on an Applied Biosystems AB4700 Proteomics analyzer in reflectron positive ion mode, with α-Cyano-4-hydroxycinnamic acid as the matrix. Purified HPLC fractions were then lyophilized, sealed, and stored at -30 ℃.

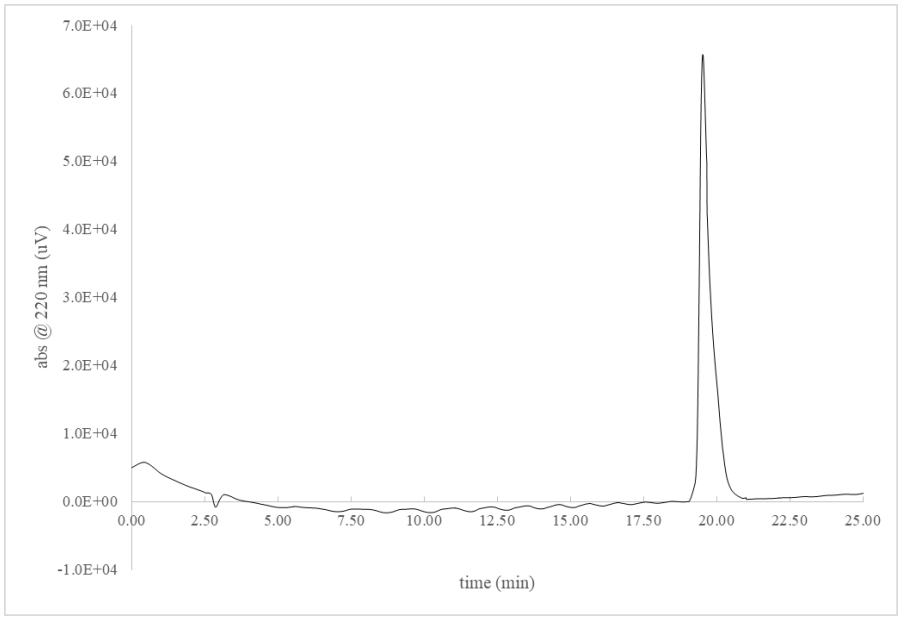

Figure 4.34. Analytical HPLC trace of ROX321.

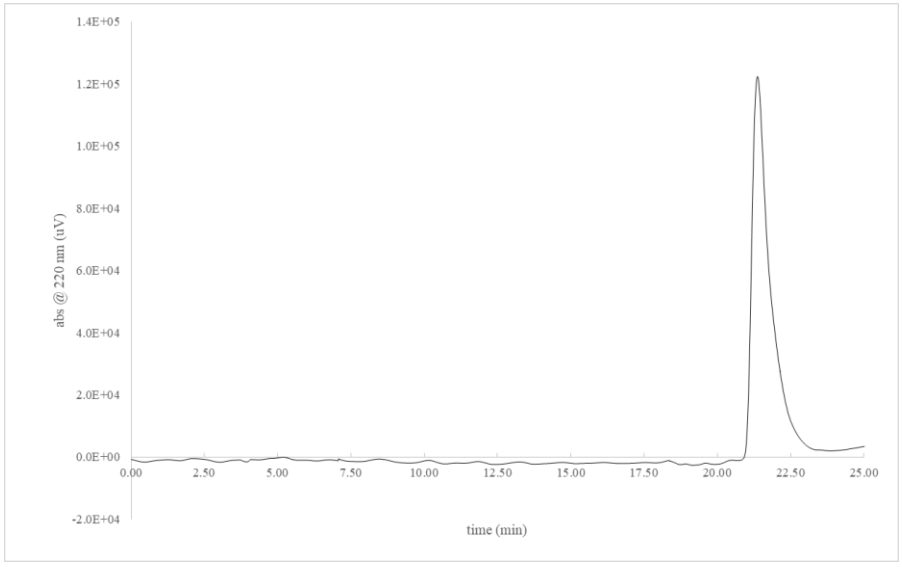

Figure 4.35. Analytical HPLC trace of ROX321gILE.

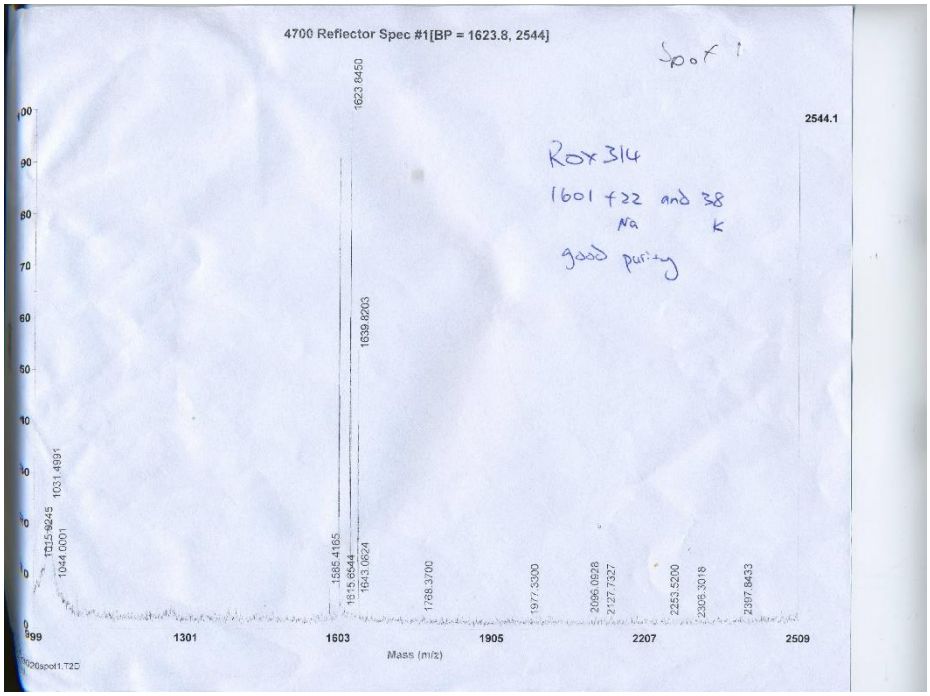

Figure 4.36. MALDI-TOF MS spectrum of ROX314. Expected mass = 1601 g/mol.

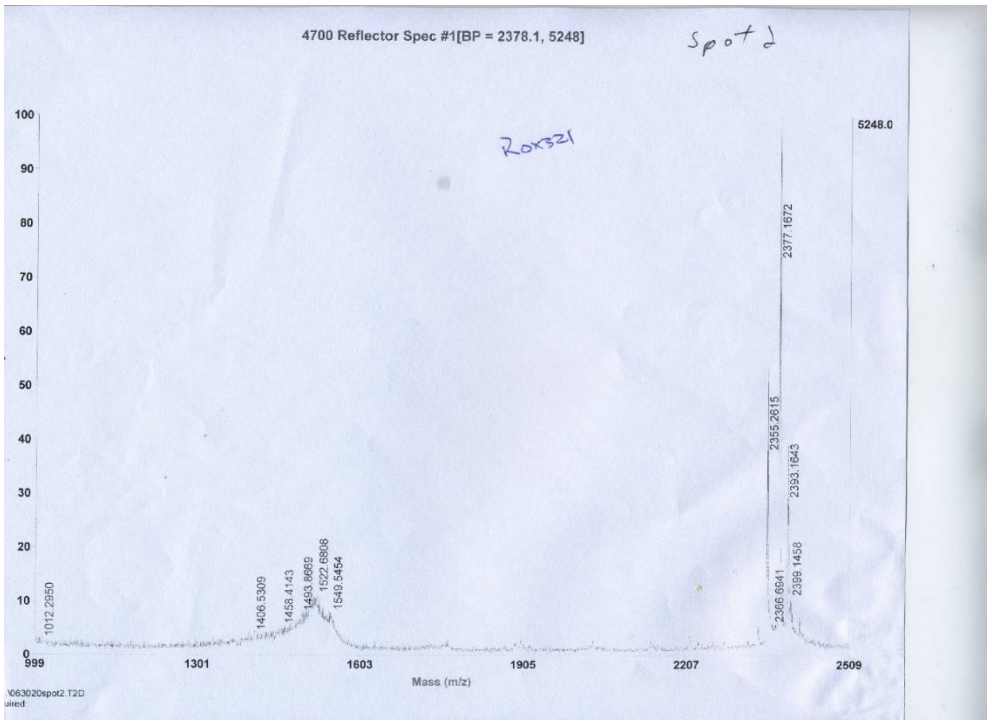

Figure 4.37. MALDI-TOF MS spectrum of ROX321. Expected mass = 2355 g/mol.

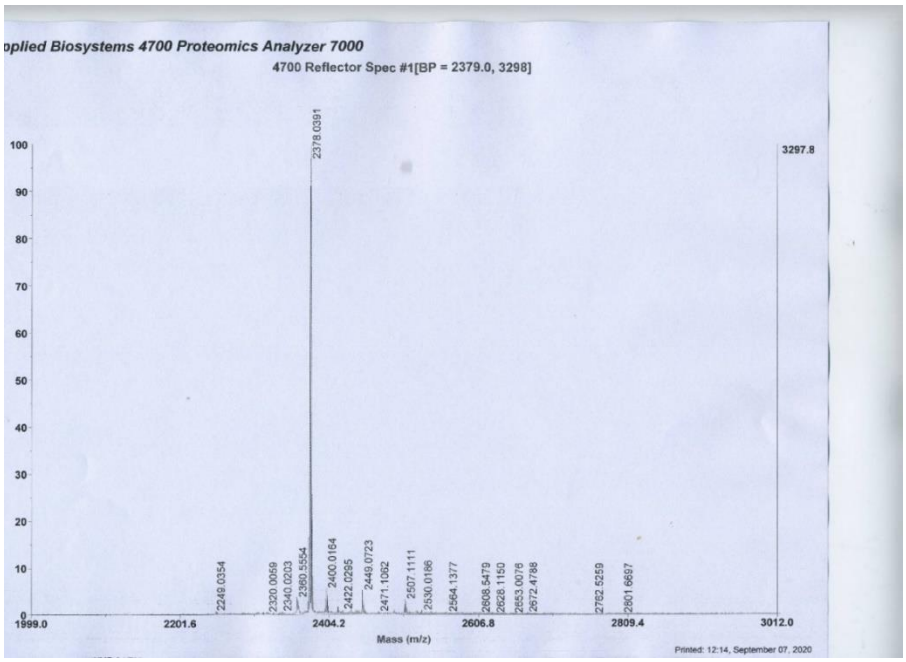

Figure 4.38. MALDI-TOF MS spectrum of ROX321-NMR. Expected mass = 2355 g/mol.

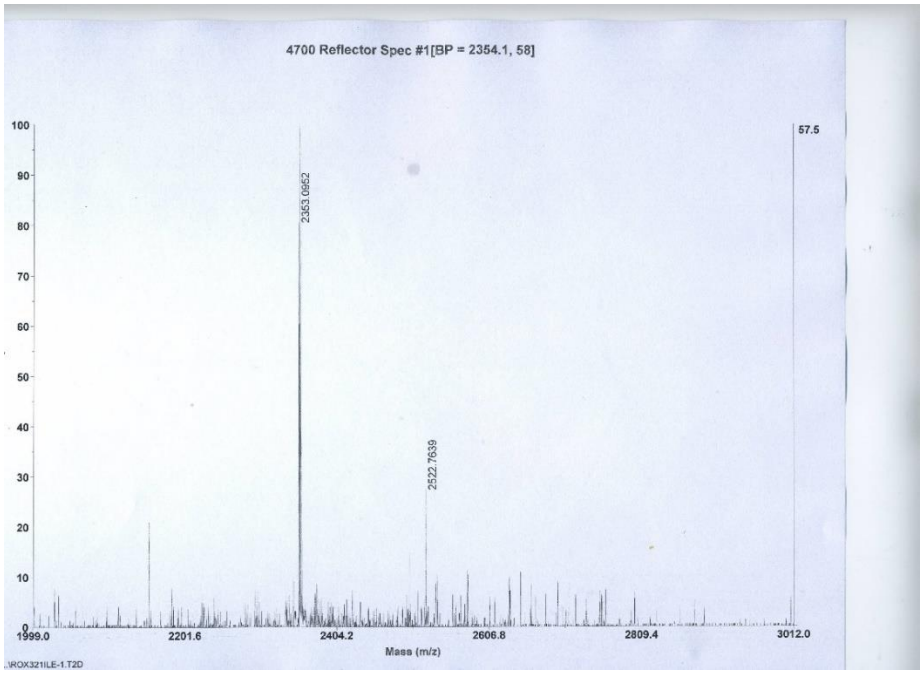

Figure 4.39. MALDI-TOF MS spectrum of ROX321gIle. Expected mass = 2355 g/mol.

Peptide Assembly. Stock solutions of ROX321, ROX314, ROX328, ROX321eILE, ROX321gILE were prepared by solubilizing 0.4 mg of purified, lyophilized peptide in 200 μL of 10 mM acetate, pH 4.0; 10 mM acetate, pH 5.0; 10 mM MES, pH 6.0; 10 mM MOPS, pH 7.0; 10 mM TAPS, pH 8.0 buffer, the final peptide concentrations were ~840 μM. Immediately after mixture, the solutions were titrated to the respective buffer pH using 100 mM sodium hydroxide solution. The samples were incubated at ~20 ℃ on the benchtop. For some samples, solutions were thermally annealed using the following thermal cycler protocol: (1) rapid heating to 50/70/90 ℃ for 30 minutes; and (2) cooling to 25 ℃ at a rate of 0.2 ℃ / minute.

Circular Dichroism Spectropolarimetry. CD measurements were performed on a Jasco J-1500 CD spectropolarimeter in 0.1 mm quartz cells (Hellma Analytics), at various μM peptide concentration where the final HT voltage reading at 190 nm was less than 500 V in all measurements. Spectra were recorded from 260 to 190 nm, at a scanning rate of 100 nm/min and a data pitch of 0.2 nm, with 3 accumulations.

Transmission Electron Microscopy. TEM specimens were prepared from aqueous solutions of PSMβ2: 4 μL of the PSMβ2 samples were deposited onto 200 mesh carbon-coated copper grids from Electron Microscopy Services (Hatfield, PA). After 90 seconds of incubation period, the samples were wicked away until a thin film of sample remained, then the grids were stained with 4 μL of 1:1 mix of nano-W and nanoVan stains from Nanoprobes (Yaphank, NY). After 60 seconds of stain incubation period, all liquids were wicked away, and the grids were dried in a tabletop desiccator under vacuum. TEM measurements were acquired on a Hitachi HT-7700 transmission electron microscope with a tungsten filament and AMT CCD camera, at an accelerating voltage of 80 kV.

Cryo-electron Microscopy and Image Processing. The ROX321 was applied to glow-discharged lacey carbon grids and vitrified in a Vitrobot Mark IV (FEI, Inc.). Grids were imaged in a Titan Krios at 300 keV and recorded with a Falcon II direct electron detector at 1.05 Å per pixel. Images

were collected using a defocus range of 0.5–3.0 μm, with a total exposure of 2 s (amounting to 70 electrons ·Å-2) dose-fractionated into seven chunks. All the images were first motion corrected by the MotionCorr v2 (1), and then the CTFFIND3 (2) program was used for determining the actual defocus of the images. Images with poor CTF estimation as well as defocus > 3 μm were discarded. A total of 386 images were selected and peptide filaments of varying lengths were boxed using the e2helixboxer program within EMAN2 (3). The CTF was corrected by multiplying the images from the first two chunks (containing a dose of ~ 20 electrons ·Å -2) with the theoretical CTF. Overlapping 256-px long boxes with a shift of 5 pixels (~ 1.5 times of the axial rise) were cut from the long filaments. The determination of the helical symmetry was by trial and error, searching for a symmetry which yielded recognizable secondary structure. Power spectra from the filaments suggested a variability in the helical parameters. A reference-based sorting procedure was used to bin the segments based on the axial rise and azimuthal rotation. Then 56,421 out of 356,100 segments were selected after this sorting and the IHRSR (4) method implemented in in Spider (5) was used to produce the final reconstructions at ~6 Å. The helical hand was determined by the fit of crystal structures into the cryo-EM map.

Scanning Transmission Electron Microscopy. STEM data were acquired at Brookhaven National Laboratory (BNL). The STEM instrument operates at 40 keV with a scanning probe of 0.3 nm diameter produced from a cold field-emission source. Each electron emerging from the specimen is detected by one of the scintillator photomultiplier detectors collecting 0−15 mRadian (bright field), 15−40 mRadian (small-angle dark field) and 40−200 mRadian (large-angle dark field). The large-angle signal is proportional to the mass of atoms in the path of the beam. Specimen quality and mass calibration were assessed by detailed comparison of the image to the known structure of tobacco mosaic virus (TMV). For mass-per-length (M/L) measurements, TMV rafts at a theoretical M/L value of 13.1 kDa/Å were employed for calibration.

ROX321 specimens were deposited on thin carbon (circa 2 nm thick) supported on a thicker holey carbon film mounted on a titanium grid using the wet-film, hanging-drop method. TMV was added to the grid first as an internal control, followed by injection buffer, then specimen solution (in 10 mM MES buffer, pH 6.0) for 1 min, then 10 washes of 20 mM ammonium acetate pH 7.0. Excess solution was wicked from the edge with filter paper between each injection. After the last wash, the grid was wicked to a thin layer (ca. 1 mm), fast frozen by plunging into liquid nitrogen slush and stored under liquid nitrogen. Grids were freeze-dried overnight in an ion pumped chamber with an efficient cold trap and transferred under vacuum to the STEM cold stage (−160 °C). Imaging typically uses a dose of 20 e–/Å2 (causing < 5% mass loss, corrected by comparison to TMV). Mass per length measurements of the PSMβ2 nanotubes were performed with the software PCMass32.

Small- and Wide-Angle X-Ray Scattering Measurements. Synchrotron SAXS/WAXS measurements were taken at the 12-ID-B beamline of the Advanced Photon Source at Argonne National Laboratory in Lemont, Illinois. ROX321 sample was dialyzed into 10 mM pH 4 acetate, with a 1% glycerol additive to stabilize against X-ray radiation damage. SAXS/WAXS measurements were then taken on the peptide solutions at 25 ℃ in a quartz capillary flow cell (1.5 mm). The solutions were raised and lowered in the flow cell to minimize radiation damage. Twenty 2D images were collected per sample, and then azimuthally averaged into 1D SAXS scattering curves after solid angle correction and normalization against the transmitted X-ray beam intensity, using the software package at beamline 12-ID-B. The 1D scattering curves were then averaged, and the averaged signal from the MES buffer was subtracted out.

References

1. Chiti, F.; Dobson, C. M., Protein Misfolding, Amyloid Formation, and Human Disease: A Summary of Progress Over the Last Decade. *Annual Review of Biochemistry* **2017,** *86* (1), 27-68.
2. Murphy, M. P.; LeVine, H., 3rd, Alzheimer's disease and the amyloid-beta peptide. *J Alzheimers Dis* **2010,** *19* (1), 311-323.
3. Marshall, K. E.; Marchante, R.; Xue, W.-F.; Serpell, L. C., The relationship between amyloid structure and cytotoxicity. *Prion* **2014,** *8* (2), 192-196.
4. López de la Paz, M.; Goldie, K.; Zurdo, J.; Lacroix, E.; Dobson, C. M.; Hoenger, A.; Serrano, L., *De novo* designed peptide-based amyloid fibrils. *Proceedings of the National Academy of Sciences* **2002,** *99* (25), 16052.
5. Kammerer, R. A.; Kostrewa, D.; Zurdo, J.; Detken, A.; García-Echeverría, C.; Green, J. D.; Müller, S. A.; Meier, B. H.; Winkler, F. K.; Dobson, C. M.; Steinmetz, M. O., Exploring amyloid formation by a *de novo* design. *Proceedings of the National Academy of Sciences of the United States of America* **2004,** *101* (13), 4435.
6. Gebbink, M. F.; Claessen, D.; Bouma, B.; Dijkhuizen, L.; Wösten, H. A., Amyloids--a functional coat for microorganisms. *Nat Rev Microbiol* **2005,** *3* (4), 333-41.
7. Plissonneau, M.; Pansieri, J.; Heinrich-Balard, L.; Morfin, J.-F.; Stransky-Heilkron, N.; Rivory, P.; Mowat, P.; Dumoulin, M.; Cohen, R.; Allémann, É.; Tóth, É.; Saraiva, M. J.; Louis, C.; Tillement, O.; Forge, V.; Lux, F.; Marquette, C., Gd-nanoparticles functionalization with specific peptides for ß-amyloid plaques targeting. *J Nanobiotechnology* **2016,** *14* (1), 60-60.
8. Ladiwala, A. R. A.; Bhattacharya, M.; Perchiacca, J. M.; Cao, P.; Raleigh, D. P.; Abedini, A.; Schmidt, A. M.; Varkey, J.; Langen, R.; Tessier, P. M., Rational design of potent domain antibody inhibitors of amyloid fibril assembly. *Proceedings of the National Academy of Sciences* **2012,** *109* (49), 19965.
9. Jansens, K. J. A.; Rombouts, I.; Grootaert, C.; Brijs, K.; Van Camp, J.; Van der Meeren, P.; Rousseau, F.; Schymkowitz, J.; Delcour, J. A., Rational Design of Amyloid-Like Fibrillary Structures for Tailoring Food Protein Techno-Functionality and Their Potential Health Implications. *Compr Rev Food Sci F* **2019,** *18* (1), 84-105.
10. Baldwin, A. J.; Bader, R.; Christodoulou, J.; MacPhee, C. E.; Dobson, C. M.; Barker, P. D., Cytochrome Display on Amyloid Fibrils. *J Am Chem Soc* **2006,** *128* (7), 2162-2163.
11. Díaz-Caballero, M.; Navarro, S.; Fuentes, I.; Teixidor, F.; Ventura, S., Minimalist Prion-Inspired Polar Self-Assembling Peptides. *Acs Nano* **2018,** *12* (6), 5394-5407.
12. Maji, S. K.; Schubert, D.; Rivier, C.; Lee, S.; Rivier, J. E.; Riek, R., Amyloid as a depot for the formulation of long-acting drugs. *PLoS Biol* **2008,** *6* (2), e17-e17.
13. Close, W.; Neumann, M.; Schmidt, A.; Hora, M.; Annamalai, K.; Schmidt, M.; Reif, B.; Schmidt, V.; Grigorieff, N.; Fändrich, M., Physical basis of amyloid fibril polymorphism. *Nat Commun* **2018,** *9* (1), 699.
14. Sabate, R., When amyloids become prions. *Prion* **2014,** *8* (3), 233-239.
15. Zheng, Y.; Joo, H. S.; Nair, V.; Le, K. Y.; Otto, M., Do amyloid structures formed by Staphylococcus aureus phenol-soluble modulins have a biological function? *Int J Med Microbiol* **2018,** *308* (6), 675-682.
16. Tayeb-Fligelman, E.; Salinas, N.; Tabachnikov, O.; Landau, M., Staphylococcus aureus PSMalpha3 Cross-alpha Fibril Polymorphism and Determinants of Cytotoxicity. *Structure* **2020,** *28* (3), 301-313 e6.
17. Zhang, S.-Q.; Huang, H.; Yang, J.; Kratochvil, H. T.; Lolicato, M.; Liu, Y.; Shu, X.; Liu, L.; DeGrado, W. F., Designed peptides that assemble into cross-α amyloid-like structures. *Nature Chemical Biology* **2018,** *14* (9), 870-875.

18. Rhys, G. G.; Wood, C. W.; Lang, E. J. M.; Mulholland, A. J.; Brady, R. L.; Thomson, A. R.; Woolfson, D. N., Maintaining and breaking symmetry in homomeric coiled-coil assemblies. *Nature Communications* **2018,** *9* (1), 4132.
19. Fletcher, J. M.; Boyle, A. L.; Bruning, M.; Bartlett, G. J.; Vincent, T. L.; Zaccai, N. R.; Armstrong, C. T.; Bromley, E. H.; Booth, P. J.; Brady, R. L.; Thomson, A. R.; Woolfson, D. N., A basis set of de novo coiled-coil peptide oligomers for rational protein design and synthetic biology. *ACS Synth Biol* **2012,** *1* (6), 240-50.
20. Fairman, R.; Chao, H. G.; Lavoie, T. B.; Villafranca, J. J.; Matsueda, G. R.; Novotny, J., Design of heterotetrameric coiled coils: evidence for increased stabilization by Glu(-)-Lys(+) ion pair interactions. *Biochemistry-Us* **1996,** *35* (9), 2824-2829.
21. Lyu, P. C.; Sherman, J. C.; Chen, A.; Kallenbach, N. R., Alpha-helix stabilization by natural and unnatural amino acids with alkyl side chains. *Proceedings of the National Academy of Sciences of the United States of America* **1991,** *88* (12), 5317-5320.
22. Hellmund, K. S.; Lospichl, B. v.; Böttcher, C.; Ludwig, K.; Keiderling, U.; Noirez, L.; Weiß, A.; Mikolajczak, D. J.; Gradzielski, M.; Koksch, B., Functionalized peptide hydrogels as tunable extracellular matrix mimics for biological applications. 2020.
23. Barczewski, A. H.; Ragusa, M. J.; Mierke, D. F.; Pellegrini, M., The IKK-binding domain of NEMO is an irregular coiled coil with a dynamic binding interface. *Scientific Reports* **2019,** *9* (1), 2950.
24. Thomson, A. R.; Wood, C. W.; Burton, A. J.; Bartlett, G. J.; Sessions, R. B.; Brady, R. L.; Woolfson, D. N., Computational design of water-soluble α-helical barrels. *Science* **2014,** *346* (6208), 485-488.
25. Parry, D. A. D.; Squire, J. M., Fibrous Proteins: Structures and Mechanisms. In *Subcellular Biochemistry*, [Online] 1st ed.; Springer International Publishing : Imprint: Springer,: Cham, 2017; pp. 1 online resource (VIII, 629 pages 154 illustrations, 123 illustrations in color.
26. Sheridan, R. P.; Levy, R. M.; Salemme, F. R., alpha-Helix dipole model and electrostatic stabilization of 4-alpha-helical proteins. *Proceedings of the National Academy of Sciences of the United States of America* **1982,** *79* (15), 4545-4549.
27. Stoscheck, C. M., [6] Quantitation of protein. In *Methods Enzymol*, Deutscher, M. P., Ed. Academic Press: 1990; Vol. 182, pp 50-68.
28. Collie, G. W.; Pulka-Ziach, K.; Lombardo, C. M.; Fremaux, J.; Rosu, F.; Decossas, M.; Mauran, L.; Lambert, O.; Gabelica, V.; Mackereth, C. D.; Guichard, G., Shaping quaternary assemblies of water-soluble non-peptide helical foldamers by sequence manipulation. *Nature Chemistry* **2015,** *7* (11), 871-878.
29. Howard, K. P.; Liu, W.; Crocker, E.; Nanda, V.; Lear, J.; Degrado, W. F.; Smith, S. O., Rotational orientation of monomers within a designed homo-oligomer transmembrane helical bundle. *Protein science : a publication of the Protein Society* **2005,** *14* (4), 1019-1024.
30. Truebestein, L.; Leonard, T. A., Coiled-coils: The long and short of it. *Bioessays* **2016,** *38* (9), 903-916.
31. Surkont, J.; Diekmann, Y.; Ryder, P. V.; Pereira-Leal, J. B., Coiled-coil length: Size does matter. *Proteins* **2015,** *83* (12), 2162-9.
32. Testa, O. D.; Moutevelis, E.; Woolfson, D. N., CC+: a relational database of coiled-coil structures. *Nucleic Acids Research* **2008,** *37* (suppl_1), D315-D322.
33. Su, J. Y.; Hodges, R. S.; Kay, C. M., Effect of Chain Length on the Formation and Stability of Synthetic .alpha.-Helical Coiled Coils. *Biochemistry-Us* **1994,** *33* (51), 15501-15510.
34. Zhu, B. Y.; Zhou, N. E.; Kay, C. M.; Hodges, R. S., Packing and hydrophobicity effects on protein folding and stability: effects of beta-branched amino acids, valine and isoleucine, on the formation and stability of two-stranded alpha-helical coiled coils/leucine zippers. *Protein Sci* **1993,** *2* (3), 383-94.
35. Magnotti, E. L.; Hughes, S. A.; Dillard, R. S.; Wang, S. Y.; Hough, L.; Karumbamkandathil, A.; Lian, T. Q.; Wall, J. S.; Zuo, X. B.; Wright, E. R.; Conticello, V. P.,

Self-Assembly of an alpha-Helical Peptide into a Crystalline Two-Dimensional Nanoporous Framework. *J Am Chem Soc* **2016,** *138* (50), 16274-16282.
36. Dai, B.; Li, D.; Xi, W.; Luo, F.; Zhang, X.; Zou, M.; Cao, M.; Hu, J.; Wang, W.; Wei, G.; Zhang, Y.; Liu, C., Tunable assembly of amyloid-forming peptides into nanosheets as a retrovirus carrier. *Proceedings of the National Academy of Sciences* **2015,** *112* (10), 2996.
37. Wood, C. W.; Heal, J. W.; Thomson, A. R.; Bartlett, G. J.; Ibarra, A. Á.; Brady, R. L.; Sessions, R. B.; Woolfson, D. N., ISAMBARD: an open-source computational environment for biomolecular analysis, modelling and design. *Bioinformatics* **2017,** *33* (19), 3043-3050.
38. McIntosh-Smith, S.; Price, J.; Sessions, R. B.; Ibarra, A. A., High performance in silico virtual drug screening on many-core processors. *Int J High Perform Comput Appl* **2015,** *29* (2), 119-134.
39. Kwok, S. C.; Hodges, R. S., Stabilizing and Destabilizing Clusters in the Hydrophobic Core of Long Two-stranded α-Helical Coiled-coils. *Journal of Biological Chemistry* **2004,** *279* (20), 21576-21588.
40. Egelman, E. H.; Xu, C.; DiMaio, F.; Magnotti, E.; Modlin, C.; Yu, X.; Wright, E.; Baker, D.; Conticello, V. P., Structural plasticity of helical nanotubes based on coiled-coil assemblies. *Structure* **2015,** *23* (2), 280-9.

Chapter 5: Designed 2D Assemblies via Engineering Inter-coiled-coil Bundle Interfaces

5.1 Introduction

Peptide-based 2D nanomaterials can be designed as monomers propagating via designed interfaces, such as: metal ion chelation through a cyclic moiety such as imidazole or pyridine[1]; disulfide linkage via oxidated cysteines[2]; local electrostatic innteractions[3], geometrically frustrated local electrostatic interactions[4] and hydrophobic interactions[5-6]; computational de novo design creating a minimum energy configuration with a target space group symmetry[6, 7-8]; equivalent binding energies of the mating of both sides of β-strand[9], or simply phenylalaines[10]. Peptide monomers can be either parallel or perpendicular to the nanosheet plane. For example, the PSM cross-α structures characterized in earlier chapters theoretically could assemble into 2D assemblies as PSM peptides stack to form fibrils and then laterally associate to form laminated nanosheets, where PSM helices are parallel to the nanosheet plane. Collagen mimetic NSI and NSII[3], β-strand KLVFFAK[9], designed α-helical proteins crystal P6-a and P6-d[8], and α-helical crystalline network 3FD[11] are examples where peptide monomers are perpendicular to the nanosheet plane. Lastly computationally designed α-helical oligomers such as P3Z_42, P6_9H, P4Z_9 were shown to adopt P 3 2 1, P 6 and P 6 space group symmetries while forming 2D crystalline arrays, where manual rational design would be difficult.

While computational 2D protein crystal design resulted in several crystal structures with various point group symmetries and high predicted atomic-level accuracy, these peptides often do not assemble into their targeted lattices. Since many deposited protein crystallography structures contain point group symmetry information, and such point group symmetries can be used to computationally design protein crystals, perhaps the deposited structures with desired point group

symmetries can be used as design templates for crystalline 2D protein assemblies. For example, there are 23 results for space group P 3 2 1, 1 result for P 3, and 34 results for P 4 2_1 2 searching for PDB entries with < 6 kda molecular weight as of Nov 2nd, 2020 in the Protein Database Bank, where all symmetries have been computationally designed in forming protein crystals. This chapter will explore and screen the designability of 3TQ2, a coiled-coil protein crystal with P3 group symmetry, to form 2D crystalline peptide assemblies via rational redesigns.

5.2 Results and discussion

5.2.1 Designs of CC3V2, CC3V7 and CC3V8

A coiled-coil trimer bundle with P3 space group symmetry is used as the design template (PDB: 3TQ2) to be optimized for crystalline 2D peptide assembly. Using PDBePISA (Proteins, Interfaces, Structures and Assemblies)[12], one trimeric coiled-coil intra-bundle hydrophobic interface (surface area 7170 $Å^2$, buried area 4790 $Å^2$, free energy of assembly dissociation ΔG^{diss} = 28.9 kcal/mol, very positive and thermodynamically stable) and one trimeric coiled-coil inter-bundle (surface area 9950 $Å^2$, buried area 2010 $Å^2$, free energy of assembly dissociation ΔG^{diss} = 2.6 kcal/mol, only slightly positive and thermodynamically stable) interface are identified. The dimeric inter-bundle interface has an interface area of 271.0 $Å^2$ and a solvation free energy gain upon formation of the interface $\Delta^i G$ of -6.5 kcal/mol; in comparison, the dimeric intra-helical interface has an interface area of 733.7 $Å^2$ and a $\Delta^i G$ of -14.4 kcal/mol (Table 1). Low $\Delta^i G$ values suggest both interface interactions are strong; in addition, this dimeric inter-helical interface has a 0.863 complex formation significance score (CSS) in PDBePISA, which suggests this interface plays an essential role in complex formation. PDBePISA suggests Leu17, Met18, Phe21, Glu 14 are the key residues mediating this interface because they all contribute to more than 50 $Å^2$ buried areas. In this symmetry group, 3TQ2 coiled-coil bundles have a packed hexagonal honeycomb arrangement where one central bundle interacts with 6 other bundles (Figure 5.1). However, PDBePISA could only identify one dimeric intra-helical interface accounting for the interactions with 3 coiled-coil bundles, where the interactions between the center coiled-coil bundle with the other 3 coiled-coil bundles are not identified or not existent. This lack of inter-bundle interactions could contribute to 3TQ2 not able to self-assemble into 2D crystalline peptide assemblies.

Interface Summary XML

	Structure 1		Structure 2	
Selection range	A		A	
class	Protein		Protein	
symmetry operation	x,y,z		-y+1,x-y+1,z	
symmetry ID	1_555		2_665	
Number of atoms				
interface	55	19.9%	78	28.3%
surface	238	86.2%	238	86.2%
total	276	100.0%	276	100.0%
Number of residues				
interface	17	48.6%	19	54.3%
surface	35	100.0%	35	100.0%
total	35	100.0%	35	100.0%
Solvent-accessible area, Å				
interface	787.7	20.6%	679.6	17.8%
total	3815.8	100.0%	3815.8	100.0%
Solvation energy, kcal/mol				
isolated structure	-19.2	100.0%	-19.2	100.0%
gain on complex formation	-7.3	37.8%	-7.1	36.9%
average gain	-5.9	30.9%	-8.4	44.0%
P-value	0.280		0.564	

Interface Summary XML

	Structure 1		Structure 2	
Selection range	A		A	
class	Protein		Protein	
symmetry operation	x,y,z		-y,x-y+1,z	
symmetry ID	1_555		2_565	
Number of atoms				
interface	30	10.9%	23	8.3%
surface	238	86.2%	238	86.2%
total	276	100.0%	276	100.0%
Number of residues				
interface	9	25.7%	6	17.1%
surface	35	100.0%	35	100.0%
total	35	100.0%	35	100.0%
Solvent-accessible area, Å				
interface	263.3	6.9%	278.6	7.3%
total	3815.8	100.0%	3815.8	100.0%
Solvation energy, kcal/mol				
isolated structure	-19.2	100.0%	-19.2	100.0%
gain on complex formation	-3.1	16.0%	-3.4	17.7%
average gain	-3.2	16.9%	-2.5	13.0%
P-value	0.544		0.358	

Table 1. PISA interface summaries of 3TQ2's inter-bundle interface (left) and intra-bundle interface (right).

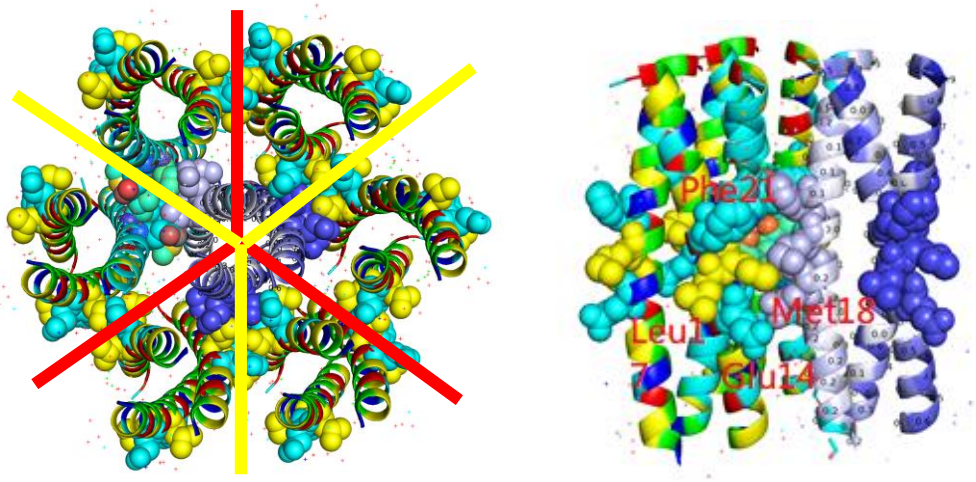

Figure 5.1. Top view and side-view of 3TQ2. Leu17, Met18, Phe 21, Glu 14 shown in spheres are the interface identified by PISA with total surface area = 9950 A^2, buried area = 2010 A^2, ΔG^{diss} = 2.6 kcal/mol. In P3 symmetry each coiled coil bundle interacts with 6 other bundles, however the PISA identified interface only connects 3 other bundles (shown in YELLOW lines going through residues shown in sphere), and the other 3 bundles are not stabilized by such interfaces (shown in RED lines).

To design 3TQ2 for 2D self-assembly, 3TQ2's base sequence is first further optimized by known coiled-coil design rules, where all residues at 3TQ2's *d* face are changed to Val for consistency; all residues at 3TQ2's *e, g* faces are changed to complimentary polar residues to further stabilize the coiled-coil trimeric bundle through polar interactions; and 3TQ2's *c, f, b* faces are the main design targets to implement extra stabilizing interfaces.

The interface optimization is designed as follows: the superhelix pitch of trimeric coiled-coil bundles (e.g. COIL-VALD, PDB: 1COI) is the spacing of 84 residues[13], or 12 heptads; in other words, each heptad contributes to 30 °of the superhelix twist. In order to create 2 sets, or a total of 6 stabilizing interfaces in 3TQ2's P3 symmetry arrangement (Figure 5.2), each interface must have a twist of 360 ° / 6 = 60 °, which corresponds nicely to 2 heptads in 3TQ2, a trimeric coiled-coil bundle. This means by designing two interfaces spaced 2 heptads apart, each helix will account for 2 * 60 °= 120 °of interfaces, and 3 helices will make up a full turn. Based on this principle, several peptides with the same 5 heptad length as 3TQ2 are proposed (Figure 5.3): CC3V2 aims to re-create 3TQ2's PISA identified interface consisting of Leu17, Met18, Phe 21, Glu 14 in both the upper (residue 7-14, Leu11, Met10, Phe14, Glu7; Leu11 and Met10 switched faces due to reversed symmetry as the top and bottom helical interactions are flipped) and lower (residue 21-28, Leu24, Met25, Phe28, Lys21) portions of 3TQ2; CC3V7 creates an anion binding interface targeting to bind chloride ions with Thr11 and Asn10, while moving 3TQ2's intra-helical interface to the lower portion of the sequence (Leu24, Met25, Phe28, Lys21); CC3V8 designs a polar interface with Asp11, Arg10, and Gln14, while also moving 3TQ2's intra-helical interface to the lower portion of the sequence. The other residues at 3TQ2's *c, b* faces are designated to be Ala to promote helicity; the other residues at 3TQ2's *f* face are designated to be Lys and Glu to promote water solubility and to maintain a near-neutral isoelectric point. All peptides are capped with Glu at the C-terminus and Glu at the N-terminus to prevent termini stacking via complimentary charges/hydrophobic interactions. The newly designed interface will strengthen the interactions between each coiled-coil

bundle with 6 other bundles surrounding it, resulting in 2D propagation and nanosheet self-assembly.

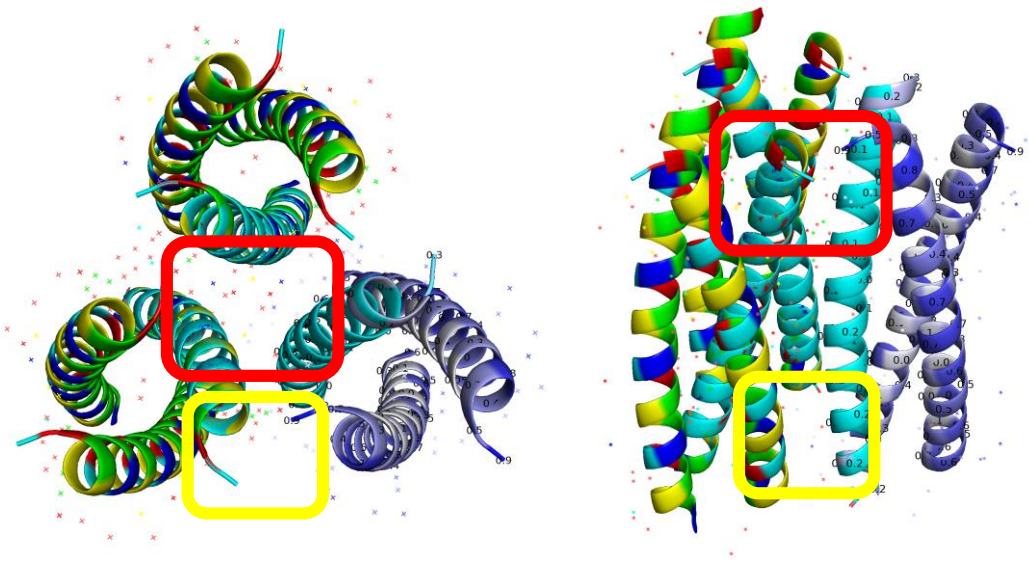

Figure 5.2. proposed designing 2 interfaces instead of 1 boxed in red and yellow.

	gabcdef gabcdef gabcdef gabcdef gabcdef
3TQ2:	Ac-KVSALKE KVSALKE QFLMLMF KVSALKE KVSALKE -NH_2
CC3V2:	Ac-EVEALKE KVMLLEF KVAALEK EVLMLKF KVAALEK G-NH_2
CC3V7:	Ac-EVEALKE KVNTLDI KVAALEK EVLMLKF KVAALEK G-NH_2
CC3V8:	Ac-EVEALKE KVRDLEQ KVAALEK EVLMLKF KVAALEK G-NH_2

A B C

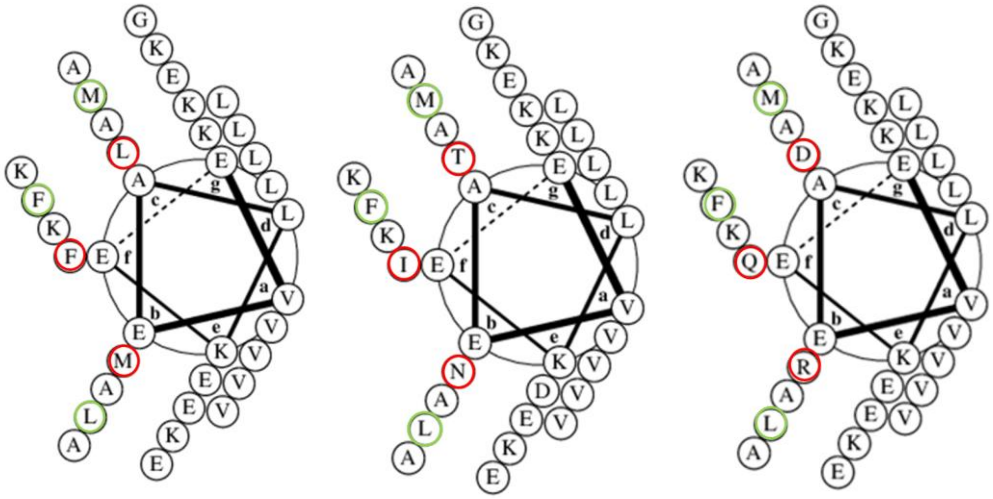

Figure 5.3. Heptad representations of A) CC3V2, B) CC3V7, and C) CC3V8. The interface designed in residue 1-14 is labeled in red; the interface designed in residue 14-28 is labeled in green.

5.2.2 Self-assembly of CC3V2, CC3V7 and CC3V8

CC3V2, CC3V7 and CC3V8 were synthesized via solid-phase peptide synthesis with N-terminal acetylation and C-terminal amidation to reduce termini charges. Peptide was purified by preparative HPLC, characterized by MALDI and its purity was confirmed by MALDI and analytical HPLC. All peptides were first screened in 10 mM buffers from pH 5.0 to pH 8.0 at an increment of pH 1.0, room temperature and annealed at 90 ℃, and 2.5-3.0 mg/mL peptide concentrations to assess their self-assembly behaviors.

CC3V2 spontaneously crystallized in all conditions screened. The crystal sizes are larger at near neutral pH in comparison to at pH 5, and showed no difference between samples incubated at room temperature and annealed. Small crystals can be observed via TEM, as well as some sheet-like assemblies (Figure 5.4); at > 5 days of assembly time, peptide crystals are large enough to have good quality diffraction signals collected by Dr. John Basca at Emory University. While in solution, all CC3V2 samples show α-helical CD signatures with minima at 208 nm and 223 nm, although the signals of the annealed at 90 ℃ samples are very low compared to the signals of the incubated at room temperature samples, due to crystallization in annealed samples happened faster leaving less peptides in solution (Figure 5.5).

A B

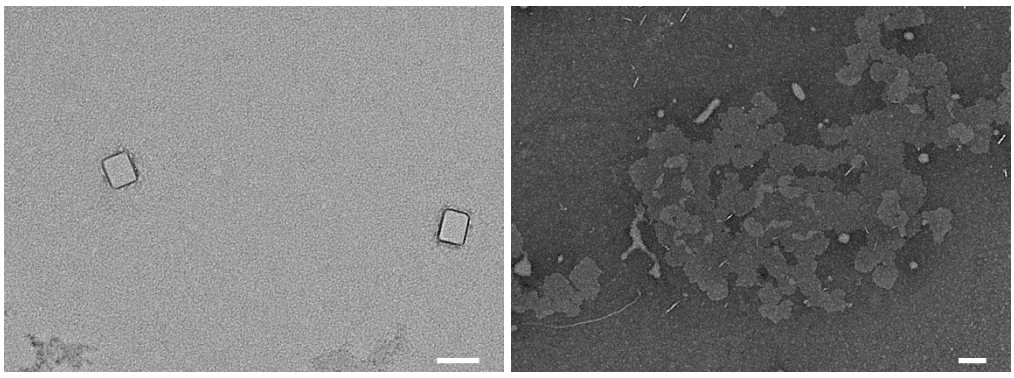

Figure 5.4. Representative TEM images of 632 μM CC3V2, after 3 days of assembly time, in A) 10 mM pH 5 acetate; B) 10 mM pH 8 TAPS. All scale bars = 100 nm.

A B

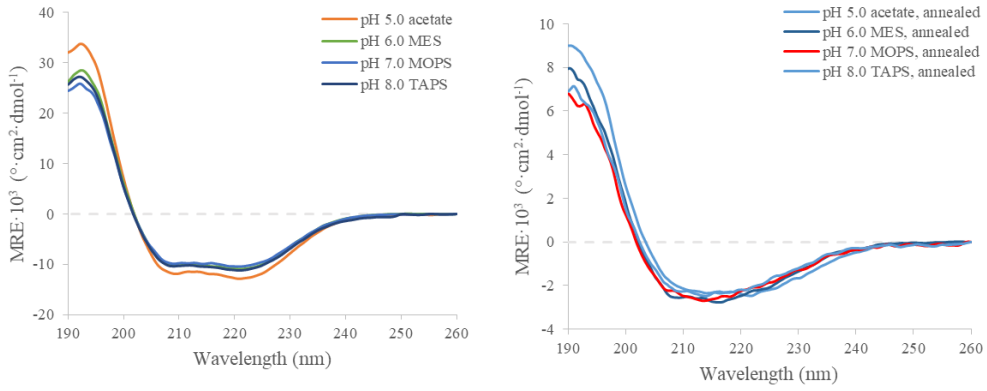

Figure 5.5: Circular dichroism spectra of of 632 μM CC3V2, in A) pH 5 – pH 8 buffer; B) pH 5 – pH 8 buffer, annealed at 90 ℃.

CC3V2's crystal structure suggests the designed interfaces are partially successful: CC3V2 monomers still assembled into a coiled-coil trimeric bundle; both designed faces are present, however, their mating is slipped that the top interface (Leu11, Met10, Phe14) and the bottom interface (Leu24, Met25, Phe28) mate each other, rather than top mates top and bottom mates bottom (Figure 5.6). CC3V2 did show single-layer sheet self-assemblies (Figure 5.4B), suggesting the correct, in-phase interface mating is possible, but perhaps not as favorable. PDBePISA identified only the trimeric coiled-coil inter-bundle hydrophobic interface (surface area 6840 Å^2, buried area 4090 Å^2, ΔG^{diss} = 25.9 kcal/mol) in its assemblies list, but the slipped intra-bundle interface can be identified in PDBePISA's interface list (interface area 222.9 Å^2, $\Delta^i G$ of -6.8 kcal/mol (Table 2), accounting for residues Phe14, Met10, Leu11 and Lys15 from one helix, and Phe28, Met25, Leu24 and Lys21 from the other helix, which are the designed interfaces of CC3V2. This interface is not detected in PDBePISA's assemblies list as it has a complexation significance score of 0 out of 1, i.e. no significance for assembly formation.

Interface Summary XML

	Structure 1		Structure 2	
Selection range	A		A	
class	Protein		Protein	
symmetry operation	x,y,z		-y+2,x-y+1,z	
symmetry ID	1_555		1_765	
Number of atoms				
interface	56	19.7%	65	22.9%
surface	221	77.8%	221	77.8%
total	284	100.0%	284	100.0%
Number of residues				
interface	16	44.4%	18	50.0%
surface	36	100.0%	36	100.0%
total	36	100.0%	36	100.0%
Solvent-accessible area, Å				
interface	698.7	19.2%	665.3	18.3%
total	3642.4	100.0%	3642.4	100.0%
Solvation energy, kcal/mol				
isolated structure	-20.1	100.0%	-20.1	100.0%
gain on complex formation	-9.2	45.7%	-4.9	24.4%
average gain	-7.4	36.9%	-8.9	44.1%
P-value	0.252		0.846	

Interface Summary XML

	Structure 1		Structure 2	
Selection range	A		A	
class	Protein		Protein	
symmetry operation	x,y,z		-y+5/3,x-y+4/3,z+1/3	
symmetry ID	1_555		4_665	
Number of atoms				
interface	21	7.4%	27	9.5%
surface	221	77.8%	221	77.8%
total	284	100.0%	284	100.0%
Number of residues				
interface	4	11.1%	7	19.4%
surface	36	100.0%	36	100.0%
total	36	100.0%	36	100.0%
Solvent-accessible area, Å				
interface	238.9	6.6%	206.8	5.7%
total	3642.4	100.0%	3642.4	100.0%
Solvation energy, kcal/mol				
isolated structure	-20.1	100.0%	-20.1	100.0%
gain on complex formation	-3.8	18.9%	-3.0	14.9%
average gain	-2.8	13.8%	-3.7	18.3%
P-value	0.306		0.642	

Table 2. PISA interface summaries of CC3V2's inter-bundle interface (left) and intra-bundle interface (right).

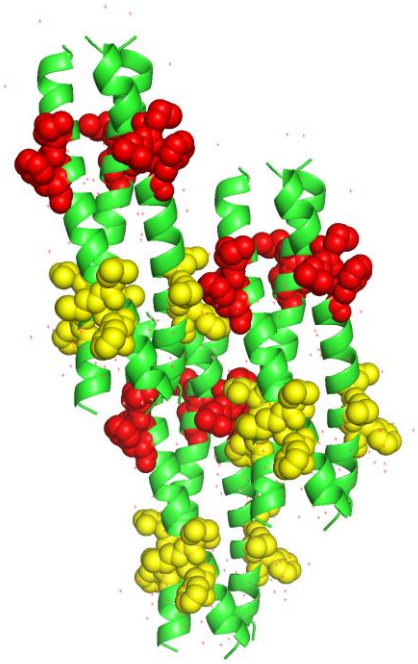

Figure 5.6. crystal structure of CC3V2. The top interface (Leu11, Met10, Phe14) is colored in red and the bottom interface (Leu24, Met25, Phe28) is colored in yellow, all shown in spheres. Model rendered in PyMol.

In order to force the correct mating order, a derivative of CC3V2 is proposed where both termini are PEGylated with 4 or 8 chain long PEG; the PEG chains are expected to associate with each other, effectively forcing the helices to align either in a parallel or an anti-parallel fashion without slipping. PEGlyation on α-helical peptides was shown to not disrupt the coiled-coil formation[14], thus PEGylating CC3B2 was expected to not disrupt its trimeric coiled-coil structure and instead direct the "correct" interface matching as the PEG chains associate with each other.

CC3V2: Ac-EVEALKE KVMLLEF KVAALEK EVLMLKF KVAALEK G-NH_2

CC3V2-PEG: CH_3-PEG_4-EVEALKE KVMLLEF KVAALEK EVLMLKF KVAALEK G-PEG_8-NH_2

CC3V2-PEG was synthesized via solid-phase peptide synthesis with N-terminal acetylation and C-terminal amidation to reduce termini charges, by preparative HPLC, characterized by MALDI and its purity was confirmed by MALDI and analytical HPLC. CC3V2-PEG is screened at CC3V2's crystallization conditions. In all conditions CC3V2-PEG showed stacked, irregular sheet self-assemblies mixed with fibrils (Figure 5.7). The expected sheet height, CC3V2's helix length of 5.0 nm and 12 chain long PEG length of 4.2 nm summing up to 9.2 nm can be observed via AFM, suggesting the possibility of CC3V2-PEG assembled as expected,

although its 2D propagation isn't optimized. All CC3V2-PEG samples show α-helical CD signatures with minima at 208 nm and 223 nm (Figure 5.8).

A B

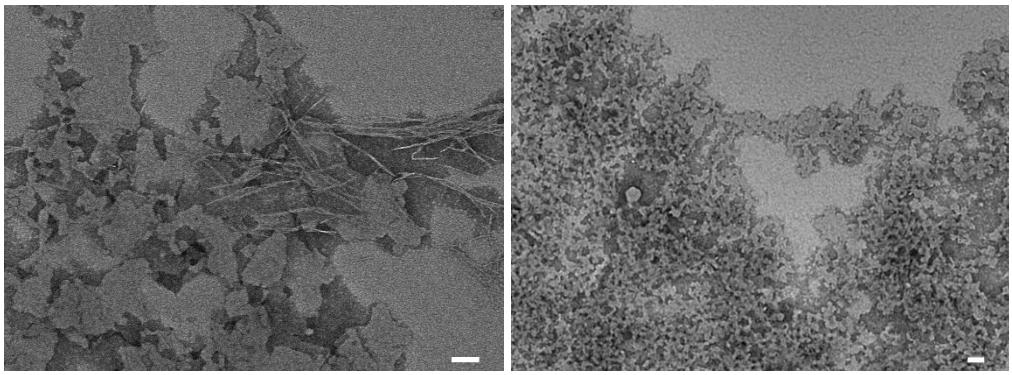

C

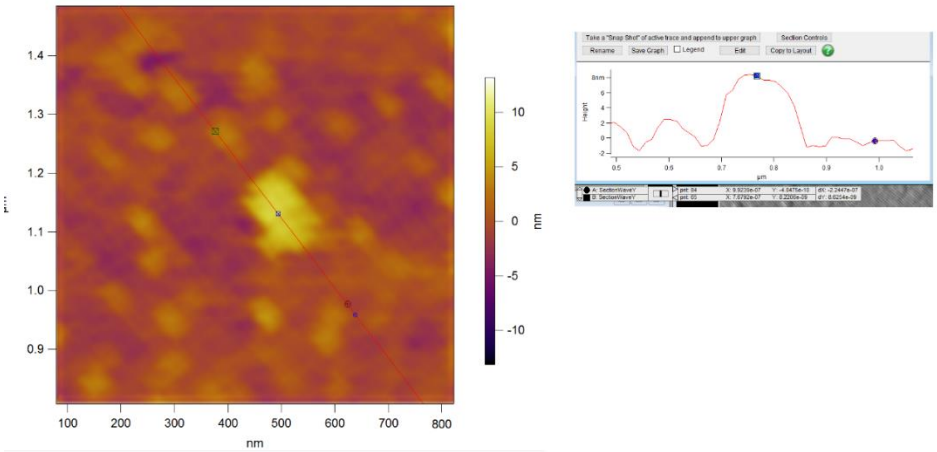

Figure 5.7. A, B) Representative TEM images of 467 μM CC3V2-PEG, after 3 days of assembly time, in A) 10 mM pH 6 MES, annealed at 90 ℃; B) 10 mM pH 8 TAPS. All scale bars = 100 nm. C) AFM image of 467 μM CC3V2-PEG, after 3 days of assembly time in 10 mM pH 6 MES, annealed at 90 ℃. Measured height = 8.83 nm.

A B

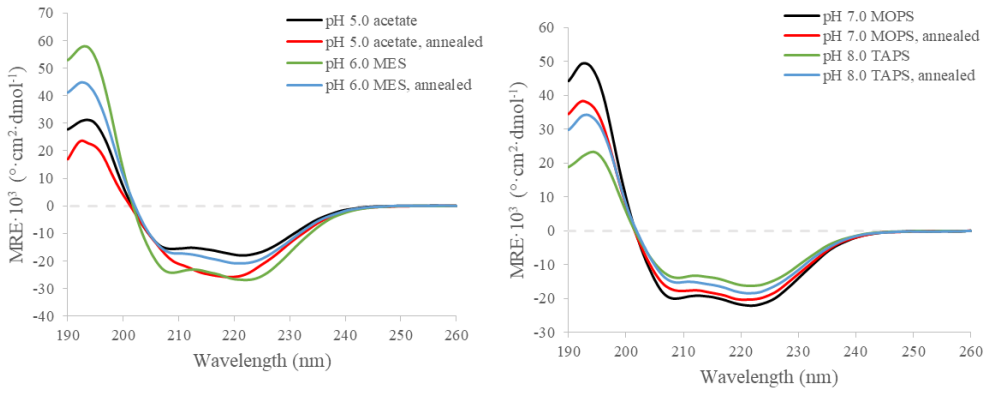

Figure 5.8. Circular dichroism spectra of of 467 μM CC3V2-PEG, in A) pH 5 – pH 8 buffer; B) pH 5 – pH 8 buffer, annealed at 90 ℃.

CC3V7 was screened both in the presence of NaCl with chloride ion as the source of anion, and without NaCl as a control in 718 μM peptide concentration, 10 mM pH 5 – 8 buffer, incubated at room temperature or annealed at 90 ℃. Interestingly, no sheet assemblies were found in conditions with various amount of NaCl added (Figure 5.9C, D); sheet assemblies were observed in conditions with no NaCl added (Figure 5.9A, B) with larger sheet size and better sheet edge definition observed in the 10 mM pH 5 acetate, annealed at 90 ℃ sample, but only in acetate buffers; CC3V7 in MES, MOPS and TAPS did not show sheet assemblies. All CC3V7 samples assembled with no NaCl presence show α-helical CD signatures with minima at 208 nm and 223 nm (Figure 5.10).

A B

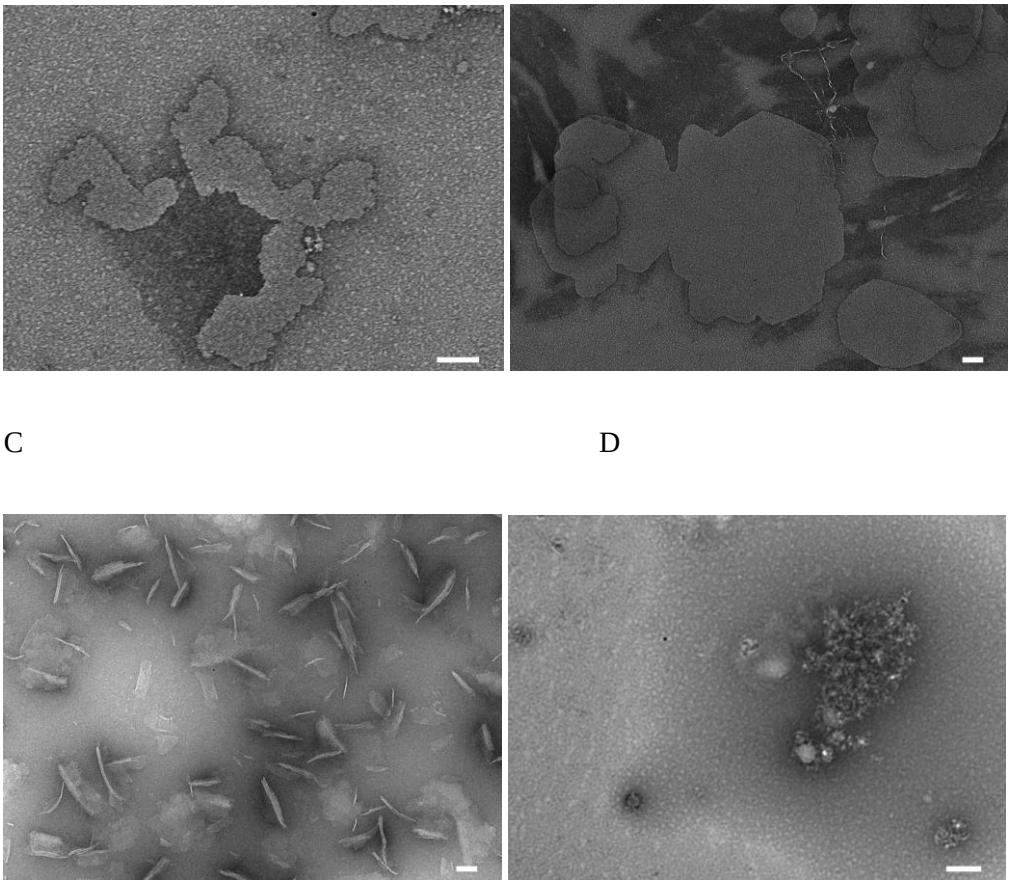

Figure 5.9. Representative TEM images of 718 μM CC3V7, after 1 day of assembly time, A) in 10 mM pH 5 acetate; B) in 10 mM pH 5 acetate, annealed at 90 ℃; C) in 10 mM pH 5 acetate and 10 mM NaCl, D) in 20 mM pH 7 MOPS and 20 mM NaCl. All scale bar = 100 nm.

A B

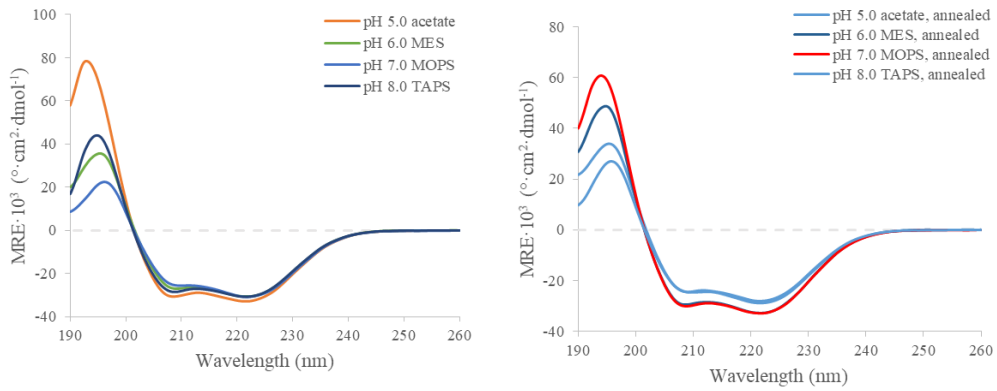

Figure 5.10. Circular dichroism spectra of 718 μM CC3V7, in A) pH 5 – pH 8 buffer; B) pH 5 – pH 8 buffer, annealed at 90 ℃.

CC3V8 was screened in 921 μM peptide concentration,10 mM pH 5 – 8 buffer, incubated at room temperature or annealed at 90 ℃. CC3V8 self-assembled in a variety of morphologies including fibrils and sheets with varied sizes dependent on pH (Figure 5.11); CC3V8's sheet self-assembly seems to be induced at pH 8, and optimized when annealed at 90 ℃. Both single-layer and stacked nanosheets were observed, thus it is possible CC3V8's interface alignment is also slipped similar to CC3V2's. All CC3V8 samples show α-helical CD signatures with minima at 208 nm and 223 nm (Figure 5.12).

A B

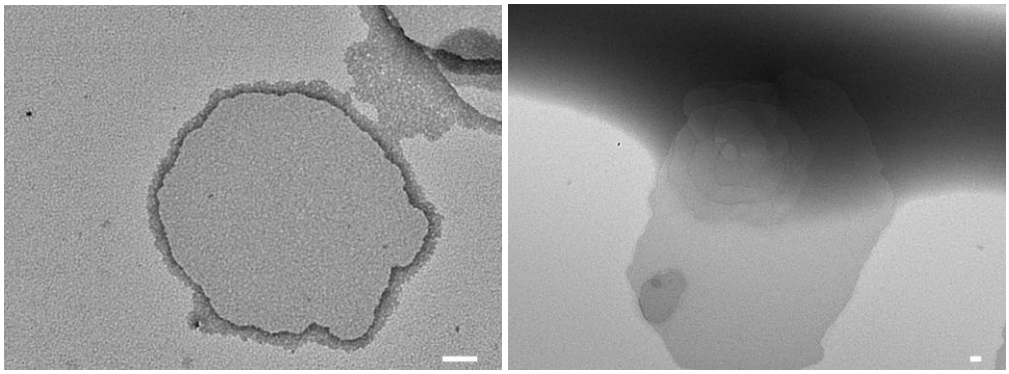

C D

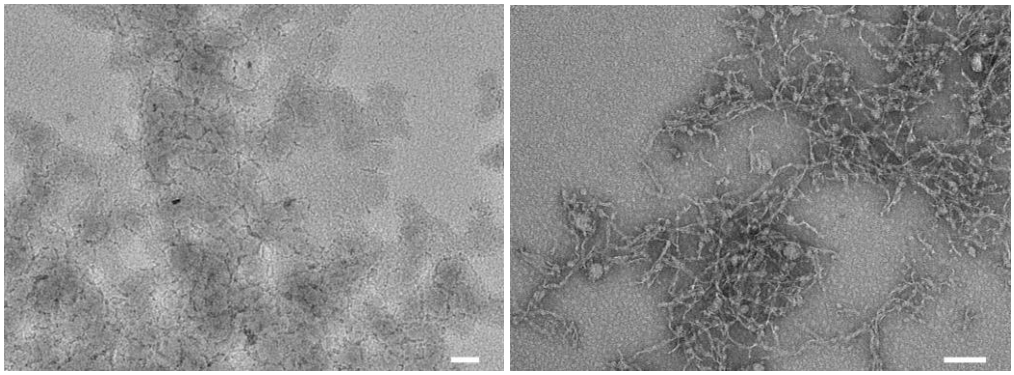

Figure 5.11 Representative TEM images of 921 μM CC3V8, after 8 days of assembly time, A, B) in 10 mM pH 8 TAPS, annealed at 90 ℃; C) in 10 mM pH 5 acetate, annealed at 90 ℃; D) in 10 mM pH 8 TAPS. All scale bar = 100 nm.

A B

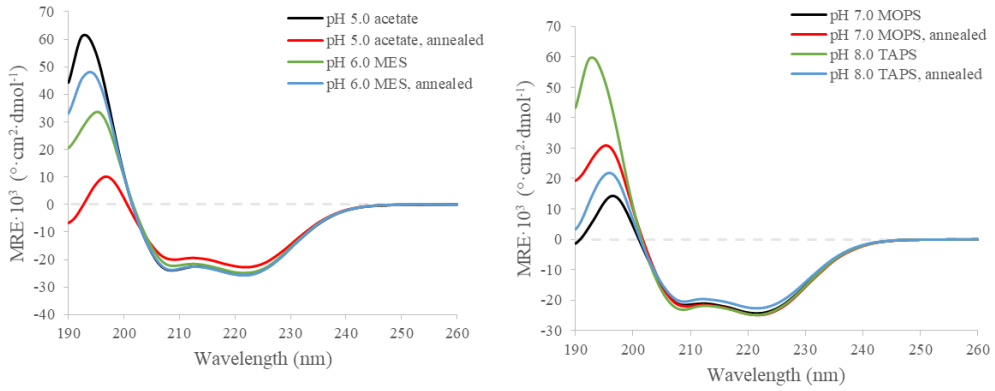

Figure 5.12. Circular dichroism spectra of 921 μM CC3V8, in A) pH 5 – pH 6 buffer; B) pH 7 – pH 8 buffer; both contains samples incubated at room temperature and annealed at 90 ℃.

5.3 Conclusion

In summary, the three 3TQ2-derived 5 heptad peptides shown above all have varied degrees of success. All 3 peptides aim to create 2 interfaces in two portions, the upper (residue 1-14) and the lower (residue 21-35) portion of the peptide based on 3TQ2. CC3V2 is characterized the most via crystallization, where the results showed the designs of two interfaces are successful at re-creating 3TQ2's intra-helical interface, however the two interfaces are identical and preferred to interact with each other to cause misalignment. Early time-points (< 24 hours) of CC3V2 did reveal some degree of 2D sheet self-assembly, however disappeared at later time-points as crystallization is more favored. PEGylating CC3V2 did not lead to optimized 2D nanosheet self-assembly, where PEG chains might force CC3V2 helices to align in-order.

CC3V7 and CC3V8 both designed two distinct interfaces, where one interface is inherited from 3TQ2. This theoretically would distinguish the two interfaces, thus misalignment should not occur. From preliminary screening data, they indeed show promising 2D assemblies, and should be characterized with high-resolution methods such as SAXS and cryo-EM to confirm their designs, and perhaps to be used as future design and functionalization guidelines.

Despite data being very preliminary, the fact CC3V2, CC3V7 and CC3V8 all showed promising 2D self-assemblies suggests this re-design using characterized protein structures with a desired space group symmetry could be a viable option. While there are more engineered interface candidates available to create distinguished interfaces in this system, computational redesign tools such as Rosetta[6] or DTERMen[15] may also prove to be powerful tools to further refine peptide 2D self-assemblies similar to how they were used to design protein crystals.

5.4 Methods

Materials and Reagents. All Fmoc protected amino acids were purchased from Aapptec; all other chemical reagents were purchased from Sigma-Aldrich, unless otherwise specified. Peptide synthesis resin was ordered from Applied Biosystems (Foster City, CA).

Peptide Synthesis. The CC3V2, CC3V7, CC3V8, CC3V2-PEG peptides were prepared via a microwave assisted solid phase peptide synthesis, on a CEM Liberty Blue instrument as the *N*-acetyl, *C*-amide capped derivatives. Applied Biosystem's Fmoc-PAL-PEG-PS resin was used for synthesizing these peptides at a 0.1 mmol scale. Coupling reactions were conducted with 0.2 M N-fluorenylmethyloxycarbonyl (Fmoc)-protected amino acids in N,N-Dimethylformamide (DMF, activated with 0.5 M N,N'-Diisopropylcarbodiimide (DIC) in DMF and 0.5 M Ethyl cyanohydroxyiminoacetate (oxyma) in DMF. The coupled amino acid was deprotected using 20% piperidine in DMF. All amino acids were deprotected with 5 ml piperidine solution, 75 ℃ temperature and 155 W microwave power for 15 seconds as the first stage, and 75 ℃ temperature and 155 W microwave power for 15 seconds as the second stage; coupled with 2.5 ml DIC solution, 75 ℃ temperature and 170 W microwave power for 15 seconds as the first stage, and with 2.5 ml oxyma solution, 90 ℃ temperature and 30 W microwave power for 110 seconds as the second stage. C-terminal amide modification was done after all amino acids were coupled, with 2.5 ml 20% acidic anhydride in DMF, 75 ℃ temperature and 155 W microwave power for 15 seconds as the first stage, and 75 ℃ temperature and 155 W microwave power for 15 seconds as the second stage. Peptides were cleaved from the resin by incubation at room temperature for 3 hours in a 20 ml cocktail consisting of 92.5% trifluoroacetic acid (TFA), 2.5% distilled water, 2.5% triisopropylsilane, and 2.5% 2,2'- (ethylenedioxy)-diethanethiol. The cleaved peptide solution was filtered and precipitated with 60 ml of 4 ℃ diethyl ether. The peptide/diethyl ether mixture was then centrifuged at 4 ℃ at 4,000 rpm for 10 min. The supernatant was then discarded, and the precipitate allowed to desiccate overnight. Following desiccation, the crude peptide gels were

resolubilized in 3 mL of a 50:50 mixture of acetonitrile and water (0.1% TFA additive) and purified by reversed-phase high-pressure liquid chromatography (HPLC) using two Shimadzu LC-20AP pumps running at 60 ml/min, a Shimadzu SPD-20A UV detector monitoring at 220 nm, on a Kinetex 5 μm C18 column, 250 mm long * 30 mm wide with a water-acetonitrile (0.1% TFA-additive) gradient. For CC3V2, the gradient used was 25% acetonitrile at 0 min, then gradually increased to 75% acetonitrile at 50 min, and finally was held at 90% acetonitrile for 10 min; CC3V2 eluted at 11.4 min. For CC3V2-PEG, the gradient used was 30% acetonitrile at 0 min, then gradually increased to 80% acetonitrile at 50 min, and finally was held at 90% acetonitrile for 10 min; CC3V2-PEG eluted at 10.1 min. For CC3V7, the gradient used was 25% acetonitrile at 0 min, then gradually increased to 75% acetonitrile at 50 min, and finally was held at 90% acetonitrile for 10 min; CC3V7 eluted at 11.8 min. For CC3V8, the gradient used was 25% acetonitrile at 0 min, then gradually increased to 75% acetonitrile at 50 min, and finally was held at 90% acetonitrile for 10 min; CC3V8 eluted at 12.5 min. Peptide masses were confirmed using MALDI-TOF mass spectrometry on an Applied Biosystems AB4700 Proteomics analyzer in reflectron positive ion mode, with α-Cyano-4-hydroxycinnamic acid as the matrix. Purified HPLC fractions were then lyophilized, sealed, and stored at -30 ℃.

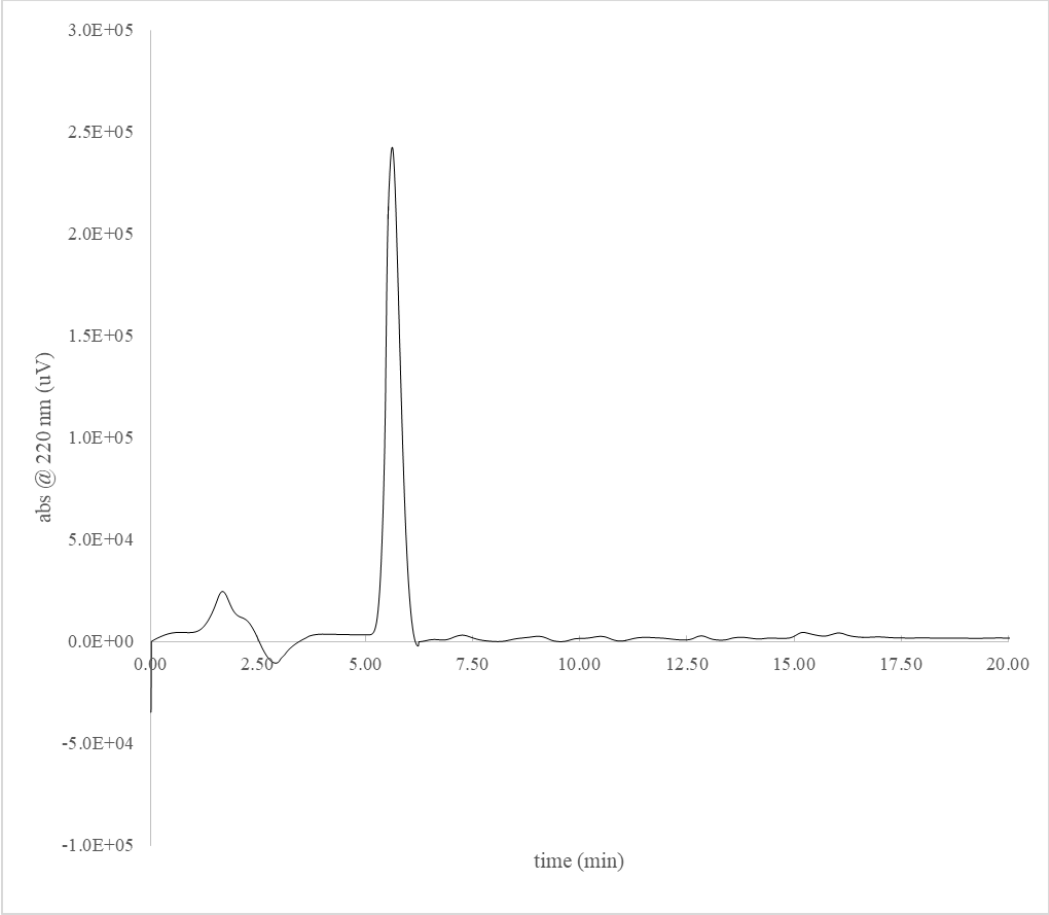

Figure 5.13. Analytical HPLC trace of CC3V2.

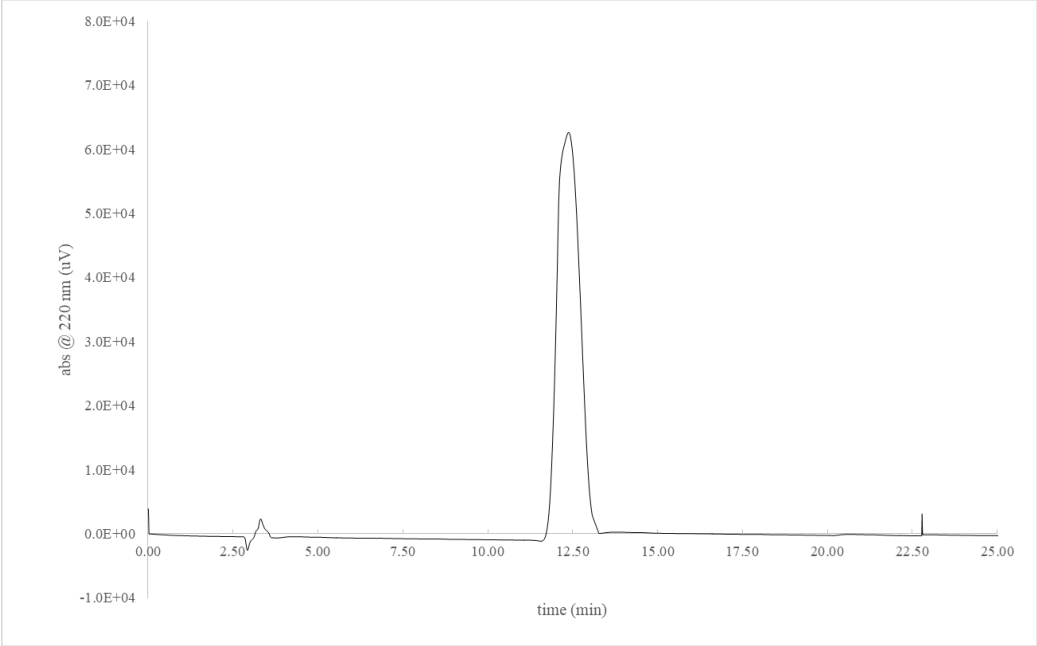

Figure 5.14. Analytical HPLC trace of CC3V2PEG.

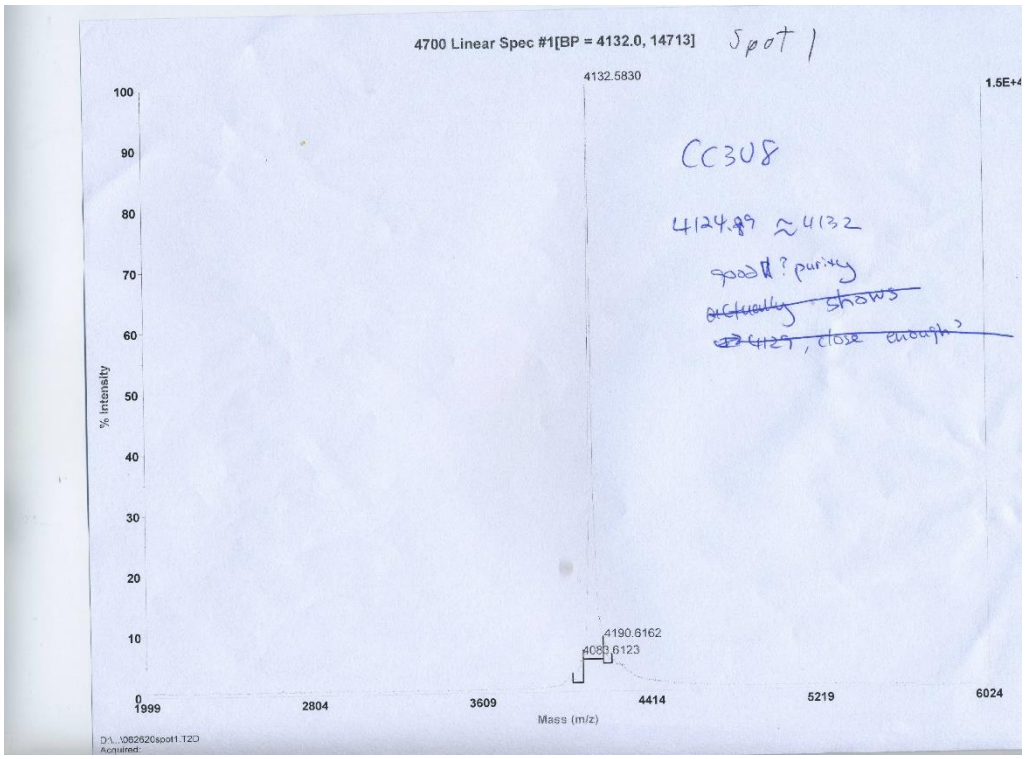

Figure 5.15. MALDI-TOF MS spectrum of CC3V8. Expected mass = 4125 g/mol.

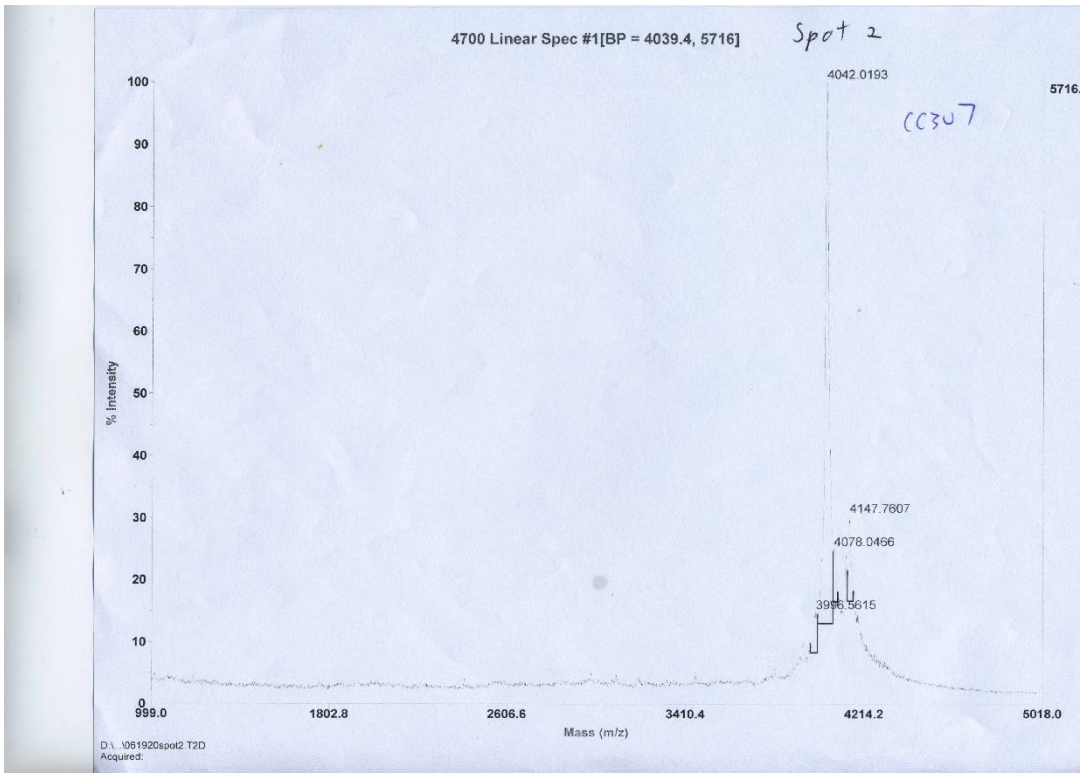

Figure 5.16. MALDI-TOF MS spectrum of CC3V7. Expected mass = 4125 g/mol.

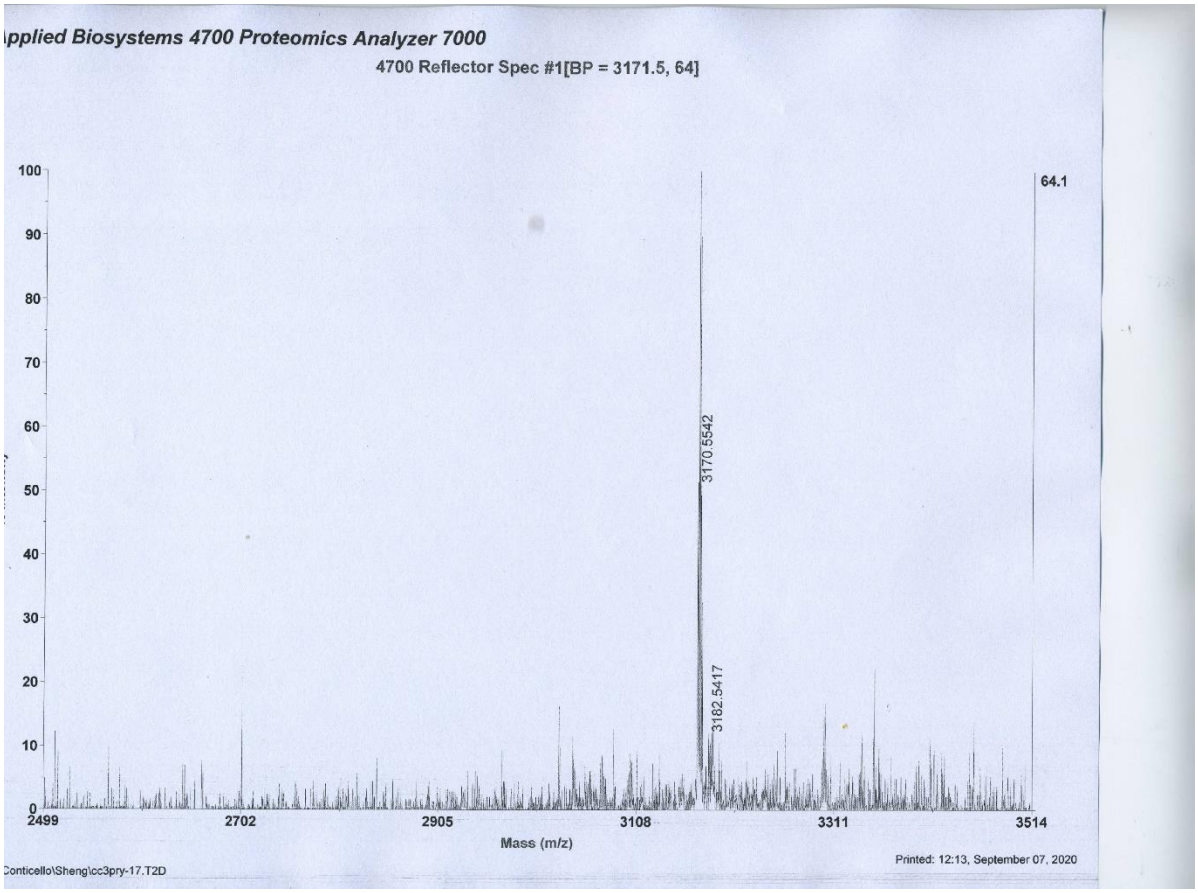

Figure 5.17. MALDI-TOF MS spectrum of ROX321gIle. Expected mass = 2355 g/mol.

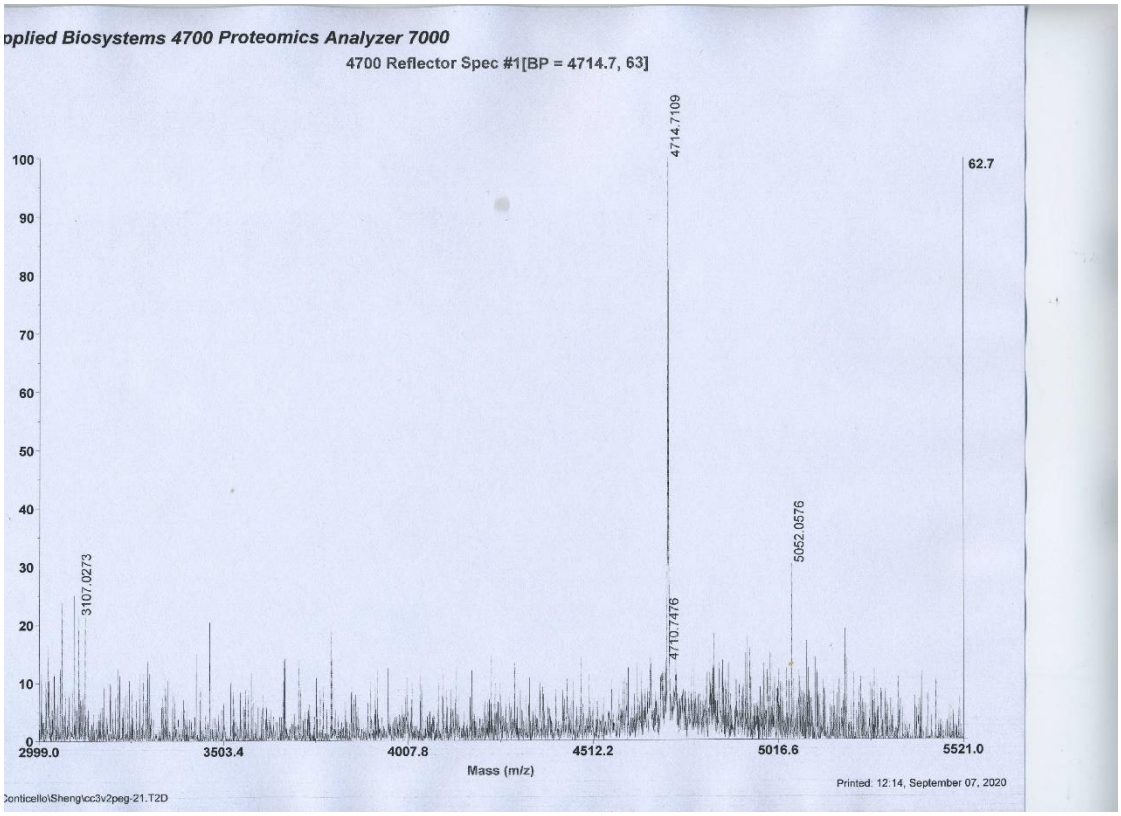

Figure 5.18. MALDI-TOF MS spectrum of CC3V2-PEG. Expected mass = 2355 g/mol.

Peptide Assembly. Stock solutions of CC3V2, CC3V2PEG, CC3V7, and CC3V8 were prepared by solubilizing 0.5 to 1.5 mg of purified, lyophilized peptide in 10 mM acetate, pH 2.6, 2.9 and 5; 10 mM MES, pH 6.0 and 6.5; 10 mM MOPS, pH 7.0 and 7.5; 10 mM TAPS, pH 8.0 and 8.5; 10 mM CAPS, pH 9.0 and 9.5; or 10 mM CHES, pH 10.0 buffer, at a final peptide concentration of 189 μM to 556 189 μM. Immediately after mixture, the solutions were titrated to the respective buffer pH using 100 mM sodium hydroxide solution except for the PSMa3 sample with HPLC water. Half of all solutions were thermally annealed using the following thermal cycler protocol: (1) rapid heating to 90 ℃ for 30 minutes; and (2) cooling to 25 ℃ at a rate of 0.2 ℃ / minute.

Circular Dichroism Spectropolarimetry. CD measurements were performed on a Jasco J-1500 CD spectropolarimeter in 0.1 mm quartz cells (Hellma Analytics), at various peptide concentrations,

where the final HT voltage reading at 190 nm was less than 500 V in all measurements. Spectra were recorded from 260 to 190 nm at a scanning rate of 100 nm/min and a data pitch of 0.2 nm. CD melting experiments were performed in the temperature range of 5 ℃ to 95 ℃, at a heating rate of 60 ℃/hour; the intensity of the CD signal at 209 nm was monitored as a function of temperature.

Transmission Electron Microscopy. TEM specimens were prepared from aqueous solutions of CC3V2, CC3V2PEG, CC3V7, and CC3V8. To cover the entire sample grid, 4 μL of the samples were deposited onto 200 mesh carbon-coated copper grids from Electron Microscopy Services (Hatfield, PA). After 90 seconds of incubation period, the samples were wicked away until a thin film of sample remained, then the grids were stained with 1% uranyl acetate solution, filtered with 0.2 μm Whatman filter from G.E. Healthcare Services. After 60 seconds of stain incubation period, all liquids were wicked away, and the grids were dried in a tabletop desiccator under vacuum. TEM measurements were acquired on a Hitachi HT-7700 transmission electron microscope with a tungsten filament and AMT CCD camera, at an accelerating voltage of 80 kV.

References

1. Brodin, J. D.; Ambroggio, X. I.; Tang, C.; Parent, K. N.; Baker, T. S.; Tezcan, F. A., Metal-directed, chemically tunable assembly of one-, two- and three-dimensional crystalline protein arrays. *Nature Chemistry* **2012,** *4* (5), 375-382.
2. Jang, H.-S.; Lee, J.-H.; Park, Y.-S.; Kim, Y.-O.; Park, J.; Yang, T.-Y.; Jin, K.; Lee, J.; Park, S.; You, J. M.; Jeong, K.-W.; Shin, A.; Oh, I.-S.; Kwon, M.-K.; Kim, Y.-I.; Cho, H.-H.; Han, H. N.; Kim, Y.; Chang, Y. H.; Paik, S. R.; Nam, K. T.; Lee, Y.-S., Tyrosine-mediated two-dimensional peptide assembly and its role as a bio-inspired catalytic scaffold. *Nat Commun* **2014,** *5* (1), 3665.
3. Jiang, T.; Xu, C.; Liu, Y.; Liu, Z.; Wall, J. S.; Zuo, X.; Lian, T.; Salaita, K.; Ni, C.; Pochan, D.; Conticello, V. P., Structurally Defined Nanoscale Sheets from Self-Assembly of Collagen-Mimetic Peptides. *Journal of the American Chemical Society* **2014,** *136* (11), 4300-4308.
4. Jiang, T.; Xu, C. F.; Zuo, X. B.; Conticello, V. P., Structurally Homogeneous Nanosheets from Self-Assembly of a Collagen-Mimetic Peptide. *Angew Chem Int Edit* **2014,** *53* (32), 8367-8371.
5. Magnotti, E. L.; Hughes, S. A.; Dillard, R. S.; Wang, S. Y.; Hough, L.; Karumbamkandathil, A.; Lian, T. Q.; Wall, J. S.; Zuo, X. B.; Wright, E. R.; Conticello, V. P., Self-Assembly of an alpha-Helical Peptide into a Crystalline Two-Dimensional Nanoporous Framework. *J Am Chem Soc* **2016,** *138* (50), 16274-16282.
6. Gonen, S.; DiMaio, F.; Gonen, T.; Baker, D., Design of ordered two-dimensional arrays mediated by noncovalent protein-protein interfaces. *Science* **2015,** *348* (6241), 1365.
7. Zhang, H. V.; Polzer, F.; Haider, M. J.; Tian, Y.; Villegas, J. A.; Kiick, K. L.; Pochan, D. J.; Saven, J. G., Computationally designed peptides for self-assembly of nanostructured lattices. *Science Advances* **2016,** *2* (9), e1600307.
8. Lanci, C. J.; MacDermaid, C. M.; Kang, S.-g.; Acharya, R.; North, B.; Yang, X.; Qiu, X. J.; DeGrado, W. F.; Saven, J. G., Computational design of a protein crystal. *Proceedings of the National Academy of Sciences* **2012,** *109* (19), 7304.
9. Dai, B.; Li, D.; Xi, W.; Luo, F.; Zhang, X.; Zou, M.; Cao, M.; Hu, J.; Wang, W.; Wei, G.; Zhang, Y.; Liu, C., Tunable assembly of amyloid-forming peptides into nanosheets as a retrovirus carrier. *Proceedings of the National Academy of Sciences* **2015,** *112* (10), 2996.
10. Lin, Y.; Thomas, M. R.; Gelmi, A.; Leonardo, V.; Pashuck, E. T.; Maynard, S. A.; Wang, Y.; Stevens, M. M., Self-Assembled 2D Free-Standing Janus Nanosheets with Single-Layer Thickness. *J Am Chem Soc* **2017,** *139* (39), 13592-13595.
11. Magnotti, E. L.; Hughes, S. A.; Dillard, R. S.; Wang, S.; Hough, L.; Karumbamkandathil, A.; Lian, T.; Wall, J. S.; Zuo, X.; Wright, E. R.; Conticello, V. P., Self-Assembly of an α-Helical Peptide into a Crystalline Two-Dimensional Nanoporous Framework. *J Am Chem Soc* **2016,** *138* (50), 16274-16282.
12. Krissinel, E.; Henrick, K., Inference of Macromolecular Assemblies from Crystalline State. *Journal of Molecular Biology* **2007,** *372* (3), 774-797.
13. Ogihara, N. L.; Weiss, M. S.; Degrado, W. F.; Eisenberg, D., The crystal structure of the designed trimeric coiled coil coil-V(a)L(d): Implications for engineering crystals and supramolecular assemblies. *Protein Sci* **1997,** *6* (1), 80-88.
14. Klok, H.-A.; Vandermeulen, G. W. M.; Nuhn, H.; Rösler, A.; Hamley, I. W.; Castelletto, V.; Xu, H.; Sheiko, S. S., Peptide mediated formation of hierarchically organized solution and solid state polymer nanostructures. *Faraday Discussions* **2005,** *128* (0), 29-41.
15. Zhou, J.; Panaitiu, A. E.; Grigoryan, G., A general-purpose protein design framework based on mining sequence–structure relationships in known protein structures. *Proceedings of the National Academy of Sciences* **2020,** *117* (2), 1059.

Chapter 6: Conclusion

This thesis explored and characterized the designability of a recently discovered peptide structure, cross-α, and a well-explored peptide structure, coiled-coil. The first two chapters show two natural peptides, phenol soluble modulin (PSM) α3 and β2 secreted by *Staphylococcus aureus* could self-assemble into nanotubes via the lateral association of their cross-α fibril assemblies, and both PSMα3 and PSMβ2 nanotube atomic structures were analyzed by cryo-EM reconstruction, SAXS and STEM. PSMα3 could selectively assemble into nanotubes in extremely acidic (~pH 2) conditions and high temperature (heated above 80 ℃) conditions, as well as selectively and reversibly assemble in pH 8 when incubated at room temperature or 37 ℃. PSMβ2 could assemble into nanotubes in pH neutral to very basic (pH 10.5) conditions, although at a lower selectivity due to PSMβ2 adopting a helix-turn-helix monomer structure. The selectivity and reversibility of these nanotubes open possibilities of utilizing such higher-order cross-α assemblies as designable smart nanomaterials. The third chapter explored the designability of cross-α fibrils, where a coiled-coil peptide, ROX321 selectively self-assembles into a cross-α fibril instead of a traditional coiled-coil bundle or barrel. ROX321's cross-α fibril atomic structure was also further analyzed by cryo-EM reconstruction and SAXS. Leu to Ile mutations at ROX321's cross-α stacking interface (ROX321eIle, ROX321gIle) showed an interesting cross-α selectivity towards a specific stacking interface. In the last chapter, a series of coiled-coil peptides (CC3V2, CC3V7, CC3V8) are designed to explore designing inter-coiled-coil interfaces to promote 2D lateral association and afford nanosheet self-assembly. The preliminary results of CC3 peptides showed the designed peptides successfully propagates in a 2D fashion, and the crystal structure of CC3V2 showed CC3V2 monomers indeed associate through the designed interfaces.

Such discovery in peptide self-assembly